

**Real-Time Dynamics and Critical Phenomena
of Quantum Impurity Systems**

A Hybrid Numerical Renormalization Group Approach

Dissertation
zur Erlangung des Doktorgrades
der Naturwissenschaften
der Fakultät Physik an der
Technischen Universität Dortmund

vorgelegt von

Fabian Güttge
aus Köln

Oktober 2012

Erster Gutachter Prof. Dr. Frithjof B. Anders
Zweiter Gutachter Prof. Dr. Götz S. Uhrig
Tag der mündlichen Prüfung 8. Februar 2013

Kontakt zum Autor fabian.guettge@tu-dortmund.de

*I'm astounded by people who want to 'know' the universe
when it's hard enough to find your way around Chinatown.*

Woody Allen

Contents

Abstract	v
Zusammenfassung	vii
Publication list	ix
Table of Abbreviations	xi
Introduction	1
1 Numerical Methods	5
1.1 Overview of methods	6
1.1.1 Exact diagonalization	6
1.1.2 Renormalization group	7
1.1.3 Quantum monte carlo	7
1.1.4 Numerical and density-matrix renormalization group	7
1.1.5 Dynamical mean-field theory	8
1.2 Matrix product states	9
1.2.1 A-matrix representation	9
1.2.2 Application of an operator	11
1.2.3 Change of basis	12
1.2.4 Expectation values	12
1.2.5 Reduced density matrix	13
1.3 Numerical renormalization group	15
1.3.1 Discretization and mapping	15
1.3.2 Iterative diagonalization	20
1.3.3 Bosonic reservoir	24
1.3.4 Time dependence	26
1.4 Density-matrix renormalization group	31
1.4.1 Infinite DMRG	32
1.4.2 Finite DMRG	39
1.4.3 Time-dependent DMRG	39

1.5	Summary	41
2	Bosonic Models	45
2.1	Spin-boson model	46
2.1.1	Model Hamiltonian	46
2.1.2	Phase transition	48
2.1.3	Physical realizations	50
2.2	Dissipative harmonic oscillator	52
2.2.1	Model	53
2.2.2	Occupation number	54
2.2.3	Results	54
2.2.4	Mass-flow error	56
2.3	Toy models	64
2.3.1	Displaced oscillator	65
2.3.2	Spin with bosons	68
2.4	Numerical renormalization group results	77
2.4.1	Choice of parameters	77
2.4.2	NRG level flow	78
2.4.3	Phase diagram	79
2.4.4	Critical exponent	81
2.4.5	Flow of critical coupling strength	81
2.4.6	Numerical errors	84
2.5	Density-matrix renormalization group results	85
2.5.1	Choice of parameters	86
2.5.2	Optimal bosonic basis	87
2.5.3	Phase diagram	92
2.5.4	Critical exponents	93
2.5.5	Without DMRG sweeping	94
2.5.6	Numerical errors	95
2.6	Summary	96
3	Discretization Artifacts in the Resonant-Level Model	97
3.1	Objective of the studies	99
3.2	Resonant-level model	100
3.2.1	Model Hamiltonians	101
3.2.2	Green's function solution for the continuous model	101
3.2.3	Exact diagonalization of the discretized model	105
3.3	Reflections within the chain	106
3.3.1	Tight-binding chain	107
3.3.2	Wilson chain	109
3.3.3	Hybrid chains	113

3.4	Density of states	127
3.5	Summary	128
4	Hybrid Method	129
4.1	Description of new hybrid method	130
4.1.1	Wave-function formulation	130
4.1.2	Evaluation of expectation values	131
4.1.3	Interface between the TD-NRG and the hybridized approach	133
4.1.4	Hybrid NRG+DMRG	137
4.2	Hybrid method results for the resonant-level model	140
4.2.1	Choice of parameters	141
4.2.2	Norm of initial state	141
4.2.3	Time-dependence	145
4.3	Summary	148
5	Nonequilibrium Simulations of Interacting Resonant-Level Model	151
5.1	Model Hamiltonians	152
5.2	Fixed point properties	153
5.3	Choice of parameters	154
5.4	Determining effective Γ	155
5.5	Time dependence	156
5.5.1	Fidelity	158
5.5.2	Von Neumann entropy	159
5.5.3	Analytic frequency and damping	160
5.6	Numerical errors	161
5.7	Comparison to TD-DMRG	164
5.8	Summary	165
6	Conclusions	167
A	Diagonalization of the Dissipative Harmonic Oscillator	171
A.1	Continuous bath	171
A.1.1	Critical coupling	171
A.1.2	Critical exponent	173
A.2	Discretized bath	174
A.2.1	Green's function	178
B	Fits of Critical Exponents	179
C	Diagonalization of Resonant-Level Model	181
C.1	Level occupation	181
C.2	Propagation time	183

D Strong Coupling Treatment of Interacting Resonant-Level Model	185
Bibliography	189
Acknowledgments	201
Lebenslauf	203

Abstract

Since its proposal in 1975 the numerical renormalization group (NRG) has developed to a widely used standard tool to simulate quantum impurity systems (QISs) at low temperatures. The three essential steps of this method are to discretize the bath on a logarithmic mesh, map it to a Wilson chain, and then diagonalize this chain iteratively. There are numerous extensions to the NRG two of which are of relevance in this work: the treatment of bosonic reservoirs and the investigation of real-time dynamics. With the bosonic NRG we find wrong critical exponents for a quantum phase transition (QPT) of the spin-boson model (SBM) and we observe a discrepancy between the real-time dynamics of a system with a continuous and a discretized bath.

The iterative diagonalization of the Wilson chain neglects at each iteration the rest-chain. For bosonic systems this leads to an iteration dependent renormalization of the critical coupling. On the basis of the sub-ohmic SBM we show that this effect leads to wrong critical exponents. We show by density-matrix renormalization group (DMRG) calculations that one recovers the correct results by taking the rest-chain properly into account. This requires an optimal bosonic basis which we determine in the course of the DMRG variationally.

On the basis of nonequilibrium calculations for the resonant-level model (RLM) we show that the logarithmic discretization leads to unphysical results of the impurity occupation number. We attribute these to internal reflections of a charge wave within the Wilson chain. We propose an optimal chain construction avoiding these reflections. These chains consist of two Wilson chains patched together.

Because the separation of energy scales is lost for such systems the NRG is rendered unsuitable. Hence, we develop a new hybrid method: the NRG is used to construct an effective low-energy Hamiltonian which, in turn, is simulated with the time-dependent density-matrix renormalization group (TD-DMRG). This allows to simulate the system on time scales unreachable with the TD-DMRG. The new method is tested on the basis of the RLM. As a first application of the new method it is applied to the interacting resonant-level model (IRLM). For this model we find interaction-enhanced oscillations and new time scales which are not present in the thermodynamics. The results of the new hybrid method are in excellent agreement with analytic predictions based on an

expansion in $\frac{1}{U}$. Our new hybrid method yields not only correct results for $U \rightarrow 0$ and $U \rightarrow \infty$ but it is applicable in the whole parameter regime.

Zusammenfassung

Die Numerische-Renormierungsgruppe (NRG) hat sich zu einem Standardwerkzeug zur Simulation von Quantenstörtstellensystemen bei tiefen Temperaturen entwickelt. Für solche Simulationen sind drei Schritte notwendig: das Bad wird logarithmisch diskretisiert, auf eine Wilson Kette abgebildet und diese wird iterativ diagonalisiert. Für die NRG existieren zahlreiche Erweiterungen, von denen zwei für diese Arbeit relevant sind: zum einen die Behandlung bosonischer Systeme und zum anderen die Untersuchung von zeitabhängigen Prozessen. Wir stellen fest, dass die bosonische NRG falsche kritische Exponenten für den Phasenübergang des Spin-Bose-Modells (SBM) liefert und dass bei Nicht-Gleichgewichtsrechnungen Diskrepanzen zwischen den Ergebnissen eines kontinuierlichen und eines diskretisierten Bades bestehen.

Durch die iterative Diagonalisierung der Wilson-Kette wird auf jeder Iterationsstufe eine Restkette vernachlässigt. Bei bosonischen Systemen führt dies zu einer iterationsabhängigen Renormierung der kritischen Kopplung. Anhand des Spin-Bose-Modells im sub-ohmischen Regime zeigen wir, dass dieser Effekt zu falschen kritischen Exponenten führt. Mit Dichtematrix-Renormierungsgruppe (DMRG) Rechnungen zeigen wir, dass man, unter Berücksichtigung der Restkette, die korrekten kritischen Exponenten bestimmen kann. Dies setzt eine optimierte bosonische Basis voraus, die wir während der DMRG variationell bestimmen.

Anhand von Nicht-Gleichgewichtsberechnungen für das Resonant-Level-Model (RLM) zeigen wir, dass die logarithmische Baddiskretisierung zu unphysikalischen Ergebnissen der Störstellenbesetzung führt. Die Ursache hierfür führen wir auf interne Reflektionen einer Ladungswelle in der Wilson-Kette zurück. Um diese zu vermeiden, schlagen wir einen optimierten aus zwei aneinandergehängten Wilson-Ketten Kettenaufbau vor.

Da es bei diesen Systemen keine klare Trennung der Energieskalen mehr gibt, ist die NRG nicht für die Berechnung solcher Systeme geeignet. Daher entwickeln wir eine neue Hybrid-Methode, bei der die NRG einen effektiven Niederenergie-Hamiltonoperator erzeugt, der anschließend mit der zeitabhängigen Dichtematrix-Renormierungsgruppe (TD-DMRG) simuliert wird. Durch dieses Schema erreicht man Zeitskalen, die sonst mit der TD-DMRG unerreichbar bleiben. Die neue Methode wird am RLM getestet. Als erste Anwendung der neuen Methode wird diese auf das wech-

selwirkende Resonant-Level-Modell (IRLM) angewendet. Bei diesem Modell beobachten wir durch die Wechselwirkung hervorgerufene Oszillationen und neue Zeitskalen, die keine thermodynamische Entsprechung haben. Die Ergebnisse der neuen Hybrid-Methode reproduzieren analytische Vorhersagen basierend auf einer $\frac{1}{U}$ Entwicklung. Die neue Hybrid-Methode liefert nicht nur in den Grenzwerten $U \rightarrow 0$ und $U \rightarrow \infty$ korrekte Ergebnisse, sondern ist im vollständigen Parameterregime anwendbar.

Publication list

During the course of the work for this thesis several articles have been published or made available as preprints on arxiv.org.

- Vojta, M.; Bulla, R.; Güt tge, F.; Anders, F.: *Mass-flow error in the numerical renormalization-group method and the critical behavior of the sub-Ohmic spin-boson model*. In: [Phys. Rev. B 81 \(2010\), p. 075122](#).
- Eidelstein, E.; Schiller, A.; Güt tge, F.; Anders, F. B.: *Coherent control of correlated nanodevices: A hybrid time-dependent numerical renormalization-group approach to periodic switching*. In: [Phys. Rev. B 85 \(2012\), p. 075118](#).
- Güt tge, F.; Anders, F. B.; Schollwö ck, U.; Eidelstein, E.; Schiller, A.: *Hybrid NRG-DMRG approach to real-time dynamics of quantum impurity systems*. [arXiv:1206.2186](#)

Table of Abbreviations

CNOT	controlled not
CFE	continued fraction expansion
CET	Chebyshev expansion technique
DHO	dissipative harmonic oscillator
DMFT	dynamical mean field theory
DMRG	density-matrix renormalization group
DOS	density of states
DWC	double Wilson chain
ED	exact diagonalization
IRLM	interacting resonant-level model
iTEBD	infinite time-evolving block decimation
NRG	numerical renormalization group
NRG+DMRG	numerical renormalization group density-matrix renormalization group hybrid
MPO	matrix product operator
MPS	matrix product state
NN	nearest-neighbor
PEPS	projected entangled pair state
QCP	quantum critical point
QD	quantum dot
QMC	quantum Monte Carlo
QIS	quantum impurity system
QPT	quantum phase transition
RG	renormalization group
RLM	resonant-level model
SBM	spin-boson model
SIAM	single impurity Anderson model
SVD	singular-value decomposition
TEBD	time-evolving block decimation
TD-DMRG	time-dependent density-matrix renormalization group
TD-NRG	time-dependent numerical renormalization group
TSD	Trotter-Suzuki decomposition
WTBC	Wilson tight-binding hybrid chain

Introduction

When in 1934 de Haas, de Boer, and van dën Berg brought their gold samples to low temperatures and measured an unexpected minimum of the electrical resistance at $T = 3.7\text{ K}$ [1], one could hardly imagine the profound impact this discovery would have on the field of condensed matter physics and beyond until the present day. Not only did experiments like theirs inspire physicists to carry out further low-temperature experiments, but theoretical tools devised to understand the observed effect are indispensable today.

Soon it became clear that the resistance minimum is due to impurity atoms diluted in the host metal. But it took another 30 years before Jun Kondo provided a physical explanation of the observations [2, 3] and since then it is usually referred to as the Kondo effect.

The Kondo effect is only one of many important discoveries in the field of low-temperature physics. Another prominent example is the discovery of superconductivity by Kamerlingh-Onnes in 1911 [4] and its explanation by Bardeen, Cooper, and Schrieffer in 1957 [5]. A phenomenon similar to superconductivity is provided by Bose-Einstein condensation, but the history of its discovery is just the opposite: it was first theoretically predicted – by Bose and Einstein in 1924/25 – and then experimentally observed in 1995 in ultracold gases [6, 7], sparking a vast research activity in the field of ultracold gases [8, 9]. These experiments include studying Mott insulators [10, 11] or exploring the path towards quantum simulators [12, 13] and may lead to nonequilibrium experiments simulating complicated Hamiltonians [14].

Besides impurity atoms diluted in host metals another physical realization of quantum impurity systems (QISs) has recently gained a lot of attention: the so-called quantum dots (QDs) [15]. Usually a QD is a charged semiconductor device. The key feature of a QD is that the charge carriers are confined in all space dimensions and therefore exhibit discrete energy levels. Hence, one sometimes refers to QDs as artificial atoms. If the number of energy levels is reduced to just two, one can store one qubit with a QD. A lot of research aims at building quantum computers with qubits realized by QDs [16, 17, 18].

If one uses a spin in a QD as a qubit (like in all physical realizations of qubits) it is technically important to have coherent control over the spin and that the spin relaxes

slowly [19]. An experimental example for the transfer of an electron onto a QD and the measurement of the electron's spin relaxation rate is given in Ref. 20 .

As techniques to experimentally simulate or theoretically describe realistic systems for long times are still limited, one has to revert to simple model systems. An archetypical model Hamiltonian in this field is the so-called Kondo model which describes a single impurity atom represented as one spin diluted in an uncorrelated host metal. Of high relevance for this thesis are furthermore the spin-boson model (SBM) [21] and the interacting resonant-level model (IRLM) [22, 23].

The SBM is used to model any two-level system in a dissipative environment. The IRLM is well suited to carry out nonequilibrium studies of a QD: the QD is represented by a single electronic level tunnel-coupled to a lead. Furthermore, the interaction due to the Coulomb repulsion between the dot and the lead electrons is taken into account.

One can theoretically describe a QD coupled to some leads by the Anderson impurity model [24]. This model, which has attracted a lot of interest by itself [3], contains, in a limiting case, the Kondo model and hence the Kondo effect is experimentally observable in a QD [25, 26, 27].

It is astonishing that in the Kondo model a single impurity can have such a strong effect on a considerably larger system. At the time of its proposal [2] none of the available methods succeeded at explaining this behavior. Treating the model with perturbative methods fails for temperatures below the so-called Kondo temperature T_K . Therefore, theoretical methods to solve the Kondo model and to understand the reason for this unexpected behavior have been devised in the 1970/80s [3].

In 1975 Wilson succeeded with his numerical renormalization group (NRG) in explaining the Kondo effect [28] and proposed a new method capable of solving a certain class of problems, quantum impurity systems (QISs), in which the Kondo model falls. Since then the NRG was used to investigate several different QISs [29]. A few years later, in 1980, Bethe ansatz calculations by Andrei [30] and Vigman [31] yielded an exact solution for the Kondo model.

When simulating the Kondo model with the NRG the host metal is modeled as a continuous bath of fermions. Thus, the total system has an infinite number of degrees of freedom. This poses a challenge for numerical simulations, as the dimension of the Hamilton matrix is infinite. In order to reduce the number of degrees of freedom one discretizes the continuous bath by selecting only some energy levels to represent the whole energy spectrum [28]. However, the Hilbert space of the system grows exponentially with the number of selected energy states and, therefore, only small systems are treatable.

The way the NRG approaches the issue of an exponentially growing Hilbert space is to let the system grow iteratively and truncate the Hilbert space to an upper dimension by discarding high-energy states at each iteration step [28]. A different approach, inspired by this idea, is taken by the density-matrix renormalization group (DMRG):

here one discards the eigenstates of the density matrix with a low weight [32]. This conceptual difference in the truncation scheme has profound consequences on the results and the treatable models: the NRG calculates some low-energy states and is only applicable to QISs, whereas the DMRG determines the ground state and is applicable to generic one-dimensional systems with short-range interactions.

For QISs both methods have in common that one has to discretize the continuous bath and map it to a chain: for the NRG this is a necessarily a so-called Wilson chain [28], whereas the DMRG is able to handle Wilson as well as other chains. In any case one neglects an infinite number of bath states causing discretization artifacts [33, 34, 35] which may eventually corrupt the results of the simulation.

It is the objective of this thesis to calculate nonequilibrium real-time dynamics for QISs very accurately and to determine critical exponents of the SBM. In the course of these simulations we identify discretization artifacts appearing due to the neglect of some parts of the bath. Hence, we propose new ways how to eliminate these artifacts. These proposals are implemented and extensively tested on the basis of the SBM and the IRLM.

In the SBM the discretization errors are due to the neglect of the rest-chain at a given NRG iteration. This results in the so-called mass-flow error [36] causing the NRG to calculate critical exponents [37, 38] not agreeing with predictions based on a mapping of the SBM to an Ising model. This discrepancy started a discussion in the literature whether the NRG results are correct or wrong.

Despite the mismatch between NRG and the Ising model results, there are authors arguing that the NRG results are correct [39]. We claim that an NRG calculation yields indeed the wrong critical exponents and that this failure could be cured by taking the rest-chain properly into account. This is accomplished by simulating the system with the DMRG. Furthermore, to calculate correct results one has to employ an optimal bosonic basis and we propose a way how to determine this basis efficiently.

Our nonequilibrium simulations of the dynamics of the IRLM show that due to discretization artifacts one observes an unphysical behavior of the occupation number of the local level: instead of a thermalization after a sudden local quench one observes, even on short time scales, wiggles in the time-dependent occupation number. We show that these are caused by internal reflection within the Wilson chain of the charge wave, which is injected into the chain due to the change of the occupation number of the local level after the sudden quench. To reduce these artifacts we leave the pure Wilson discretization of the bath. This, however, means that the system is no longer treatable with the NRG.

The elimination of this obstacle is one of the central results of this thesis: we propose a new hybrid method combining the merits of the NRG and the DMRG. The NRG is used to calculate an effective low-energy Hamiltonian which is simulated with the

DMRG. This facilitates the simulation of strongly correlated systems in parameter regimes and on time scales inaccessible by the NRG or the DMRG on their own.

This thesis is organized as follows: in Chapter 1 we give a brief overview of numerical methods relevant for the simulation of QISs. We present the NRG and DMRG in more detail, as these methods are extensively employed in this thesis. Chapter 2 analyzes the effect of the iterative diagonalization and bath discretization of the NRG on the SBM. In some preliminary studies we first investigate the effect of the truncated bosonic basis and the mass-flow error on toy models. With these results one understands why the NRG fails at reproducing the correct critical exponents for the SBM. These findings are used to set up a DMRG yielding the correct critical exponents.

The following chapters deal with the nonequilibrium dynamics of the IRLM after a sudden local quench. In Chapter 3 we investigate an exactly solvable model, the resonant-level model (RLM), to investigate the effects of the bath discretization on the time-dependent impurity occupation number. We find a qualitative deviation between the results for the model with a continuous and a discretized bath. However, by employing new discretization schemes we are able to fix this mismatch and to reproduce the results of a continuous bath with a discretized one. As the NRG cannot handle these new discretization schemes we propose in Chapter 4 a new hybrid method, which allows to hybridize the NRG with a suitable other method. In our case this second method is the DMRG and we establish the reliability of this new hybrid method by means of RLM results. Finally, in Chapter 5 we apply the new hybrid method to the IRLM and find oscillations with a frequency and damping rate depending on the Coulomb repulsion. We compare the numerical with analytic results of a strong coupling treatment for the model. The new hybrid method does not just yield excellent results in the strong coupling limit or in the non-interacting case, but it is capable of simulating the IRLM in whole parameter regime.

As a final note we want to mention that throughout this thesis the convention $\hbar = k_B = 1$ is used; here, \hbar denotes the reduced Planck constant and k_B the Boltzmann constant.

Chapter 1

Numerical Methods

Over the last decades quantum impurity systems (QISs) have attracted a lot of attention. Historically the first QIS examined consists of a few iron ions solved in gold. This setup shows an unexpected behavior of the electrical resistance at low temperatures [1] which ultimately lead to the Kondo problem [3] and its solution by Wilson [28].¹ A more recent example of a QIS is an electron spin trapped in a quantum dot (QD) coupled to some leads [16, 17].

Common to all QISs is that they consist of a small subsystem (iron ion, electron spin, etc.) and a large subsystem (gold, leads, bosonic bath, etc.). The small subsystem is called *impurity* and the large subsystem is called *bath*, *reservoir*, (*conduction*) *band* or just *environment*. These expressions are used synonymously throughout this work; though when referring to a band, most likely a fermionic band, and when referring to a reservoir, most likely a bosonic reservoir will be meant.

For both subsystems on their own most, if not all, properties can easily be calculated. The environment consisting of an infinite number of non-interacting modes is usually already given in its eigenbasis. The impurity is by definition small enough to be diagonalized exactly very easily. However, the situation changes once one couples the impurity to the environment. Due to interactions between the impurity and the environment or non-trivial couplings, the compound system is not necessarily efficiently solvable² and new many body properties might emerge.

This chapter deals with numerical methods designed to investigate many body systems. It helps to understand the simulations carried out in the following chapters and lays the foundation of a new hybrid method developed in Chapter 4. After giving a short overview of numerical methods used in the field of condensed matter physics, with a special focus on QISs, we turn to the two methods implemented in this work: the numerical renormalization group (NRG) [28] and the density-matrix renormalization group (DMRG) [32]. As both methods can be formulated in the language of matrix

¹ In 1982 Wilson was awarded the Nobel prize for this work [40].

² A quantum system is efficiently solvable if the numerical effort to simulate the system on a classical computer scales polynomially with the number of degrees of freedom [41].

product states (MPSs) we discuss some concepts of these states before presenting the NRG and DMRG in more detail.

In the following chapters these methods are applied to two models. One is the so-called spin-boson model (SBM), describing a spin coupled to a bosonic bath [21]. The second is the interacting resonant-level model (IRLM). Here, a single fermionic level is coupled to a fermionic bath and a Coulomb repulsion is taken into account. For both models we need numeric methods to produce results. Furthermore, we investigate some toy-models which are exactly solvable.

1.1 Overview of methods

Even though there is no general exact solution to all QISs a wide variety of methods has been developed to analytically and numerically solve these system approximately.³ In the following we present a short overview of methods related to the methods used in this work.

1.1.1 Exact diagonalization

Conceptually the simplest way to simulate a QIS – or any other quantum system – is to numerically diagonalize the Hamilton matrix [44]. Once all eigenstates are determined one can calculate all properties or the time-evolution of an arbitrary initial state. However, all involved calculations are very demanding regarding CPU time and memory consumption and therefore not feasible for systems living in a large Hilbert space.

There are some cases in which one can save computational resources. If one is only interested in the ground state of the system it is not necessary to completely diagonalize the Hamilton matrix. One can use e.g. the Lanczos algorithm [44, 45] instead. For example, with this method it is possible to simulate a fermionic Hubbard model with up to 24 sites [46].

With a completely diagonalized Hamilton matrix one has access to all excited states and hence it is straightforward, but still very resource demanding, to calculate the time evolution of a system. An alternative is to expand the time-evolution operator in Chebyshev polynomials, the so called Chebyshev expansion technique (CET) [47]. This limits the time up to which one can faithfully describe the system but is very accurately up to this point.

Since exact diagonalization methods demand a lot of CPU time and memory these methods are in general, with a few exceptions e.g. Ref. 48, not used to simulate QISs. However, in this thesis important insights are gained by solving some toy models by completely diagonalizing the Hamilton matrix, albeit the Hilbert space dimension of these systems is small enough.

³ Standard textbooks covering these topics are e.g. Refs. 42, 43.

1.1.2 Renormalization group

The renormalization group (RG) is a framework to examine the physics of many-body problems [49]. One observes phenomena where effects on different scales are important. An example is a system close to or at a quantum critical point (QCP): here the correlation length ξ diverges and therefore quantum fluctuations of all length scales become important [50].

The RG approach is to find an effective low-energy description of the system: successively high-energy degrees of freedom are integrated out and the physical parameters – the coupling constants and the fields – are renormalized in order to keep the physical properties invariant under the RG transformation. This procedure produces a so-called RG flow reaching eventually a fixed point where the effective system becomes invariant under the RG transformation. By using the Keldysh formalism one can even treat time-dependent systems [51].

1.1.3 Quantum monte carlo

One standard method to simulate quantum many-body systems is quantum Monte Carlo (QMC), though it is hard to refer to it as *one* method (for a review see Ref. 52). More precisely it is a class of methods like variational and diffusion QMC [53] or the loop algorithm [54].

To simulate QISs one can use the algorithm by Hirsch and Fye [55]. With this method one calculates the impurity Green's function by discretizing the system's action on the imaginary time axis. After applying some transformations on this quantity one calculates the Green's function by a stochastic Monte Carlo sampling. However, the Hirsch-Fye method suffers from some problems connected with the imaginary time discretization or a lack of generality: a transformation needed for the algorithm, the Hubbard-Stratonovich transformation, may become complex and as a consequence the stochastic sampling gets difficult.

One way to avoid some of the Hirsch-Fye problems is to avoid the discretization of the imaginary time; this leads to the continuous time QMC [56]. As with all QMC methods one may encounter the so-called sign problem: in QMC algorithms one has to calculate weights which are interpreted as probabilities. These weights can, especially for fermionic systems, become negative and therefore the interpretation as probability fails. Due to the sign error the complexity of the problem grows exponentially with decreasing temperature and increasing system size [56].

Examples of QMC applied to QISs are given Refs. 57, 58.

1.1.4 Numerical and density-matrix renormalization group

The NRG was designed to solve the Kondo problem [28] and is nowadays applicable to a large variety of different QISs [29]. The NRG starts by mapping the bath onto

a Wilson chain. Then the compound system consisting of the impurity coupled to the Wilson chain is solved iteratively. Since the Hilbert space of the system grows exponentially with the number of chain sites an exact solution is only possible for a few lattice sites. In order to continue the iterative diagonalization the Hilbert space is truncated by keeping only a certain number of low-energy states. The NRG reveals its RG character by renormalizing the effective energy scale at each iteration step. Hence, with each iteration step one zooms in more on the low-energy sector.

The DMRG [32] is more versatile in the sense that it is not limited to the solution of Wilson chains, but it is applicable to 1D chains with short-range interaction. The Wilson chain is just a special case of valid systems and therefore when dealing with QISs one can solve a Wilson chain with the DMRG. The DMRG and the NRG share some basic concepts, one of which is the truncation of the Hilbert space to keep the computational cost feasible. In contrast to the NRG the DMRG does not keep the low-energy states, but it keeps the states with a large weight in the density matrix. As a consequence the DMRG does not yield an effective low-energy Hamiltonian, but the ground state of the system.⁴

Both methods are extensively used in this thesis and are therefore discussed in detail in sections 1.3 and 1.4. One main result of this work is the combination of both methods (cf. Chapter 4), by employing the NRG to generate an effective low-energy Hamiltonian which, in turn, is solved with the DMRG.

1.1.5 Dynamical mean-field theory

A mean field theory approximates a complicated many-body system by an effective single-particle system: the effect of the other particles are encapsulated in effective fields applied to the single remaining particle. Technically, the simplest way to achieve this is to take a many-body Hamiltonian and replace the operators of all but one particle by the corresponding mean values; these mean values have to be determined self-consistently.

The dynamical mean field theory (DMFT) [59, 60] is a mean-field theory which retains quantum fluctuations. This is achieved by mapping a lattice model to a QIS with an effective bath. This system is then solved by the method of choice (QMC, DMRG, NRG, non-crossing approximation, ...). In this process the impurity Green's function is determined self-consistently: the impurity is coupled to an effective medium, which depends on the impurity Green's function. The self-consistency loop, that is, determining the impurity Green's function by solving an impurity model with an effective medium and then using this function to determine an effective medium for the next iteration, is repeated until the impurity Green's function converges.

⁴ In general, the DMRG is capable of targeting other states as well; however, in this thesis we are only interested in the ground state.

1.2 Matrix product states

The main results of this work are obtained with the NRG and DMRG. Both methods can be formulated in the language of matrix product states [61, 62, 63]. Though not the traditional way of presenting the NRG we follow this approach. In a recent publication [64] it was noticed that the use of MPSs even allows to formulate the NRG as a variational method making it possible to borrow the concept of sweeping, that is, iteratively improving the state (see Sec. 1.4.2), from the DMRG. Hence, there is a close connection between both methods.

The main idea of matrix product states (MPSs) is to associate one matrix with three indices – a so-called A-matrix – with each lattice site of the system. The wavefunction can then be written as a product of these A-matrices, hence the name. An advantage of writing a state as a MPS and not expanding the state in the basis of the total system and saving the coefficients is that local operators applied to one site affect only the A-matrix of this site. If one writes the state as a linear combination of basis states and applies a local operator, in general, all coefficients change. Furthermore, in a certain gauge, it is technically easy to calculate expectation values or reduced density matrices. When discussing the DMRG in Sec. 1.4, MPSs show their real merit: MPSs support naturally the DMRG truncation scheme.

In this section we summarize the most relevant properties of MPSs without explicit derivations. A more thorough presentation of MPSs, especially in connection with the DMRG, is given in Refs. 63, 65. After establishing the MPSs as a tool we continue to present the NRG (Sec. 1.3) and DMRG (Sec. 1.4) using MPSs.

1.2.1 A-matrix representation

We start by considering a quantum mechanical system consisting of a chain with N lattice sites. A state $|\psi\rangle$ of this system is then given by

$$|\psi\rangle = \sum_{s_1, s_2, \dots, s_N} c(s_1, s_2, \dots, s_N) |s_1\rangle_1 \otimes |s_2\rangle_2 \otimes \dots \otimes |s_N\rangle_N \quad c(s_1, s_2, \dots, s_N) \in \mathbb{C}. \quad (1.1)$$

The local Hilbert space of the i th site is of dimension d_i . Hence a local basis of the i th site is formed by the vectors $\{|s\rangle_i | 1 \leq s \leq d_i\}$. The sum in Eq. (1.1) runs over all basis states. The main idea behind MPSs is to write the coefficients $c(s_1, s_2, \dots, s_N)$ as a product of matrices. This is achieved by making extensive use of the Schmidt decomposition [66, 67, 68]: step by step one eliminates the dependency of c on one physical index s_i . As a result, after $N - 1$ steps one arrives at a form in which for each site i all physical relevant information is encoded in a matrix A_i . This matrix has three indices: two so-called bond indices and one physical index.⁵ The bond indices connect

⁵ In our notation the bond indices are written as subscripts and the physical index is given in square brackets.

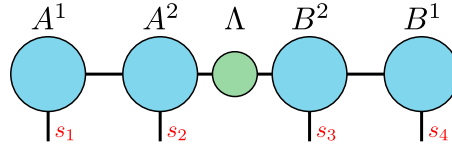


Figure 1.1: Diagrammatic representation of an MPS for a chain with four sites. Each circle represents a matrix and each line an index of the matrix. One sums over lines connecting two circles: this represents a matrix-matrix multiplication. Matrices with three indices are so-called A-matrices: the horizontal lines indicate bond- and the vertical lines physical-indices. In the following diagrams the labels of the open indices are omitted. A-matrices denoted by A (B) are left (right) orthonormalized, Eq. (1.3).

two neighboring A-matrices, while the physical index enumerates the basis states of the local basis. Hence, one has d_i two-index matrices at each site i , where d_i is the dimension of the local Hilbert space at site i .

Furthermore, we split the chain at an arbitrary site L and denote matrices of the left (right) block with A (B). The state of Eq. (1.1) is now given in its MPS form by [69]

$$|\psi\rangle = \sum_{s_1, s_2, \dots, s_N} A^1[s_1] \cdots A^L[s_L] \Lambda B^L[s_{L+1}] \cdots B^1[s_N] |s_1\rangle_1 \otimes |s_2\rangle_2 \otimes \cdots \otimes |s_N\rangle_N. \quad (1.2)$$

Later we assume an implicit summation over the physical indices $\{s_0, \dots, s_L\}$ and omit the basis state $|s_1\rangle_1 \otimes |s_2\rangle_2 \otimes \cdots \otimes |s_N\rangle_N$. Furthermore, in Eq. (1.2) the indexing of the A-matrices A^i and B^i assumes that the left and right block are of equal sizes. In general, both blocks can have arbitrary sizes.

When constructing a MPS one has a gauge freedom which is fixed by introducing the center matrix Λ and demanding the orthonormalization

$$\begin{aligned} \sum_s A^\dagger[s] A[s] &= 1 && \text{in the left block} \\ \text{and } \sum_s B[s] B^\dagger[s] &= 1 && \text{in the right block.} \end{aligned} \quad (1.3)$$

The center matrix Λ has two indices. Because it is diagonal one is effectively left with one index. If the orthonormalization Eq. (1.3) is satisfied the norm of $|\psi\rangle$ is given by

$$\langle \psi | \psi \rangle = \text{Tr}[\Lambda]. \quad (1.4)$$

The bond separating the left from the right block is not fixed: by rotating the center matrix Λ to the left or right [63] it is possible to let one block grow while the other one shrinks. This is of relevance in the sweeping phase of the DMRG (cf. Sec. 1.4.2).

Instead of writing down the equations it is often easier to use an equivalent diagrammatic representation of MPSs (cf. Fig. 1.1). The key idea is to represent matrices by circles and each index is represented by a line connected to this circle. If a line

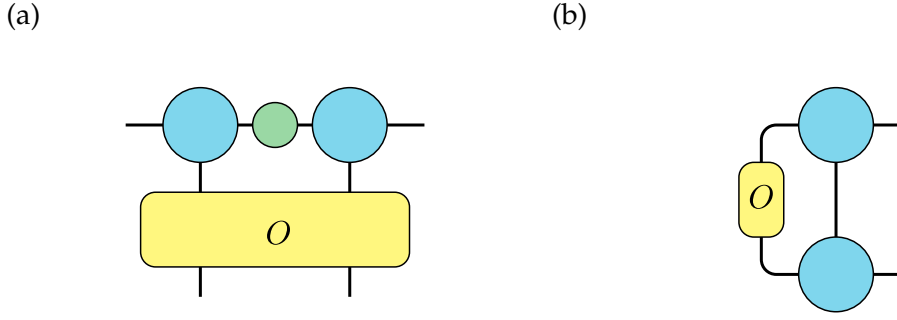


Figure 1.2: (a) Diagrammatic representation of a two-site operator O acting on a MPS. (b) Rotation of the operator O into a new basis.

connects two circles, one has to sum over this index; effectively this is a matrix multiplication. Therefore the diagram in Fig. 1.1 shows the term

$$\sum_{\alpha\beta\gamma\delta} A_{\alpha}^1[s_1]A_{\alpha\beta}^2[s_2]\Lambda_{\beta\gamma}B_{\gamma\delta}^2[s_3]B_{\delta}^1[s_4]. \quad (1.5)$$

In this equation the physical indices are left open while one contracts over the bond indices. Eq. (1.5) does not exploit that Λ is diagonal; this would cancel out the summation over either β or γ .

Usually, when physical indices are left open in a diagram we assume, as in the mathematical notation, that one multiplies the term with the corresponding basis state. As a further convention we declare that in diagrams physical indices are indicated by vertical lines and if circles representing A-matrices are ordered in two rows one has to take the complex-conjugate of A-matrices in the lower row.

1.2.2 Application of an operator

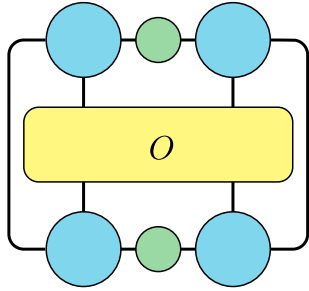
The application of an operator O on the MPS alters only A-matrices associated with the sites on which the operator acts. Assuming that the operator O acts only on two consecutive sites i and $i + 1$, its matrix elements are defined via

$$O = \sum_{s_i, s'_i} \sum_{s_{i+1}, s'_{i+1}} O_{s_i s_{i+1}, s'_i s'_{i+1}} (|s'_i\rangle \otimes |s'_{i+1}\rangle) (\langle s_i| \otimes \langle s_{i+1}|). \quad (1.6)$$

Here, $\{|s_i\rangle\}$ is the basis of the i th site. To calculate the action of the operator O on the A-matrices associated with site i and $i + 1$, A and B respectively, one has to contract the MPS depicted in Fig. 1.2a. This yields the tensor

$$\Theta_{\alpha,\gamma}[s'_i, s'_{i+1}] = \sum_{\beta} \sum_{s_i, s_{i+1}} A_{\alpha\beta}[s_i]\Lambda_{\beta\beta}B_{\beta\gamma}[s_{i+1}]O_{s_i s_{i+1}, s'_i s'_{i+1}}. \quad (1.7)$$

(a)



(b)

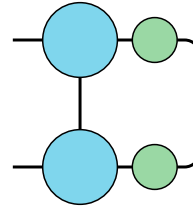


Figure 1.3: (a) Evaluation of the expectation value of a two-site operator O . (b) Reduced density matrix of left block.

By calculating the singular-value decomposition (SVD) [68, Sec. 2.1.10] of Θ one gets the new A-matrices \tilde{A} and \tilde{B} which are properly orthonormalized, i.e. they obey Eq. (1.3),

$$\Theta[s_i, s_{i+1}] = \tilde{A}[s_i] \Lambda \tilde{B}[s_{i+1}]. \quad (1.8)$$

Here the SVD is merely a tool to calculate the Schmidt decomposition of Θ .

1.2.3 Change of basis

Any operator O is defined in a certain basis. This could, for example, be the occupation number or the spin s_z component. However, often it is convenient to perform calculations in the eigenbasis of some other operator Q ; this could be the Hamiltonian (in the NRG) or the density matrix (in the DMRG). The rotation matrix from one basis to the other can be formulated as an A-matrix A .

If an A-matrix is a rotation matrix, it fulfills the orthonormalization condition Eq. (1.3). The rotation of an operator O is defined by (cf. Fig. 1.2b)

$$\tilde{O} = \sum_s A^\dagger[s] O A[s]. \quad (1.9)$$

In the new basis the operator is given by \tilde{O} . In general, this rotation is not unitary. If one does this rotation for the operator Q , then \tilde{Q} is by definition diagonal.

1.2.4 Expectation values

In a similar fashion one can calculate the expectation value of the operator O , $\langle \psi | O | \psi \rangle$. Conceptual this is done in two steps: first the operator is applied to the state $|\psi\rangle$. This yields the new state $|\psi'\rangle = O|\psi\rangle$. In a second step one has to calculate the scalar product $\langle \psi | \psi' \rangle$. For a two-site operator O the states $|\psi'\rangle$ and $|\psi\rangle$ differ only in two

A-matrices. Exploiting the orthonormalization conditions Eq. (1.3) one can trace out the rest of the chain and gets (cf. Fig. 1.3a)

$$\langle \psi | O | \psi \rangle = \sum_{\alpha\beta\gamma\delta} \sum_{s_1 s_2} \sum_{s'_1 s'_2} A_{\alpha\beta}[s_1] A_{\gamma\alpha}^*[s'_1] \Lambda_{\beta\beta} \Lambda_{\gamma\gamma} B_{\beta\delta}[s_2] B_{\delta\gamma}^*[s'_2] O_{s_1 s_2, s'_1 s'_2} \quad (1.10)$$

This concept can easily be extended to operators acting only on one site or on more than two sites.

1.2.5 Reduced density matrix

Suppose the operator O acts only on sites of the left block of the MPS. One can therefore write it as $O = O_A \otimes \mathbb{1}$. Here O_A denotes a local operator of the left block. With the density matrix $\rho = |\psi\rangle\langle\psi|$ of the total system the expectation value of O is given by

$$\langle O \rangle = \text{Tr}[\rho O] = \text{Tr}[\rho O_A \otimes \mathbb{1}]. \quad (1.11)$$

The trace is evaluated with the states $|s\rangle = |s_A\rangle \otimes |s_B\rangle$, with $|s_A\rangle$ ($|s_B\rangle$) being the eigenstates of the left (right) block:

$$\langle O \rangle = \sum_{s_A s_B} \langle s_A s_B | \rho O_A \otimes \mathbb{1} | s_A s_B \rangle \quad (1.12)$$

$$= \sum_{s_A} \langle s_A | \rho_A O_A | s_A \rangle, \quad (1.13)$$

$$\text{with } \rho_A = \text{Tr}_B[\rho] = \sum_{s_B} \langle s_B | \rho | s_B \rangle. \quad (1.14)$$

Here we have introduced the reduced density matrix ρ_A [68, Sec. 3.4.3].

To calculate the reduced density matrix of one block one has to trace out the other block. For simplicity we show how to calculate the reduced density matrix of the left block for an MPS consisting of only two sites in total and, therefore, one site in each block. The generalization to the right block and larger block sizes is straightforward [63].

The MPS is given by

$$|\psi\rangle = \sum_{s_1 s_2} A[s_1] \Lambda B[s_2] |s_1 s_2\rangle, \quad (1.15)$$

where A and B are A-matrices orthonormalized according to Eq. (1.3). The density matrix reads

$$\rho = |\psi\rangle\langle\psi| = \sum_{s'_1 s'_2} \sum_{s_1 s_2} A[s'_1] \Lambda B[s'_2] B^\dagger[s_2] \Lambda^\dagger A^\dagger[s_1] |s'_1 s'_2\rangle \langle s_1 s_2|. \quad (1.16)$$

To calculate the reduced density matrix one has to trace over the eigenstates $|s_B\rangle$ of the right block (cf. Fig. 1.3b)

$$\rho_A = \text{Tr}_B [\rho] = \sum_{s_B} \sum_{s'_1 s'_2} \sum_{s_1 s_2} A[s'_1] \Lambda B[s'_2] B^\dagger[s_2] \Lambda^\dagger A^\dagger[s_1] \underbrace{\langle s_B | s'_1 s'_2 \rangle}_{=\delta_{s_B, s'_2}} \underbrace{\langle s_1 s_2 | s_B \rangle}_{=\delta_{s_2, s_B}} \quad (1.17)$$

$$= \sum_{s'_1 s_1} A[s'_1] \Lambda \Lambda^\dagger A^\dagger[s_1] |s'_1\rangle \langle s_1|. \quad (1.18)$$

The calculation of the reduced density matrix for a block with more than one site is shown below in Fig. 1.10.⁶

Fidelity

Suppose we have two reduced density matrices ρ and σ . These could be for the ground states of two different Hamiltonians with the same Hilbert space. To measure the distance between the states we define the fidelity

$$F(\rho, \sigma) = \text{Tr} \left[\sqrt{\rho^{\frac{1}{2}} \sigma \rho^{\frac{1}{2}}} \right]. \quad (1.19)$$

This value can take values in the range $0 \leq F(\rho, \sigma) \leq 1$. For $\sigma = \rho$ the fidelity is $F(\rho, \rho) = 1$. If the density matrices describe pure states, $\rho = |\psi\rangle\langle\psi|$ and $\sigma = |\phi\rangle\langle\phi|$, the fidelity is equivalent to the modulus of the overlap, $F(|\psi\rangle\langle\psi|, |\phi\rangle\langle\phi|) = |\langle\psi|\phi\rangle|$. In this case it is obvious that the fidelity vanishes for orthogonal states. More properties of the fidelity are given in Ref. 68, Sec. 9.2.2.

This work employs the fidelity as an indicator if a subsystem, described by the time-dependent reduced density matrix $\rho(t)$, thermalizes after a sudden local quench. To this end the fidelity $F(\rho(t), \sigma)$ is calculated. Here, σ is thermal reduced density matrix of the same subsystem. If a subsystem thermalizes one obtains

$$\lim_{t \rightarrow \infty} F(\rho(t), \sigma) = 1. \quad (1.20)$$

Von Neumann entropy

Another important quantity one encounters when bipartitioning a system is entanglement [70, 71]. Though this quantity is an essential ingredient in the understanding of why the concept of MPSs works for DMRG [72] we do not discuss this vast field in detail. At this point we merely introduce the von Neumann entropy,

$$S = -\text{Tr} [\rho \log_2 \rho] \quad (1.21)$$

⁶ Note, that this figure is for the NRG and shows no Λ matrix as this is not needed in the NRG.

for the density matrix ρ . For an MPS one can calculate this quantity easily from the eigenvalues λ_α of the density matrix [63],

$$S = - \sum_{\alpha} \lambda_{\alpha} \log_2 \lambda_{\alpha}. \quad (1.22)$$

Only terms with $\lambda_{\alpha} > 0$ enter the sum. The eigenvalues λ_{α} are calculated in the course of the DMRG easily as they are given as the squared singular values in the SVD.

The von Neumann entropy is a measure for entanglement and it assesses the spectrum of the density matrix: if the density matrix has only one non-vanishing eigenvalue the von-Neumann entropy vanishes and the entanglement is zero. For a maximally entangled state all eigenvalues of the density matrix are equal. As a consequence for the DMRG it gets harder to simulate the system with increasing entanglement. Then again, the ground state of a system with $S = 0$ can be calculated exactly with the DMRG.

1.3 Numerical renormalization group

A long persisting issue in the field of condensed matter physics was the Kondo problem [3], lacking a solution until Wilson developed the numerical renormalization group (NRG) [28]. This new method proved to be suited for other systems as well, e.g. the single impurity Anderson model (SIAM) [73], and has become an essential tool for examining QISs [29]. Numerous extension to the NRG were proposed and are commonly implemented nowadays. Here we restrict our discussion to the two variants used in this work: the bosonic NRG [74, 75] and the time-dependent numerical renormalization group (TD-NRG) [76, 77]. A recent summary of the NRG with its different variations and with a special focus on MPS is given in Ref. 78 .

The NRG consists of three major steps: (i) discretization of the bath, (ii) mapping the discretized bath to a lattice model, and (iii) iteratively solving the lattice model. In principle, for solving a QIS with the DMRG the same steps apply. However, the way the model is iteratively solved in third step differs for both methods.⁷ Our discussion of the NRG steps follows the presentation of Ref. 29 .

1.3.1 Discretization and mapping

The general Hamiltonian of a QIS is

$$H = H_{\text{imp}} + H_{\text{coup}} + H_{\text{band}}, \quad (1.23)$$

⁷ For the NRG the discretization and mapping has to be done as presented in the following; at this point the DMRG is more flexible and allows for other schemes, e.g. determining the chain parameters via a continued fraction expansion [79] of the hybridization function.

where H_{imp} is the Hamiltonian of the impurity, H_{band} of the band, and the coupling between impurity and band is included in H_{coup} . The band Hamiltonian is given by

$$H_{\text{band}} = \sum_{\nu} \sum_k \epsilon_{\nu k} c_{\nu k}^{\dagger} c_{\nu k}. \quad (1.24)$$

The index ν is the flavor index of the bath. In general this is a composite index denoting different spins and different leads. The band's energy dispersion is given by $\epsilon_{\nu k}$ and $c_{\nu k}^{\dagger}$ ($c_{\nu k}$) are the creation (annihilation) operators of flavor ν in the energy mode k .

The impurity has some energy levels coupling to the band. The creation (annihilation) operators of these levels are denoted by d_{ν}^{\dagger} (d_{ν}). The coupling Hamiltonian is then given by

$$H_{\text{coup}} = \sum_{\nu\nu'} \sum_k V_{\nu\nu'k} \left(c_{\nu'k}^{\dagger} d_{\nu} + d_{\nu}^{\dagger} c_{\nu'k} \right). \quad (1.25)$$

$V_{\nu\nu'k}$ is the hybridization between the impurity and band level.

The following discussion does not depend on the specific form of H_{imp} . The only assumption playing an important role at the iterative diagonalization is that the dimension of H_{imp} is small enough so that exact diagonalization is feasible. Furthermore, if the model has an interaction term between the impurity and the band, e.g. $d_{\nu}^{\dagger} d_{\nu} c_{\nu'k}^{\dagger} c_{\nu'k}$, this term is included in H_{imp} . In the discussion of the interacting resonant-level model (Chapter 5) such a term is important. Even though the bath has to be, so far, fermionic, the impurity can in principle have bosonic modes, for example a SIAM with a phonon [80].

In the following discussion we drop the flavor index ν for both the band and the impurity. Effectively this means that we consider a spin-less impurity coupled to a single spin-less band. However, the generalization to a spin-full model with more than one lead is straightforward.

The effect the band has on the impurity is fully characterized by the band hybridization function

$$\Delta(\omega) = \pi \sum_k V_k^2 \delta(\omega - \epsilon_k). \quad (1.26)$$

For a k -independent hybridization, $V_k \equiv V$, this function is related to the density of states (DOS) $\rho(\omega)$ via

$$\Delta(\omega) = \pi V^2 \rho(\omega). \quad (1.27)$$

We assume that the support of $\rho(\omega)$ lies in the interval $[-D, D]$ where $2D$ is the bandwidth. Further, in the wide-band limit we can define the width of the impurity level

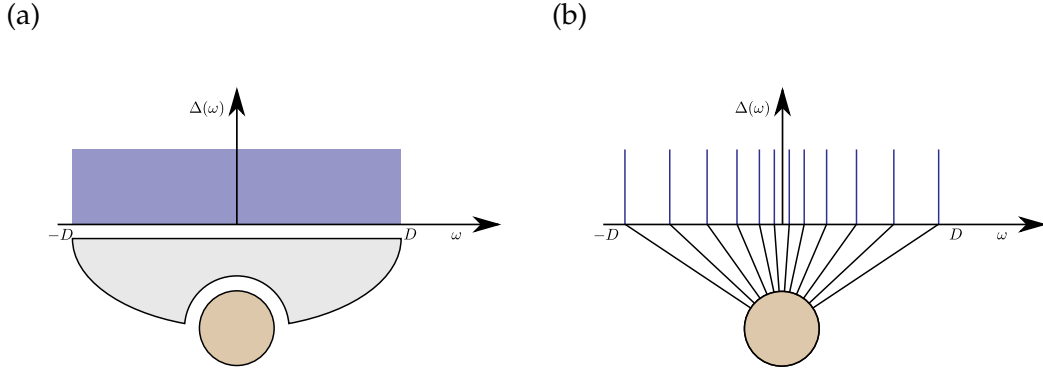


Figure 1.4: Discretization of the continuous band described by the hybridization function $\Delta(\omega)$ and the bandwidth $2D$. (a) The impurity couples to all energies of the continuous band. (b) For each energy scale one representative energy state is selected: the impurity couples to some discrete energy levels of the band.

due to its coupling to the band as $\Gamma = \text{Im} \left\{ \Delta(-i0^+) \right\}$. In the special case that $V_k \equiv V$ and with a constant DOS, $\rho(\omega) = \frac{1}{2D} \Theta(|\omega| - D)$ the level width is given by

$$\Gamma = \frac{\pi V^2}{2D}. \quad (1.28)$$

In Chapter 3 the width Γ is used as the energy unit. For the discussion of the NRG it is more convenient to use D as the energy unit and therefore we set $D = 1$ henceforth.

With this definition of the hybridization function we reformulate the band and coupling Hamiltonian in energy space [81],

$$H = H_{\text{imp}} + \int_{-1}^1 d\epsilon g(\epsilon) a_\epsilon^\dagger a_\epsilon + \int_{-1}^1 d\epsilon h(\epsilon) (d^\dagger a_\epsilon + a_\epsilon^\dagger d). \quad (1.29)$$

Here, a_ϵ^\dagger (a_ϵ) creates (annihilates) one fermion with energy ϵ in the band. Furthermore, $g(\epsilon)$ is the dispersion and $h(\epsilon)$ is the hybridization. These functions are related to the hybridization function via

$$\Delta(\omega) = \pi \frac{d\epsilon(\omega)}{d\omega} h(\epsilon(\omega))^2 \quad (1.30)$$

with $\epsilon(\omega)$ being the inverse function to $g(\epsilon)$.

From Eq. (1.29) it is evident that the impurity couples to the whole energy spectrum of the conduction band (cf. Fig. 1.4a). This corresponds to a Hamilton matrix of infinite dimension. Numerically one cannot deal with this matrix and therefore one needs a

strategy to eliminate degrees of freedom. Wilson proposed [28] to discretize the band on a logarithmic mesh. This is defined by a set of discretization points

$$x_n^\pm = \pm \Lambda^{-n}, \quad n = 0, 1, 2, \dots \quad (1.31)$$

The parameter Λ is the so-called discretization parameter. The interval between two points is of the width

$$d_n = \left| x_n^\pm \right| - \left| x_{n+1}^\pm \right| = \Lambda^{-n} (1 - \Lambda^{-1}). \quad (1.32)$$

This width shrinks logarithmically with the interval index n . Because (i) the discretization points need to lie within the interval $[-1, 1]$, that is, within the band, and (ii) the width of the intervals has to be finite, $d_n > 0$, Λ has to fulfill the condition $\Lambda > 1$.

The impurity is now coupled to one representative energy level of each interval (cf. Fig. 1.4b). Since the interval width decreases, the discretized DOS is more dense around the Fermi energy and contains only a few high-energy states. This is justified by the goal that we are eventually interested in the low temperature behavior of the system and in this case the states close to the Fermi energy play the dominant role.

To transform the Hamiltonian of the continuous band Eq. (1.29) into a discretized form, one defines a complete basis for each energy interval and expands the conduction band operators in this basis [29]. At this point one has to distinguish between positive and negative energy intervals in the spectrum and therefore the expansion yields two sets of fermionic annihilation operators, a and b . With these operators the discretized Hamiltonian is given by

$$H = H_{\text{imp}} + \sum_{n=0}^{\infty} \left(\zeta_n^+ a_n^\dagger a_n + \zeta_n^- b_n^\dagger b_n \right) + \frac{1}{\pi} \sum_{n=0}^{\infty} \left(d^\dagger \left(\gamma_n^+ a_n + \gamma_n^- b_n \right) + \left(\gamma_n^+ a_n^\dagger + \gamma_n^- b_n^\dagger \right) d \right) \quad (1.33)$$

with

$$\zeta_n^\pm = \frac{\int^{\pm, n} d\epsilon \Delta(\epsilon) \epsilon}{\gamma_n^{\pm 2}}, \quad (1.34)$$

$$\gamma_n^{\pm 2} = \int^{\pm, n} d\epsilon \Delta(\epsilon) \quad (1.35)$$

and the convention

$$\int^{+, n} d\epsilon \equiv \int_{x_{n+1}}^{x_n} d\epsilon, \quad \int^{-, n} d\epsilon \equiv \int_{-x_n}^{-x_{n+1}} d\epsilon. \quad (1.36)$$

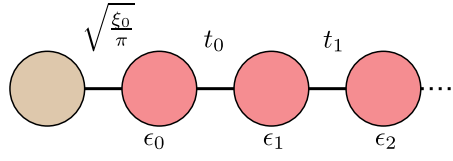


Figure 1.5: Impurity couples to a Wilson chain. The chain parameters, t_i and ϵ_i , and the hybridization $\sqrt{\frac{\xi_0}{\pi}}$ depend on the bath. Each circle represents one chain site and the lines indicate the coupling.

This completes the first step of the NRG procedure: the discretization of the conduction band.

The second step of the NRG algorithm is to map the discretized Hamiltonian Eq. (1.33) to a lattice Hamiltonian (cf. Fig. 1.5),

$$H = H_{\text{imp}} + \sqrt{\frac{\xi_0}{\pi}} (d^\dagger c_0 + c_0^\dagger d) + \sum_{n=0}^{\infty} (\epsilon_n c_n^\dagger c_n + t_n (c_n^\dagger c_{n+1} + c_{n+1}^\dagger c_n)) \quad (1.37)$$

$$\text{with } \xi_0 = \int_{-1}^1 d\epsilon \Delta(\epsilon) . \quad (1.38)$$

The transformation from Eq. (1.33) to Eq. (1.37) is a Householder transformation, which maps the operators a_n and b_n to c_n . The operators c_n^\dagger and c_n create and annihilate a fermion on the n -th lattice site. Because this is a one dimensional lattice, this is called a Wilson Chain. Thus the original system is mapped to a new system, consisting of the impurity coupled to a semi-infinite Wilson chain.

The hopping parameters t_n and the on-site energies ϵ_n depend on $\Delta(\omega)$ and, in general, have to be calculated numerically [29]. However, for a hybridization function constant in the interval $[-1, 1]$, $\Delta(\omega) \equiv \Delta_0$, the hopping parameters are given by

$$t_n = \frac{(1 + \Lambda^{-1})(1 - \Lambda^{-n-1})}{2\sqrt{1 - \Lambda^{-2n-1}}\sqrt{1 - \Lambda^{-2n-3}}} \Lambda^{-\frac{n}{2}} \quad (1.39)$$

and the on-site energies are, as for all hybridization functions symmetric around the Fermi energy, $\epsilon_n = 0$. In the limit of large n the hopping parameters are

$$t_n = \frac{1}{2} (1 + \Lambda^{-1}) \Lambda^{-\frac{n}{2}} . \quad (1.40)$$

Furthermore, for a k -independent hybridization, Eq. (1.27), the coupling between impurity and Wilson chain is given by

$$\sqrt{\frac{\xi_0}{\pi}} = V . \quad (1.41)$$

It is standard procedure to use the factor

$$A_\Lambda = \frac{1}{2} \frac{\Lambda + 1}{\Lambda - 1} \ln \Lambda \quad (1.42)$$

to correct V , $V' = \sqrt{A_\Lambda} V$, in order to compensate the shortcoming of the NRG of underestimating the hybridization function [33]. In this thesis all results are calculated using this correction factor.

Note that the hopping parameters t_n decrease exponentially. This is due to the logarithmic discretization of the conduction band and has a strong impact on the nonequilibrium dynamics producing non-physical artifacts (Sec. 3.3). However, this property is vital for the NRG, because that is how the separation of energy scales is guaranteed. This is part of the discussion in the next section which focuses on the diagonalization of the system.

1.3.2 Iterative diagonalization

To actually calculate properties of the system one has to diagonalize the Hamiltonian Eq. (1.37). Doing this by exact diagonalization is impossible, as the dimension of the Hamilton matrix is still infinite. However, since the system is described by an semi-infinite chain, one can start with a finite chain with N lattice sites,

$$H_N = \Lambda^{\frac{N-1}{2}} \left(H_{\text{imp}} + V \left(d^\dagger c_0 + c_0^\dagger d \right) + \sum_{n=0}^N \epsilon_n c_n^\dagger c_n + \sum_{n=0}^{N-1} t_n \left(c_n^\dagger c_{n+1} + c_{n+1}^\dagger c_n \right) \right) \quad (1.43)$$

and take the limit

$$H = \lim_{N \rightarrow \infty} \Lambda^{-\frac{N-1}{2}} H_N. \quad (1.44)$$

Here we have introduced the scaling factor $\Lambda^{\frac{N-1}{2}}$. This originates from the RG character of the NRG: at each RG step the energies are renormalized. This idea leads to the RG transformation in the NRG, which adds one site to the Wilson chain,

$$H_{N+1} = \sqrt{\Lambda} H_N + \Lambda^{\frac{N}{2}} \left(\epsilon_{N+1} c_{N+1}^\dagger c_{N+1} + t_N \left(c_N^\dagger c_{N+1} + c_{N+1}^\dagger c_N \right) \right). \quad (1.45)$$

The prefactor $\Lambda^{\frac{N}{2}}$ cancels the n dependency of t_n out, resulting in an hopping parameter of the order $\mathcal{O}(1)$. This means, that each NRG step is associated with a well-defined energy scale $\Lambda^{-\frac{N}{2}}$. Eq. (1.45) defines a series of Hamiltonians with the initial condition

$$H_0 = \Lambda^{-\frac{1}{2}} \left(H_{\text{imp}} + \epsilon_0 c_0^\dagger c_0 + V \left(c_0^\dagger d + d^\dagger c_0 \right) \right). \quad (1.46)$$

Usually one wants to calculate the expectation values of a set of operators O_i or the spectral function of the system. Therefore one needs to diagonalize the Hamiltonian. In the NRG this is done in an iterative manner: one starts with a system small enough to be exactly solvable. Then one adds one site after another. Thereby the dimension of the Hilbert space increases at each step. When the Hilbert space dimension exceeds a certain threshold one employs a truncation scheme to keep the dimension below the threshold: high-energy states are truncated. This implies that one has to diagonalize the Hamiltonian at each iteration.

The first step is to diagonalize H_0 by calculating all eigenvectors and eigenvalues, $H_0|r\rangle_0 = E_r^0|r\rangle_0$. These vectors set up the matrix U diagonalizing H_0 , $U^\dagger H_0 U = \text{diag}(E_0^0, E_1^0, \dots)$. In an MPS language one gets the A-matrix

$$A_{\alpha\beta}^0[s] = U_{s\alpha,\beta}, \quad (1.47)$$

associated with the first iteration. With this A-matrix we rotate the operators O_i , the band operators c_0^\dagger and c_0 , and the Hamiltonian H_0 into the eigenbasis of H_0 . For any operator O_i this rotation is given by

$$\tilde{O}_i = \sum_s A^\dagger[s] O_i A[s]. \quad (1.48)$$

After this rotation one can construct the next Hamiltonian H_1 of the series according to Eq. (1.45); in this step the rotated operators are used.

These three steps - diagonalization, rotation, and adding one site - constitute one NRG iteration. The definition Eq. (1.44) demands to iterate infinite times; that is the price one has to pay to work with a semi-infinite Wilson chain. However, in practice that is not possible and therefore one has to stop iterating after reaching a certain chain length. Below we discuss how to choose the length of the chain. Before that, the question is, what is the maximum chain length reachable with the method discussed so far?

On a computer one has technical limits set by the memory available to store H_N and the time needed for the diagonalization. With $d = \dim(H_N)$ the memory consumption is of the order $\mathcal{O}(d^2)$ and the CPU time for diagonalization is even of the order $\mathcal{O}(d^3)$. Since the dimension of the Hilbert space d grows exponentially with the number of iterations N , the computational demands increase rapidly and one has to find a strategy to keep those on a manageable level.

The approach the NRG takes is to truncate high-energy states. To justify this we consider the density matrix at iteration N ,

$$\rho_N = \frac{\sum_i e^{-\beta(E_i - E_0)} |i\rangle\langle i|}{\sum_i e^{-\beta(E_i - E_0)}}, \quad (1.49)$$

where E_i is the energy of the eigenstate $|i\rangle$. We assume that states are ordered by energy, $E_i \leq E_j \forall i < j$; thus E_0 is the ground-state energy. Furthermore, we have introduced the inverse temperature β which is chosen to be $\beta \cong 1$; this is equivalent to lowering the temperature of the system with each iteration. At iteration N the system has an effective inverse temperature

$$\bar{\beta}_N \cong \frac{D}{2}(1 + \Lambda^{-1})\Lambda^{\frac{-N-1}{2}}. \quad (1.50)$$

In this sense iterating further is equivalent to cooling the system.

Due to the renormalization of energies at each NRG iteration step the lowest eigenenergies are of order $\mathcal{O}(1)$. In Eq. (1.49) high-energy states are therefore exponentially suppressed and have a vanishing weight in the density matrix. This concludes the argument why truncating high-energy states is a good approximation.

The practical consequence of the truncation is that not all eigenstates of H_N enter the transformation matrix A^N ; only N_s states are kept at iteration N . With $d = \dim H_N$ and d_{loc} as the dimension of the local Hilbert space of the N th site the truncated A-matrix associated with iteration N is defined by

$$A_{\alpha\beta}^N[s] = U_{s\alpha,\beta}^N, \quad \text{with } s \in [1, d_{\text{loc}}], \alpha \in \left[1, \frac{d}{d_{\text{loc}}}\right], \text{ and } \beta \in [1, N_s]. \quad (1.51)$$

There are two basic strategies to choose N_s : (i) one fixes N_s at a constant value for all iterations or (ii) one defines a threshold energy and keeps all states below this energy. Using the second variant the number of states can be different at each iteration and therefore it is hard to predict the computational resources needed for a run. To avoid problems resulting from the lack of computational resources the first variant is preferred in practice. However, one has to be careful when choosing N_s and it is advisable to repeat calculations with a different number of states to make sure the results are converged.

Besides convergence with the number of states one usually wants the results to converge with the number of iterations [82]. If that is the case the RG transformation has reached a stable fixed point. At such a point the effective low-energy Hamiltonian is invariant under the RG transformation: it does not change with further iterations.⁸ Thus the energy spectrum of the Hamiltonian is invariant under a NRG step. Fig. 1.6 shows some of the lowest eigenenergies E_r of the interacting resonant-level model (IRLM) at

⁸ If one is interested in the physics at a certain temperature there is a different way to determine the number of iterations. In this case the last NRG iteration is the one setting the desired temperature scale according to Eq. (1.50).

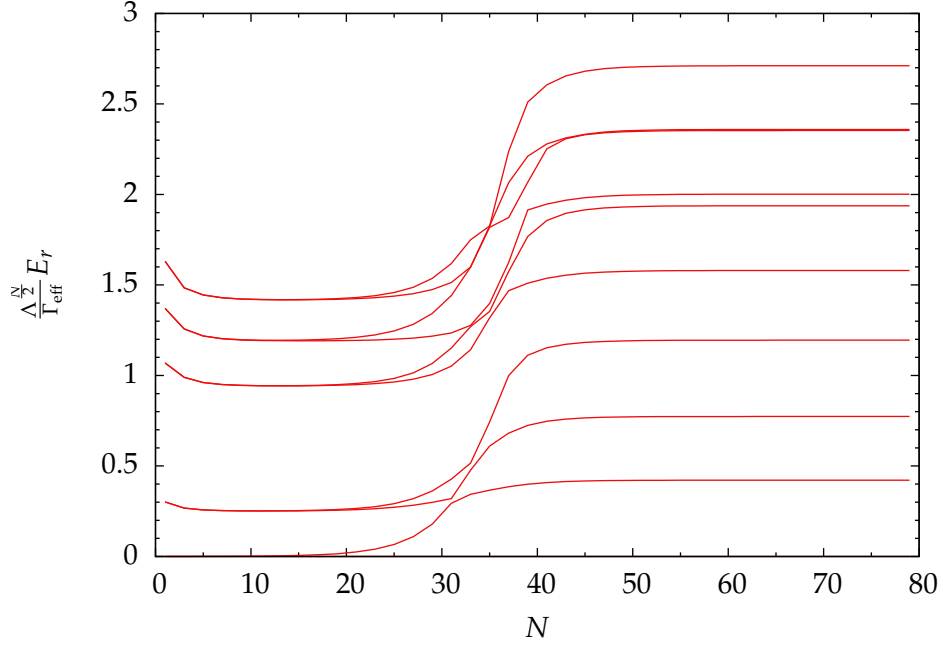


Figure 1.6: Level-flow of the lowest eigenenergies E_r for the IRLM with $\Lambda = 1.8$, $E_d = -\Gamma_{\text{eff}}$, $U = D$, $D = 10^5 \Gamma_{\text{eff}}$. Shown are only the odd iterations. The meaning of the parameters is not of interest at this point and is discussed in Chapter 5.

different iterations.⁹ The level-flow of this model shows an unstable fixed point for $N \lesssim 20$ and a stable fixed point for $N \gtrsim 40$.

Besides determining fixed points the energy spectrum is also useful to calculate expectation values of an operator O . This is achieved by evaluating

$$\langle O \rangle = \text{Tr} [\tilde{O}_N \rho_N]. \quad (1.52)$$

\tilde{O}_N denotes the operator O rotated in the basis at iteration N . The density matrix at iteration N is given by (see also Eq. (1.49))

$$\rho_N = \frac{1}{Z_N} \sum_r e^{-\bar{\beta} E_r} |r\rangle \langle r|, \quad \text{with } Z_N = \sum_r e^{-\bar{\beta} E_r}. \quad (1.53)$$

The eigenstates at iteration N are $|r\rangle$ with eigenenergies E_r . Thus the density matrix is diagonal. $\bar{\beta}$ is a positive number of $\mathcal{O}(1)$. The inverse temperature β for which the density matrix is calculated is $\beta = \Lambda^{\frac{N-1}{2}} \bar{\beta}$. The role of $\bar{\beta}$ is therefore to set the temperature. If $\bar{\beta}$ deviates from 1 too strongly the effective temperature is tuned away from the energy scale at the iteration N to a different energy scale. However, since at

⁹ The meanings of the model parameters given in the caption of Fig. 1.6 are not important at this point; these parameters and the details of the model are further discussed in Chapter 5. At this point of the discussion we merely want to show an example level-flow diagram.

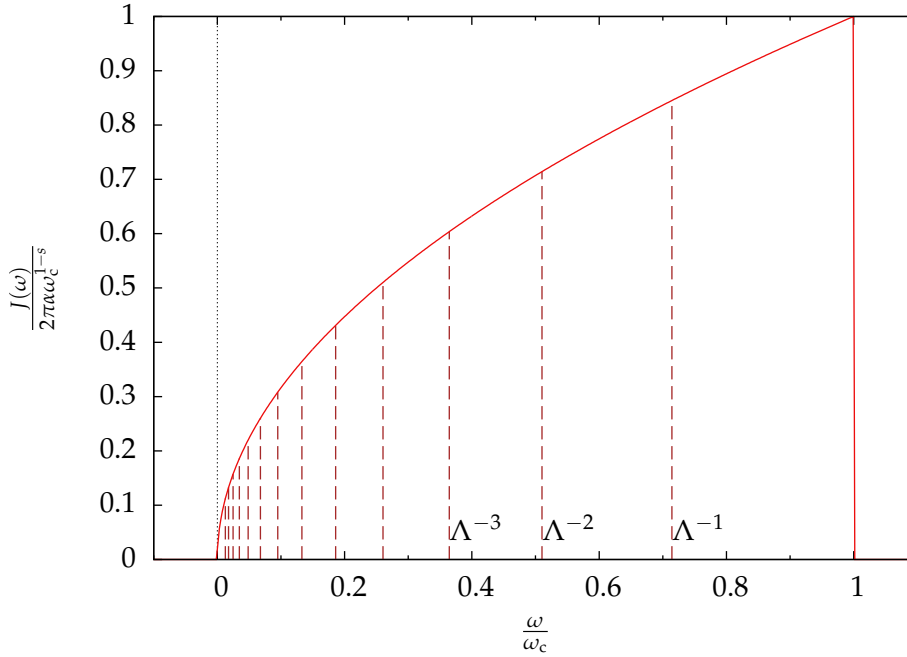


Figure 1.7: Logarithmic discretization of the bosonic spectral function $J(\omega)$, Eq. (1.56). This example shows $s = 0.5$ and $\Lambda = 1.4$. The vertical lines indicate the borders of the energy intervals x_n , Eq. (1.57). For each interval one energy state is selected to represent the whole interval.

a given iteration one has only information about the system at a certain temperature, tuning the temperature away from this scale yields unphysical results.

This concludes the short introduction of the NRG. Some important aspects are omitted during the discussion, for example z -averaging [83] or the calculation of Green's functions [84, 85], as these are techniques not used in this thesis. Besides the standard NRG, as discussed so far, two extensions are employed in later chapters: the bosonic NRG and the time-dependent numerical renormalization group (TD-NRG). The next two sections cover these topics.

1.3.3 Bosonic reservoir

Originally the NRG was designed to solve QISs with a fermionic bath. In this section we discuss the extension to systems with a bosonic bath [74, 75], on the basis of the SBM.¹⁰ This model describes a local spin coupled to the displacement of the bosonic bath modes. However, the details of the model are irrelevant for the method and therefore one could consider more complex models and even combine fermionic bands and bosonic baths [86].

¹⁰ In this section we focus on the method; below in Sec. 2.1 the SBM is discussed in more detail.

The Hamiltonian under consideration is

$$H = H_{\text{imp}} + \frac{\sigma_z}{2} \sum_i \lambda_i (a_i + a_i^\dagger) + \sum_i \omega_i a_i^\dagger a_i, \quad (1.54)$$

where H_{imp} is the Hamiltonian of the impurity. This impurity consists of a spin represented by the Pauli matrix σ_z . The creation and annihilation operators of the i th bosonic mode of the bath are a_i^\dagger and a_i . The parameters λ_i and ω_i depend on the bath, which is fully characterized by its spectral function

$$J(\omega) = \pi \sum_i \lambda_i^2 \delta(\omega - \omega_i) \quad (1.55)$$

and we use the standard parametrization [21]

$$J(\omega) = \begin{cases} 2\pi\alpha\omega_c^{s-1}\omega_s & 0 < \omega < \omega_c \\ 0 & \text{else} \end{cases}. \quad (1.56)$$

With this parametrization the bath depends on three quantities: the coupling strength α , the cutoff frequency ω_c , and the bath parameter s . We choose ω_c as the energy unit and set $\omega_c = 1$ in the following.

The goal is, as with the standard NRG, to discretize the spectral function and map it to a Wilson chain. Since the spectral function is strictly positive the discretization points are given by (cf. Fig. 1.7)

$$x_n = \Lambda^{-n} \quad (1.57)$$

and the width of each interval is

$$d_n = \Lambda^{-n}(1 - \Lambda^{-n}). \quad (1.58)$$

In contrast to the fermionic NRG, where one defines operators for the positive and negative part of the spectrum, the bosonic spectrum is purely positive and – unlike the fermionic Hamiltonian Eq. (1.33) – the discretized Hamiltonian consists of only one set of operators,

$$H = H_{\text{imp}} + \sum_{n=0}^{\infty} \xi_n a_n^\dagger a_n + \frac{\sigma_z}{2\sqrt{\pi}} \sum_{n=0}^{\infty} \gamma_n (a_n^\dagger + a_n), \quad (1.59)$$

$$\text{with } \gamma_n = \int_{\Lambda^{-n+1}}^{\Lambda^n} d\omega J(\omega) \quad \text{and} \quad \xi_n = \gamma_n^{-2} \int_{\Lambda^{-n+1}}^{\Lambda^n} d\omega J(\omega)\omega. \quad (1.60)$$

The operators a_n are obtained by expanding the operators a_i in a basis spanned by a complete set of functions, which only have support in the n th interval.

The Hamiltonian (1.59) describes a system of a spin coupled to a bosonic mode at each energy scale; this is the so-called star-topography. This is now mapped to a Wilson chain, with the bosonic creation and annihilation operators b_n^\dagger and b_n . The Hamiltonian of the semi-infinite Wilson chain with the impurity is given by

$$H = H_{\text{imp}} + \sqrt{\frac{\eta_0}{\pi}} \frac{\sigma_z}{2} (b_0 + b_0^\dagger) + \sum_n \left(\epsilon_n b_n^\dagger b_n + t_n (b_n^\dagger b_{n+1} + b_{n+1}^\dagger b_n) \right). \quad (1.61)$$

The structure of this Hamiltonian is of the same structure as the corresponding Hamiltonian of the fermionic NRG Eq. (1.37). The coupling between spin and bosonic bath is given by

$$\eta_0 = \int d\omega J(\omega) \quad (1.62)$$

and in the case that the spectral function is of the form Eq. (1.56) the coupling parameter is given by

$$V = \sqrt{\frac{\eta_0}{\pi}} = \sqrt{\frac{2\alpha\omega_c^2}{s+1}}. \quad (1.63)$$

The chain parameters t_n and ϵ_n have to be calculated numerically [75]. One important difference to the fermionic case is that these parameters fall off as Λ^{-n} and not as $\Lambda^{-\frac{n}{2}}$. The reason for this lies in the different discretizations: with each energy interval only one (positive) energy interval is associated and not two (one positive and one negative) as in the fermionic case.

The algorithm for the iterative diagonalization is almost the same as described in the previous section, except for two changes: (i) all factors $\Lambda^{\pm\frac{n}{2}}$ have to be replaced by $\Lambda^{\pm n}$ and (ii) the number of bosonic modes has to be truncated. Each boson spans a Hilbert space of infinite dimension. Numerically it is not possible to keep all modes and therefore one has to restrict the bosonic Hilbert space to a few modes N_b . In practice this number is usually $N_b \lesssim 20$. As discussed below in Sec. 2.5.2 errors due to the truncation of the bosonic basis can be reduced by choosing an optimal basis.

1.3.4 Time dependence

The TD-NRG was developed to track the real-time dynamics of QISs [76, 77]. Several models are already investigated with this method: the resonant-level model (RLM) and the SIAM [76], the SBM [77, 87], and the Kondo model [77, 88]. Furthermore the TD-NRG paved the way for the development of the scattering-states NRG [89]. This approach uses the same formalism as the TD-NRG, but instead of calculating the real-

time dynamics of some observable, the $t \rightarrow \infty$ limit is performed analytically; this allows to calculate steady-state currents.¹¹

The TD-NRG simulates QISs with an abrupt quench at time $t = 0$. This quench perturbs the Hamiltonian H^i , which is of the form Eq. (1.23), locally. The basic strategy of the TD-NRG is to determine the equilibrium density operator before the quench and calculate the time evolution of this operator with the perturbed Hamiltonian. For this purpose one has to diagonalize both Hamiltonians with the NRG and one has to calculate transformation matrices to change the basis from the initial eigenbasis to the final eigenbasis.

The entire system is characterized by the density operator

$$\rho_0 = \frac{e^{-\beta H^i}}{\text{Tr} [e^{-\beta H^i}]} \quad (1.64)$$

at time $t = 0$, when a static perturbation ΔH is suddenly switched on: $H(t \geq 0) = H^i + \Delta H \equiv H^f$. Because H^f is time-independent, the density operator evolves according to

$$\rho(t) = e^{-itH^f} \rho_0 e^{itH^f} \quad (1.65)$$

for $t \geq 0$. The objective is to use the NRG to compute the expectation value $\langle O \rangle(t)$ of a general local operator O . As shown in Refs. 76, 77, the result can be written as

$$\langle O \rangle(t) = \sum_m^N \sum_{r,s}^{\text{trun}} e^{it(E_r^m - E_s^m)} O_{r,s}^m \rho_{s,r}^{\text{red}}(m), \quad (1.66)$$

where E_r^m and E_s^m are the dimension-full NRG eigenenergies of the perturbed Hamiltonian at iteration $m \leq N$, $O_{r,s}^m$ is the matrix representation of the operator O at that iteration, and $\rho_{s,r}^{\text{red}}(m)$ is the reduced density matrix defined for the NRG in Eq. (1.72) below.¹² The restricted sum over r and s requires that at least one of these states is discarded at iteration m . N denotes the NRG chain length.

The derivation of Eq. (1.66) relies on two key ingredients: (i) The identification of a complete basis set of the many-body Fock space of the Wilson chain based on the NRG eigenstates at different iterations. (ii) Expectation values are obtained by explicitly tracing over this complete basis set using a suitable resummation procedure.

Complete basis set

In this section, we review the complete basis set of the Wilson chain [76, 77] generated by the NRG approach.

¹¹ The following text of Sec. 1.3.4 has been published in [90] and is ©2012 American Physical Society.

¹² The general definition is given in Eq. (1.14).

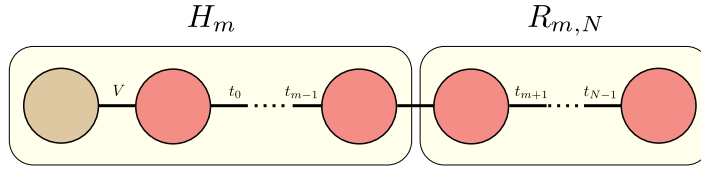


Figure 1.8: The full Wilson chain of length N is divided into a subchain of length m and the environment $R_{m,N}$. The Hamiltonian H_m can be viewed either as acting only on the subchain of length m , or as acting on the full chain of length N , but with the hopping matrix elements t_m, \dots, t_{N-1} all set to zero. The former picture is the traditional one. In the TD-NRG one adopts the latter point of view.

The NRG targets the iterative solution of a finite chain of N bath chain links.¹³ One can view the NRG procedure as a set of operations, where at first all hopping matrix elements along a given chain of fixed length m are set to zero, $t_n = 0$ for $n \geq m$, and at each successive step another hopping matrix element is switched on. The full Hamiltonian H_N is recovered once all hopping matrix elements have been switched on. The entire sequence of Hamiltonians H_m with $m \leq N$ act on the same Fock space of the N -site chain, hence each NRG eigenenergy of H_m has an extra degeneracy of $d^{(N-m)}$, where d is the number of distinct states at each site along the chain. The extra degeneracy stems from the $N - m$ environment sites at the end of the chain, denoted by $R_{m,N}$ in Fig. 1.8 which remain decoupled from the impurity at iteration m .

When acting on the m -site chain, we label the NRG eigenstates and eigenenergies of H_m by $\{|r; m\rangle\}$ and E_r^m , respectively. Consider now the action of H_m on the full N -site chain. Enumerating the different configurations of site i by $\{\alpha_i\}_{i=1,\dots,d}$, each of the tensor-product states $|r; m\rangle \otimes |\alpha_{m+1}, \dots, \alpha_N\rangle$ with arbitrary $\alpha_{m+1}, \dots, \alpha_N$ is a degenerate eigenstate of H_m with energy E_r^m . To label these states we introduce the shorthand notation $|r, e; m\rangle$, where the environment variable $e = \{\alpha_{m+1}, \dots, \alpha_N\}$ encodes the $N - m$ site labels $\alpha_{m+1}, \dots, \alpha_N$, and the index m is used to record where the chain is partitioned into a subsystem and an environment (cf. Fig. 1.8).

In order to keep only a manageable amount of number of basis states, the high-energy states are discarded after each iteration, which is fully justified in equilibrium by the hierarchy of scales along the Wilson chain and the Boltzmann form the density operator ρ_0 . It has been shown [76, 77] that the set of all those discarded states defines a complete basis set of approximate NRG eigenstates for the full N -site chain.

To understand this important point, consider the first iteration m_{\min} at which states are discarded. In order to keep track of the complete basis set of the N -site chain, the eigenstates $|r, e; m_{\min}\rangle$ can formally be divided into two distinct subsets: the discarded high-energy states $\{|l, e; m_{\min}\rangle_{\text{dis}}\}$ and the kept low-energy states $\{|k, e; m_{\min}\rangle_{\text{kp}}\}$. Ob-

¹³ Even though the chain has $N + 1$ sites we call it a chain of length N for a convenient notation.

viously, the sum of both subset $\{|l, e; m_{\min}\rangle_{\text{dis}}\}$ and $\{|k, e; m_{\min}\rangle_{\text{kp}}\}$ form a complete basis set of the full chain.¹⁴

At the next NRG iteration only the kept states are used to construct the NRG eigenstates of $H_{m_{\min}+1}$ within the truncated subspace spanned by $\{|k, e; m_{\min}+1\rangle\}$. The resulting NRG eigenstates can again be divided into two subsets of discarded and kept states which, when combined with the discarded eigenstates of iteration m_{\min} , form a complete basis set of the Fock space \mathcal{F}_N of the full N -site chain.

Repeating this procedure at all subsequent iterations, one continues to maintain a complete basis set of \mathcal{F}_N up to the final NRG iteration $m = N$. We thus arrive at the following completeness relation:

$$\sum_{m=m_{\min}}^N \sum_{l,e} |l, e; m\rangle \langle l, e; m| = \sum_{m=m_{\min}}^N \hat{P}_m = 1, \quad (1.67)$$

where the summation over m starts from the first iteration m_{\min} at which a basis-set reduction is imposed. The summation indices l and e implicitly depend on m , and the projector onto the discarded states at iteration $m_{\min} \leq m \leq N$ is defined as

$$\hat{P}_m = \sum_{l,e} |l, e; m\rangle \langle l, e; m|. \quad (1.68)$$

The projector $\hat{\mathbf{1}}_m^+$ onto the retained subspace spanning H_{m+1} ($m < N$), defined as

$$\hat{\mathbf{1}}_m^+ = \sum_{k,e} |k, e; m\rangle \langle k, e; m|, \quad (1.69)$$

must be obviously identical to

$$\hat{\mathbf{1}}_m^+ = \sum_{m'=m+1}^N \hat{P}_{m'}, \quad (1.70)$$

since all states retained at iteration m are necessarily discarded at some later iteration m' , because all states of the last iteration considered as discarded. In particular, $\hat{\mathbf{1}}_{N-1}^+$ coincides with \hat{P}_N , and we set $\hat{\mathbf{1}}_N^+ = 0$. Therefore, the completeness of our basis set (1.67) can also be partitioned into

$$1 = \sum_{m=m_{\min}}^M \hat{P}_m + \hat{\mathbf{1}}_M^+ \quad (1.71)$$

for any $m_{\min} \leq M \leq N$ using Eq. (1.69).

¹⁴ In the following, the subscripts $_{\text{dis}}$ and $_{\text{kp}}$ are discarded: the labeling with l (k) is sufficient to uniquely identify discarded (kept) states.

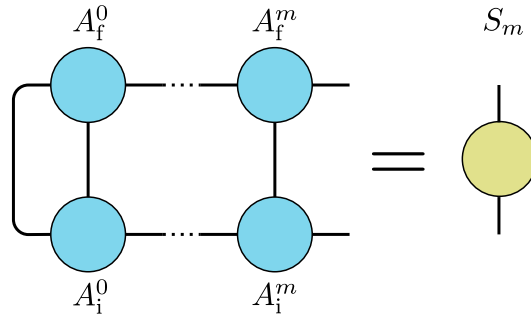


Figure 1.9: Calculation of the overlap matrix $S(m)$ at iteration m . The overlap matrix is calculated by contracting over a tensor-network consisting of the A-matrices of the initial and final Hamiltonian.

Reduced density matrix and the TD-NRG algorithm

After a sudden quench, the Hamiltonian H^f governs the time evolution of the system while the initial condition is determined by the density matrix ρ_0 . For QISs, all relevant information on the initial condition is contained in Eq. (1.66) in the form of the reduced density-matrices [76, 77] $\rho_{s,r}^{\text{red}}(m)$ defined as

$$\rho_{s,r}^{\text{red}}(m) = \sum_e \langle s, e; m | \rho_0 | r, e; m \rangle. \quad (1.72)$$

Here the states $|r, e; m\rangle$ and $|s, e; m\rangle$ pertain to the Hamiltonian H^f , and the summation runs over the environment degrees of freedom e . The only approximation entering Eq. (1.66) is the standard NRG approximation [28, 29] whereby $H_N |r, e; m\rangle \approx H_m |r, e; m\rangle = E_r^m |r, e; m\rangle$, which leads to the simple time-dependent exponents $e^{it(E_r^m - E_s^m)}$. Apart from this point, Eq. (1.66) constitutes an exact evaluation of $\langle O \rangle(t)$ on the discretized N -site chain.

Practical calculations hinge on the ability to accurately compute the reduced density-matrices of Eq. (1.72). For a general ρ_0 this can be a daunting task. However, in the case of interest where ρ_0 has the standard Boltzmann form of Eq. (1.64), the summation over e can be carried out exactly. Hence $\rho_{s,r}^{\text{red}}(m)$ can be evaluated at the same level of accuracy that ρ_0 is represented in the equilibrium NRG.

Technically this goal is achieved by implementing two independent NRG runs, one for the unperturbed Hamiltonian H^i to construct ρ_0 via Eq. (1.64), and another for the Hamiltonian H^f . The reduced density matrix $\rho_{s,r}^{\text{red}}(m)$ is first evaluated with respect to the eigenstates of the initial Hamiltonian, and then rotated [76, 77] to the eigenstates of the full Hamiltonian using the overlap matrices

$$\langle q_i; m | r; m \rangle = S_{q_i, r}(m). \quad (1.73)$$

Here $|r; m\rangle$ denotes an NRG eigenstate of the full Hamiltonian at iteration m , and $|q_i; m\rangle$ is an NRG eigenstate of the initial Hamiltonian at the same iteration. Both NRG runs

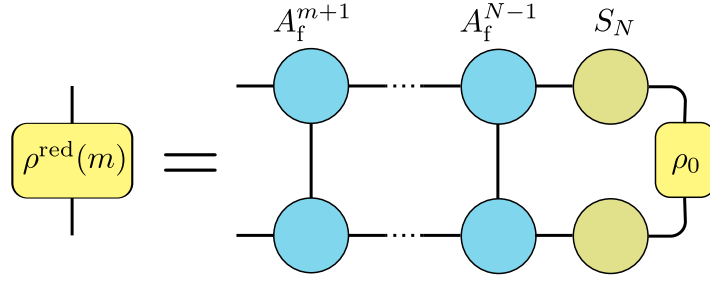


Figure 1.10: Calculation of the reduced density matrix $\rho^{\text{red}}(m)$ at iteration m in the basis of H^f . The density matrix ρ_0 is determined at the last iteration of the NRG run for the initial Hamiltonian, rotated in the final basis with the overlap matrix $S(N)$, and afterwards successively rotated through the Wilson chain with the final A-matrices A_f^n .

produce a MPS; we denote the A-matrix of iteration n (defined analogous to Eq. (1.47)) of the initial (final) run by A_i^n (A_f^n). The practical calculation of the overlap matrix $S(m)$ is illustrated in Fig. 1.9. Figure 1.10 illustrates how to calculate the reduced density matrix $\rho^{\text{red}}(m)$ needed to calculate $\langle O \rangle(t)$ in Eq. (1.66). In practice, one has not to contract over the whole tensor-network for each iteration, but one can calculate $\rho^{\text{red}}(m)$ recursively from $\rho^{\text{red}}(m+1)$; this involves only two matrix-multiplications and a sum over the physical index (cf. Fig. 1.10).

This concludes the discussion of the NRG. In Chapter 4 we use the presented formalism - especially the complete Fockspace basis - to formulate a new hybrid method. This hybrid method combines the TD-NRG with any other suitable method, for example the time-dependent density-matrix renormalization group (TD-DMRG). Therefore we continue in the next section with a presentation of the DMRG and its extension to time dependence.

1.4 Density-matrix renormalization group

The density-matrix renormalization group (DMRG) [91] was proposed by White in 1992 [32] to eliminate an essential drawback of the NRG: it cannot be applied to other problems than quantum impurity systems (QISs). In particular, it is not possible to solve general quantum lattice problems with the NRG. By overcoming this obstacle the DMRG has established itself as widely used method for a large number of applications [63, 91, 92], e.g. the simulation of ultracold gases [14] or QISs [93, 94, 95].

Later, a connection between DMRG and MPSs [96, 97] was found which lead to the formulation of the DMRG in an MPS language [63, 69]. It was understood that MPSs belong to a larger class of states, the so-called tensor networks [98], and based on this concept new methods were developed [99] and the understanding of the DMRG was deepened [100]. As the DMRG is limited to one dimensional systems there are proposals how to design methods based on DMRG and MPSs for higher dimensions. One pro-

posal to simulate two dimensional systems are projected entangled pair states (PEPSs) [99, 101, 102]. One can view PEPSs as the extensions of MPSs to two dimensions: instead of two bond indices each A-matrix has now four bond indices.

The objective of the DMRG is to calculate the ground state of a Hamiltonian acting on a chain. This is achieved in two steps: (i) in the warm-up phase one finds a first approximate ground state and (ii) in the sweeping phase the state is optimized; this optimization aims at lowering the ground-state energy further. Subsequently, one can calculate expectation values of the ground state or do a time evolution. In this section the details of these steps are discussed.

1.4.1 Infinite DMRG

The DMRG was designed to solve models on a 1D chain and with Hamiltonians including only operators acting on one site or on two neighboring sites. While the last limitation can in principle be lifted, leaving a 1D chain is, with some exception e.g. ladder structures even with more legs [103], in general not possible; one example where both is done is Ref. 104 .

The Hamiltonian under consideration in the discussion of the DMRG is of the form

$$H = \sum_{i=0}^{N-1} \sum_{\nu}^{N_{\nu}} \epsilon_{\nu}^i O_{\nu}^i + \sum_{i=0}^{N-2} \sum_{\nu\nu'}^{N_{\nu}} t_{\nu\nu'}^i O_{\nu}^i O_{\nu'}^{i+1}. \quad (1.74)$$

The complex constants ϵ_{ν}^i and $t_{\nu\nu'}^i$ take numeric values depending on the model and O_{ν}^i is an operator acting only on site i ; ν labels different operators.¹⁵ N is the length of the chain and for simplicity we assume this number to be even. N_{ν} is the number of different operators.

For example, if one wishes to describe a Wilson chain with Eq. (1.74) one could choose

$$\epsilon_0^i \equiv \epsilon_1^i \equiv 0, \quad \epsilon_2^i \equiv \epsilon_i, \quad (1.75)$$

$$t_{01}^i \equiv t_{10}^i \equiv t_i, \quad t_{mn}^i \equiv 0 \text{ for } m+n \neq 1, \quad (1.76)$$

$$O_0^i \equiv c_i^{\dagger}, \quad O_1^i \equiv c_i, \quad \text{and} \quad O_2^i \equiv c_i^{\dagger} c_i, \quad (1.77)$$

where ϵ_i and t_i are the Wilson chain's on-site energies and hopping parameters respectively. With these definitions the ν -sums in Eq. (1.74) run over $\nu = 0, 1, 2$.

¹⁵ Note, that these operators can be fermionic or bosonic. A distinction between a fermionic DMRG and a bosonic DMRG, as it was necessary for the NRG, is not needed. Of course, the number of bosonic modes of the bosonic operators have to be truncated.

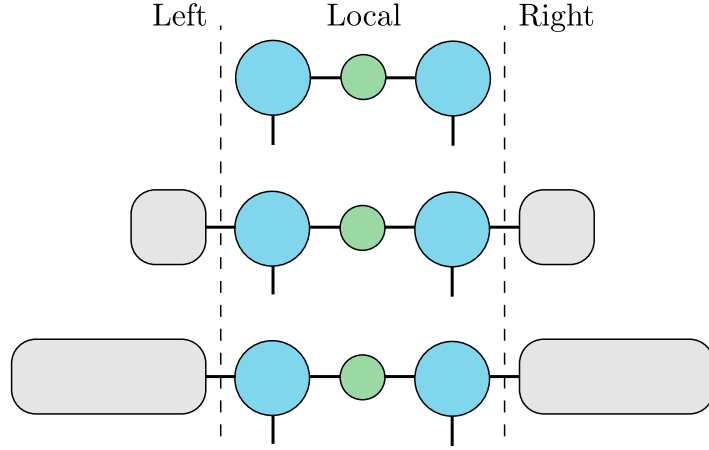


Figure 1.11: Schematic representation of the infinite DMRG method. At the first iteration the whole system consists only of a local block. At each iteration the local block is optimized and afterwards one A-matrix of the local block is moved into the left block and the other one into the right block; new A-matrices are inserted into the local block. The size of the left and right block is increased until the desired chain length is reached.

The infinite DMRG¹⁶ starts with a small system and increases the system size until the desired chain length is reached. The start Hamiltonian is given by

$$H_0 = \sum_{i \in \{0, N-1\}} \sum_{\nu} \epsilon_{\nu}^i O_{\nu}^i + \sum_{\nu\nu'} t_{\nu\nu'}^0 O_{\nu}^0 O_{\nu'}^{N-1}. \quad (1.78)$$

Analogous to the RG-step in the NRG, Eq. (1.45), the ground state of the whole chain is calculated iteratively by adding further lattice sites step-by-step. In contrast to the NRG where one site per iteration is added, the DMRG adds two sites at each iteration. The Hamiltonian at iteration m is given by

$$H_m = \sum_{i=0}^m \sum_{\nu} \epsilon_{\nu}^i O_{\nu}^i + \sum_{i=N-1-m}^{N-1} \sum_{\nu} \epsilon_{\nu}^i O_{\nu}^i + \sum_{i=0}^{m-1} \sum_{\nu\nu'} t_{\nu\nu'}^i O_{\nu}^i O_{\nu'}^{i+1} + \sum_{i=N-1-m}^{N-2} \sum_{\nu\nu'} t_{\nu\nu'}^i O_{\nu}^i O_{\nu'}^{i+1} + \sum_{\nu\nu'} t_{\nu\nu'}^0 O_{\nu}^m O_{\nu'}^{N-1-m}. \quad (1.79)$$

In other words, at each iteration two sites are inserted into the center of the existing chain. This concept becomes more clear when considering the ground state at each iteration.

The state of the system is an MPS defined by the matrices $\{A^0, \dots, A^{\frac{N}{2}-1}, \Lambda, B^{\frac{N}{2}-1}, \dots, B^0\}$, (cf. Fig. 1.1). The idea of the DMRG is to partition the state into three blocks: *left*, *local*, and *right*. At a given iteration m both the left and the right block represent m

¹⁶ The infinite DMRG is not to be confused with the iDMRG [105]; this method's objective is to simulate systems in thermodynamic limit with the DMRG and is closely related to the infinite time-evolving block decimation (iTEBD) method [106].

sites¹⁷ and the local block represents two sites. To calculate the ground state at this iteration the A-matrices of the local block are optimized. After this optimization the left (right) A-matrix of the local block is moved into the left (right) block and is kept constant for the remaining part of the infinite DMRG run (cf. Fig. 1.11).

The crucial part of the algorithm is how the A-matrices of the local block are optimized. The optimization criterion is to minimize the energy of the state under the constraints that the left and right block are held constant and the state is an eigenstate of the Hamiltonian. To this end, one splits the Hamiltonian at iteration m into five parts,

$$H_m = H_L + H_{L\bullet} + H_{\bullet\bullet} + H_{\bullet R} + H_R \quad (1.80)$$

where

- H_L acts only on the left block,
- $H_{L\bullet}$ is the coupling between left and local block,
- $H_{\bullet\bullet}$ acts only on the local block,
- $H_{\bullet R}$ is the coupling between local and right block,
- and H_R acts only on the right block.

As discussed in Sec. 1.2.2 an operator changes only the A-matrices of the sites it acts on. This means that H_L and H_R have only an effect on the left and right block. Consequently, because the A-matrices of these blocks are constant at the optimization of the local block, one can define the matrices E^m and F^m , which describe the environment of the local block; each environment matrix depends on the Hamiltonian and the A-matrices of the respective block. How these matrices are constructed explicitly is shown below (cf. Fig. 1.14). Before going further into detail how to optimize the local block, we first establish how to formulate the Hamiltonian as a matrix product operator (MPO).

Matrix product operators

When using MPSs it is convenient to express Hamiltonians as MPOs [69, 107]. In this spirit one associates one matrix W^m with each site m . The matrix elements of W^m are

¹⁷ The first iteration is denoted by $m = 0$.

The matrix W^m for a Wilson chain with hopping parameters t_m and on-site energies ϵ_m is given by

$$W^m = \begin{pmatrix} \mathbb{1} & 0 & 0 & 0 \\ c_m^\dagger & 0 & 0 & 0 \\ c_m & 0 & 0 & 0 \\ \epsilon_m c_m^\dagger c_m & t_m c_m^\dagger & t_m c_m & \mathbb{1} \end{pmatrix}.$$

Here, $N_\nu = 2$, but as the Hamiltonian is particle number conserving W^m is a 4×4 matrix and not 6×6 as the general W-Matrix, Eq. (1.81), for $N_\nu = 2$. Suppose the Wilson chain has only two sites, one can construct the Hamiltonian of the total system by Eq. (1.82)

$$\begin{aligned} H &= W^0 W^1 \Big|_{\text{first column, last row}} \\ &= \begin{pmatrix} \mathbb{1} & 0 & 0 & 0 \\ c_0^\dagger & 0 & 0 & 0 \\ c_0 & 0 & 0 & 0 \\ \epsilon_0 c_0^\dagger c_0 & t_0 c_0^\dagger & t_0 c_0 & \mathbb{1} \end{pmatrix} \begin{pmatrix} \mathbb{1} & 0 & 0 & 0 \\ c_1^\dagger & 0 & 0 & 0 \\ c_1 & 0 & 0 & 0 \\ \epsilon_1 c_1^\dagger c_1 & t_1 c_1^\dagger & t_1 c_1 & \mathbb{1} \end{pmatrix} \Big|_{\text{first column, last row}} \\ &= \epsilon_0 c_0^\dagger c_0 + \epsilon_1 c_1^\dagger c_1 + t_0 (c_0^\dagger c_1 + c_1^\dagger c_0). \end{aligned}$$

Figure 1.12: Example how to construct W matrices for a Wilson chain.

operators acting only on site m . For a Hamiltonian of the form Eq. (1.74) with $N_\nu = 2$ the MPO matrix W^m is given by

$$W^m = \begin{pmatrix} \mathbb{1} \\ O_0^m \\ O_0^m \\ O_1^m \\ O_1^m \\ \sum_\nu \epsilon_\nu^i O_\nu^i & t_{00}^m O_0^m & t_{10}^m O_1^m & t_{01}^m O_0^m & t_{11}^m O_1^m & \mathbb{1} \end{pmatrix}. \quad (1.81)$$

The Hamiltonian of the total system is then given by the matrix element, corresponding to the local Hamiltonian, of the product matrix of all W matrices,

$$H = \left(\prod_{m=0}^{N-1} W^m \right) \Big|_{\text{first column, last row}}. \quad (1.82)$$

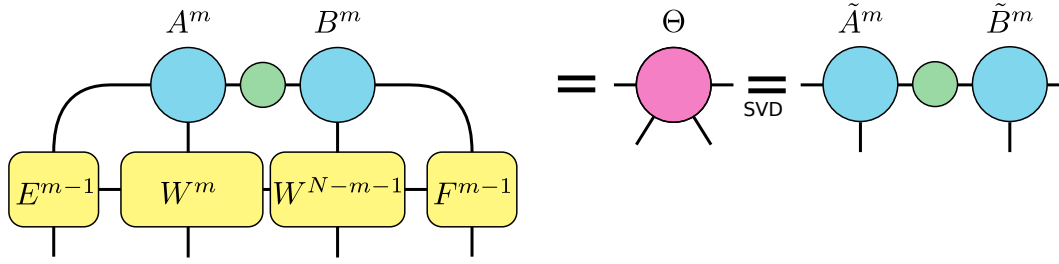


Figure 1.13: Application of the Hamiltonian to the local block. W^m and W^{N-m-1} are the MPO matrices representing the Hamiltonian; the influence of the left and right block is encoded in E^{m-1} and F^{m-1} . Contracting over the tensor network yields a tensor Θ with four indices. Using a SVD Θ can be recast into a MPS. Notice that for W the horizontal lines refer to the outer indices, that is, the cell of the matrix, and the vertical lines refer to the inner indices, that is, the physical indices of the operator in that cell.

Fig. 1.12 gives an explicit example how the W -matrices are constructed for a Wilson chain. As mentioned above, in the DMRG one splits the Hamiltonian into three blocks

$$H = \underbrace{\prod_{m \in \text{left block}} W^m}_{=: E'} \prod_{m \in \text{local block}} W^m \underbrace{\prod_{m \in \text{right block}} W^m}_{=: F'} \Bigg|_{\text{first column, last row}}. \quad (1.83)$$

Due to the special form the W matrices, that is, only the first column and the last row have non-vanishing elements,¹⁸ only the last row of E' and the first column of F' contribute to the product. Therefore we define the environment vectors

$$E = E'_{\text{last row}} \quad (1.84)$$

$$\text{and } F = F'_{\text{first column}}. \quad (1.85)$$

With these definitions the Hamiltonian Eq. (1.82) is written as

$$H = E^t \cdot \left(\prod_{m \in \text{local block}} W^m \right) \cdot F \Bigg|_{\text{first column, last row}}. \quad (1.86)$$

Optimization and truncation of the local block

At each iteration the A-matrices of the local block are optimized by using the Lanczos algorithm [45] to calculate the ground state. For this algorithm one has to define the matrix-vector multiplication $H|\psi\rangle$ in the MPS formalism. The state $|\psi\rangle$ is represented

¹⁸ This is only true for Hamiltonians with nearest-neighbor and local terms.

by the A -matrices of the local block and the Hamiltonian by the W -matrices of the local block and the E and F matrices of the environment. A diagrammatic representation of the multiplication is shown in Fig. 1.13. The result of this multiplication Θ is a tensor with four indices: two physical and two bond indices. For the Lanczos algorithm this multiplication has to be repeated several times. Numerically the input data of the Lanczos routine is therefore the Θ tensor of the previous Lanczos iteration¹⁹ and a functor routine multiplying Θ with H , that is contracting over the first tensor network in Fig. 1.13.

After the running Lanczos routine, one uses a SVD to write the tensor Θ as a product of two A -matrices and thereby recapturing the MPS structure of the state. This yields the optimized matrices \tilde{A} and \tilde{B} , by which the energy of the state is minimized.

The DMRG suffers from the same problem as the NRG: the dimension of the Hilbert space grows exponentially with the system size. To limit the number of kept states one has to truncate the Hilbert space. Technically the procedure to truncate the Hilbert space is the same for the DMRG as it is for the NRG: one chooses a new incomplete basis and rotates the state and all operators into this new basis. In this process information is lost. The error due to this is called truncation error.

To keep the truncation error small one does not choose an arbitrary new basis, but one which still captures the essential physical properties of the system. The question is, what one considers the *essential* information. Here, the NRG and DMRG have a different interpretation. The NRG aims at calculating an effective low-energy Hamiltonian, whereas the DMRG targets only the ground state of the system. Due to these different goals, the truncated basis is chosen differently: the NRG rotates the state into a basis spanned by the eigenvectors to low-energy eigenvalues of the Hamiltonian. On the other hand, in the DMRG the basis is spanned by the eigenvectors of the reduced ground-state density matrix with the largest eigenvalues.²⁰

The most convenient way to calculate and truncate the eigenvectors of the reduced density matrix is to use a SVD [69]. When calculating the SVD of the tensor Θ (cf. Fig. 1.13),

$$\Theta_{s_A, s_B} = \tilde{A}[s_A] \Lambda \tilde{B}[s_B], \quad (1.87)$$

the resulting matrix \tilde{A} (\tilde{B}) contains the eigenvectors of the left (right) reduced density matrix. The eigenvalues λ_i of the left and right reduced density-matrices are equal. The center matrix Λ is given by $\Lambda = \text{diag}(\lambda_1^2, \lambda_2^2, \dots)$. We assume that the eigenvectors are ordered by the magnitude of the eigenvalues, $\lambda_i \geq \lambda_j \forall i < j$. The DMRG truncation

¹⁹ For the first Lanczos iteration Θ is initialized with random numbers.

²⁰ One reason why this procedure works is that states realized in nature usually live only in a very small region of the Hilbert space [108].

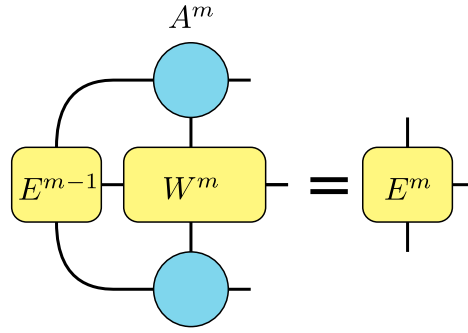


Figure 1.14: The environment matrix E is iteratively calculated from the previous environment matrix, the A-matrices, and the Hamiltonian. Contracting over this tensor network saves the Hamiltonian of the whole left block in E^m and transforms all operators, including the newly calculated Hamiltonian, into the new basis.

scheme is to keep only the N_s states with the largest eigenvalues. Formally one achieves this by defining the truncated matrices

$$A^{\text{trunc}}[s]_{ij} = \tilde{A}[s]_{ij} \quad i < N_s, j < N_s, \quad (1.88)$$

$$\Lambda_{ii}^{\text{trunc}} = \Lambda_{ii}^{\text{red}} \quad i < N_s, \quad (1.89)$$

$$\text{and } B^{\text{trunc}}[s]_{ij} = \tilde{B}[s]_{ij} \quad i < N_s, j < N_s. \quad (1.90)$$

The error induced by this truncation can be quantified by

$$\epsilon = \sum_{i \in \text{trunc}} \lambda_i^2. \quad (1.91)$$

Increasing the length of the chain

After optimizing the local block, the next step is to increase the chain length. Assuming the chain consists of $2m$ sites, the optimization of the local block yields the matrices A^m and B^m . For the purpose of increasing the chain length, one has to incorporate W^m (W^{N-m-1}) in the left (right) block and thereby defining the next environment matrix E^m (F^m). Furthermore one has to rotate the operators of the left (right) block into the new basis defined by A^m (B^m). Fig. 1.14 illustrates the calculation of the new environment matrix E^m .²¹ After increasing the left and right block one inserts new A-matrices into the local block and jumps back to the optimization.

By repeating these steps – optimization of the local block and calculating new block matrices – the size of the chain is iteratively increased. So far the discussion was focused on the question how one calculates the environment matrices from the previous ones. This leads to the question, how one initializes the first matrices E^{-1} and F^{-1} . To answer this question, a few words about the general structure of E and F are in order.

²¹ Roughly speaking, one has to flip this figure horizontally and replace E by F and A by B to calculate F^m .

E has the same structure as the last row of a W -matrix: the first element is the local Hamiltonian, in the case of E the Hamiltonian of the left block; the last element is the identity operator; and all operators in between are for the coupling between the sites.²² At the beginning of the DMRG run the left block is empty – thus all operators for the coupling and the Hamiltonian of the left block is zero,

$$E_i^{-1} = \begin{cases} \mathbb{1} & i \hat{=} \text{last element} \\ 0 & \text{else} \end{cases}, \quad F_i^{-1} = \begin{cases} \mathbb{1} & i \hat{=} \text{first element} \\ 0 & \text{else} \end{cases}. \quad (1.92)$$

1.4.2 Finite DMRG

When building up a chain with the infinite DMRG the A -matrices are computed one after another. This means that sites added later have no effect on the A -matrices of sites already included in the chain. In other words, a site at a given iteration is not affected by the rest-chain added later in the iteration process. However, the rest-chain can have a significant impact on the site and therefore it cannot be neglected.

The way the DMRG deals with this problem is to use the infinite DMRG to built up a chain and use the ground state as the initial state for the finite DMRG. This method iteratively improves the ground state further by a process called sweeping. The idea is to move the local block site by site through the chain, by letting one block grow and the other one shrink (cf. Fig. 1.15). At a each position the local block is optimized as discussed above. The initial guess vector for the Lanczos algorithm is given by the already calculated A -matrices of the local block. At each sweep step the block matrix – E or F – of the growing block is newly generated. Because one works at a fixed chain length, the whole chain affects the local block.

In one complete sweep the local block is first moved from the center of the chain leftwards until it reaches the left border, then it is moved to the right border and from there back to the center.

1.4.3 Time-dependent DMRG

The discussion so far was focused on the core DMRG algorithm. Since its development several extensions to the DMRG were made [63, 91, 92]; one extension is the adaptive time-dependent density-matrix renormalization group (TD-DMRG) [109], which is discussed more deeply in this section. A different approach to calculate the time evolution of a state is given in Ref. 110; however, as this thesis does not implement this approach we do not discuss it further.

Using the finite DMRG one can accurately calculate the ground state of the system. Unlike the NRG the DMRG does not calculate the spectrum of the Hamiltonian. There-

²² In principle the structure of F is the same but reversed.

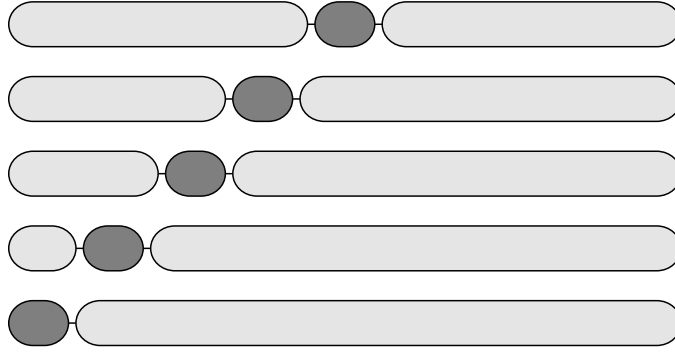


Figure 1.15: The state is improved by sweeping through the chain. This sketch shows the first quarter of a whole sweep. The local block represented by the dark shape, whereas the left and right block are represented by the light shape coupled to the local block. Initially, the local block is in the center of the chain. After moving the local block to the left end, it is moved to the right end and then back to the center. At each step the A-Matrices of the local block are optimized.

fore one needs a different strategy to trace the time-evolution of a given state $|\psi\rangle$. This is accomplished by applying the time-evolution operator $U(t)$ to the state,²³

$$|\psi\rangle(t) = U(t)|\psi\rangle = e^{iHt}|\psi\rangle. \quad (1.93)$$

However, it is impractical to apply $U(t)$ to the whole state at once. It is more convenient to calculate the Trotter-Suzuki decomposition (TSD) [112, 113] of $U(t)$ and apply the decomposed operator to the state. For this decomposition we write the Hamiltonian H as

$$H = \sum_{i \text{ even}} F_i + \sum_{i \text{ odd}} G_i, \quad (1.94)$$

with the operators F_i and G_i acting only on the two sites with index i and $i + 1$. If H is of the form Eq. (1.74) writing it as a sum over two-site operators, Eq. (1.94), is possible exactly. The TSD of U is given by

$$U(\delta t) = e^{iH\delta t} \approx \prod_{i \text{ even}} e^{iF_i\delta t} \prod_{i \text{ odd}} e^{iG_i\delta t} + \mathcal{O}(\delta t^2). \quad (1.95)$$

²³ As a side note we wish to mention that if one replaces the real time t by the imaginary time $t \rightarrow i\tau$ the time-evolution is performed in imaginary time and thereby cooling the system; this is the approach taken by the time-evolving block decimation (TEBD) method to calculate the ground state of a system [111].

This decomposition introduces a new error, because in general the operators do not commute, $[F_i, G_i] \neq 0$. This is the so-called Trotter error. With this decomposition of the time-evolution operator the state at time t is given by

$$|\psi\rangle(t) = \left(\prod_{i \text{ even}} e^{iF_i \delta t} \prod_{i \text{ odd}} e^{iG_i \delta t} \right)^{N_t} |\psi\rangle \quad (1.96)$$

$$\text{with the number of Trotter steps } N_t = \frac{t}{\delta t}. \quad (1.97)$$

With the TSD the time-evolution is reduced to a multiple application of two-site operators as discussed in Sec. 1.2.2.

For a deeper understanding of the Trotter error we consider a minimal example with the Hamiltonian $H = A + B$ where A and B are some arbitrary operators. The time evolution operator is hence given by

$$U = e^{i(A+B)\delta t} \approx e^{iA\delta t} e^{iB\delta t} e^{\frac{\delta t^2 [A,B]}{2}}. \quad (1.98)$$

This approximation gets exceedingly more correct for $\delta t \rightarrow 0$; however, this limit is in practice not reachable.

The exponential $e^{\frac{\delta t^2 [A,B]}{2}}$ is dominated by the largest eigenvalue of $[A, B]$ – assuming that $[A, B] \neq 0$. If the operators A and B mediate a hopping between two sites – as will be the case for all Hamiltonians considered in this thesis – the largest eigenvalue of $[A, B]$ is of the order $D_A D_B$, where D_A (D_B) is the hopping parameter of operator A (B). For modeling a bath the hopping parameters are of the order of the bandwidth D . Hence the dominant term in the exponential is of the order $\delta t^2 D^2$. Therefore, to keep the Trotter error small, the Trotter step δt has to fulfill the condition $\delta t \ll \frac{1}{D}$. This means, that with increasing bandwidth D the simulation gets more demanding. Notice, that for $\delta \geq \frac{1}{D}$ the TD-DMRG fails.

Besides reducing the Trotter step, another strategy to reduce the Trotter error is to use a higher order TSD [63, 114]. In this thesis a second order TSD is employed.

1.5 Summary

This chapter discussed different numerical methods to simulate quantum mechanical many-body systems. In this thesis two methods are employed: the numerical renormalization group (NRG) [28, 29] and the density-matrix renormalization group (DMRG) [32, 63, 91]. Both method can be formulated in the language of matrix product states (MPSs) [78]. The core concept of these states is to associate one matrix with each site of the system, a so-called A-matrix. For one dimensional systems an A-matrix has three indices: two bond indices connecting A-matrices of neighboring sites, and one physical index enumerating the basis states of the local basis at this site. We presented

	NRG	DMRG
Control parameter	Number of states	Number of states
System	Wilson chain with small impurity	1D chain with NN interactions
Truncation criterion	Energy	Eigenvalues of density matrix
Result	Energy spectrum/density matrix	Ground state
Improvement of result	None	Sweeping
Time-evolution	Analytic	Iterative
Error time-evolution	No additional	Trotter, Hilbert space truncation

Table 1.1: Comparison of some properties of the NRG and the DMRG.

some basic properties and algorithms for these states, concentrating on those which are important for this thesis, e.g. calculating expectation values or the reduced density matrix.

For this thesis an existing NRG implementation by Anders was used and extended, while a DMRG implementation was developed. Both methods share some similarities and differ in some aspects (cf. Tab. 1.1): the issue of an exponentially growing Hilbert space is in both methods resolved by iteratively increasing the size of the system and truncating the Hilbert space if its dimension grows beyond some threshold. However, the criterion which states to keep and which to discard differs for both methods: the NRG keeps the low-energy eigenstates of the Hamiltonian while the DMRG keeps the eigenstates of the ground-state density matrix with the largest weight. This allows the NRG to generate an effective low-energy Hamiltonian of the system including all excitations up to a certain threshold, whereas the DMRG targets only few states of the system. The price one has to pay in the NRG is that one can only deal with a certain type of chain – the so-called Wilson chain; the DMRG only requires short-range interactions.

The different results of NRG and DMRG – on the one hand the low lying energy states and on the other hand only the ground state or just a few states – have a profound consequence for the time-evolution. Due to the knowledge about excited states there is an analytic formula to calculate time-dependent expectation values with the NRG [76, 77]. In the time-dependent density-matrix renormalization group (TD-DMRG), however, time-dependent expectation values are calculated by explicitly evolving the ground state in time. We presented how this is done employing a Trotter-Suzuki decomposition (TSD). However, a discretization of time and the iterative evolution of a state is a concept inherent to all TD-DMRG approaches [109, 110, 115].

This concludes the discussion of the basic NRG and DMRG algorithms with the extension to time-dependence and bosonic systems. In the next chapter these methods are applied to the spin-boson model (SBM) and we discuss why both methods yield different results. For other system, e.g. the resonant-level model (RLM), both methods yield the same results for $T \rightarrow 0$ but these are corrupted by discretization artifacts. The source and a way to reduce these artifacts are discussed in Chapter 3. However, the presented solution is incompatible with the NRG and therefore we propose in Chapter 4 a new hybrid method combining the advantages of the NRG with those of the DMRG.

Chapter 2

Bosonic Models

One particular interesting quantum impurity system (QIS) is the spin-boson model (SBM) [21]. This model describes a spin- $\frac{1}{2}$ coupled to a bath of non-interacting bosons. The model and its several variations are used to examine the effects of dissipation induced by the bath manifesting dephasing and decoherence [116] for example in double quantum dots [117], solid-state qubits [118] or single-molecular magnets [119].

Our objective is to calculate critical exponents of the SBM with the numerical renormalization group (NRG) and density-matrix renormalization group (DMRG). For these calculations two difficulties arise: (i) the truncation of the bosonic basis and (ii) the so-called mass-flow error. The truncation of the bosonic basis is necessary for the employed numerical methods, because one has to represent the bosonic creation and annihilation operators as matrices. For bosons the matrix dimension is infinite. Hence, numerical applications cannot keep all bosonic states, but one has to truncate the matrix representation of the bosonic operators. The problems induced by this truncation are investigated in Sec. 2.3 at the example of a spin coupled to a single boson or to a chain of two bosons. The insight gained by this investigation helps to improve the bosonic basis by displacing the bosons.

The second problem, the mass-flow error, is due to an NRG iteration dependent renormalization of model parameters, caused by neglecting the rest-chain at a given iteration. This leads to the calculation of wrong critical exponents in some parameter regimes. In Sec. 2.2 we investigate an exactly solvable toy model in which the mass-flow effect is present and discuss the source of this effect. In Sec. 2.4 we show that the NRG yields the correct phase-diagram of the SBM but fails at calculating the correct critical exponents in some parameter regimes.

Unlike the NRG the DMRG is able to explicitly take the rest-chain into account. This is accomplished by the DMRG sweeping. Hence, the DMRG does not suffer from the mass-flow effect, but it still suffers from the truncation of the bosonic basis. Therefore we propose a method how to determine the optimal displacement parameters needed to represent the ground state with as few bosonic modes as possible. With this method we calculate in Sec. 2.5 the correct critical exponents for the SBM.

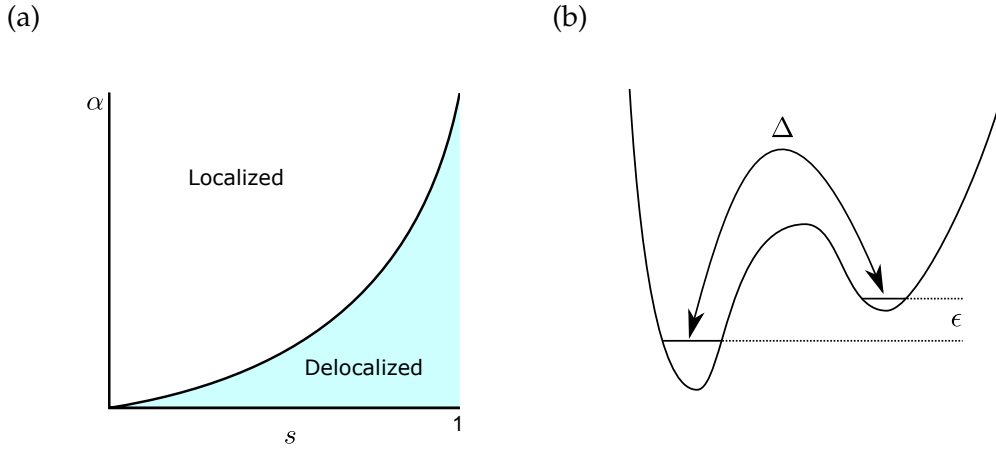


Figure 2.1: (a) Schematic phase diagram of the SBM. The coupling strength is given by α and the bath parameter by s . (b) Energy levels of the SBM. The energy difference between the states in the left and in the right well is ϵ and both states are tunnel-coupled by Δ .

However, before we discuss the toy models and perform our numerical simulations, we want to set the stage in the next section by introducing the SBM and highlighting some of its important physical properties and applications.

2.1 Spin-boson model

In this section general aspects of the spin-boson model (SBM) are discussed. However, before numerically solving this model with the NRG and DMRG in Secs. 2.4 and 2.5 the influence of the truncation of the bosonic Hilbert space and the discretization is examined with suitable toy models in Sec. 2.3.

2.1.1 Model Hamiltonian

The SBM consists of an impurity coupled to a bosonic bath. Here the impurity is a single spin with two states labeled $\sigma_z = \pm 1$. The energy splitting between the states is given by ϵ and the states are tunnel-coupled via Δ (cf. Fig. 2.1b). Therefore the impurity Hamiltonian is given by

$$H_{\text{imp}} = -\frac{\Delta}{2}\sigma_x + \frac{\epsilon}{2}\sigma_z, \quad (2.1)$$

where σ_x and σ_z are the usual Pauli matrices.

The bosonic bath consists of non-interacting bosons with the creation and annihilation operators b_i^\dagger and b_i . The displacement of the bosons is coupled to the z -direction of the impurity spin. The full Hamiltonian of the SBM is therefore given by

$$H = -\frac{\Delta}{2}\sigma_x + \frac{\epsilon}{2}\sigma_z + \frac{\sigma_z}{2} \sum_i \lambda_i (b_i + b_i^\dagger) + \sum_i \omega_i b_i^\dagger b_i, \quad (2.2)$$

where ω_i is oscillator frequency of the i th bosonic mode and λ_i is the coupling parameter between the spin and the i th bosonic mode.

The effect of the bosonic bath on the impurity is fully determined by the bath spectral function

$$J(\omega) = \pi \sum_i \lambda_i^2 \delta(\omega - \omega_i). \quad (2.3)$$

Of course, it is impractical to deal with the bath in this way, because, so far, the parameters λ_i are arbitrary; physically they depend on the investigated system [120]. It is desirable to express $J(\omega)$ as a function which still captures the essential physics of most systems, but which does not depend on an infinite number of parameters λ_i . As all the information is contained in the function $J(\omega)$ one just has to find an appropriate form for $J(\omega)$.

The physical behavior is dominated by the low-frequency modes. For $\omega \rightarrow 0$ real systems show the behavior $J(\omega) \sim \omega^s$. The standard parametrization [21] for $J(\omega)$ is given by

$$J(\omega) = \begin{cases} 2\pi\alpha\omega_c^{1-s}\omega^s & 0 < \omega < \omega_c \\ 0 & \text{else} \end{cases}. \quad (2.4)$$

The bath is thereby parametrized by the bath parameter s , the coupling constant α , and a high-frequency cutoff ω_c . This frequency is chosen as the energy unit in all following calculations. The bath parameter s determines whether the bath is ohmic ($s = 1$), subohmic ($0 < s < 1$) or superohmic ($s > 1$). This work is primarily concerned with subohmic baths. Finally, the coupling constant α determines how strongly the bath and the spin are coupled.

Using the methods of the bosonic NRG [74, 75] described in Sec. 1.3.3 the bath is discretized and mapped to a Wilson chain. This discretized Hamiltonian is given by

$$H_N = -\frac{\Delta}{2}\sigma_x + \frac{\epsilon}{2}\sigma_z + \sqrt{\alpha}V\frac{\sigma_z}{2} (b_0^\dagger + b_0) + \sum_{n=0}^{N-1} \epsilon_n b_n^\dagger b_n + \sum_{n=0}^{N-2} t_n (b_n^\dagger b_{n+1} + b_{n+1}^\dagger b_n). \quad (2.5)$$

The operators b_n^\dagger (b_n) create (annihilate) a boson at site n . The length of the Wilson chain is given by N , ϵ_n are the oscillator frequencies, and t_n the hopping parameters. These parameters have to be calculated numerically [74, 75] and depend on the discretization

parameter Λ and the bath exponent s . The hybridization strength between the spin and the bath is given by $\sqrt{\alpha}V$, with α being the coupling strength and

$$V^2 = \int_{-\infty}^{\infty} d\omega J(\omega), \quad (2.6)$$

where $J(\omega)$ is given in Eq. (2.3).

When modeling physical system the question if the model is actually a good description of the physical reality arises. If one wishes to make predictions about a certain experiment this question is of vital importance. However, in this work the physical modeling process is excluded to a certain extent: of course, one could consider the discretization of the bath as part of the modeling process. In any case, the bath itself is already just a model of the physical reality and hence it is not clear where to make the distinction of what is part of the modeling process and what is part of the numerical method. However, we do not concern ourselves with this question further: in this thesis all models are considered as given and we do not make any explicit connection to the physical reality. This is justified, as in this thesis we are mainly interested in methodical questions and errors inherent to the discretization of the bath. We make no connections or compare our data to real experiments.

2.1.2 Phase transition

For $\epsilon = 0$ the zero-temperature phase diagram of the SBM with a subohmic bath ($s < 1$) shows two distinct phases: the so-called localized phase and the delocalized phase. The first one is characterized by a spontaneously broken symmetry which results in a degenerate ground state and $|\langle \sigma_z \rangle| > 0$, whereas in the delocalized phase $\langle \sigma_z \rangle = 0$ holds [74, 121]. The two phases are separated by a quantum phase transition (QPT) at the critical coupling strength α_c , which depends on the bath-parameter s and the model-parameter Δ . A schematic phase diagram is shown in Fig. 2.1a. The ohmic case ($s = 1$) displays a Kosterlitz-Thouless transition between a localized and a delocalized phase [122, 123], whereas the system is delocalized in the whole parameter regime $\Delta \neq 0$ for a superohmic ($s > 1$) bath [121].

The reason for this QPT, or to be more precise, boundary QPT, lies in the renormalization of the tunnel splitting Δ caused by interactions with the bosonic bath. In the following we are only interested in the subohmic regime: for $s \leq 1$ the bath perturbation is relevant and causes Δ to be renormalized to zero, $\Delta \rightarrow 0$, above a critical coupling strength α_c [50]. A vanishing tunnel splitting, $\Delta = 0$, causes the spin to be trapped in one of the two potential wells and therefore a localized phase emerges. As there are two possible ground states the impurity entropy in the localized phase is given by $S = \ln 2$. In the delocalized phase, only one ground state exists, which is a superposition of the spin-up and spin-down state, and thus the impurity entropy van-

ishes, $S = 0$. For the same reason all eigenstates of the Hamiltonian in the localized phase are two-fold degenerate, while the eigenstates in the delocalized phase are not degenerate.

To characterize the QPT further we define the critical exponents δ and β by [124]

$$M_{\text{loc}}(\alpha = \alpha_c, T = 0) \propto |\epsilon|^{\frac{1}{\delta}} \quad (2.7)$$

$$\text{and } M_{\text{loc}}(\alpha > \alpha_c, T = 0, \epsilon = 0) \propto (\alpha - \alpha_c)^\beta. \quad (2.8)$$

The local magnetization in z -direction, which is the order parameter, is defined by $M_{\text{loc}} = \frac{1}{2} \langle \sigma_z \rangle$.

In the literature has been a lot of discussion about the question what values these critical exponents take in the subohmic ($s < 1$) regime. Especially the question if these and other critical exponents take mean-field values for $s \leq \frac{1}{2}$, which are $\delta = 3$ and $\beta = \frac{1}{2}$, is disputed. There are two factions: one, to which we belong, claiming that one should observe mean-field exponents for $s \leq \frac{1}{2}$ and no mean-field exponents for $\frac{1}{2} < s < 1$, while the other faction claims that one does not observe mean-field exponents but hyper-scaling relations in the whole subohmic regime. The discussion was started by NRG calculations supporting the latter claim [124]. However, the discussion continued though these findings were retracted [37].

A quantum-to-classical mapping [125] predicts mean-field exponents. The idea behind this approach is to map the SBM to an one-dimensional Ising model with long-range interactions $J_{ij} = \frac{J}{|i-j|^{1+s}}$. From analyzing this model it is expected that the SBM obeys mean-field behavior for $0 < s \leq \frac{1}{2}$ [122, 126]. However, the critical exponents obtained with the first NRG calculations suggested that the quantum-to-classical mapping fails by showing non-mean-field critical exponent for $s \leq 1$ [124]. Subsequent quantum Monte Carlo (QMC) [127], exact diagonalization (ED) [48], and DMRG studies [128] contradict the NRG results: these studies found a mean-field critical behavior for $s \leq \frac{1}{2}$.

Two errors responsible for not reproducing the quantum-to-classical mapping results with the NRG have been identified [37]: the truncation of the bosonic Hilbert space [129, 130] and the mass-flow error [36], which is discussed in more detail in Sec. 2.2.4. In Ref. 38 it is shown that the interplay between both error sources is the reason that the critical exponents calculated with NRG obey hyper-scaling relations even for $s \leq \frac{1}{2}$.

Despite these insights there are still claims [131] that the original NRG data from Ref. 125 is correct, even though the authors of Ref. 125 published an erratum, which retracts the claim that the quantum-to-classical mapping fails [37]. In the studies by Kirchner *et al.* [39, 131] the interpretation is that the quantum-to-classical mapping fails and therefore the phase transition of the SBM is governed by non-mean-field exponents in the whole parameter regime $s < 1$ and not just in the regime $\frac{1}{2} < s < 1$; this is in contrast to the consensus in Refs. 36, 38, 48, 127, 128, 132, 133.

In Sec. 2.4 the published NRG results [124] are reproduced and compared to the results of the dissipative harmonic oscillator (DHO) in order to verify that the reason for the failure of the NRG is the mass-flow effect. Then, in Sec. 2.5, the findings of the toy-models on how to construct an optimized displaced bosonic basis are applied to the DMRG to show that the quantum-to-classical mapping does not fail for $s \leq \frac{1}{2}$ and mean-field exponents are obtained.

2.1.3 Physical realizations

At the end of this section and before actually performing some calculations for the SBM we want to briefly discuss some applications and physical realizations of the SBM and similar models. Of course, this list is by no means complete.

Donator-acceptor system

Ref. 134 discusses a model consisting of two electronic sites. The electronic Hamiltonian of the two sites corresponds to a Hubbard model: there is a hopping term between the site, an on-site energy and Coulomb repulsion, and an inter-site Coulomb repulsion. Each site can be unoccupied, occupied with a spin-up or spin-down electron, or doubly occupied. This electronic Hamiltonian has already been studied 35 years ago [135]. However, the connection to the SBM is that the occupation of each site is coupled to the displacement of a bosonic bath. The bosonic bath renormalizes the on-site Coulomb interaction and energy dissipates from the two-site system into the bath. In the single-electron subspace this model is equivalent to the SBM.

A physical realization of this model is the electron transfer in a DNA molecule. Here the question arises if the dominant transfer mechanism is single-electron or two-electron transfer. In Refs. 136, 137 this question was examined using the time-dependent numerical renormalization group (TD-NRG).

But what is the physical justification of the bosonic bath and how does the dissipation process work? In reality the DNA strand is a long molecule, but the model considers only one base pair. Figuratively speaking, the electrons of all other base pairs of the strand give rise to an electronic cloud, which, by Coulomb repulsion, is coupled to the electrons of the local base pair. By changing the occupation of the local site one excites vibrational modes of the surrounding electronic cloud and therefore it is physically justified to encapsulate the dissipative effects of the DNA molecule in a bosonic bath coupled to the local site. Furthermore, the excitation of vibrational modes cost energy and this is why energy dissipates from the local site into the bosonic bath.

Quantum phase transitions

The SBM can be used as a testbed to study QPTs [50]. Unlike classical phase transitions these are driven by non-thermal control parameters and the quantum critical

point (QCP) occurs only at temperature $T = 0$, though signatures of the QCP are visible at higher temperatures. Phase transitions of classical systems are driven by the temperature. As all thermal fluctuations freeze out at $T = 0$ one does not observe phase transitions at $T = 0$ in classical models. Quantum models show the reverse behavior: here the phase transition depends on quantum fluctuations and these survive even for the ground state of the system, that is at $T = 0$. For $T > 0$ one observes an interplay between thermal and quantum fluctuations. Hence the SBM is well suited to study QPTs as the bosonic bath can be used to model the quantum fluctuations.

One system suited to study the QPT is proposed in Ref. 138 . This consists of a mesoscopic ring with a small quantum dot coupled to an external circuit, which is the source of the quantum fluctuations. The local two-level system of the SBM is mapped to the charge degrees of freedom of the quantum dot. Through the ring flows a persistent current used as an indicator of the QPT. The bosonic bath models the quantum fluctuations of the electromagnetic field of the external circuit.

Quantum computing

Using the resources of quantum physics to build computers, which explicitly exploit the entire Hilbert space of a many-particle system, leads to the idea of the growing research field of quantum computation [18, 68]. A classical computer stores information as a bit which can be in either of two states: $|0\rangle$ or $|1\rangle$. A physical realization of one bit could be a cluster of as few as 12 iron atoms [139], but for practical applications like computer hard disks millions of atoms are involved. On the other hand, a quantum computer stores information in so called qubits, which, in general, are in a coherent superposition state $|\psi\rangle \propto \alpha|0\rangle + \beta|1\rangle$. Physical realizations of such systems can in principle be any quantum mechanical two-state systems, e.g. a spin which could be confined in a quantum dot [17] or in some other material [140], trapped atoms, or superconductors to name but a few [18].

Among other problems quantum computation suffers from dephasing and dissipation [141]: due to interaction with the environment the superposition state is perturbed, the coherent phase and thereby information is lost. Usually the dissipative environment can be modeled by a bosonic bath: thinking of a spin-qubit the surrounding (electron or nuclear) spins add up to collective vibrational modes, which can be described as a bosonic bath. A qubit in an dissipative environment can therefore be described by the SBM.

Quantum computing algorithms consist of a sequence of so-called gates, which are applied to the multi-qubit state. A gate is a unitary operator applied to the state. To build a general quantum computer, however, it is sufficient to implement only one- and two-qubit gates, as all gates involving more qubits can be decomposed into a series of one- and two-qubit gates. Furthermore, of all possible two-qubit gates it is sufficient to

implement the controlled not (CNOT) gate.¹ This gate rotates the first qubit depending on the state of the second qubit.

In Ref. 142 the effect of a dissipative environment on the application of the CNOT gate, which was experimentally realized for the first time in a trapped atom in 1995 by Monroe *et al.* [143], is investigated. As the CNOT gate acts on two qubits, this system is modeled by two Pauli matrices interacting with coupling strength $J(t)$ and to each Pauli matrix the field $\vec{B}_j(t)$ is applied. The CNOT gate is decomposed in a pulse sequence which determines the time-dependence of $J(t)$ and $\vec{B}_j(t)$. The authors of Ref. 142 identify two errors due to the interaction to the bosonic bath: spin-flip errors and phase errors. To model these errors, both the σ_x and the σ_z operator couple to the bosonic bath. The bath is described by an ohmic spectral function. One finding of Ref. 142 is that the quality of the gate strongly depends on the interaction strength.

From these three examples we see that the SBM – with some extensions – is suitable to model different physical systems. In all shown cases the bosonic bath is interpreted differently: as charge, quantum, or spin fluctuations. However, despite these different interpretations the underlying modeling is similar and that is one thing what makes studying the SBM interesting.

Before actually studying the SBM in Secs. 2.4 and 2.5 and investigating the phase transition discussed in this section we continue in the next sections with a toy model showing the same QPT as the SBM in the sub-ohmic regime. As this model is exactly solvable we can study the model without errors due to the truncation of the bosonic Hilbert space.

2.2 Dissipative harmonic oscillator

As the SBM is not exactly solvable, we first present some results of a model using the same bosonic bath but with the spin replaced by an harmonic oscillator: the so-called dissipative harmonic oscillator (DHO).

The DHO describes an harmonic oscillator which is displacement-coupled to a bosonic bath. As the Hamiltonian is bilinear, it is analytically solvable and does not suffer from the errors due to the truncation of the bosonic Hilbert space. In this section we investigate the phase diagram of this model and calculate a critical exponent. The central result, however, is that we discover the mass-flow effect in this model and are able to explain its source. We find different signatures of this effect which help us to show that the mass-flow effect is present in the SBM as well.

¹ In classical computing this gate is equivalent to the two-bit XOR operator.

2.2.1 Model

The Hamiltonian of the DHO with a continuous bosonic bath is defined as

$$H = \Omega a^\dagger a + \sum_q \omega_q b_q^\dagger b_q + (a^\dagger + a) \sum_q \lambda_q (b_q^\dagger + b_q). \quad (2.9)$$

Here a^\dagger and a are the creation and annihilation operators of a local harmonic oscillator with frequency Ω . The harmonic oscillator is coupled to a bosonic bath with the mode frequencies ω_q . The coupling constants between the impurity and each bosonic mode are λ_q ; the creation and annihilation operators of the bosonic bath are b_q^\dagger and b_q . As for the SBM, the bath is characterized by its spectral function

$$J(\omega) = \pi \sum_q \lambda_q^2 \delta(\omega - \omega_q) \quad (2.10)$$

and we use the parametrization [21]

$$J(\omega) = 2\pi\alpha\omega_c^{s-1}\omega^s, \quad 0 < \omega < \omega_c, \quad s > -1. \quad (2.11)$$

The frequency ω_c defines a sharp-cutoff frequency: for our considerations only the low energy modes are important. The coupling strength to the bath is given by α .

The question is, whether it is possible to simulate the DHO with the NRG. This method has two major sources of errors: one stems from the discretization of the continuous bosonic bath and the other is the omnipresent truncation error of both the bosonic Hilbert space and the high-energy eigenstates of the Hamiltonian. At this point, we are mainly interested in the discretization error induced by the finite number of states to represent an originally continuous bath.²

To investigate the effects of the error due to the discretization of the bath, we employ the same discretization as the NRG, but we solve the model exactly on an operator level in order to circumvent the truncation errors. Furthermore, to compare results, the model is solved exactly with a continuous bath as well. Any deviations between the solutions of the discretized bath and the continuous are solely due to the bath discretization. By mapping the continuous bosonic bath to a discretized chain we arrive at a discretized Hamiltonian

$$H = \Omega a^\dagger a + \sqrt{\alpha}V (a^\dagger + a) (b_0^\dagger + b_0) + \sum_{n=0}^{N-1} \epsilon_n b_n^\dagger b_n + \sum_{n=0}^{N-2} t_n (b_n^\dagger b_{n+1} + b_{n+1}^\dagger b_n). \quad (2.12)$$

The local Hamiltonian of the harmonic oscillator has not changed, but now we have the new operators b_n^\dagger (b_n) which create (annihilate) a boson at chain site n . In order to discretize the bath the discretization parameter $\Lambda > 1$ is introduced. In the combined

² The truncation of the bosonic Hilbert space is discussed in Sec. 2.3.

limit $\Lambda \rightarrow 1$ and $N \rightarrow \infty$ and with properly chosen parameters V, ϵ_n and t_n both Hamiltonians, Eq. (2.9) and Eq. (2.12), are equivalent.

Usually the chain parameters V, ϵ_n and t_n are calculated numerically [75] and depend on Λ and $J(\omega)$. For convenience, the α dependence from the spectral function is shifted into the Hamiltonian.

In Appendix A it is shown that the DHO shows two distinct phases: a stable and an unstable one. The first is characterized by a finite occupation number of the impurity harmonic oscillator while in the latter phase the occupation number diverges. The phase transition is driven by the coupling strength α .

2.2.2 Occupation number

Analytically it can be shown (see Appendix A) that the model with a continuous bath (2.9) is unstable at a coupling strength $\alpha_c = \frac{s\Omega}{8\omega_c}$. An indicator of this instability is a diverging occupation number of the local harmonic oscillator $n = \langle a^\dagger a \rangle$. We want to analyze if the discretized model (2.12) yields the same critical coupling strength α_c^D as the continuous model. For this we have to calculate

$$\langle n \rangle = \text{Tr} \left[\rho a^\dagger a \right] \quad (2.13)$$

$$\text{where } \rho \text{ is the density operator } \rho = \frac{e^{-\beta H}}{Z} \text{ and } Z = \text{Tr} \left[e^{-\beta H} \right] \quad (2.14)$$

the partition sum; the inverse temperature is given by β . The explicit calculations of the occupation number for the discretized and the continuous case are presented in Appendix A.

2.2.3 Results

In this section we discuss and summarize our numerical results. For all calculations we set $\Omega = 0.1\omega_c$, and use ω_c as energy scale. All the other parameters (Λ, s, N, α) are tuned according to the particular question. Throughout this section, unless otherwise stated, the inverse temperature is – in the NRG spirit – set to $\beta = \omega_c \Lambda^N$.

Critical coupling

The numeric results for the discretized model are shown in Fig. 2.2a: the curves for the occupation number show a divergence above a certain critical value α_c^D while for $\alpha \ll \alpha_c^D$ the results are dominated by numerical noise.³ A discussion of the source of the noise and an analytic derivation for the critical coupling strength of the continuous

³ The superscript D in α_c^D indicates that this denotes the critical coupling strength of the discretized model.

Λ	N	Λ	N	Λ	N
1.04	858	1.1	353	1.7	63
1.05	690	1.2	185	1.8	57
1.06	577	1.3	128	1.9	52
1.07	497	1.4	100	2.0	49
1.08	437	1.5	83		
1.09	390	1.6	72		

Table 2.1: Length of the Wilson chain depending on Λ . The criterion to choose N is that Λ^{-N} is approximately the same for all Λ .

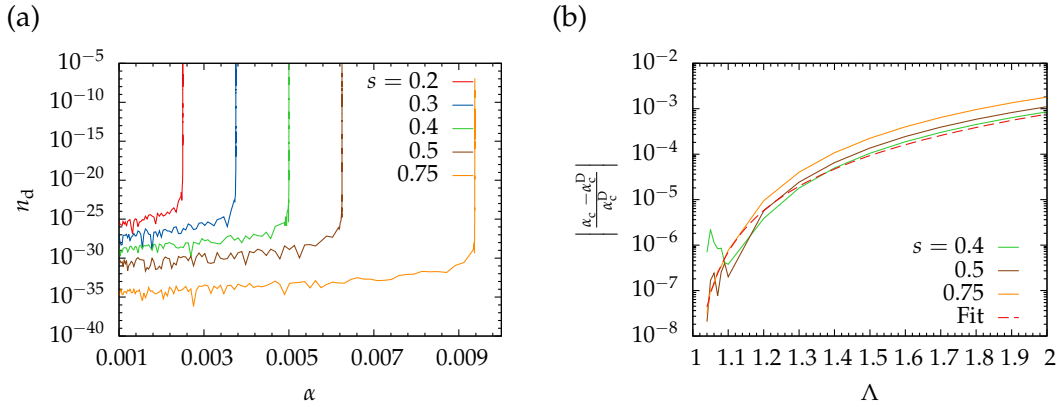


Figure 2.2: (a) Occupation number of the harmonic oscillator versus coupling strength for different values of s . The discretization parameter is $\Lambda = 1.4$ and the chain consists of $N = 100$ sites. The critical coupling strength α_c^D is defined as the value at which n_d diverges. (b) Relative error of the critical coupling strength α_c^D , by comparing the numerically determined values for the discretized bath α_c^D (see left panel) with the analytic values α_c , Eq. (2.15). Length of the Wilson chain N is given in Tab. 2.1. The dash curved is a fit of $f(\Lambda) = a(\Lambda - 1)^b + c$ to the $s = 0.75$ curve.

Hamiltonian (2.9) are presented in Appendix A. The analytic result for the s dependence of the critical coupling strength for the continuous model, Eq. (A.18), is given by

$$\alpha_c = \frac{s\Omega}{8\omega_c}. \quad (2.15)$$

The critical coupling strength α_c^D for the discretized Hamiltonian (2.12) is defined as the largest value of α for which the matrix M defined in Eq. (A.30) exhibits no vanishing eigenvalue. This condition is equivalent to the largest α for which the occupation number of the local harmonic oscillator does not diverge.

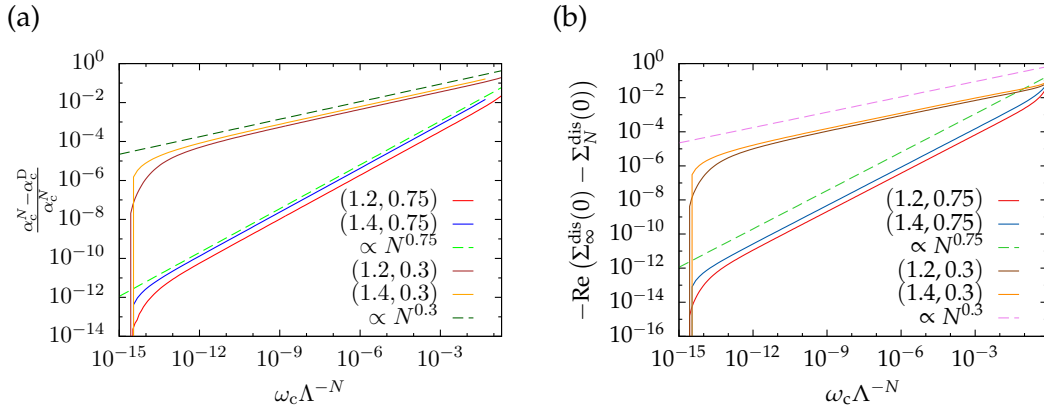


Figure 2.3: (a) Dependence of the critical coupling on the length of the chain. (b) Dependence of the real part of the self-energy on the length of the chain. The coupling is set to $\alpha = \alpha_c^D(s, \Lambda)$. In both plots the numbers in the legend are of the format (Λ, s) and the dashed lines are guides to the eye. The oscillator frequency is $\Omega = 0.1\omega_c$.

Numerically this value is determined by slowly approaching the critical coupling strength from the left, that is $\alpha < \alpha_c^D$. The coupling strength α is increased in steps of a certain length until the occupation number diverges. At this point one decreases the step length by one order of magnitude and restarts with the last value of α still in the stable phase. The smallest step length is 10^{-14} ; thus this is the absolute numerical error when determining the critical coupling strength for the discretized model α_c^D .

Fig. 2.2b shows the relative deviation of the numerical value from the analytical one. The deviation depends on s and Λ . The Wilson chain length is chosen in such a way that the energy of the last iteration is the same for all values of Λ (the values used are given in Tab. 2.1).

The relative deviation shrinks for $\Lambda \rightarrow 1.1$. However, for Λ close to one the curves show an unexpected non-monotonic behavior and therefore a $\Lambda \rightarrow 1$ extrapolation is not possible for $s \neq 0.75$. The fit curve in Fig. 2.2b shows the function $f(\Lambda) = a(\Lambda - 1)^b + c$ which yields $f(\Lambda = 1) = 4 \cdot 10^{-17}$ – this is the extrapolated error of α_c^D for $\Lambda \rightarrow 1$ and $N \rightarrow \infty$. The extrapolated error is of the same order as the numeric error and hence it is safe to say that the discretization error vanishes within numerical accuracy.

2.2.4 Mass-flow error

The critical coupling α_c^D used to calculate the data plotted in Fig. 2.2b is determined for a fixed chain length N given in Tab. 2.1. But how does the critical coupling depend on the chain length?

Fig. 2.3a shows the relative difference between the critical coupling strength α_c^N determined for a Wilson chain of length $N \leq N_{\max}$ and the critical coupling strength α_c^D determined for a Wilson chain of length N_{\max} , with N_{\max} taking the values given

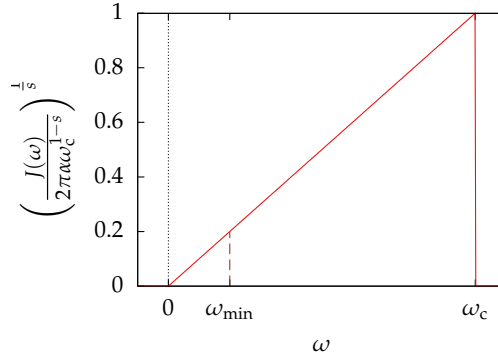


Figure 2.4: Sketch of bath spectral function $J(\omega)$, Eq. (2.4).

in Tab. 2.1. The critical coupling depends on the length of the chain. This is due to the so-called mass-flow error [36]: the continuous bath is approximated by a chain of length N and this leads to an effective shift of real part of the self-energy Σ .

We associate with the chain length N a minimum energy scale ω_{\min} (cf. Fig. 2.4). Bath modes below this energy scale are not taken into account, yet. The real part of the self-energy is given by

$$\text{Re}\Sigma(\omega) = \pi\text{P} \int_{-\infty}^{\infty} d\omega' \frac{J(\omega')}{\omega - \omega'} = \pi\text{P} \int_0^{\omega_c} d\omega' \frac{J(\omega')}{\omega - \omega'}. \quad (2.16)$$

In this equation P denotes the principal value of the integral. We define the shift of the real part as

$$\Delta m = \text{Re}\Sigma(0) \quad (2.17)$$

$$= -\pi\text{P} \int_{\omega_{\min}}^{\omega_c} d\omega' \frac{J(\omega')}{\omega'} - \underbrace{\pi\text{P} \int_0^{\omega_{\min}} d\omega' \frac{J(\omega')}{\omega'}}_{\Delta m^{\text{eff}}(\omega_{\min})}. \quad (2.18)$$

Hence, the shift $\Delta m^{\text{eff}}(\omega_{\min})$ is not taken into account resulting in an chain length dependent real part of the self-energy.

To actually recapture the continuum one needs the full semi-infinite Wilson chain in order to take the limit $\omega_{\min} \rightarrow 0 \Rightarrow \Delta m^{\text{eff}}(\omega_{\min}) \rightarrow 0$. Therefore at each iteration an effective rest-chain – or an effective bath – is missing, which accounts for the discarded states of the bath. Such a rest-chain would repair the discretization errors and thereby fix the mass-flow error.

Since the bath spectral function is not symmetric and vanishes for negative frequencies the real part of the bath propagator at $\omega = 0$ is not zero but depends on the chain length. This induces an effective mass in the order parameter – hence the name

mass-flow error – and renormalizes the critical coupling and the oscillator frequency. The oscillator frequency is renormalized even for a continuous bath, but the important point is that for a discretized bath the renormalization depends on the Wilson chain length. In the NRG language one would say that the renormalization is temperature-dependent.

The Green's function of the dissipative harmonic oscillator reads

$$\ll a|a^\dagger \gg (z) = \frac{1}{z - \Omega - \Sigma(z)}. \quad (2.19)$$

The self-energy $\Sigma(z)$ accounts for all effects of the bath on the impurity. Hence, we have to distinguish between the self-energy of the continuous model $\Sigma^{\text{conti}}(z)$ and the self-energy $\Sigma_N^{\text{dis}}(z)$ of the discretized bath mapped onto a chain with N sites.

For the continuous bath the real part of self-energy, Eq. (A.5), is given by

$$\text{Re}\Sigma^{\text{conti}}(\omega - i\delta) = \frac{(\omega + \Omega) \left(A_r(\omega)\omega + \Omega A_r(\omega) + A_r(\omega)^2 + A_i(\omega)^2 \right)}{\omega^2 + 2\omega\Omega + 2A_r(\omega)\omega + \Omega^2 + 2\Omega A_r(\omega) + A_r(\omega)^2 + A_i(\omega)^2}. \quad (2.20)$$

Here $A_r(\omega)$ and $A_i(\omega)$ are the real and imaginary part of the function $A(z) = \Gamma(z) + \Gamma(-z)$ which can be calculated using equation of motion techniques, see Appendix A. Here, $\Gamma(z)$ is the bare bath propagator defined in Eq. (A.2).

For a Wilson chain the self-energy is given by Eq. (A.52) and for the real part of the self-energy for a chain of length $N = 1$ we obtain

$$\text{Re}\Sigma_1^{\text{dis}}(\omega - i\delta) = -2 \frac{\sqrt{\alpha} V^2 \epsilon_0 (\omega + \Omega)}{-\omega^2 \Omega + \Omega \epsilon_0^2 - 2\epsilon_0 \sqrt{\alpha} V^2 - \omega^3 + \omega \epsilon_0^2}. \quad (2.21)$$

The condition for the critical coupling is that the denominator of Eq. (2.19) vanishes for $\omega = 0$,

$$\ll a|a^\dagger \gg (-i\delta) = \frac{1}{-\Omega - \text{Re}\Sigma(-i\delta) - i \text{Im}\Sigma(-i\delta) - i\delta}. \quad (2.22)$$

As usual, the bare oscillator frequency is shifted by the real part of the self-energy. For $\delta \rightarrow 0$ the imaginary part of the denominator vanishes, and if the real part vanishes as

well the occupation number diverges and the system is unstable. For the continuous bath this leads to

$$-\Omega = \text{Re}\Sigma^{\text{conti}}(0) = \frac{\Omega A_r(0)}{\Omega + A_r(0)} \quad (2.23)$$

$$\Leftrightarrow 0 = -\Omega \left(1 + \frac{\Omega A_r(0)}{\Omega + A_r(0)} \right) \quad (2.24)$$

$$\Rightarrow \Omega = -2A_r(0) = \frac{8\alpha\omega_c}{s} \quad (2.25)$$

We use Eq. (A.52) to calculate the real part of the self-energy of a chain with N sites, $\text{Re}\Sigma_N^{\text{dis}}(0)$, and show the flow of the real part in Fig. 2.3b. Here $\text{Re}\Sigma_\infty^{\text{dis}}(0)$ is the value obtained for the longest chain. Therefore, the dependence of the critical coupling on the chain length is due to the mass-flow effect. This causes a chain length or – in NRG language – temperature dependent renormalization of the oscillator frequency. This renormalization depends on both s and Λ . However, as Fig. 2.3 shows, the dependence on s is the dominant influence, as the curves with different s deviate stronger from each other than the curves with different Λ . Since the corrections scale as $(\alpha_c^N - \alpha_c^D) \propto \Lambda^{-sN}$ the mass-flow effect is stronger for smaller s .

The rest-chain, which is not yet taken into account, would generate an additional shift in the real part of the self-energy. This has crucial effects on the NRG results. At a given iteration the renormalized oscillator frequency differs from its values at later iterations. In particular, it is different from its value if one would consider the continuous bath. In the NRG, however, due to the truncation of the Hilbert space the system is stabilized at a point with a wrong order parameter mass. Therefore the bosonic NRG is prone to yield wrong results if one does not explicitly compensate the mass-flow effect [36].

Critical exponent

We have seen that the DHO shows two distinct phases: a stable and an unstable one. In this section we investigate how the system approaches the QPT. It is expected that the occupation number of the impurity harmonic oscillator shows a power-law behavior in the vicinity of the critical coupling strength

$$\langle n(\delta\alpha) \rangle \propto (\delta\alpha)^p, \quad \delta\alpha := \alpha_c - \alpha \ll 1. \quad (2.26)$$

The critical exponent $p = -1$ obtained from the analytic solution is independent of the model parameters (see Sec. A.1.2). To check if the discretized model yields the same critical exponent the impurity occupation number is calculated for different $\delta\alpha$.

As shown in Fig. 2.2a the occupation number suffers heavily from numerical noise, because the occupation number depends on the difference of two terms f_x and f_y which are of the same order of magnitude, $\langle n(\delta\alpha) \rangle = f_x(\delta\alpha) - f_y(\delta\alpha)$ (cf. Eq. (A.47)).

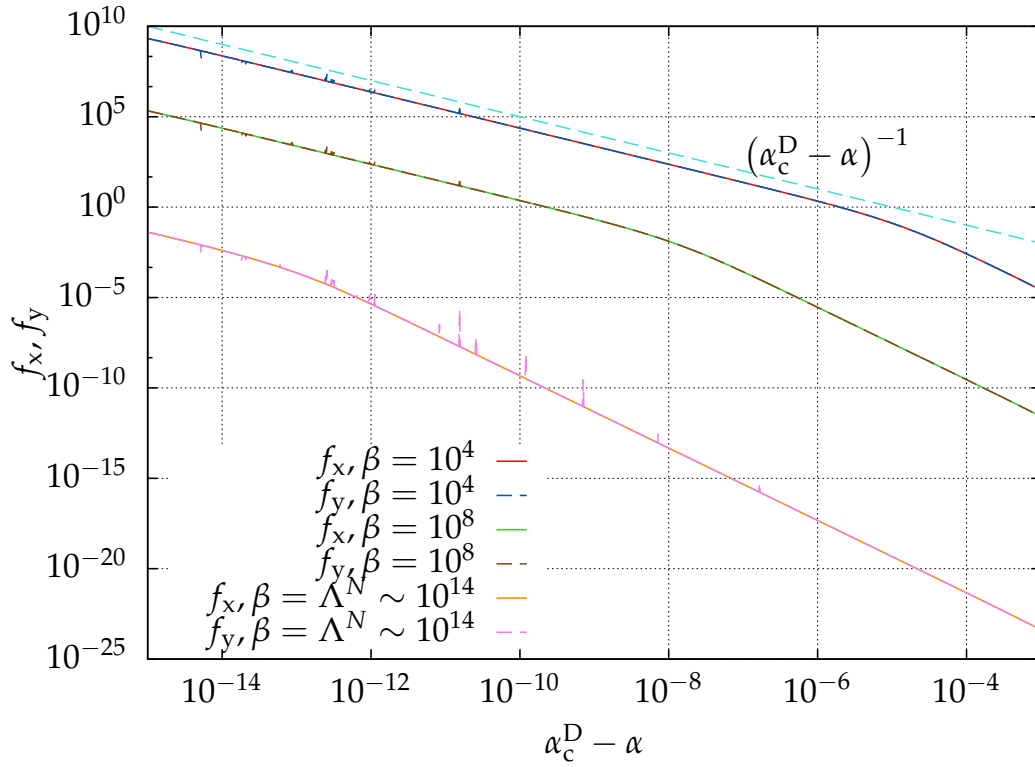


Figure 2.5: Determination of the critical exponent p . Shown are the terms f_x and f_y contributing to occupation of the impurity harmonic oscillator Eq. (A.47) in the vicinity of the numerical critical coupling strength $\alpha_c^D = 9.37 \cdot 10^{-3}$ for $\Lambda = 1.6, s = 0.75$, and different temperatures β . The dashed line, $\delta\alpha^{-1}$, is a guide to the eye.

To circumvent the problem of the numerical subtraction we do not fit a function $f(x) = ax^p$ to the expectation value $\langle n(\delta\alpha) \rangle$ in order to determine p , but we do the fit prior to the numeric subtraction. This allows us to perform the subtraction analytically and thereby reducing numerical errors. Therefore the power-law is fitted to $f_x(\delta\alpha)$ and $f_y(\delta\alpha)$ independently,

$$f_x(\delta\alpha) = a_x \delta\alpha^{p_x} \quad (2.27)$$

$$\text{and } f_y(\delta\alpha) = a_y \delta\alpha^{p_y}. \quad (2.28)$$

The critical exponent p of the expectation value is then determined by

$$a\delta\alpha^p = a_x \delta\alpha^{p_x} - a_y \delta\alpha^{p_y}. \quad (2.29)$$

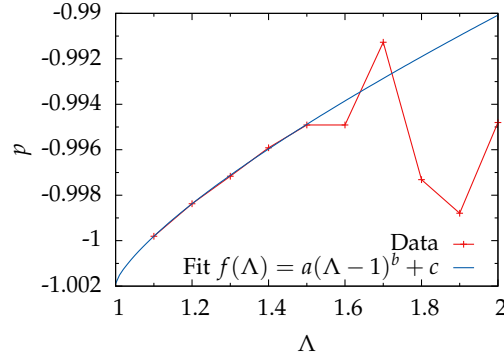


Figure 2.6: Critical exponent p for the DHO versus Λ determined with Eqs. (2.33) by fitting power-law functions to the $\beta = 10^4$ curves of f_x and f_y (cf. Fig. 2.5). The analytic estimate is $p = -1$.

To determine a and p from the fitting parameters a_x, a_y, p_x , and p_y we write Eq. (2.29) as

$$0 = a_x \delta \alpha^{p_x} - a_y \delta \alpha^{p_y} - a \delta \alpha^p \quad (2.30)$$

$$= \delta \alpha^p \left(a_x \delta \alpha^{p_x - p} - a_y \delta \alpha^{p_y - p} - a \right) \quad (2.31)$$

$$\approx \delta \alpha^p \left(a_x - a_y - a + \ln(\delta \alpha) \left(a_x (p_x - p) + a_y (p_y - p) \right) \right). \quad (2.32)$$

As the result should be independent of $\delta \alpha$ both bracketed terms must vanish. This yields

$$a = a_x - a_y \quad \text{and} \quad p = \frac{a_x p_x + a_y p_y}{a_x + a_y}. \quad (2.33)$$

This derivation relies on the assumptions $|p_x - p| \ll 1$ and $|p_y - p| \ll 1$. For p we eliminated the subtraction completely.

In Fig. 2.5 the curves f_x and f_y are shown. Both agree well with the critical exponent $p = -1$ up to $\delta \alpha \sim \frac{1}{\beta}$: starting at this order of magnitude the curves show a power-law behavior with a different exponent. Thus the assumptions for p_x and p_y are justified and Eqs. (2.33) can be used to determine the critical exponent p from two independent fits to f_x and f_y .

The critical exponent p is determined employing Eqs. (2.33) for different values of Λ (cf. Fig. 2.6). A $\Lambda \rightarrow 1$ extrapolation is performed by fitting the function $f(\Lambda) = a(\Lambda - 1)^b + c$ to the data points $\Lambda \leq 1.5$. This yields with $f(\Lambda = 1) = -1.00189$ a value which is close to the expectation $p = -1$. The main error sources are due to the f_x and f_y fits and numerical noise apparent in the f_y data in Fig. 2.5. However, in the limit $\Lambda \rightarrow 1$ the analytic expectation, $p = -1$, is well reproduced. For $\Lambda > 1$ the critical exponent is renormalized due to the bath discretization.

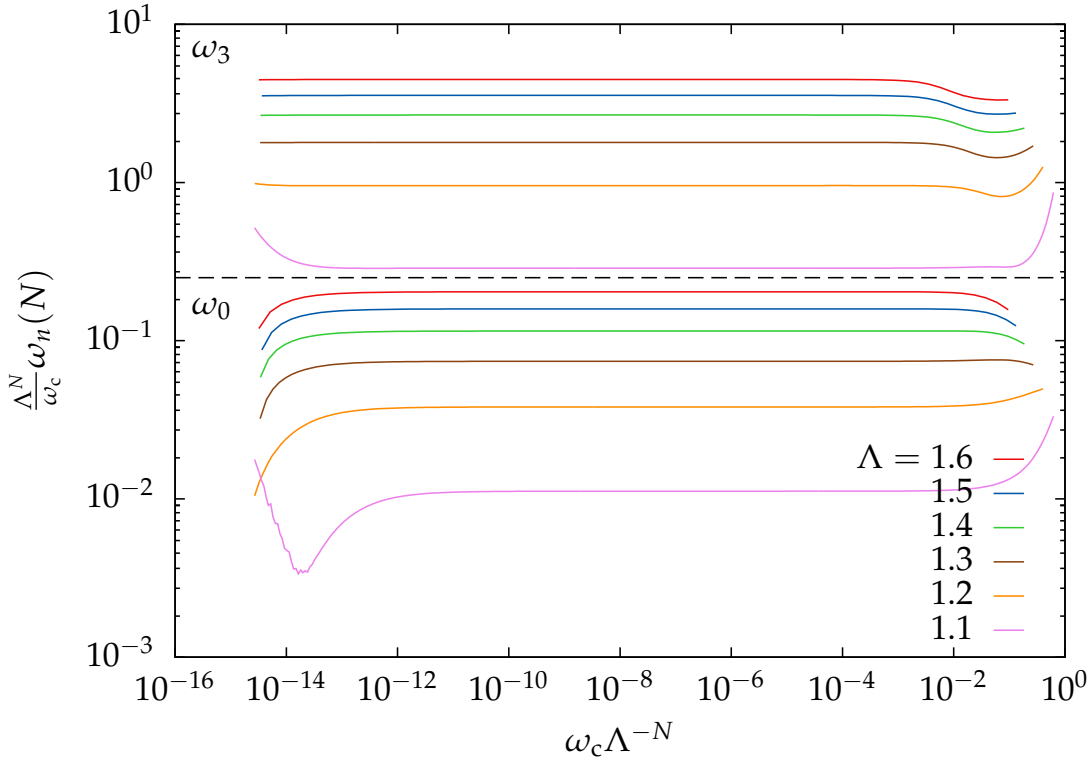


Figure 2.7: Level-flow of eigenenergies ω_0 and ω_3 obtained with Eq. (A.34) at different energy scales $\omega_c \Lambda^{-N}$. The bath parameter is $s = 0.75$ and the coupling strength is set to the numerically determined critical coupling α_c^D obtained for the chain length given in Tab. 2.1.

Level flow

In the NRG the level flow is used to identify the fixed points of the renormalization group (RG) transformation. For these flow diagrams one plots the rescaled energies of the lowest eigenstates versus the number of the iteration. A fixed point is reached when the level positions at one iteration remain invariant under further NRG steps.

To mimic an NRG-like flow diagram Fig. 2.7 shows the lowest and one highest eigenvalue, ω_0 and ω_3 respectively. Therefore, the system is exactly diagonalized with a chain of $N < N_{\text{crit}}$ sites. This yields the single particle energies $\omega_n > 0$, Eq. (A.34). An exactly solved chain of length N corresponds to the NRG iteration number N . The critical chain length N_{crit} coincides with the numbers given in Tab. 2.1 as for all iterations N the coupling strength α is set to the critical coupling $\alpha_c^D(s, \Lambda, N_{\text{crit}})$.

The flow diagram Fig. 2.7 shows a softening of the lowest mode: for $N \rightarrow N_{\text{crit}}$ the lowest eigenvalue approaches zero (the actual zero value is not shown due to the logarithmic scale), whereas the higher mode ω_3 reaches a fixed point after a few iterations. The $\Lambda = 1.1$ curve shows an increase rather than a softening of ω_0 for $\omega_c \Lambda^{-N} \lesssim 1.5 \cdot 10^{-14}$ for increasing N . We suspect that this increase is unphysical and due to numerical errors in the diagonalization procedure. The matrix to be diagonal-

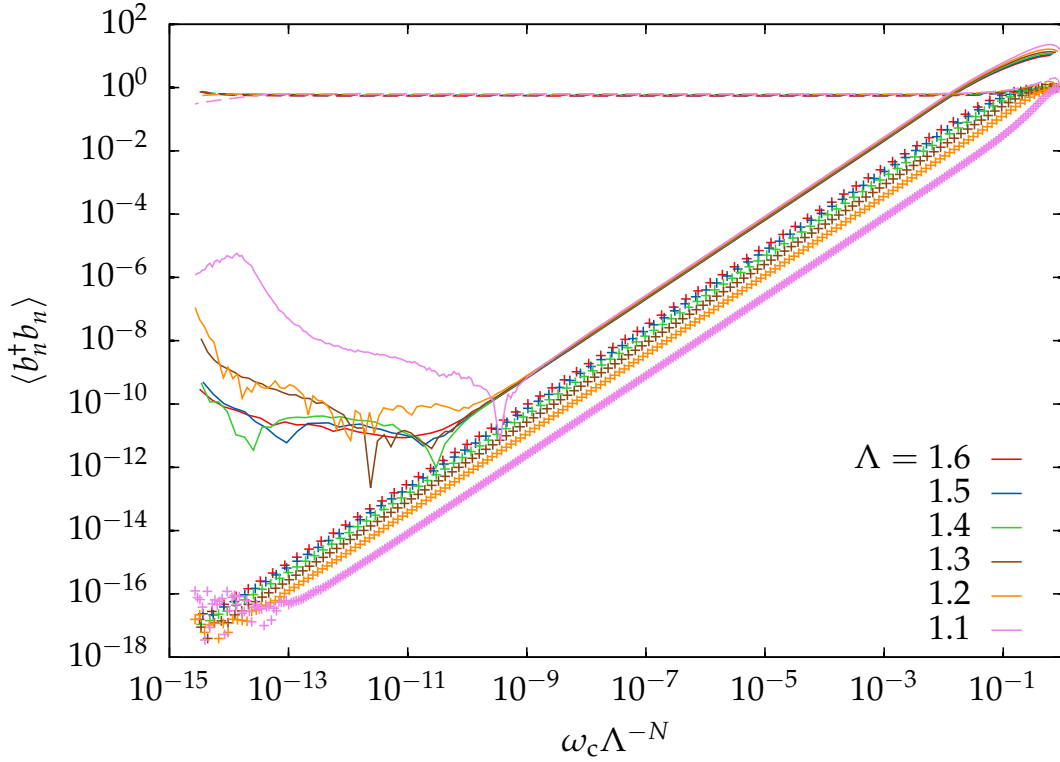


Figure 2.8: Iteration number N dependent occupation number of the last site in the chain (dashed line) and the impurity (solid line). The symbols indicate the corresponding matrix elements entering the calculation of the impurity occupation number, Eq. (A.47). The same parameters as in Fig. 2.7 are used.

ized has entries ranging over of 14 orders of magnitude and numerical errors add up for larger matrices. Furthermore, these errors provoke the unexpected behavior of the critical coupling strength in Fig. 2.2b.

Occupation of last site

The results of the exact diagonalization can be used to evaluate expectation values. Fig. 2.8a shows the occupation of the local oscillator and occupation of the last chain site for increasing chain length. At each iteration the temperature is set to $\beta = \omega_c \Lambda^{-N}$.

The level flow shows a fixed point after a few iterations. This behavior is reflected in the occupation of the last chain site (dashed lines in Fig. 2.8a): once one reaches the fixed point, the occupation number of the last chain site is independent of the chain length N . When approaching the critical chain length, the lowest mode is softened. Consequently, the Bose function in Eq. (A.47) of this mode diverges. Hence, the occupation numbers of all chain sites and of the impurity diverge. This is not visible in Fig. 2.8, because the last iteration, $N = N_{\text{crit}}$, is not shown. This indicates the QPT from the stable to the unstable phase.

According to Eq. (A.47) the impurity occupation number depends on the level spectrum ω_n and the matrix elements X and Y . At the fixed point the renormalized level spectrum is independent of N and, since the temperature is tuned accordingly, the Bose functions in Eq. (A.47) do not depend on N . Therefore, the N -dependence of the impurity occupation number is generated only by the matrix elements of X and Y .

To a good approximation, the Bose function of the lowest mode ω_0 dominates the impurity occupation. In particular, this is the case because this is the mode which is softened at the QPT. We checked that the matrix elements associated with this mode decline with N proportionally to the impurity occupation: the dots in Fig. 2.8 are the matrix elements, Eq. (A.49), entering the calculation of the impurity occupation for the lowest mode. Obviously the impurity occupation follows the matrix elements up to the point where numerical errors start to dominate.

As expected the occupation number shows the same numerical artifacts for $\Lambda = 1.1$ and close to N_{crit} as seen in the level flow. Especially the drop of the occupation number of the last site is connected to this error.

From the discussion of the DHO we learn that this model exhibits a stable and an unstable phase. The analytic and the numerical analysis agree well on the critical coupling strength and the critical exponent. However, the critical coupling strength depends on the number of chain sites due to the mass-flow effect. This effect plays crucial role when performing NRG calculations and is further discussed in Sec. 2.4.

Prior to this we want to address another issue when dealing with bosonic systems: the truncation of the bosonic Hilbert space. The results of this section were obtained by exactly diagonalizing the Hamiltonian on an operator level. Therefore it is not necessary – and not even possible without violating bosonic commutation relations – to truncate the bosonic Hilbert space. However, for the bosonic NRG and DMRG the infinitely large Fockspace of a harmonic oscillator has to be truncated. In the next section the effects of this truncation are analyzed on the basis of toy models.

2.3 Toy models

One advantage of the DHO is that this model is exactly solvable on an operator level: errors due to the truncation of the bosonic Hilbert space do not occur. When solving the SBM with the NRG or DMRG these errors play an important role. Before solving the SBM with these methods it is therefore in order to further examine the effects of the bosonic Hilbert space truncation. We investigate the effects of the chosen bosonic basis on the numerical results on the basis of two toy models: a displaced harmonic oscillator and a spin coupled with one or two bosonic modes.

To gauge the influence of the bosonic basis we compare numerical results, which are obtained by using a truncated bosonic basis, with analytic results. We find that the number of kept bosonic states N_b is crucially important: for a high accuracy one

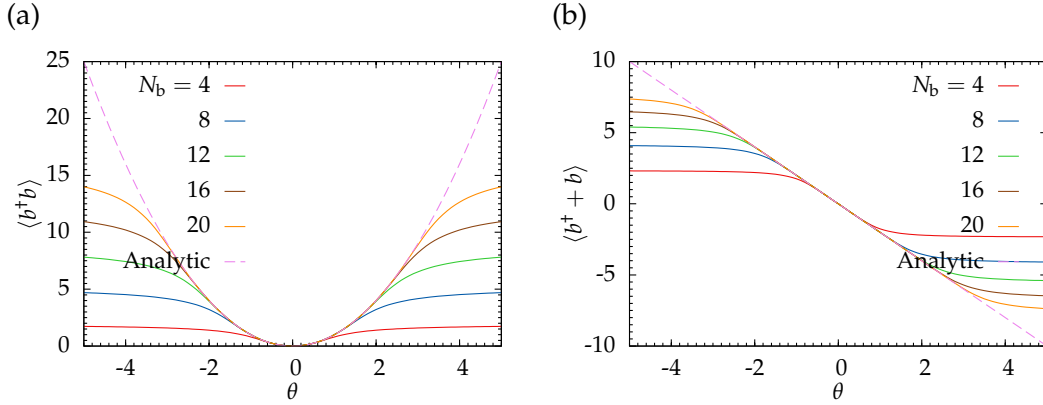


Figure 2.9: Expectation values of the (a) occupation operator, $b^\dagger b$, and (b) the displacement operator, $b^\dagger + b$, of an displaced harmonic oscillator versus the displacement model parameter θ for different dimensions of the bosonic Hilbert space, N_b . The Hamiltonian for this system is given by Eq. (2.34) and the system is diagonalized exactly. The dashed lines indicate the analytic results, Eq. (2.37) and Eq. (2.39).

needs more bosonic states. As the computational demands grow with N_b we present a way how to reduce N_b by employing an optimal basis by displacing the original basis. We investigate the effects of the displacement and propose a method how to choose optimal displacement parameters.

If one fixes the number of bosonic states N_b , it is clear how many but not which bosonic modes to select. Our first results are all obtained by selecting the eigenstates of a (displaced) harmonic oscillator with the lowest occupation number eigenvalues. At the end of this section we explore some prospects of different state selections.

All these questions are examined on the basis of two models: a displaced harmonic oscillator and a spin coupled to one or two bosons. In a truncated bosonic basis one can numerically diagonalize both models exactly, whereas only for the first model an analytic solution is available. The second model is a first step towards the full SBM as it represents a spin- $\frac{1}{2}$ with one or two Wilson chain sites.

2.3.1 Displaced oscillator

The model under inspection in this section is a displaced oscillator b described by the Hamiltonian

$$\frac{H}{\Omega} = \theta(b^\dagger + b) + b^\dagger b. \quad (2.34)$$

We use Ω as the energy unit and set $\Omega \equiv 1$ in the following. The transformation $\tilde{b} = b + \theta$ diagonalizes the Hamiltonian,

$$H = \tilde{b}^\dagger \tilde{b} - \theta^2. \quad (2.35)$$

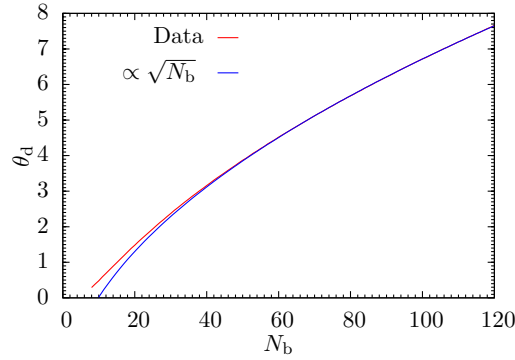


Figure 2.10: Value of threshold displacement θ_d , at which the numerical data starts deviating from the analytic data in Fig. 2.9.

We denote the ground state of H by $|0\rangle$, and in this state the following expectation values are given:

$$\langle 0 | \tilde{b}^\dagger \tilde{b} | 0 \rangle = 0 \quad (2.36)$$

$$\Rightarrow \langle 0 | b^\dagger b | 0 \rangle = \theta^2 \quad (2.37)$$

$$\langle 0 | \tilde{b}^\dagger + \tilde{b} | 0 \rangle = 0 \quad (2.38)$$

$$\Rightarrow \langle 0 | b^\dagger + b | 0 \rangle = -2\theta. \quad (2.39)$$

To examine the effect of the truncation of the bosonic Hilbert space the Hamiltonian (2.34) is numerically diagonalized using a truncated bosonic basis. The expectation values are compared with the analytic values given in Eqs. (2.37) and (2.39). One observes (cf. Fig. 2.9) that for $|\theta| > \theta_d$ the numeric curves deviate from the analytic results. The so defined threshold displacement θ_d depends on the number of bosonic states N_b .

To find an analytic estimate for the maximum displacement θ_d a bosonic basis can describe for a given basis dimension N_b we first note from Eqs. (2.37) and (2.39) that

$$\left| \langle 0 | b^\dagger + b | 0 \rangle \right| = 2\sqrt{\langle 0 | b^\dagger b | 0 \rangle} \quad (2.40)$$

and we make the assumptions that for a truncated bosonic basis

$$\lim_{\theta \rightarrow \infty} \langle 0 | b^\dagger b | 0 \rangle \propto N_b \quad (2.41)$$

$$\text{and } \lim_{\theta \rightarrow \infty} \langle 0 | b^\dagger + b | 0 \rangle \propto \theta_d. \quad (2.42)$$

The first assumption reflects that a bosonic basis with the N_b lowest occupation number states cannot describe states with an occupation number larger than N_b . The second assumption states that the maximum value of the displacement achievable with this

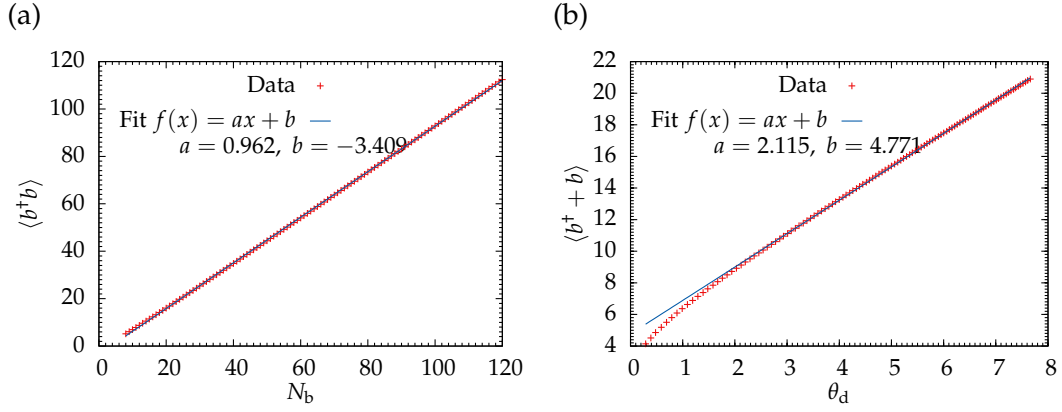


Figure 2.11: (a) Test of assumption Eq. (2.41) and (b) Eq. (2.42).

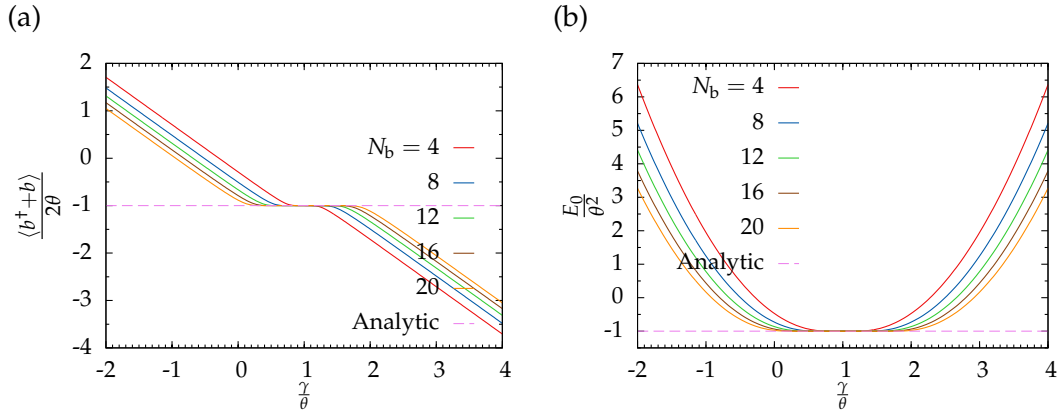


Figure 2.12: (a) Measured displacement and (b) ground-state energy of the Hamiltonian Eq. (2.34). The bosonic basis is displaced by γ . The ground-state energy E_0 shows a minimum plateau for $\gamma \approx -\theta$ which is symmetric around $\gamma = -\theta$. The dashed lines indicate the analytic results, Eq. (2.37) and Eq. (2.39); these are independent of γ as this value only influences the basis employed for numerical calculations.

basis coincides with the value of θ where the numerical and analytical values start deviating. With these assumptions the threshold value of the displacement is given by (cf. Fig. 2.10)

$$\theta_d^2 \propto 4N_b. \quad (2.43)$$

To test the validity of this estimate we show by comparison with numerical data that the assumptions are correct. Fig. 2.11 shows that a linear fit-function reproduces the numerical data well. Moreover, if one uses the fit-functions to calculate θ^2 for different N_b , one recovers the numerically extracted data (not shown). Therefore, we are confident that the assumptions are correct.

This means that only in a window of the width $\mathcal{O}(\sqrt{N_b})$ in which the physical displacement of the system and the displacement of the bosonic basis agree the results are reliable. In this toy model, the physical displacement is set by the parameter θ . To test the behavior of the numerics the Hamiltonian (2.34) is numerically diagonalized in a displaced basis, $\tilde{b} = b + \gamma$. We measure the displacement expectation value $\langle 0|b^\dagger + b|0\rangle$ and the ground-state energy (cf. Fig. 2.12). We notice that the results are only correct if $\gamma \approx -\theta$, whereby the allowed tolerance is, as expected, of the order $\mathcal{O}(\sqrt{N_b})$. If the basis displacement γ deviates too strongly from the physical displacement θ , the ground-state energy and the displacement expectation value deviate from the analytic value, because the bosonic basis is no longer capable to faithfully represent the ground state. To describe a strong displacement higher bosonic modes are excited which results in an increasing ground-state energy and a linearly deviating displacement expectation value.

The conclusion of this section is two-fold: (i) if the physical system is displaced by θ one needs approximately θ^2 bosonic states to numerically represent this displacement; and (ii), if one chooses a displaced bosonic basis with a displacement equal to the displacement of the physical system it is numerically possible to represent this system exactly. In such a basis the effective displacement vanishes and therefore no numerical error due to the truncation of the bosonic Hilbert space is induced. The main obstacle is that usually, when constructing the basis, one has no knowledge about the physical displacements. This point is further discussed in the next section.

2.3.2 Spin with bosons

In the previous section we have shown the importance of an optimal bosonic basis. However, in general the optimal displacement parameter γ is *a priori* unknown. This section proposes a way to estimate the displacement parameter and shows the limitations of this estimate. To this end, we make a first step towards the SBM by considering the local spin with the first two Wilson shells; this is equivalent to H_2 defined by Eq. (2.5). The spin is described by the Pauli matrices σ_x and σ_z and two bosons, b_1 and b_2 . The Hamiltonian of this model is given by

$$H = \frac{\Delta}{2}\sigma_x + \frac{\epsilon}{2}\sigma_z + \alpha\sigma_z(b_0^\dagger + b_0) + \lambda(b_0^\dagger b_1 + b_1^\dagger b_0) + \sum_{i=1}^2 \omega_i b_i^\dagger b_i. \quad (2.44)$$

The tunnel-coupling between both spin states is given by Δ and the energy-splitting between the spin-up and spin-down state by ϵ . The spin couples with the strength α to the displacement of the first boson. The coupling strength between both bosonic modes is λ and ω_i are the oscillator frequencies. As we do not solve this model with the NRG we do not make assumptions about the parameters, e.g. $\omega_i \propto \Lambda^{-i}$ does not have to be fulfilled.

Optimal displacement

To determine the optimal basis the Hamiltonian Eq. (2.44) is written in terms of the displaced operators $\tilde{b}_i = b_i + \gamma_i$. With these operators the Hamiltonian takes the form

$$H = \frac{\Delta}{2} \sigma_x + \left(\frac{\epsilon}{2} - 2\alpha\gamma_0 \right) \sigma_z + (\alpha\sigma_z - \lambda\gamma_1 - \omega_0\gamma_0) (\tilde{b}_0^\dagger + \tilde{b}_0) + \lambda(\tilde{b}_0^\dagger \tilde{b}_1 + \tilde{b}_1^\dagger \tilde{b}_0) + \sum_{i=1}^2 \omega_i \tilde{b}_i^\dagger \tilde{b}_i - (\lambda\gamma_0 + \omega_1\gamma_1) (\tilde{b}_1^\dagger + \tilde{b}_1) + E_0(\gamma_0, \gamma_1). \quad (2.45)$$

The constant energy shift $E_0(\gamma_0, \gamma_1)$ is taken into account in the following calculations but the details are of no interest at this point. In Eq. (2.45) one can identify two terms of the form $(\tilde{b}_i^\dagger + \tilde{b}_i)$ generating a displacement of the bosons. If one chooses γ_i in such a way that these terms vanish, the oscillators \tilde{b}_i are not displaced but are centered around zero, as there is no source term for a displacement anymore.

To make these terms vanish one has to make sure that the prefactors of these terms are zero. In general, this is not possible as one prefactor depends explicitly on the operator σ_z . Here we make a mean-field like approximation and replace the operator by its expectation value, $\sigma_z \rightarrow \langle \sigma_z \rangle$. The validity of this approximation is discussed below. This yields the equations

$$\alpha \langle \sigma_z \rangle - \lambda\gamma_1 - \omega_0\gamma_0 = 0 \quad (2.46)$$

$$\lambda\gamma_0 + \omega_1\gamma_1 = 0. \quad (2.47)$$

We interpret the solution for these equations as conditional equations for the displacement parameters

$$\gamma_0 = \frac{\alpha \langle \sigma_z \rangle}{\omega_0 - \frac{\lambda^2}{\omega_1}} \quad \text{and} \quad \gamma_1 = -\frac{\lambda\gamma_0}{\omega_1}. \quad (2.48)$$

Below, in Sec. 2.5.2, this idea is generalized to a Wilson chain. These equations have to be solved self-consistently. If these conditional equations are fulfilled the expectation values of the bosonic displacements are given by

$$\langle \tilde{b}_i^\dagger + \tilde{b}_i \rangle = 0 \Rightarrow \langle b_i^\dagger + b_i \rangle = 2\gamma_i. \quad (2.49)$$

The achievement is that in a parameter regime where the mean-field approximation $\sigma_z \approx \langle \sigma_z \rangle$ is valid the numerical self-consistent solution of these equations does not depend on N_b ; in other words, finding a solution is possible even for small N_b and once one has found a solution there is no error at all due to the truncation of the bosonic basis.

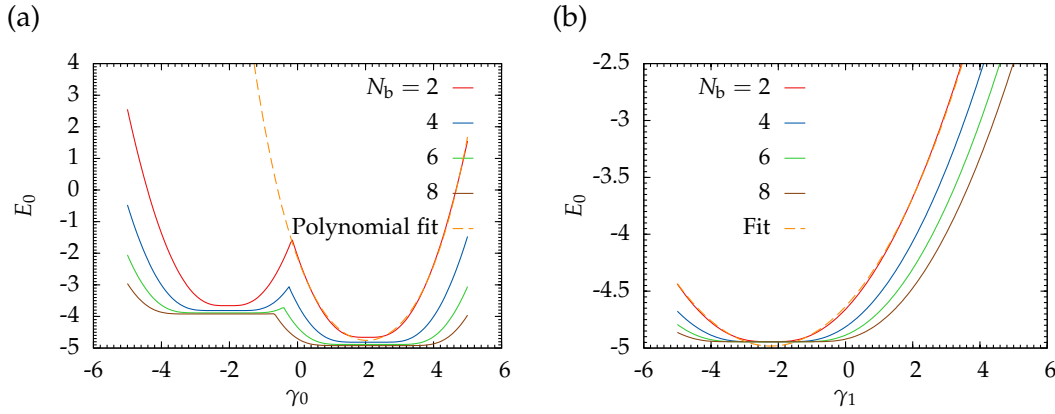


Figure 2.13: Ground-state energy of the Hamiltonian Eq. (2.44) versus displacement parameters, γ_0 and γ_1 , of bosonic basis to iteratively solve the self-consistent Eqs. (2.48). (a) γ_0 scan is performed with $\gamma_1 = 0$. With a polynomial fit up to fourth order (only even orders) the position of the energy minimum is determined. (b) γ_0 is set to the position of the energy minimum and a γ_1 scan is performed. These two steps are iterated until the parameters converge. The parameters are $\alpha = 4, \Delta = 0, \omega_0 = \epsilon = 1$, and $\omega_1 = \lambda = 0.1$.

We proceed by providing numerical evidence that the statements from above are correct. For the moment we consider only the case $\Delta = 0$. We start by finding optimal values γ_i which minimize the ground-state energy and then show, that these values solve the Eqs. (2.48). The optimal values are determined by setting $\gamma_1 = 0$ and varying γ_0 to minimize the ground-state energy (cf. Fig. 2.13). This value is then used for γ_0 when a γ_1 scan is performed. The procedure of independently determining an optimal γ_i while holding the other value constant is iterated until convergence is reached.

Fig. 2.13a shows that the value of the energy minimum at the first iteration, that is, with all displacement parameters set to zero, depends on N_b . At the second iteration when varying γ_1 the plot does not resolve differences of this value between different N_b . This means that the first guess for γ_0 is close to the actual optimal value.

Once the optimal displacement parameters are found it is expected that the ground-state energy does not depend on N_b anymore. As Fig. 2.14 shows, this is indeed the case: with an undisplaced basis the ground-state energy depends on the number of bosonic states N_b . For small N_b the basis cannot represent the ground state faithfully as the ground state consists of a fully polarized displacing the bosonic modes. According to Eqs. (2.48) with the parameters of Fig. 2.13 the displacement parameter is given by $\gamma_0 = \frac{20}{9}$. Therefore the expectation value of the displacement operator is $\langle b^\dagger + b \rangle = 2\gamma_0 \approx 4.4$. With an undisplaced basis the results converges to this value, whereas the optimized basis yields this value for any N_b (cf. Fig. 2.14b). This means that Eqs. (2.48) yield the optimal displacement parameters for the bosonic basis.

In the case $\Delta \neq 0$ this picture changes. Unlike in the $\Delta = 0$ case, the commutator $[H, \sigma_z]$ does not vanish anymore and therefore the two subspaces $\sigma_z = \pm 1$ are

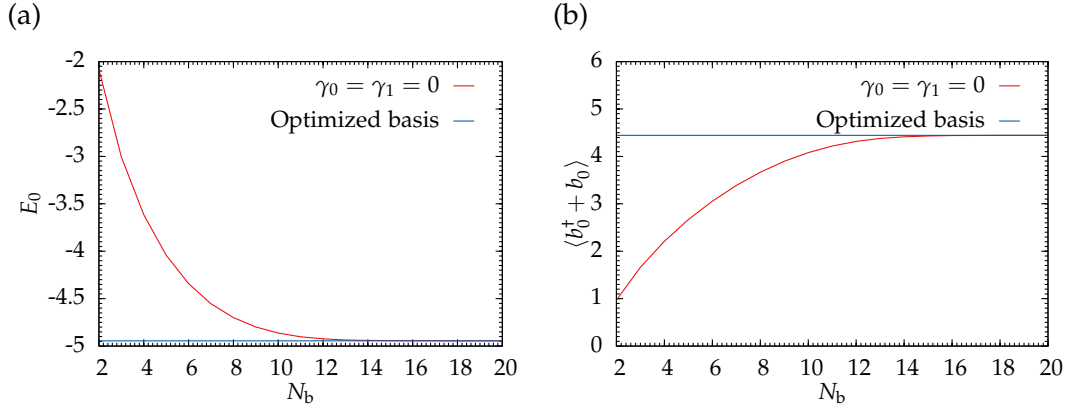


Figure 2.14: (a) Ground-state energy and (b) expectation value of the displacement operator versus N_b for Hamiltonian Eq. (2.44) calculated with an optimal displaced and an undisplaced basis: with an optimal basis the results are independent of N_b . The parameters are as in Fig. 2.13.

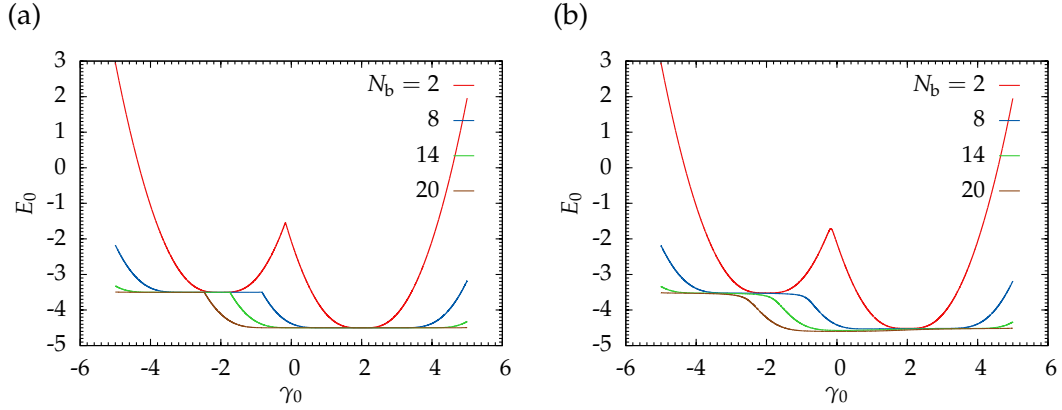


Figure 2.15: Ground-state energy E_0 of Hamiltonian Eq. (2.44) versus the displacement parameter of the bosonic basis γ_0 for a spin coupled to one boson. The parameters are $\alpha = 4, \epsilon = \omega_0 = 1$. The tunnel-coupling is set to (a) $\Delta = 0$, and (b) $\Delta = 1$.

connected. Eigenstates of H are not anymore eigenstates of σ_z but are, in general, superpositions of σ_z eigenstates. As the displacement of the first harmonic oscillator is coupled to σ_z , this harmonic oscillator is now in a superposition of being displaced in positive and negative γ direction. It is therefore more difficult to find an optimal basis by displacing the basis in one direction.

To illustrate this we consider the case $\omega_1 = \lambda = 0$. Effectively this reduces the model to a spin coupled to a single bosonic site: this is just the spin with the first Wilson shell. From the previous discussion one could expect that there exists a γ_0 independent of N_b which displaces the bosonic basis optimally. Fig. 2.15a shows the expected behavior: for $\Delta = 0$ the minimal ground-state energy is independent of N_b and found at the same value of γ_0 for all N_b . However, for $\Delta \neq 0$ (cf. Fig. 2.15b) this not the case; the value and the position of the minimal ground-state energy depend on N_b .

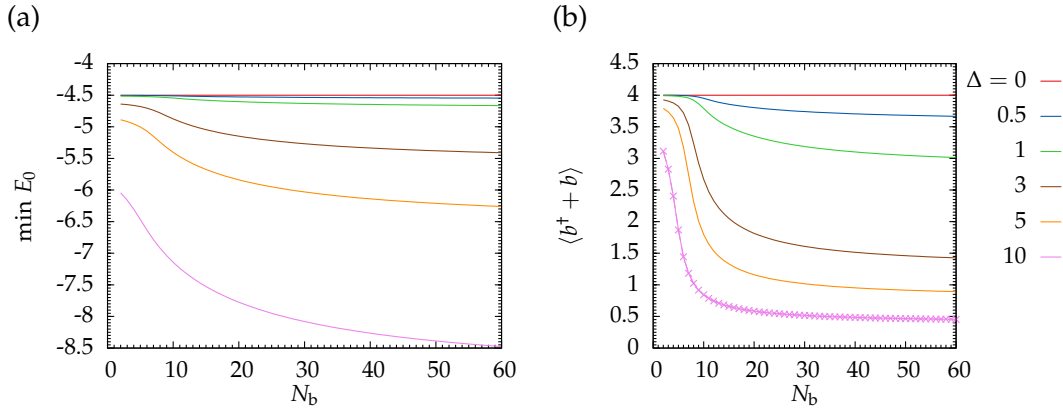


Figure 2.16: (a) Minimal ground-state energy E_0 and (b) expectation value of displacement operator of Hamiltonian Eq. (2.44) at the point of the minimal ground-state energy for different number of bosonic states N_b . The same parameters as in Fig. 2.15 are used. The crosses show the displacement calculated from $\langle \sigma_z \rangle$ by using Eqs. (2.49) and (2.48).

This dependence is further analyzed in Fig. 2.16. Fig. 2.16a shows the minimum of E_0 for a γ_0 scan. Unlike the $\Delta = 0$ case, where the minimum ground-state energy is independent of N_b , for $\Delta \neq 0$ this value shrinks with increasing N_b . A similar observation is made for the expectation value $\langle b^\dagger + b \rangle$: for $\Delta = 0$ and with an optimal basis this value is independent of N_b . Even if the basis is optimized for each value of N_b , by setting γ_0 to the value minimizing the ground-state energy, $\langle b^\dagger + b \rangle$ depends on N_b . As a consequence, since the optimal basis is defined by $\gamma_i = \frac{1}{2} \langle b_i^\dagger + b_i \rangle$, the optimal displacement parameter depends on N_b . This is in stark contrast to the $\Delta = 0$ case.

The derivation of the self-consistent equations (2.48) for the optimal displacement parameters does not depend on σ_x . Hence, these equations are still valid for $\Delta \neq 0$. To show this the displacement parameter is set to the value minimizing the ground-state energy and σ_z is measured. The result is used in Eqs. (2.48) to calculate the optimal displacements γ_0 . From these the expectation value of the displacement operator is calculated with Eq. (2.49) and the results are shown in Fig. 2.16b for $\Delta = 10$ as points: there is a perfect agreement between the measured displacement and the displacement needed to fulfill the self-consistent Eqs. (2.48). Therefore, these equations are valid for $\Delta \neq 0$.

The displacement expectation value $\langle b^\dagger + b \rangle$ shrinks with increasing Δ (cf. Fig. 2.16). The reason for this behavior is that for $\epsilon \neq 0 \neq \Delta$ the σ_z and σ_x operators compete: for the σ_z (σ_x) operator a fully (un-)polarized spin in z direction is energetically favorable. For $\frac{\epsilon}{\Delta}$ finite the spin is in a superposition of the $|\uparrow\rangle$ and $|\downarrow\rangle$ states. Hence, for increasing $|\Delta|$ the value $|\langle \sigma_z \rangle|$ shrinks and thereby reducing the bosonic displacement.

To illustrate this for a decoupled spin, $\alpha = 0$, the spin polarization can be calculated analytically and leads to

$$\langle \sigma_z \rangle = \frac{\epsilon \left(\sqrt{\Delta^2 + \epsilon^2} + \epsilon \right)}{\Delta^2 + \epsilon^2 + \epsilon \sqrt{\Delta^2 + \epsilon^2}} \quad (2.50)$$

$$\text{and } \langle \sigma_x \rangle = \frac{\Delta \left(\sqrt{\Delta^2 + \epsilon^2} + \epsilon \right)}{\Delta^2 + \epsilon^2 + \epsilon \sqrt{\Delta^2 + \epsilon^2}}. \quad (2.51)$$

These equations are consistent with the aforementioned limits

$$\frac{\Delta}{\epsilon} \rightarrow 0 \Rightarrow |\langle \sigma_z \rangle| \rightarrow 1, \langle \sigma_x \rangle \rightarrow 0 \quad (2.52)$$

$$\text{and } \frac{\epsilon}{\Delta} \rightarrow 0 \Rightarrow \langle \sigma_z \rangle \rightarrow 0, |\langle \sigma_x \rangle| \rightarrow 1. \quad (2.53)$$

For $\Delta \neq 0$, the ground state of the spin is a superposition of $|\uparrow\rangle$ and $|\downarrow\rangle$. The weights of both states depend on the ration $\frac{\Delta}{\epsilon}$. The effect of this superposition is, that the boson is in a superposition of being displaced in positive γ direction and negative γ direction. At our construction of the bosonic basis only one displacement direction is taken into account. This is the reason for the N_b dependence shown in Fig. 2.16: the basis is only optimized for the displacement in one direction. To faithfully represent the boson displaced in the other direction one needs more basis states. To further improve the results one option is to change the way the bosonic basis is constructed.

Construction of the bosonic basis

The matrix elements of the displaced bosonic creation operator $b_\gamma^\dagger = b^\dagger + \gamma$ are given by

$$\langle m | b_\gamma^\dagger | n \rangle = \begin{cases} \sqrt{n+1} & m = n+1 \\ \gamma & m = n \end{cases}. \quad (2.54)$$

The state $|m\rangle$ is an eigenstate of $b^\dagger b$ with eigenvalue m . Numerically the operator b_γ^\dagger is stored as an $N_b \times N_b$ matrix M . So far we truncated the bosonic Hilbert space by keeping only the states with the lowest occupation numbers,

$$M_{m,n}^{\text{low}} = \langle m | b_\gamma^\dagger | n \rangle \quad 0 \leq m, n < N_b. \quad (2.55)$$

This strategy is well justified for $\Delta = 0$, since due to the optimal displacement the occupation number is low. Choosing the bosonic basis in this fashion usually does not yield low bosonic occupation numbers for $\Delta \neq 0$, hence this strategy is questionable in this case. In the following different selections of bosonic states are compared: keeping the

states with even occupation number $2n$ and with an exponential increasing occupation $2^n - 1$,

$$M_{m,n}^{\text{even}} = \sqrt{2n}\delta_{m,n+1} + \gamma\delta_{m,n} \quad (2.56)$$

$$\text{and } M_{m,n}^{\text{exp}} = \sqrt{2^n - 1}\delta_{m,n+1} + \gamma\delta_{m,n} \quad 1 \leq m, n < N'_b - 1. \quad (2.57)$$

So far N_b has two meanings: it denotes (i) the number of bosonic states – that is the dimension of the matrix M – and (ii) the largest possible occupation number. From now on, we have to distinguish between both meanings. Hence, we have introduced the parameter N'_b , which solely denotes the matrix dimension of the truncated operator and N_b solely denotes the maximum occupation number.

To justify this procedure of selecting states one can imagine to write down $M_{m,n}^{\text{low}}$ with dimension $2N_b \times 2N_b$ and then erase all odd columns and rows of this matrix to arrive at $M_{m,n}^{\text{even}}$. Note that the truncation of the bosonic modes is done before the operators are displaced.

By selecting only a few states the canonical bosonic commutation relation $[b, b^\dagger] = 1$ is not fulfilled anymore. By selecting only the lowest states, Eq. (2.55), the matrix representation of the commutator is given by

$$\left[M^{\text{low}}, M^{\text{low}\dagger} \right]_{m,n} = \begin{cases} \delta_{m,n} & m, n < N_b - 1 \\ -(N_b - 1)\delta_{m,n} & m, n = N_b - 1 \end{cases}. \quad (2.58)$$

Hence in the matrix representation of this selection the matrix element of the last row and the last column is wrong: it is not one but $(1 - N_b)$. If one selects only the even states the matrix representation of the commutator is given by

$$\left[M^{\text{even}}, M^{\text{even}\dagger} \right]_{m,n} = 2 \left[M^{\text{low}}, M^{\text{low}\dagger} \right]_{m,n} \quad (2.59)$$

and for the exponential selection

$$\left[M^{\text{exp}}, M^{\text{exp}\dagger} \right]_{m,n} = \begin{cases} (2^n - 1)\delta_{m,n} & m, n < N'_b - 1 \\ (1 - 2^{N'_b - 1})\delta_{m,n} & m, n = N'_b - 1 \end{cases}. \quad (2.60)$$

As a rule, we see that the diagonal elements except the last are given by the number of omitted states plus one. The last diagonal element need some special treatment: it is connected to N'_b and it has a different sign compared to the other diagonal elements.

In Fig. 2.17 the three different ways to select the bosonic states are compared. Shown is $\langle S_z \rangle = \frac{1}{2}\langle \sigma_z \rangle$ calculated with an optimal displacement. This displacement is found by performing a γ_0 scan and selecting the value at which the ground-state energy is minimal. Fig. 2.17a depicts the expectation value $\langle S_z \rangle$ for different operator matrix sizes

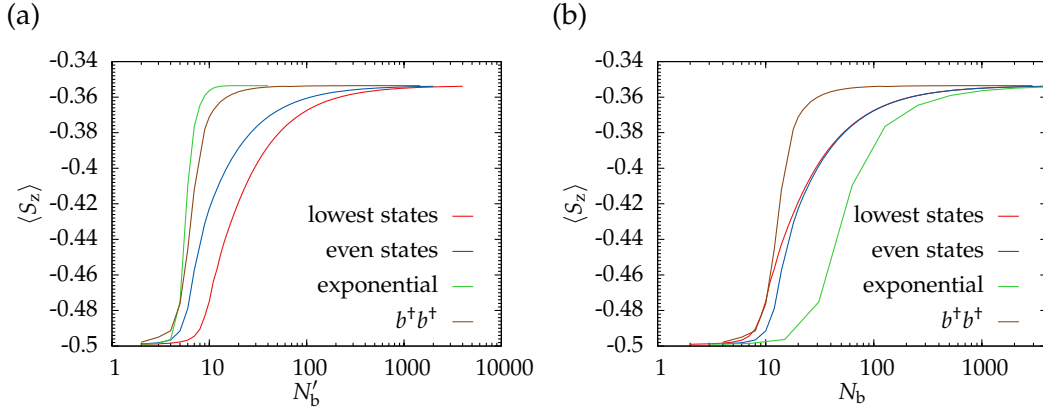


Figure 2.17: Convergence of the expectation value $\langle S_z \rangle$ with (a) N'_b bosonic states and (b) the maximum bosonic occupation N_b for different selections of kept bosonic states. The parameters are $\epsilon = \Delta = \omega_1 = 1, \alpha = 4, \omega_2 = \lambda = 0$.

N'_b . Other expectation values, like the ground-state energy, follow the same qualitative behavior. With an exponential selection of states the matrix dimension needed to reach convergence is two orders of magnitude lower compared to the other two selections. When just keeping the lowest states the matrix dimension is about twice the size than with even states.

However, when comparing the results for a fixed N_b – that is the highest available mode⁴ – the basis selecting the lowest states yields the best results (cf. Fig. 2.17b), because for this selection the total number of states is the largest and therefore the bosonic truncation error is the smallest. Hence keeping only the lowest states yields the best precision on the cost of a large matrix dimension. On the other hand, for a fixed matrix dimension N'_b selecting the lowest states is not necessarily the optimal selection.

Admittedly, the protocol presented here to construct the basis by truncating some states from the operator matrix is an *ad hoc* approximation which is not justified rigorously. For example, in the original basis one has only matrix elements connecting states differing in occupation by one. By truncating some states one implicitly constructs matrix elements connecting states differing in occupation by more than one. As a result some bosonic states are never occupied and can therefore be discarded from the bosonic Hilbert space. This reduction of dimensionality reduces the demands on the computational resources.

⁴ Technically this is just a rescaling of N_b . For the lowest states selection $N_b = N'_b$, for the even states selection $N_b = 2N'_b$, and for the exponential selection $N_b = 2^{N'_b} - 1$ holds.

A different way to achieve that some states remain unoccupied is to replace a single application of the bosonic creation operator – and analogously the annihilation operator – by two applications,

$$\tilde{b}^\dagger = b^\dagger b^\dagger. \quad (2.61)$$

This does not allow for an occupation of states with an odd occupation number. The advantage of this construction is that one does not have to tune the matrix elements in an uncontrolled way. The results using this construction are shown in Fig. 2.17 labeled $b^\dagger b^\dagger$. As a matter of principle one could generalize this idea to $\tilde{b}^\dagger = (b^\dagger)^k$ and thereby occupying only states with an occupation being an integer multiple of k . However, k must not be too large, otherwise too few low-energy states are kept to have a good resolution of the low-energy sector. For very large k even the high-energy states which apparently dominate the results for this toy-model are discarded and this approach breaks down.

The possibility to discard a large number of low lying states suggests that the results depend on high energy excitations as well. Despite common assumptions, these kind of excitations seem to play a major role. Exploiting the fact that each level of the harmonic oscillator lives on a different energy scale and with the observation that all energy scales contribute one could think of constructing an RG like scheme to further improve the handling of the truncated bosonic basis.

Bulla *et al.* proposed in Ref. 75 an optimal bosonic basis by describing a harmonic oscillator in a superposition of being displaced by γ and $-\gamma$. Since the σ_x term generates such displacements it might turn out to be advantageous to use a bosonic basis respecting this. If one wishes to keep the matrix dimension of M at $N_b \times N_b$ this new basis is constructed by two bosonic oscillator – one centered at $-\gamma$ and one at γ – with $\frac{N_b}{2}$ bosonic modes each. Using the optimal basis from Ref. 75 to calculate ground state properties of the Hamiltonian Eq. (2.44) we do not see significant improvements of the results (cf. Fig. 2.18).

Our basis choice is limited to the eigenbasis of the $b^\dagger b$ operator. A different valid choice are the coherent states $|\alpha\rangle_c = S(\alpha)|0\rangle = e^{\alpha b^\dagger - \alpha^* b}|0\rangle$. Alvermann *et al.* propose in Ref. 144 to construct so-called shifted oscillator states by orthonormalization of the set of states

$$|n\sigma\rangle_c = S(n\sigma)|0\rangle \quad n = 0, 1, \dots, N_b - 1. \quad (2.62)$$

The parameter σ plays a similar role as our displacement parameter. According to Ref. 144 this basis allows to consider large displacements with just a few bosonic modes if the guess of the displacement σ is not too far from the physical realized displacement. Again the difficulty that one does not know the optimal displacement *a priori* emerges.

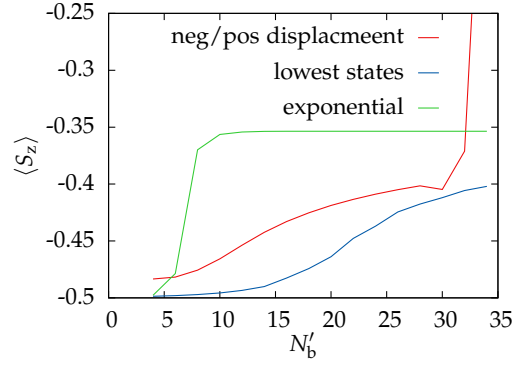


Figure 2.18: Basis constructed according to Ref. 75 compared with selection of some states. The divergence of the negative/positive displaced basis is due to numerical errors occurring when constructing the basis. Same parameters used as in Fig. 2.17.

Concluding we note that, in general, there is no optimal basis selection. Selecting other bosonic states than the N_b lowest might improve the results, but so far it is not clear how to generate an optimal set of bosonic states. Further research could examine the effects of state selection more deeply with the goal the generate a method which yields an optimal selection for a given purpose. As this method is not available yet, in the remaining part of thesis bosonic bases are constructed by the lowest bosonic states: for a sufficiently large number of bosonic states N_b this selection yields good results. As it is not *a priori* clear what *sufficiently large* means one has to carefully choose N_b .

2.4 Numerical renormalization group results

In this section the NRG is employed to solve the SBM Hamiltonian Eq. (2.5). The SBM fulfills all requirements for being solvable with the NRG: the impurity is small enough for being exactly solvable and in the form of Eq. (2.5) the bath is mapped to a Wilson chain. We calculate the phase diagram and critical exponents. By comparing these to the mean-field expectations one could conclude that the quantum-to-classical mapping (cf. Sec. 2.1.2) fails for $s \leq \frac{1}{2}$. However, the central result of this section is, that this is an error inherent to the NRG due to the neglect of the rest-chain at a given iteration.

2.4.1 Choice of parameters

The accuracy of the bosonic NRG method depends on two parameters: the number of kept states N_s and the number of bosonic modes N_b .⁵ A typical choice is $N_s \sim 100$ and $N_b \sim 8$ [75]. After asserting that the results do not change significantly for more states, we choose $N_s = 100$ to keep the numerical effort manageable.

⁵ For the truncation of the bosonic Hilbert space only the states with the lowest occupation number are kept.

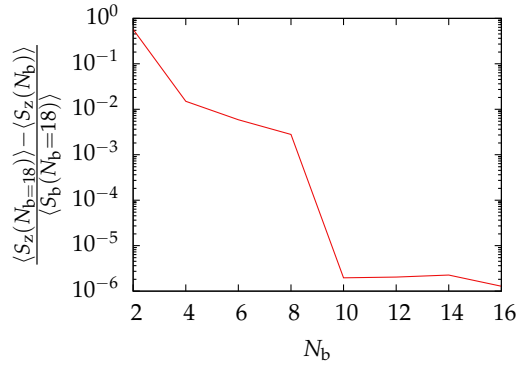


Figure 2.19: Deviation of $\langle S_z \rangle$ obtained with N_b bosonic states from calculations with $N_b = 18$ bosonic states. Results are for the SBM solved with the NRG. As the curve saturates for $N_b \geq 10$, the results are not improve further by keeping more bosonic states. The parameters are $N_s = 100, s = 0.5, \Lambda = 2, N = 40, \alpha = 8.025 \cdot 10^{-2}, \Delta = 0.1\omega_c$, and $\epsilon = 10^{-7}\omega_c$.

As discussed in Sec. 2.3.2 one has to take special care how to choose N_b . Fig. 2.19 shows the deviation between $\langle S_z(N_b) \rangle$ and $\langle S_z \rangle$ calculated with $N_b = 18$ bosonic modes. This value saturates for $N_b \geq 10$, meaning that one cannot improve the results further by increasing N_b . In the following calculations $N_b = 10$ bosonic modes are kept.

2.4.2 NRG level flow

The localized fixed point is not only characterized by a finite value of $\langle S_z \rangle$ but also that the eigenstates are two-fold degenerate. On the other hand, the eigenstates are not degenerate in the delocalized phase. Therefore the two phases can be distinguished in the NRG level flow diagram.

Fig. 2.20 shows the first few excited eigenstates above the ground state for different values of the coupling strength α . At low iteration numbers the system is influenced by both thermal and quantum fluctuations but for $N \rightarrow \infty$, which is equivalent to $T \rightarrow 0$, the effects of the QCP become visible and the quantum fluctuations dominate. That is why for high energies the state flow starts at approximately the same value for different α but the paths to the fixed points and the fixed points are different.

For $\alpha > \alpha_c$ the levels are not degenerate for $N \lesssim 10$. At later iterations two states pair up and finally the fixed point is two-fold degenerate: unlike the $\alpha \leq \alpha_c$ curves, there are only three lines visible for $\alpha > \alpha_c$ at $N = 40$ with $E_N > 0$. For $\alpha \leq \alpha_c$ one can distinguish all shown states above $E_N > 0$.

For $\alpha \neq \alpha_c$ the level flows converges to one of the two stable fixed points: the delocalized or the localized one. However, Fig. 2.20 shows that for $\alpha = \alpha_c$ a third fixed point emerges, though this critical fixed point is infrared unstable. This is only true

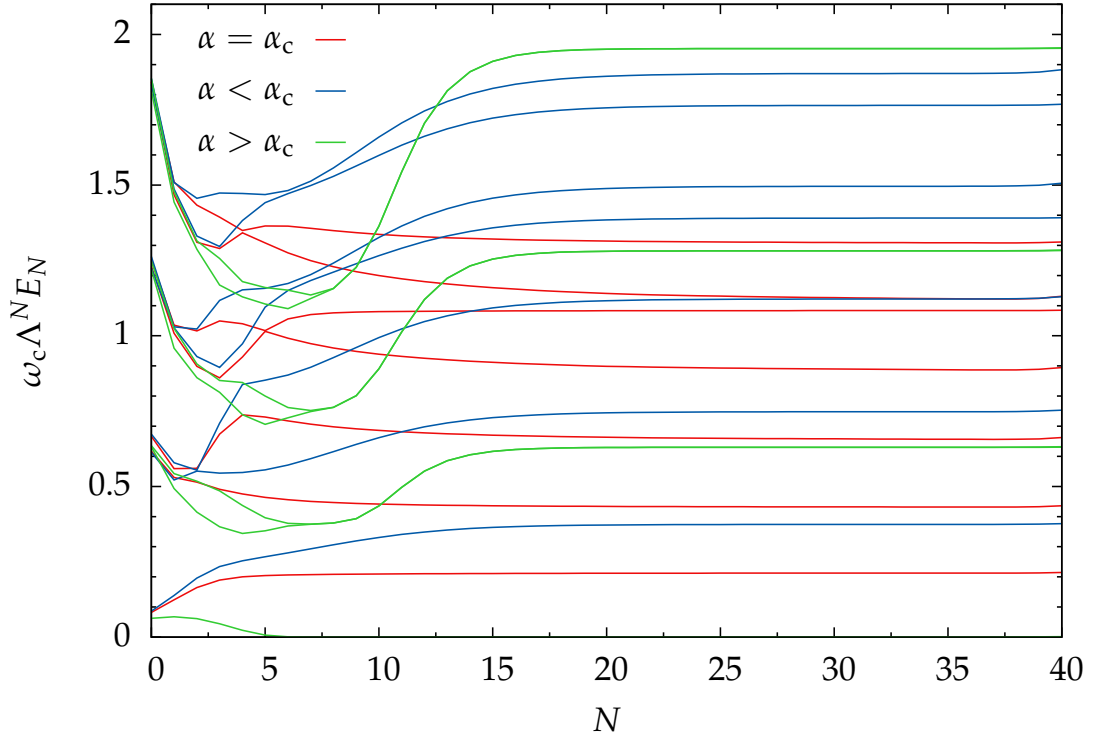


Figure 2.20: NRG level flow diagram for $s = 0.5, \Lambda = 2, N_s = 100, N_b = 10$, and $\alpha \in \{\alpha_c = 0.1062556, 8.025 \cdot 10^{-2}, 0.25\}$. Shown are the first 7 excited states above the ground state.

in the sub-ohmic regime. For an ohmic dissipation, $s = 1$, a critical fixed point is not observed due to the Kosterlitz-Thouless phase transition [74, 75].

2.4.3 Phase diagram

Rigorously, the QPT is only present in thermodynamic limit. For finite systems – such as a Wilson chain – the QPT is smeared out to a cross-over from the one phase to the other. Hence in the following we define a turning point through the cross-over scale and interpret this point as the critical coupling.

In Sec. 2.1.2 several differences between the localized and the delocalized phases are pointed out which one could use to determine the phase border. One criterion is the fixed point of the level flow as this is different below, at, and above the critical coupling. As a different option one could scan for the coupling strength at which the level degeneracy is lifted. However, one has to keep in mind that one is only able to observe a cross-over between the phases and therefore these points are not necessarily well defined. For this reason we define a criterion to determine the critical coupling strength which allows us to explicitly observe the cross-over from the delocalized to the localized phase.

To determine the critical coupling strength α_c separating both phases a very small symmetry breaking field $\epsilon = 10^{-7} \omega_c$ is applied and the point at which the transition

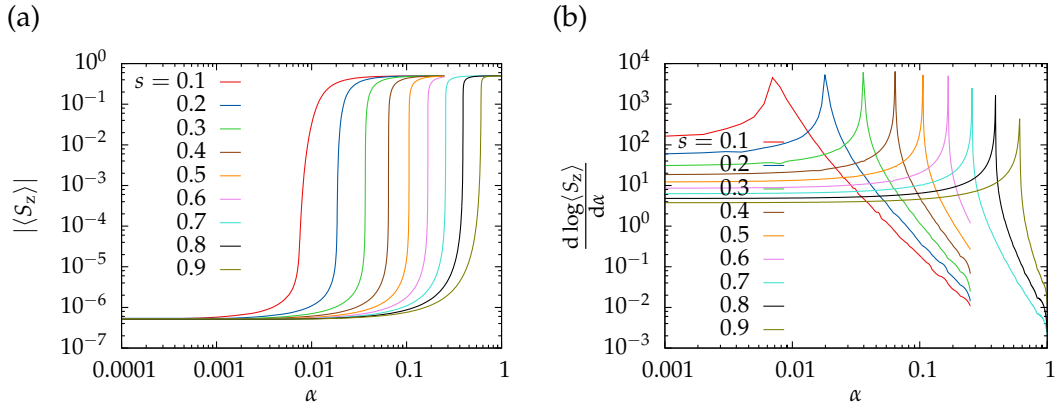


Figure 2.21: α scan for the SBM with NRG. The left panel shows $\langle S_z \rangle$ and the right panel shows the derivative. The maximum of the derivative indicates the turning point of $\langle S_z \rangle(\alpha)$. We interpret the turning point as the critical coupling strength. The parameters are $\Lambda = 2, \Delta = 0.1\omega_c, \epsilon = 10^{-7}\omega_c, N_b = 10, N_s = 100$, and $N = 40$.

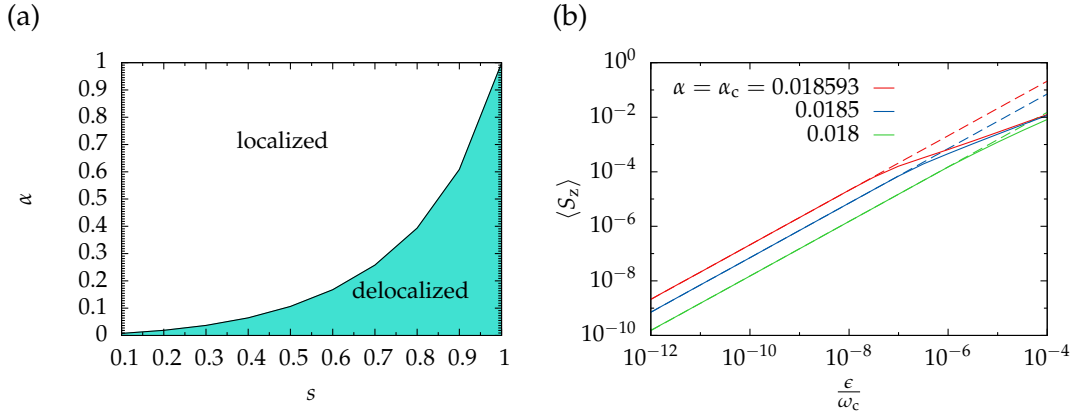


Figure 2.22: (a) Phase diagram of the SBM calculated with the NRG. Same parameters as Fig. 2.21. (b) ϵ scan for α detuned from α_c for $s = 0.2$ to observe when $\langle S_z \rangle(\epsilon)$ behaves non-linear: the closer α is to α_c the smaller is the linear range of $\langle S_z \rangle(\epsilon)$. The dashed lines show a fit $f(\epsilon) \propto \epsilon$.

from $\langle S_z \rangle \sim \mathcal{O}\left(\frac{\epsilon}{\omega_c}\right) \ll \frac{1}{2}$ to $\langle S_z \rangle = \frac{1}{2}$ occurs is located. This is achieved by finding the maximum of the derivative of $\log \langle S_z \rangle$,

$$\left. \frac{d \log \langle S_z \rangle(\alpha)}{d\alpha} \right|_{\alpha=\alpha_c} = 0, \quad (2.63)$$

since at the phase transition $\langle S_z \rangle$ drops over some orders of magnitude. To this end an α scan is performed with care taken to put more points in region where the derivative on a logarithmic scale is high (cf. Fig. 2.21). The critical coupling strength α_c is then determined by the numerical derivative of the interpolated data. The values for the critical coupling strength for different s determined in this fashion are shown in the phase diagram Fig. 2.22a.

2.4.4 Critical exponent

The critical exponent δ is determined by setting the coupling strength to its critical value, performing an ϵ scan, and fitting the function $f(\epsilon) = a\epsilon^{\frac{1}{\delta}}$ to the numerical data (cf. Fig. 2.23). Both a and δ are free fitting parameters. This fit is only valid in a certain region: for $\epsilon \sim \omega_c$ the expectation value $\langle S_z \rangle$ saturates at $\langle S_z \rangle = \frac{1}{2}$; and there is a linear regime, $\langle S_z \rangle \propto \epsilon$, for $\epsilon \lesssim 10^{-8}\omega_c$. This is due to the limited numerical precision of α_c : the numerically determined value of α_c deviates from the real physical value. Therefore one needs a finite ϵ to see the effect of the QCP. To see this effect Fig. 2.22b shows an ϵ scan for α detuned from the critical value. For an increasing detuning the threshold value of ϵ , up to which the curves show a linear behavior, grows.

For a value of ϵ too small for the spin to feel the presence of the QCP one can treat the spin as effectively quasi-free – of course with a renormalized value for Δ – and expand Eq. (2.50) around $\epsilon = 0$,

$$\langle \sigma_z \rangle = \frac{1}{2} \frac{\text{sgn}\Delta}{\Delta} \epsilon + \mathcal{O}(\epsilon^2), \quad (2.64)$$

to see that there is a linear dependence.⁶ By fitting a linear function to the $\langle S_z \rangle$ data in the range $10^{-12} \leq \frac{\epsilon}{\omega_c} \leq 10^{-8}$ (cf. Fig. 2.22b) it is possible to determine the renormalized tunnel-coupling Δ_r in the delocalized phase. At the critical point and in the localized phase the tunnel-coupling is renormalized to $\Delta_r = 0$.

The values determined by the fits (cf. Fig. 2.23) for δ and Δ_r are shown in Fig. 2.24. For δ one expects the hyper-scaling relation $\delta = \frac{1+s}{1-s}$ for $s > \frac{1}{2}$ and a mean-field exponent $\delta = 3$ for $s \leq \frac{1}{2}$. At $s = \frac{1}{2}$ both relations yield $\delta = 3$. However, as Fig. 2.24a shows the hyper-scaling relation is fulfilled in the whole parameter regime $s < 1$. When this was first observed in Ref. 124 it was believed that, despite different expectations, the quantum-to-classical mapping fails for the SBM. As we know today, the reason for the unexpected critical exponents is that the NRG suffers from the mass-flow error [36].⁷ In the following sections more evidence for this error is presented.

2.4.5 Flow of critical coupling strength

When discussing the DHO in Sec. 2.2.4 we noticed that the oscillator frequency is shifted by the real part of the bath spectral function. This leads to a renormalization of the critical coupling strength. Fig. 2.25a shows that the same effect is present in the NRG as well: the critical coupling strength depends on the length of the chain. Both Fig. 2.3 and Fig. 2.25a show the same functional dependence between α_c^N and s . In Sec.

⁶ This argument holds only if the numerical critical coupling strength is below the true one. Due to the way α_c is determined here, this is always the case. However, the main prerequisite for this argument to hold – that is, to treat the spin as free – is the linear dependence between ϵ and $\langle S_z \rangle$ for small ϵ .

⁷ A different view is presented in Ref. 131.

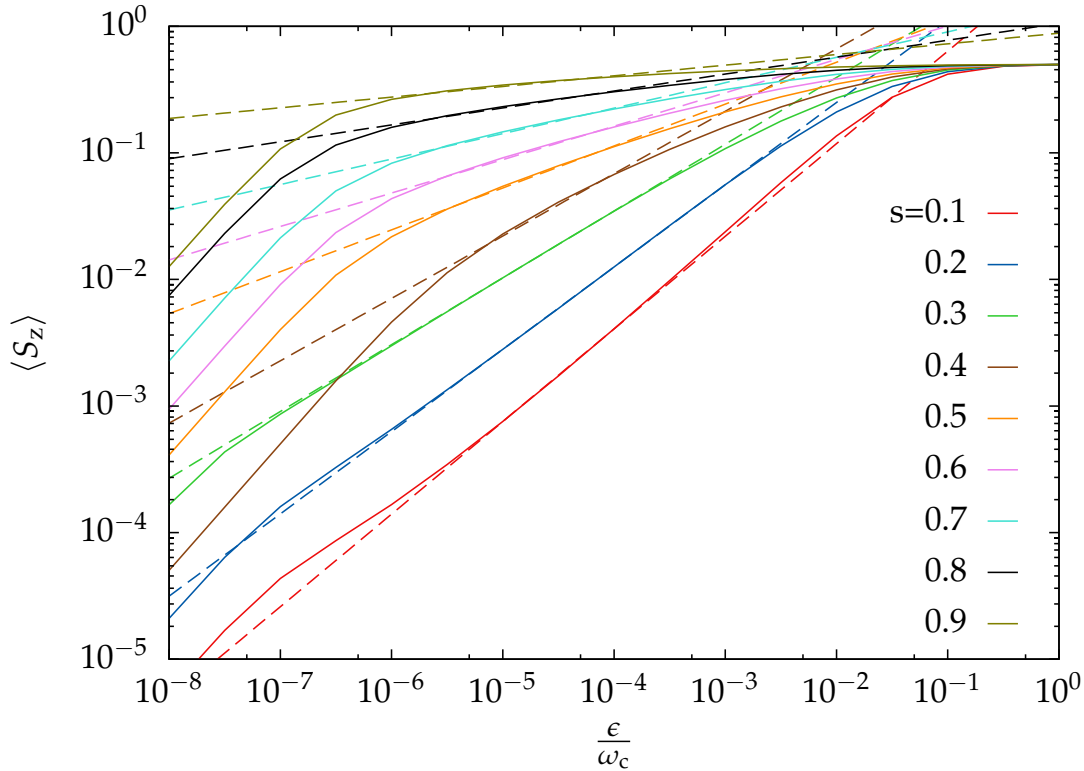


Figure 2.23: ϵ scan to determine critical exponent δ . The dashed lines are fits of the function $f(\epsilon) = a\epsilon^{\frac{1}{\delta}}$ in the interval $10^{-6} \leq \frac{\epsilon}{\omega_c} \leq 10^{-4}$. The coupling strength is set to $\alpha = \alpha_c$. Same parameters as Fig. 2.21.

2.2.4 it was shown that this dependence is due to the mass-flow effect. Therefore we conclude that this effect is also present in the NRG.

The mass-flow induces a temperature-dependent renormalization of the tunnel-coupling Δ . If the system is at its critical point for $T = 0$, meaning that $\alpha = \alpha_c$ or, equivalently, $\Delta = \Delta_c$, one observes two different trajectories for $T \rightarrow 0$ with and without mass-flow (cf. Fig. 2.25b): without the mass-flow effect the renormalization of Δ is temperature-independent and therefore the trajectory in the phase diagram is a straight line. On the other hand, with the mass-flow effect the order parameter acquires a temperature dependent mass inducing a different renormalization of Δ for each temperature T : the trajectory in the phase diagram is curved.

To explicitly calculate the flow of the renormalized tunnel-coupling Δ_r one can perform an ϵ scan for a chain with N sites. With a linear fit to the data-points $\epsilon < 10^{-8}\omega_c$ one can extract Δ_r with the method proposed in the previous section. Plotting Δ_r for different chain lengths (cf. Fig. 2.26) shows the typical s and N dependence already seen in Fig. 2.3 and Fig. 2.25a and sketched in Fig. 2.25b. This, again, shows that the mass-flow effect is present in the NRG.

The reason why the presence of the mass-flow effect leads to an error of the NRG is the following: the Wilson chain is built up iteratively. With each iteration the tem-

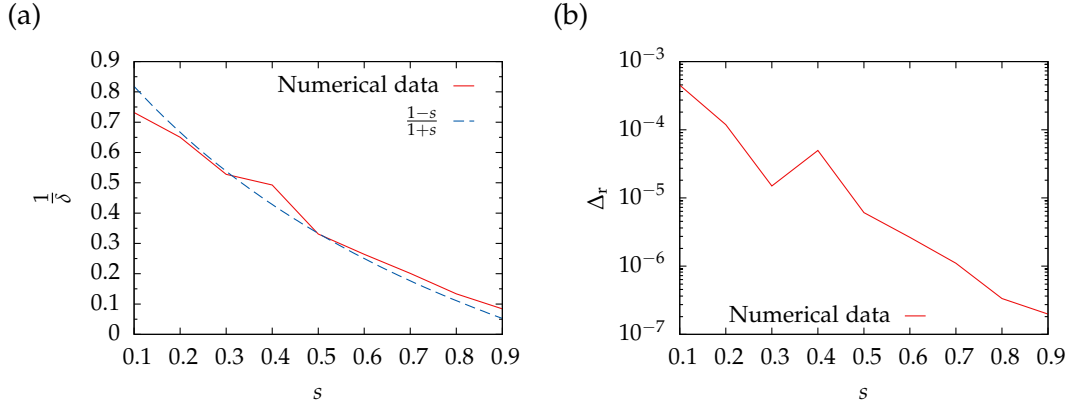


Figure 2.24: Linear fit parameters of Fig. 2.23. (a) s -dependence of the critical exponent δ (the dashed line indicates the hyper-scaling relation) and (b) renormalized tunnel-coupling Δ_r in the delocalized phase. These values are determined by fitting Eq. (2.64) to the $\langle S_z \rangle(\epsilon)$ curves for $10^{-12} \leq \epsilon \leq 10^{-8}$. Same parameters as Fig. 2.21.

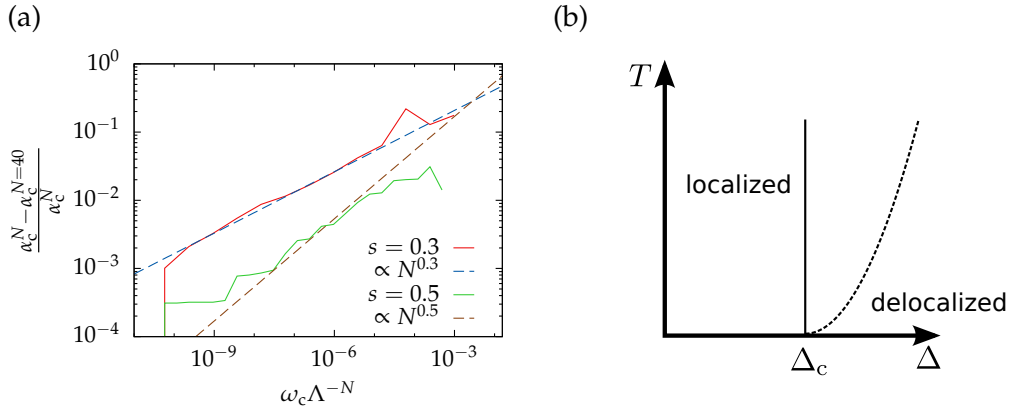


Figure 2.25: (a) Flow of critical coupling α_c^N at iteration N . Same parameters as Fig. 2.21. (b) Schematic phase diagram with (dashed line) and without (solid line) mass-flow effect.

perature is lowered and Δ is renormalized. Hence the NRG follows the curved line of Fig. 2.25b. As the NRG truncates $\frac{(N_b-1)N_s}{N_b}$ states at each iteration, the NRG targets the wrong subspace of the total Hilbert space. Hence the subspace in which the real ground state of the system lies is no longer reachable after a few NRG iterations. The ground state calculated by the NRG is therefore wrong and shows non-mean-field critical exponents. To cure the mass-flow error one has to take into account the effects of the rest-chain and thereby eliminating the temperature dependent renormalization of Δ .

One way to cure the mass-flow could be to construct an effective bath coupled to the last Wilson chain site at iteration N in such a way that the bath propagator of the Wilson chain with this effective bath at frequencies $\omega \lesssim \Lambda^{-N}\omega_c$ is the same as the continuous bath propagator. So far it is not clear how this can technically be achieved.

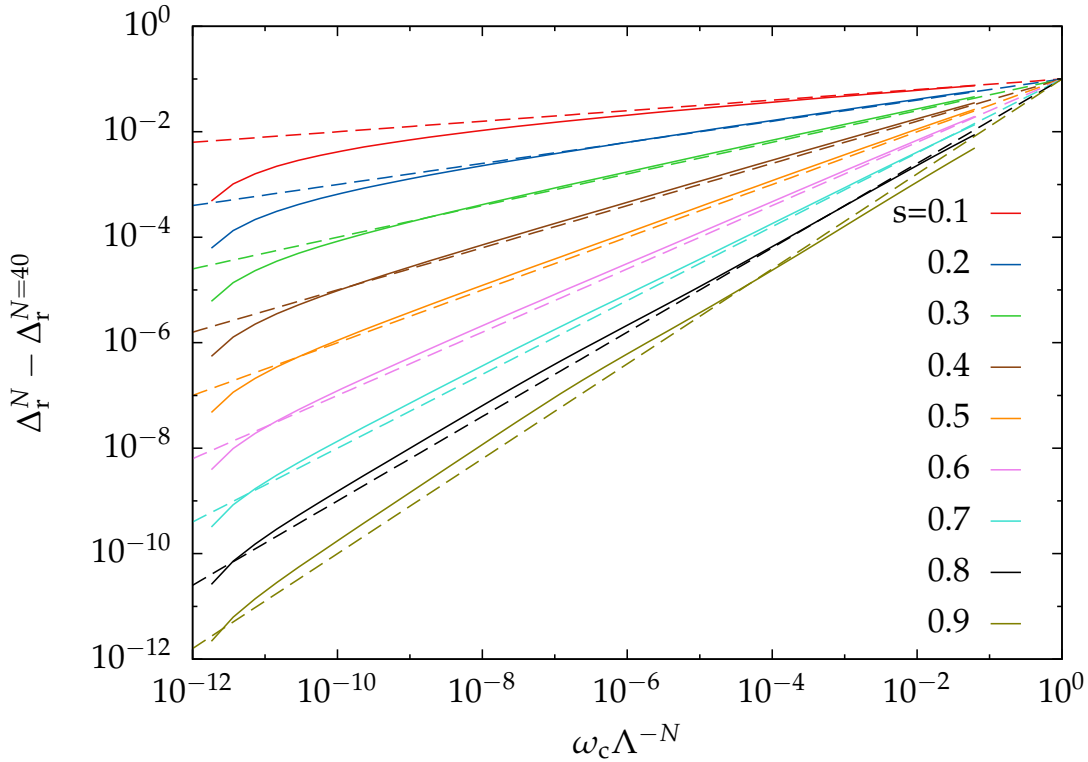


Figure 2.26: Temperature dependent renormalization of tunnel-coupling parameter in the delocalized phase. The values of Δ_r^N are determined by fitting Eq. (2.64) to the $\langle S_z \rangle(\epsilon)$ curves, as in Fig. 2.21b, for different N . The dashed lines are no fits, but show the curve $f(N) = \Delta N^s$, with Δ being the bare tunnel-coupling $\Delta = 0.1\omega_c$.

A different cure is to take the rest-chain explicitly into account. As the NRG relies on the assumption that lower energy scales have no effect on higher energy scales – that is, the separation of energy scales – it is not only technically difficult to take the rest-chain into account, but one encounters the conceptual obstacle that energy scales would mix. As, unlike the NRG, the DMRG does not rely on the separation of energy scales, this method can employ a sweeping technique to make sure that correlations can spread over the whole chain. Thereby the whole chain is taken into account.

2.4.6 Numerical errors

As all other numerical methods the NRG suffers from inevitable numerical errors, besides the errors which are inherent to the modeling process. The most fundamental ones are due to the discretization of real numbers: on a computer a real number can only be stored up to a certain precision. This limits the numerical accuracy. However, the relative error due to this effect is of the order 10^{-16} and is therefore negligible in most cases.

The dominant numerical error in the NRG is the truncation of states at each iteration. The truncation error is estimated by evaluating expectation values and deducing error

margins from these values. The upper estimate of the error margin is given by Fig. 2.19. From this we conclude that the error is $\mathcal{O}(10^{-5})$. The lower estimate is determined by performing a NRG calculation deep in the delocalized phase with $\epsilon = 0$. The analytic result is $\langle S_z \rangle = 0$, whereas the NRG gives $\langle S_z \rangle \sim \mathcal{O}(10^{-10})$. Therefore it is safe to say that the absolute error of an $\langle S_z \rangle$ measurement is not larger than 10^{-4} . However, we want to emphasize that this is not a statistical error but a systematic one: the NRG is a deterministic method, meaning that if one starts several runs with the same selection of parameters each run yields exactly the same results.

Another important quantity in this section is the critical coupling strength α_c . This is defined by the coupling at which the derivative of $\log\langle S_z \rangle$ has a maximum and is determined by an α scan. Hence, for this method of determining the critical coupling strength, the error of α_c is given by the scanning interval width. This error is minimized by scanning on an adaptive mesh where more points are inserted in a region where the slope of $\log\langle S_z \rangle$ is large. The resulting absolute error of the given α_c values is $\mathcal{O}(10^{-5})$ for small $s \lesssim 0.6$ and grows up to $\mathcal{O}(10^{-3})$ for $s = 1$.

For increasing s the decay of $\log\langle S_z \rangle$ is broadened – see Fig. 2.21 and notice the logarithmic α -axis – resulting in an increasing error for α_c . Because the calculations are not performed in thermodynamic limit the decay of $\langle S_z \rangle$ has a certain width resulting in a systematic error in the determination of α_c . To further increase the precision of α_c one would have to take the limit $\Lambda \rightarrow 1$ and $N \rightarrow \infty$.

A lower limit of the relative error of the critical exponent δ is the relative error the fit yields. In this sub-ohmic regime these errors are in the range 1%–5%. This error does not take into account any other errors. We claim that the error on α_c is negligible: we have seen that for ϵ large enough it is not important to set α precisely to its critical value (cf. Fig. 2.22b). Furthermore, the error on $\langle S_z \rangle$ is some orders of magnitude smaller than the error due to the fit. Hence, the effect of the $\langle S_z \rangle$ error on the δ error is negligible as well.

2.5 Density-matrix renormalization group results

We have shown that the effect of the rest-chain at a given NRG iteration is crucial to characterize the phase transition of the SBM correctly. Furthermore the truncation of the bosonic Hilbert space limits the accuracy of the NRG results: in the localized phase the bosons of the Wilson chain are strongly displaced. As a consequence one needs a large bosonic Hilbert space to represent this displacement numerically correct [75]. Because the displacement of the bosons grows exponentially with the chain site index i , the occupation number of the Wilson chain sites diverges [38],

$$\langle b_i^\dagger b_i \rangle \propto \langle \sigma_z \rangle^2 \epsilon_i^{s-1}. \quad (2.65)$$

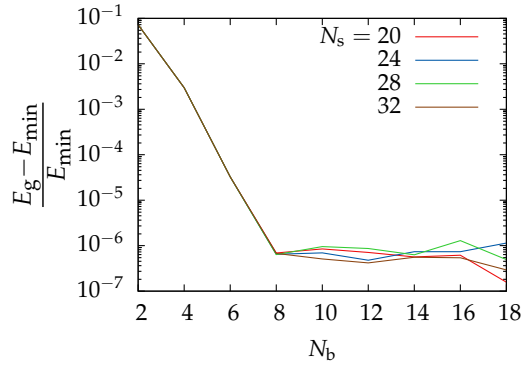


Figure 2.27: Relative ground-state energy for different number of kept (N_s) and bosonic (N_b) states. The reference ground-state energy E_{\min} was determined by a DMRG run with $N_s = 40$ and $N_b = 18$. The model parameters are $\alpha = 0.106$, $\epsilon = 10^{-7}\omega_c$, $\Delta = 0.1\omega_c$, $s = 0.5$, $\Lambda = 2$, and chain length $N = 40$.

The result is that with this naive approach one needs an infinite number of bosonic modes – this is, of course, not possible.

However, a more sophisticated approach employs an optimized basis which eliminates the problem of the truncation of the bosonic Hilbert space. This method is introduced in the following section and then applied to the DMRG to calculate the phase diagram and critical exponents of the SBM. Using the DMRG in this fashion reduces both problems of the NRG: (i) the truncation of the bosonic Hilbert space and (ii) the effects of the rest-chain at a given iteration. Therefore, the DMRG results show mean-field critical exponents for $s \leq \frac{1}{2}$ and non-mean-field critical exponents for $\frac{1}{2} < s < 1$.

2.5.1 Choice of parameters

In general, the accuracy of the bosonic DMRG relies vitally on the number of states N_s kept in the Hilbert space and on the number of bosonic modes N_b . The optimal⁸ choice of these parameters is determined by comparing the ground-state energy E_g for a given (N_b, N_s) with E_{\min} (cf. Fig. 2.27). The energy E_{\min} is the ground-state energy of a $(N_b = 18, N_s = 40)$ calculation.

As Fig. 2.27 shows, the relative error of the ground-state energy shrinks for increasing N_b up to $N_b = 8$ when the error saturates. This saturation is due to the inherent DMRG errors, specifically due to the accuracy of the Lanczos algorithm used to calculate the ground state. As the DMRG is a variational method and this error is purely of numeric nature it is no surprise that the relative error of the ground-state energy shows fluctuations, yet on a small scale. This means that the ground state is not improved by increasing N_b further and therefore we choose $N_b = 10$ for all DMRG calculations in

⁸ Optimal in this sense means to minimize the number of kept states to reduce the computational demands with the constraint that the results are still reliable.

this section. Since the accuracy of the method does not depend on the number of kept states for $N_s \geq 20$ (cf. Fig. 2.27) we use $N_s = 24$.

Because one is most interested in properties at or in the vicinity of the critical coupling strength α_c , Fig. 2.27 shows results for $\alpha \approx \alpha_c$. Of course, if one examines the regime $\alpha \gg \alpha_c$ being deep in the localized phase one needs to keep considerably more bosonic modes for the relative error to saturate.

2.5.2 Optimal bosonic basis

For the DMRG calculations one has to choose a truncated bosonic basis. Here the bosonic Hilbert space is built up by the N_b bosonic states with the lowest occupation, Eq. (2.55). As discussed in Sec. 2.3.2 it is advantageous to optimize the bosonic basis by a displacement. One advantage of the DMRG over the NRG is that it is possible to change the bosonic basis in the course of the simulation. In the NRG the local basis of each site is fixed once the next site is added. In the DMRG, however, the sweeping phase permits to change the basis of the local block. This allows to optimize the basis of the bosons with respect to the rest-chain.

One proposal how to implement this was made in Ref. 128. The idea proposed in this reference is to change the bosonic basis in some optimal way at each sweeping step. We present an alternative approach: the basis is not optimized at each sweeping step but after one DMRG run. This gives us some deeper insight how the displacement of the bosons is generated. To validate our results we compare the displacement parameters obtained with our new scheme with those obtained by variationally optimizing the displacement parameters of the local block at each sweeping step.

The optimization criterion is to find a basis in which the expectation value of the displacement operators $\langle \tilde{b}_0^\dagger + \tilde{b}_0 \rangle$ is minimized⁹ for the symmetry broken phase $\epsilon > 0$. As in Sec. 2.3.2 the displaced basis is defined by $\tilde{b}_i^\dagger = b_i^\dagger + \gamma_i$ and $\tilde{b}_i = b_i + \gamma_i$, where the displacement parameters γ_i have to be determined for each Wilson chain site individually. With Eqs. (2.48) we already have a set of equations which have to be solved self-consistently in order to determine the displacements for a chain consisting of two sites. The aim of this section is to extend this approach to longer chains.

In the displaced basis the SBM Hamiltonian Eq. (2.5) reads

$$\begin{aligned}
 H_N = & -\frac{\Delta}{2}\sigma_x + \frac{\epsilon}{2}\sigma_z + \sqrt{\alpha}V\sigma_z \left(\tilde{b}_0^\dagger + \tilde{b}_0 \right) - 2\gamma_0\sqrt{\alpha}V\sigma_z + E_0(\{\gamma_i\}) \\
 & + \sum_{i=0}^{N-1} \epsilon_n \left(\tilde{b}_i^\dagger \tilde{b}_i - \gamma_i \left(\tilde{b}_i^\dagger + \tilde{b}_i \right) + \gamma_i^2 \right) \\
 & + \sum_{i=0}^{N-2} t_i \left(\tilde{b}_i^\dagger b_{i+1}^\dagger + \tilde{b}_{i+1}^\dagger b_i^\dagger - \gamma_{i+1} \left(\tilde{b}_i^\dagger + \tilde{b}_i \right) - \gamma_i \left(\tilde{b}_{i+1}^\dagger + \tilde{b}_{i+1} \right) + 2\gamma_i\gamma_{i+1} \right). \quad (2.66)
 \end{aligned}$$

⁹ More precisely, $|\langle \tilde{b}_0^\dagger + \tilde{b}_0 \rangle|$ is minimized. In this section, *minimized* is used in the sense that the absolute value is minimized; in other words, the value is as close to zero as possible.

As we are not interested in the shift of the ground-state energy $E_0(\{\gamma_i\})$, we neglect this term in following derivations; however, in the numerical calculations this term is present.

The Hamiltonian Eq. (2.66) can be divided into two parts $H_N = H_{\text{dis}}^N + H_{\text{non-dis}}^N$. In H_{dis}^N all displacement inducing terms are collected, whereas $H_{\text{non-dis}}^N$ contains all other terms. As the optimal basis is supposed to minimize the expectation values $\langle \tilde{b}_i^\dagger + \tilde{b}_i \rangle$ all displacement source terms, $\tilde{b}_i^\dagger + \tilde{b}_i$, must vanish and hence γ_i must be chosen such that $H_{\text{dis}}^N = 0$. H_{dis}^N is given by

$$H_{\text{dis}}^N = (\sqrt{\alpha}V\sigma_z - \gamma_0\epsilon_0 - t_0\gamma_1) (\tilde{b}_0^\dagger + \tilde{b}_0) - \sum_{i=1}^{N-1} (\epsilon_i\gamma_i + t_i\gamma_{i+1}(1 - \delta_{i,N-1}) + t_{i-1}\gamma_{i-1}) (\tilde{b}_i^\dagger + \tilde{b}_i). \quad (2.67)$$

For this operator to vanish all summands have to vanish independently. Again, we replace the operator σ_z by its expectation value $\langle \sigma_z \rangle$. This leads to the matrix equation

$$\underbrace{\begin{pmatrix} \epsilon_0 & t_0 & 0 & 0 & \dots \\ t_0 & \epsilon_1 & t_1 & 0 & \dots \\ 0 & t_1 & \epsilon_2 & t_2 & \dots \\ \vdots & & \ddots & \ddots & \ddots \end{pmatrix}}_M \begin{pmatrix} \gamma_0 \\ \gamma_1 \\ \gamma_2 \\ \vdots \end{pmatrix} = \begin{pmatrix} -\sqrt{\alpha}V\langle \sigma_z \rangle \\ 0 \\ 0 \\ \vdots \end{pmatrix}. \quad (2.68)$$

The displacement parameters γ_i are then calculated by multiplying this equation with M^{-1} . For a chain with $N = 2$ sites the displacement parameters are given by

$$\gamma_0 = \frac{-\sqrt{\alpha}V\langle \sigma_z \rangle}{\epsilon_0 - \frac{t_0^2}{\epsilon_1}} \quad \text{and} \quad \gamma_1 = \frac{t_0\sqrt{\alpha}V\langle \sigma_z \rangle}{\epsilon_0\epsilon_1 - t_0^2}. \quad (2.69)$$

These equations are equal to Eqs. (2.48). For an N -site chain the displacement parameter of the first Wilson chain site is given the continued fraction

$$\gamma_0 = \frac{-\sqrt{\alpha}V\langle \sigma_z \rangle}{\epsilon_0 - \frac{t_0^2}{\epsilon_1 - \frac{t_1^2}{\epsilon_2 - \ddots}}} \quad (2.70)$$

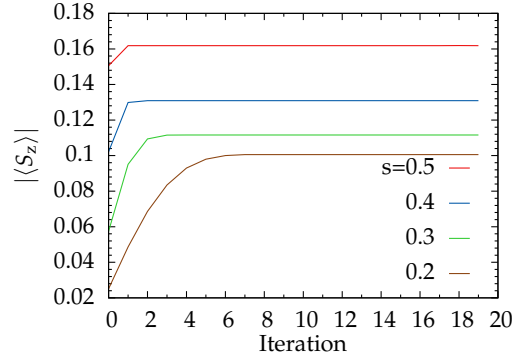


Figure 2.28: Convergence of spin-expectation value with iteration number of the self-consistency loop by which Eq. (2.71) is solved. The parameters are $N_b = 8$, $N_s = 32$, $\alpha = \alpha_c(s)$, $\Delta = 0.1\omega_c$, $\epsilon = 0.0003\omega_c$, $N = 40$, and $\Lambda = 2$.

and the other displacement parameters can be calculated recursively

$$\gamma_i = -\gamma_{i-1} \frac{t_{i-1}^2}{\epsilon_i - \frac{t_i^2}{\epsilon_{i+1} - \frac{t_{i+1}^2}{\ddots}}} \quad 1 \leq i < N. \quad (2.71)$$

By formally defining $t_{-1}^2 = \sqrt{\alpha}V$ and $\gamma_{-1} = \langle \sigma_z \rangle$ one could use the second equation for $n = 0$ as well.

Since the operator σ_z is replaced by its expectation value one has to find a self-consistent solution for these equations. This solution then fixes the displacement parameters γ_i . To determine these the following self-consistency loop is iterated.

The aim of optimizing the basis is to minimize the expectation values of the displacement operators in the displaced basis. Using this optimal basis, defined by the parameters γ_i^n ,¹⁰ the DMRG run calculates the ground state of the system taking into account all quantum fluctuations. With the ground state expectation value $\langle \sigma_z \rangle$ and Eq. (2.71) new displacement parameters γ_i^{n+1} are calculated. With these the next DMRG run is performed. By the last step the self-consistency loop is closed. This procedure is iterated until convergence of $\langle \tilde{b}^\dagger + \tilde{b} \rangle$ is reached. Initially all displacement parameters are set to $\gamma_i^0 = 0$.

The expectation value $\langle S_z \rangle$ used to calculate the displacement parameters γ_i^{n+1} for the successive iteration is shown in Fig. 2.28. After a few iterations the value of $\langle S_z \rangle$ converges. The closer the expectation value at the zeroth iteration – that is with an undisplaced basis – is to the converged value the fewer iterations are necessary to reach convergence.

¹⁰ Here, the superscript n denotes the self-consistency loop iteration number.

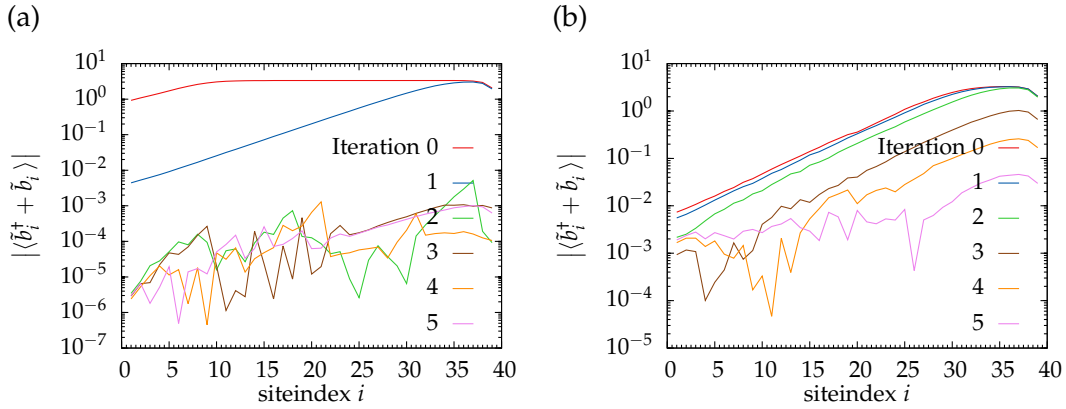


Figure 2.29: Expectation value of the site-dependent displacement operator for different iterations. The parameters are $N_b = 8$, $N_s = 32$, $s = 0.4$, $N = 40$, $\Lambda = 2$, $\alpha = \alpha_c$, $\Delta = 0.1$, and (a) $\epsilon = 0.1\omega_c$, (b) $\epsilon = 10^{-7}\omega_c$. Plotting the same data without taking absolute value would show the alternating sign of $\langle \tilde{b}_i^\dagger + b_i \rangle = (-1)^i |\langle \tilde{b}_i^\dagger + b_i \rangle|$.

The optimal basis minimizes the expectation value of the displacement operator $\langle \tilde{b}_i^\dagger + \tilde{b}_i \rangle$ at each site i of the Wilson chain. Fig. 2.29 shows the expectation values measured during the self-consistency loop iteration. At iteration number 0 the basis is not displaced. The value $\langle b_i^\dagger + b_i \rangle$ calculated exactly – that is with $N_s \rightarrow \infty$ and $N_b \rightarrow \infty$ – would be equal to the optimal values for γ_i which solve Eq. (2.68).

Due to the logarithmic discretization of the bath and the resulting exponential decrease of chain parameters, the displacement parameters γ_i are expected to grow exponentially with i . Fig. 2.29a shows that the DMRG solution of the zeroth iteration is far away from the exact solution: $\langle \tilde{b}_i^\dagger + \tilde{b}_i \rangle$ grows only exponentially for a few sites and then saturates for the same reason why the displacement expectation value of the displaced harmonic oscillator saturates (cf. Fig. 2.9): connected with a certain number of modes in the bosonic basis is the maximum occupation and this allows only a certain maximum displacement.

After the first iteration (cf. Fig. 2.29a) the basis is already better adapted to the problem and therefore it only saturates at the end of the chain; after the second iteration the basis is very well adapted to the system and the expectation value is now dominated by numerical noise. That the expectation value $\langle \tilde{b}_i^\dagger + \tilde{b}_i \rangle$ is very close to zero after a few iterations shows that the self-consistency loop iterations indeed yield the optimal results.

Fig. 2.29b shows $\langle \tilde{b}_i^\dagger + \tilde{b}_i \rangle$ in the course of the self-consistency loop iterations for $\epsilon = 10^{-7}\omega_c$. This results in a smaller value for $\langle \sigma_z \rangle$ and therefore the bosons are not displaced as strongly as for $\epsilon = 0.1\omega_c$. The saturation of $\langle \tilde{b}_i^\dagger + \tilde{b}_i \rangle$ is now only visible at the end of the chain and decreases after a few iterations. No saturation at the maximum value means that the basis is capable of faithfully describing the state.

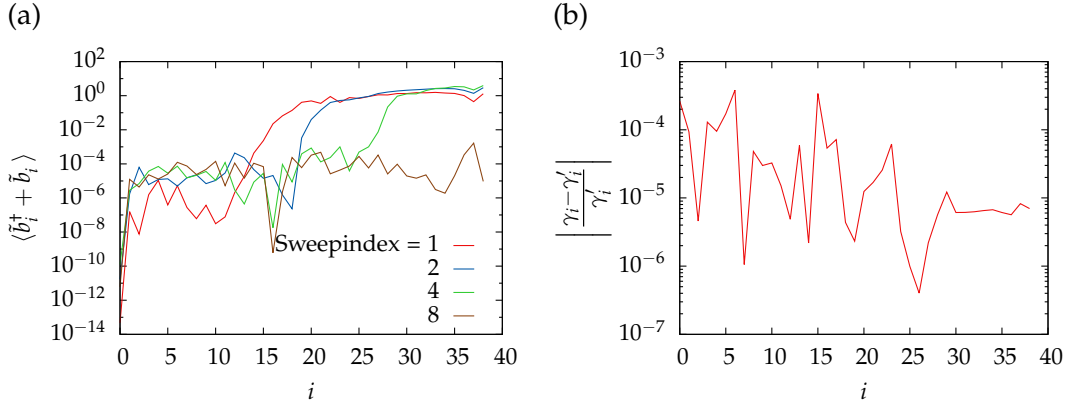


Figure 2.30: (a) Expectation value of site-dependent displacement operator in displaced basis after different number of sweeps. (b) Relative difference between variationally determined parameters γ_i and γ'_i calculated from Eq. (2.68). For both plots the parameters $s = 0.5, N = 40, \Lambda = 2, \epsilon = 0.01\omega_c, \Delta = 0.1, N_s = 32, N_b = 8$, and $\alpha = \alpha_c$ are used.

So far, the optimal basis is determined iteratively by tuning the displacement parameters depending on $\langle S_z \rangle$. After a few iterations the self-consistent Eq. (2.68) is fulfilled. Now we want to show that if one has found a basis with displacement parameters γ_i in which all $\langle \tilde{b}_i^\dagger + \tilde{b}_i \rangle$ are minimized, solving Eq. (2.68) reproduces γ_i .

The first step is to find a basis minimizing the displacement expectation values at each site. To this end, at each DMRG sweeping step after optimizing the local block the displacement parameters of both sites of the local block are set to $\gamma_i = \frac{1}{2} \langle \tilde{b}_i^\dagger + \tilde{b}_i \rangle$. Fig. 2.30a shows, that after a few DMRG sweeps this procedure minimizes the displacement expectation values of all chain sites evaluated in the new basis.

The next step is to calculate $\langle \sigma_z \rangle$ with this variationally optimized basis and use Eq. (2.68) to calculate the displacement parameters γ'_i . In Fig. 2.30b the displacement parameters γ_i which are variationally determined in the DMRG run are compared with those parameters γ'_i Eq. (2.68) yields. Fig. 2.30b shows that these are up to numerical accuracy equal. Hence, the proposed method to determine the optimal displacement parameters yields results consistent with variationally optimizing the basis.

In this section we have proposed an iterative method optimizing the displacement parameters of the bosonic basis. This procedure yields the same results as variationally optimizing these parameters in the DMRG sweeping phase. However, as we have found an analytic set of equations we have gained a deeper insight in the cause of the bosonic displacements. Unlike the variationally method we realize that the exponential growth of the displacement parameters is due to the chain parameters. Furthermore, our equations show that all chain parameters have an influence on the displacement of each Wilson chain site. Hence, the optimal displacement parameters explicitly depend on the chain length. This is a conclusive hint that for the simulation of bosonic systems employing a Wilson chain the effect of the rest-chain is vitally important.

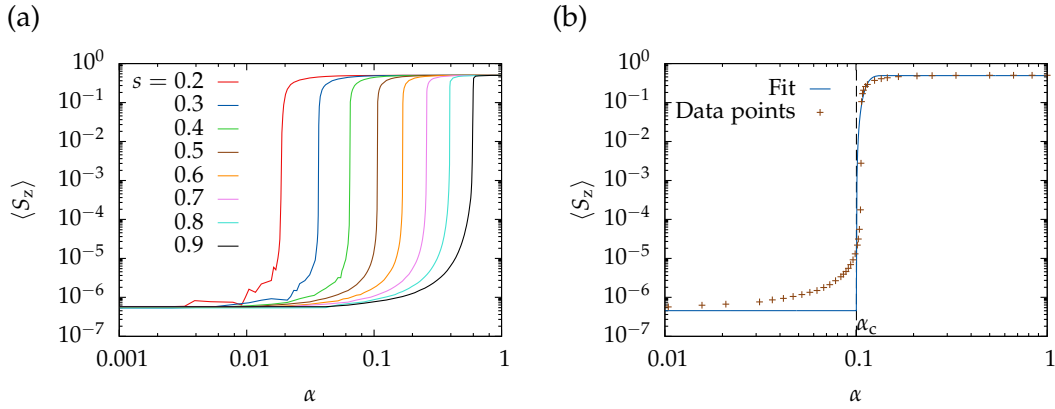


Figure 2.31: (a) DMRG calculations of the $\langle S_z \rangle$ for different α and s . (b) Determination of α_c for $s = 0.5$. The fit-function is given in Eq. (2.72). The parameters for both plots are $\Lambda = 2$, $N = 40$, $N_s = 24$, $N_b = 8$, $\Delta = 0.1\omega_c$, and $\epsilon = 10^{-7}\omega_c$. Three iterations to optimize the bosonic basis are carried out.

2.5.3 Phase diagram

In order to calculate critical exponents for the SBM we need to calculate the numeric value of the critical coupling α_c . This is achieved in two steps: first we perform an α scan (cf. Fig. 2.31) to roughly determine the position of the phase transition.¹¹ Afterwards an α scan with a smaller step size for different values of ϵ is carried out.

In the delocalized phase the expectation value $\langle S_z \rangle$ vanishes, and it is finite in the localized phase. This transition occurs rapidly and $\langle S_z \rangle$ shows a steep increase at the phase border (cf. Fig. 2.31). The critical coupling is the α value at which this increase occurs. Numerically this point is found by a first rough α scan and subsequently calculating more data points at the steep increase (cf. Fig. 2.31b). To determine the critical value the best fit of the function

$$f(\alpha) = \begin{cases} (d_0 - d_1) \exp\left(-\frac{(\alpha - \alpha_c)^2}{a^2}\right) + d_1 & \alpha > \alpha_c \\ d_0 & \alpha \leq \alpha_c \end{cases} \quad (2.72)$$

to the data points is calculated. The free fitting parameters are α_c and a ; d_0 and d_1 are the calculated data points for $\alpha = 0$ and $\alpha = 1$ respectively.

However, this way to determine α_c does not yield the desired precision and therefore is only a first estimate. The critical coupling strength is then determined by conducting an ϵ scan. One expects $\langle S_z \rangle \propto |\epsilon|^{\frac{1}{\delta}}$ for $\alpha = \alpha_c$ and thus for $\alpha = \alpha_c$ the curve of $\langle S_z \rangle(\epsilon)$ is a straight line in a log-log plot. By varying α in small steps – the smallest step size is $\delta\alpha = 10^{-7} - \alpha_c$ is defined as the value at which $\langle S_z \rangle(\epsilon)$ is as close as possible to a straight line on a log-log scale.

¹¹ As discussed in Sec. 2.4.3 one actually observes a cross-over here. Nevertheless, we continue calling it a phase transition.

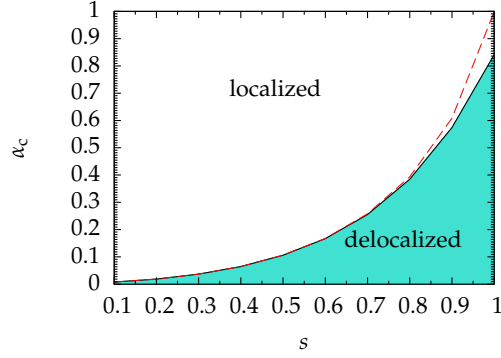


Figure 2.32: With DMRG calculated phase diagram of the SBM. The same parameters as in Fig. 2.27 are used. The dashed line indicates the NRG results from Fig. 2.22a.

The phase diagram determined in this fashion is shown in Fig. 2.32. There is a good agreement with the values determined by NRG calculations.

2.5.4 Critical exponents

Besides the critical coupling it is as well interesting how the system approaches the critical point. This is described by the critical exponents of observables such as the order parameter, in this case the local magnetization $M_{\text{loc}}(\Delta, \epsilon, \alpha) = \langle S_z \rangle = \frac{1}{2} \langle \sigma_z \rangle$. Two critical exponents, δ (cf. Eq. (2.7)) and β (cf. Eq. (2.8)), are defined

$$|\langle S_z \rangle| \propto |\epsilon|^{\frac{1}{\delta}} \quad \text{for } \alpha = \alpha_c \quad (2.73)$$

$$\text{and } |\langle S_z \rangle| \propto (\alpha - \alpha_c)^\beta \quad \text{for } \alpha > \alpha_c \text{ and } \epsilon = 0. \quad (2.74)$$

The mean-field exponents for $s \leq \frac{1}{2}$ are $\delta = 3$ and $\beta = \frac{1}{2}$. Since the DMRG targets only the ground state, a critical exponent describing the temperature dependent approach to the critical point, e.g. for the susceptibility $\chi \propto T^{-x}$, is not accessible.

The fits determining δ and β are shown in Appendix B (Fig. B.2 and Fig. B.1 respectively). The results of the fits are presented in Fig. 2.33: this figure shows that, with the DMRG calculations, for $s \leq \frac{1}{2}$ the mean-field exponents, $\delta = 3$ and $\beta = \frac{1}{2}$, are recaptured. This is the central result of this section: by taking the rest-chain into account and employing an optimized bosonic basis one gets the correct mean-field exponents. For these calculations several (up to 19) iterations to optimize the bosonic basis are carried out: the process is iterated until the results converge.

We want to emphasize that our methods do not bias the results in any direction: there are no *a priori* assumptions of the optimal displacement parameters and as the DMRG determines the ground state variationally in the whole Hilbert space there is no *a priori* selection of possible ground states.

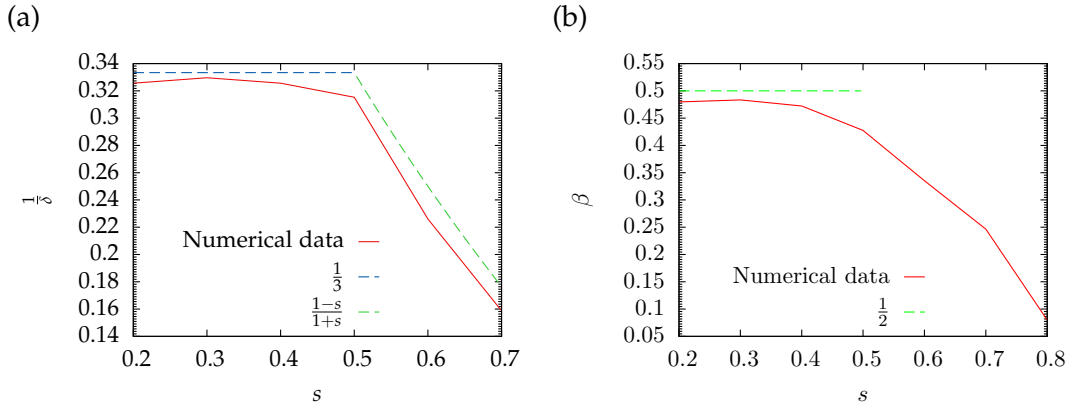


Figure 2.33: Critical exponents of the sub-ohmic SBM. The dashed lines indicate the mean-field expectation. (a) Magnetization exponent $\frac{1}{\delta}$. (b) Order parameter exponent β . The determination of both critical exponents by fitting a power-law function to the data points are shown in Fig. B.1 and Fig. B.2.

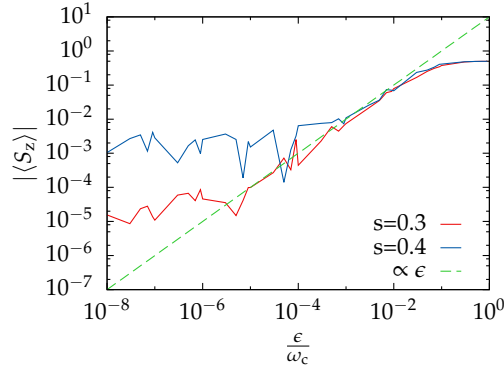


Figure 2.34: ϵ scan for $\alpha = \alpha_c$ without DMRG sweeps. At the warm-up phase $N_s = 40$ states are kept. Four iterations to improve the bosonic basis are performed. The dashed line is a guide to the eye.

2.5.5 Without DMRG sweeping

The source of the mass-flow error in the NRG is the neglect of the rest-chain. The DMRG does not suffer from this error, as in the sweeping phase the whole chain is taken into account. To simulate the effect of not taking the whole chain into account Fig. 2.34 shows DMRG results calculated without sweeping.

In this case one does not get mean-field critical exponents. Thus it is vital for bosonic systems to take into account all effects of the rest-chain. However, one cannot directly compare the DMRG results shown in Fig. 2.34 with the NRG results shown in Fig. 2.23, as both methods neglect different parts of the rest-chain: the NRG neglects all sites $i > N$, with N being the current iteration, whereas the DMRG builds up a chain of length L by inserting sites in the center. Therefore at iteration N the DMRG neglects the sites $i \in [N, L - N]$.

2.5.6 Numerical errors

The DMRG suffers from two major error sources: (i) the precision of the Lanczos method to calculate the ground state and (ii) the truncation of the Hilbert space.

When optimizing the local matrix product state (MPS) block the Lanczos method is used to iteratively calculate the ground state. The iterations are stopped when the ground state has converged. The convergence criterion is that the relative change of the ground-state energy between two iterations is less than 10^{-8} . Thus we do not expect the DMRG calculations to be more precise than this value.

After the optimization of the local block eigenstates of the density matrix are truncated. As the sum of all eigenvalues ρ_i of the density-matrix is one, the sum of all truncated eigenvalues is a measure for the truncation error, Eq. (1.91). When keeping $N_s = 24$ states the maximum truncation error during the final sweep for the presented calculations ranges from $\epsilon \sim 10^{-11}$ to $\epsilon \sim 10^{-8}$.

However, the truncation error and the Lanczos precision just give a lower limit for the error we expect for the observables. Both errors occur when optimizing the local block. Therefore these errors occur at each site of the chain. Furthermore it is not clear how both errors interact. An error estimate relying on the numerical data is to measure how the ground-state energy changes with an increasing number of states. Without numerical errors one expects that in this case the relative ground-state energy difference between two calculations with N_s and $N_s + \delta N_s$ states shrinks continuously and finally approaches zero for $N_s \rightarrow (N_b^N + 2)$; here, N is the number of Wilson chain sites and N_b the dimension of the local Hilbert space at each chain site. However, Fig. 2.27 shows that relative ground-state energy difference saturates at $\mathcal{O}(10^{-6})$. Hence, this value is a lower limit for the numerical precision.

A further – and indeed the most reliable – test is to measure $\langle S_z \rangle$. Deep in the delocalized phase one expects this value to vanish for $\epsilon = 0$. Observed are values $\langle S_z \rangle \sim \mathcal{O}(10^{-8})$. In the localized phase $\langle S_z \rangle = \frac{1}{2}$ is expected and $\frac{1}{2} - |\langle S_z \rangle| \sim \mathcal{O}(10^{-6})$ is found.¹² The maximum error of the DMRG calculations is therefore estimated to be 10^{-6} . This is consistent with the data shown in Fig. B.2: if $\frac{\epsilon}{\omega_c}$ is below the numerical resolution of the DMRG setup one observes the emergence of fluctuations.

Like in the NRG calculations the main error of the critical exponents δ and β is due to the fitting-error. The fits for both critical exponents yield errors in the range 0.5%–2.5%. This is the same relative difference by which the numerical found critical exponents and those found by the quantum-to-classical mapping deviate in Fig. 2.33. As the analytic values lie within the margin of error of the DMRG values we are confident that we reproduce the expected critical exponents with our DMRG calculations.

¹² In the localized phase the $|\uparrow\rangle$ and $|\downarrow\rangle$ states are degenerate for $\epsilon = 0$. Here fluctuations of the initial random guess wavefunction determine if the $|\uparrow\rangle$ or $|\downarrow\rangle$ state is the DMRG ground state. To avoid this random selection in the DMRG calculations a small field $\epsilon = 10^{-7}\omega_c$ is present.

2.6 Summary

This chapter dealt with different toy models to investigate the effect of truncation of bosonic states. We showed that the results depend on the selection of bosonic states. Furthermore, we showed the presence of the mass-flow effect in the dissipative harmonic oscillator (DHO) and explained this effect by a shift in the real part of the bosonic self-energy. This effect is also present in the spin-boson model (SBM) and can be cured by taking the effects of the rest-chain into account.

It was shown that the quantum-to-classical mapping does not fail for $s \leq \frac{1}{2}$ by extracting mean-field critical exponents from the density-matrix renormalization group (DMRG) data. There are two advantages of the DMRG over the numerical renormalization group (NRG) for this model:

(i) The DMRG sweeping process explicitly takes into account the effect of the whole chain. The NRG neglects at each iteration the rest-chain. This leads to a temperature dependent renormalization of model parameters – the so-called mass-flow effect – through which the NRG targets the wrong subspace.

(ii) For the DMRG an optimal way to construct the bosonic basis was proposed. This optimization relies on the displacement of the bosonic modes and fails for the NRG, because the displacement parameter of a given site depends on the rest-chain. Hence, if one would employ this iterative optimization scheme for the NRG the displacement parameters would only be optimal for the last iteration. This, again, leads to a targeting of the wrong subspace.

In contrast to the optimal basis proposed in Ref. 128, our approach only needs a single observable, $\langle S_z \rangle$, to calculate all displacement parameters. The procedure of Ref. 128 relies on optimizing the basis at each sweeping step and takes the displacement expectation value $\langle b_i^\dagger + b_i \rangle$ of site i as a guess for the optimal displacement at each sweeping step. Finally this leads to the optimal displacement. As our method, this method relies on an iterative improvement of the bosonic basis. However, in Ref. 128 this is reduced to a numerical optimization problem, while in our formulation physical insight is gained by identifying the underlying mechanism responsible for the displacements.

This concludes the discussion of the SBM. We have seen that there is a conceptual error in the NRG due to the neglect of the rest-chain. In the next chapters we discuss a different effect which comes along with the neglect of the rest-chain or, in other words, with the neglect of part of the bath: in the time-dependent numerical renormalization group (TD-NRG) one observes unphysical features in time-dependent expectation values which are due to the truncation of the bath.

Discretization Artifacts in the Resonant-Level Model

Gaining insight in the nonequilibrium dynamics of strongly correlated condensed matter systems poses a great challenge. The interest in such systems is on the one hand driven by the fundamental question of the interplay between coherent single particle dynamics with environmental induced decoherence; and, on the other hand, recent experiments with ultracold atomic gases [14, 8] and quantum dots (QDs) [20, 145, 146] succeeded in developing and probing such systems. Furthermore, new time scales might emerge not present in equilibrium.

One class of quantum systems suitable for studying nonequilibrium physics are ultracold atomic gases in optical lattices [8]. These systems allow the simulation of the dynamics of a many-body Hamiltonian under precisely tunable conditions. A recent example is the simulation of the one dimensional Bose-Hubbard model with both an ultracold gas in an optical lattice and the time-dependent density-matrix renormalization group (TD-DMRG) [14]. Here, the system is prepared in a state with every even site occupied and every odd site unoccupied. Starting at $t = 0$ the state is evolved with the Bose-Hubbard Hamiltonian for a time t after which some observables are measured. The measured values of the TD-DMRG simulation and the experimental data agree very well. However, the reachable time scales of the experiment exceed those of the TD-DMRG considerably rendering this setup a demonstration of a dynamical quantum simulator.

Another prominent example of highly controllable nonequilibrium quantum systems which were recently experimentally realized are QDs with a time-dependent gate voltage [16, 17]. The setup of Elzerman *et al.* consists of a semiconductor QD in an external magnetic field coupled to a bath [20]. The external magnetic field splits the up- and down-spin levels of the QD by the Zeeman energy. By manipulating the gate voltage it is possible to change the energy of the two levels relative to the Fermi energy. The objective of this experiment is to measure the direction and relaxation rate of the spin of an electron which tunnels out of a reservoir onto the QD.

One can control the tunneling process of electrons from the bath to the QD by manipulating the gate voltage. Initially, the gate voltage is set to a value such that both levels are above the Fermi energy thereby emptying the QD. Then the gate voltage is increased, lowering both states below the Fermi energy and allowing one electron with unknown spin to tunnel on the QD; this process happens on the time scale $\frac{1}{\Gamma}$. Double occupancy of the dot is prevented by operating in the Coulomb blockade regime.

Now that the dot is filled with one electron the gate voltage is tuned to such a value that the Fermi energy lies in the gap between the spin-up and spin-down states. For the spin-up state it is energetically favorable and for the spin-down state energetically unfavorable to be occupied. Hence, if the QD is occupied by a spin-up electron the state does not change. However, if the QD is occupied by a spin-down electron this electron hops back into the bath and, subsequently, a spin-up electron hops onto the QD. Therefore, one can distinguish both initial states by detecting the hopping process. The measurement of the current at a quantum point contact shows different signatures whether a hopping process occurs or not and thereby allows the distinction if the QD is initially occupied by a spin-up or spin-down electron. Furthermore, by varying the delay time between the filling of the quantum dot and the shift of Fermi energy in the gap between both states, this experiment allows to measure the spin-relaxation rate of the spin-down state.

Petta *et al.* demonstrated in Ref. 145 that it is possible to create a qubit with two QDs. Here, again, the key ingredient of the preparation and manipulation of the qubit state is the control of the gate voltages and the read-out relies on spin-to-charge conversion. In a more advanced setup it was shown that one can realize a qubit with three QDs [146].

In our treatment the QD is modeled using the interacting resonant-level model (IRLM) [23, 147]. This model accounts for a gate voltage, a hopping term between the dot and the lead, and a Coulomb interaction between the dot electron and the lead electrons. Thus, it is used to describe a single QD coupled to a single lead. The model can be generalized to the case of more than one lead [148]. However, in this work we are mainly concerned with presenting a numerical method suited for treating such models and we therefore restrict ourselves to the simplest case of just one lead.

When the IRLM was first proposed by Vigman and Finkel'shtein in 1978 [147] and by Schlottmann in 1980 [23] the interest was mainly driven by the desire to deepen the understanding of Kondo physics: indeed, Ref. 23 shows a mapping of the IRLM to the anisotropic Kondo model. The advent of fabrication techniques for nanodevices lead to experiments showing that the Kondo effect can be detected in QDs as well [25, 26]. Hence, it is not surprising that the IRLM is not just a model which appears in the context of Kondo physics but which is also a model for a QD dominated by charge fluctuations.

3.1 Objective of the studies

We are interested in the nonequilibrium dynamics of the IRLM. In preliminary studies we show that employing the standard time-dependent numerical renormalization group (TD-NRG) [76, 77] one observes artifacts due to the discretization of the continuous conduction band. We investigate the role these artifacts play in TD-NRG simulations and how to reduce these. Unlike other approaches dealing with discretization artifacts for numerical renormalization group (NRG) calculations [33, 34, 83, 149, 150] we do not stick to a Wilson chain [28] but explore the use of different types of chains.

This chapter and the following relate to each other. In this chapter we examine the non-interacting resonant-level model (RLM) in nonequilibrium: a single fermionic level is coupled to a conduction band and the level energy is suddenly switched from E_i to E_f at time $t = 0$. This model is exactly solvable for both a continuous conduction band and a discretized band mapped to a Wilson chain. This allows to quantify artifacts due to the discretization of the continuous conduction band. These artifacts are present in all TD-NRG simulations.

The artifacts are caused by the limited energy resolution with which the conduction band is sampled. In a nonequilibrium impurity system coupled to a Wilson chain the discretization artifacts manifest as reflections of a charge wave within or at the end of the Wilson chain. To minimize discretization errors we investigate different ways of the discretization of the conduction band by proposing the use of hybrid chains. For the first time, we explore the use of a special hybrid chain, the so-called double Wilson chain (DWC), instead of a Wilson chain. A DWC consists of two Wilson chains with different discretization parameters patched together. We find that this construction is the most advantageous as it not only minimizes the discretization errors but it also allows to simulate the system on longer time scales as compared to a pure Wilson chain.

When discretizing the continuous conduction band one has to make sure that the discretized version of the band is a good representation of the continuous band. We show that one recovers with the DWC the results for the continuous model on arbitrary long time scales. For practical calculations, this is not possible with a Wilson chain. A Wilson chain yielding results comparable to the continuous solution or a DWC needs a discretization parameter Λ very close to one and, consequently, the number of chain sites increases exponentially. In an NRG run, this would lead to a number of kept states out of reach for modern computer systems.

Hence, it is unfeasible to solve hybrid chains with the TD-NRG. Therefore we propose in Chapter 4 a new hybrid method combining the advantages of the TD-NRG and the TD-DMRG. This method employs an NRG run by which an effective low-energy Hamiltonian is constructed. Diagonalized this Hamiltonian forms the so-called hyper-impurity. One then employs a second method to simulate the time evolution of

a system consisting of this hyper-impurity coupled to a second chain. In our case this second method is the TD-DMRG, but one could use other methods like the Chebyshev expansion technique (CET) [90] as well.

The new method bipartitions the Hamiltonian in a high- and low-energy sector. Only the high-energy sector is treated with the NRG. For the low-energy sector the TD-DMRG is employed: this method simulates a system with an effective bandwidth some orders of magnitudes below the bandwidth of the original system. The requirement of the TD-DMRG for a Trotter timestep at least one order of magnitude below the inverse bandwidth renders the TD-DMRG inefficient for systems with a large bandwidth. Therefore, in the wideband-limit the original system is not solvable with the TD-DMRG on its own. Besides presenting the new method, Chapter 4 also benchmarks this method on basis of the RLM. Here one finds an excellent agreement between the new method and exact results.

Finally, in Chapter 5 we turn to the IRLM. After discussing the model in more detail, time-dependent expectation values are calculated using the new hybrid method. We discover that in the impurity occupation number oscillations develop with characteristics determined by the interaction strength. These oscillations are explained in a strong coupling treatment of the model: in the strong coupling limit the new method yields results agreeing with the analytic predictions. However, for intermediate values of the coupling strength no analytic results are available but as our method works in the whole parameter regime we obtain reliable results for this regime as well.

3.2 Resonant-level model

In this section we examine the RLM. This model serves as effective low energy model for the strong coupling fixed point of the single impurity Anderson model (SIAM) [3]. One of the first experimental relevant applications of the RLM is the fitting of a theoretical model to the experimental data of the magnetization curve of AgFe [151]. For the RLM the current through the impurity for a resonant-level coupled to two lead [152] can be calculated exactly. Furthermore, with a similar purpose as in this work, the RLM is used in Ref. 95 to benchmark the accuracy of the TD-DMRG with time-dependent Hamiltonians.

However, in this section we are mainly interested in the RLM as it is exactly solvable and thus allows us to (i) detect errors due to the discretization of the conduction band, which is necessary to treat the RLM with the NRG; and it allows us (ii) to compare the results of numerical methods with the exact results in order to quantify numerical errors.

3.2.1 Model Hamiltonians

The RLM describes one single fermionic level coupled to a bath of fermions, which in the following are considered to be spinless. The Hamiltonian is given by

$$H(t) = E_d(t)d^\dagger d + \frac{V}{\sqrt{N_I}} \sum_k \left(d^\dagger f_k + f_k^\dagger d \right) + \sum_k \epsilon_k f_k^\dagger f_k. \quad (3.1)$$

The operators d^\dagger and d create and annihilate a fermion on the local level, while the operators f_k^\dagger and f_k create and annihilate a fermion in momentum state k of the bath. The time-dependent energy of the local level is $E_d(t)$, V is the hybridization, and ϵ_k the dispersion of the bath. These parameters depend on the hybridization function which defines the effect of the bath on the impurity. The number of k -modes is given by N_I .

In the present formulation the impurity couples to all modes of a continuous bath. For NRG calculations one has to discretize the bath. After mapping the discretized bath to a Wilson chain of length N the Hamiltonian reads for a symmetric hybridization function

$$H_N(t) = E_d(t)d^\dagger d + V \left(d^\dagger c_0 + c_0^\dagger d \right) + \sum_{n=0}^{N-2} t_n \left(c_n^\dagger c_{n+1} + c_{n+1}^\dagger c_n \right). \quad (3.2)$$

The operator c_n^\dagger (c_n) creates (annihilates) a spinless fermion on the Wilson chain site n . The hybridization V is defined in Eq. (1.41) and the hopping parameters t_n for a constant hybridization function with support in the interval $[-D, D]$ are given by Eq. (1.39).

In the following two sections exact expressions for the impurity occupation number expectation value $\langle n_d \rangle = \langle d^\dagger d \rangle$ are derived for the continuous bath and the discretized bath, in order to compare the continuum results with the results for the Wilson chain.

3.2.2 Green's function solution for the continuous model

In this section the expectation value of the occupation of the local level $\langle n_d \rangle$ is calculated exactly in the wide-band limit. As the energy of the local level is time-dependent this expectation value is in general time dependent as well, $\langle n_d \rangle_{E(t)}(t)$. However, before allowing time-dependence we calculate the equilibrium occupation $\langle n_d \rangle$ with $E_d(t) \equiv E_d$.

Using an equation-of-motion ansatz one can calculate the equilibrium Green's function of the local level

$$\ll d | d^\dagger \gg (z) = \frac{1}{z - E_d - \Sigma(z)} \quad (3.3)$$

$$\text{with the self-energy } \Sigma(z) = \sum_k \frac{|V|^2}{z - \epsilon_k}. \quad (3.4)$$

For $V = 0$ these equations yield the Green's function of a free level with a δ -like spectral function peaked at E_d : the lifetime of a single level is infinitely long. When turning on the hybridization term the spectral function is broadened and the lifetime takes a finite value.

In the remaining chapters we assume a constant density of states (DOS) for the bath,

$$\rho(\omega) = \sum_k \delta(\omega - \epsilon_k) = \begin{cases} \frac{1}{2D} & |\omega| \leq D \\ 0 & |\omega| > D \end{cases}, \quad (3.5)$$

where $2D$ is the bandwidth. The imaginary part of the self-energy $\Sigma(z)$ is connected to the DOS by

$$\lim_{\delta \rightarrow 0} \text{Im} \Sigma(\omega + i\delta) = -\pi V^2 \rho(\omega) =: \Sigma_i(\omega) \quad (3.6)$$

and the real part for this DOS is obtained by the Kramers-Kronig relations and reads

$$\text{Re} \Sigma(\omega) = \frac{-V^2}{2D} \ln \left| \frac{\omega - D}{\omega + D} \right| =: \Sigma_r(\omega). \quad (3.7)$$

The spectral function of the local level is given by

$$A(\omega) = -\frac{1}{\pi} \lim_{\delta \rightarrow 0} \text{Im} \ll d | d^\dagger \gg (\omega + i\delta) \quad (3.8)$$

$$= \frac{1}{\pi} \lim_{\delta \rightarrow 0} \frac{\delta - \Sigma_i(\omega)}{(\omega - E_d - \Sigma_r(\omega))^2 + (\delta - \Sigma_i(\omega))^2}. \quad (3.9)$$

In the wide-band limit one can neglect the real part and obtains a Lorentzian

$$A(\omega) = \frac{\frac{V^2}{2D}}{(\omega - E_d)^2 + \left(\frac{\pi V^2}{2D}\right)^2}. \quad (3.10)$$

with width $\Gamma = \frac{\pi V^2}{2D}$ centered at the position of the impurity level, $\omega = E_d$. Since this is the same result as Eq. (1.28), the width of the local level is the same for the continuous and the discretized model. Consequently, the decay rates of a local level coupled to a discretized and a continuous bath are the same.

For $T = 0$ the equilibrium occupation of the local level is given by

$$\langle n_d \rangle = \int_{-\infty}^0 A(\omega) d\omega = \frac{1}{2} - \frac{1}{\pi} \arctan \left(\frac{E_d}{\Gamma} \right). \quad (3.11)$$

For finite temperatures one has to integrate over the whole ω -axis and insert the Fermi function into the integral similar to Eq. (3.12) below.

In Ref. 76 the result is generalized to systems out of equilibrium. Here the model parameters E_d and V are assumed to be time-dependent and by using the Keldysh technique Ref. 76 gives an analytic expression to calculate $\langle n_d \rangle_{E_i, E_f}(t)$ after a quench at $t = 0$. This expression, Eqs. (50) and (51) in [76], is used extensively in the following and reads

$$\langle n_d \rangle_{E_i, E_f}(t) = \rho_F \int_{-\infty}^{\infty} f_\beta(\epsilon) |K_{E_i, E_f}(\epsilon, t)|^2 d\epsilon \quad (3.12)$$

$$\text{with } K_{E_i, E_f}(\epsilon, t) = e^{-i\epsilon t} \frac{V}{\Gamma + i(E_f - \epsilon)} + e^{-(iE_f + \Gamma)t} \left(\frac{V}{\Gamma + i(E_i - \epsilon)} - \frac{V}{\Gamma + i(E_f - \epsilon)} \right). \quad (3.13)$$

With $\langle n_d \rangle_{E_i, E_f}(t)$ we denote the time-dependent occupation number of the level for a quench from the initial value E_i to the final value E_f at $t = 0$, $E_d(t) = E_i \Theta(-t) + E_f \Theta(t)$; all other parameters are constant in time.¹ ρ_F is the DOS at the Fermi energy, in this case $\rho_F = \frac{1}{2D}$, and $f_\beta(\epsilon)$ is the Fermi function at inverse temperature $\beta = \frac{1}{T}$. For $T \neq 0$ the integral in Eq. (3.12) has to be solved numerically, whereas for $T = 0$ an analytic solution is given by Eq. (53) in [76].

After quenching the impurity energy from E_i to E_f we expect the system to evolve to the thermal state of the level being at the energy position E_f . This means, that for $t \rightarrow \infty$ the level occupation is supposed to be

$$\langle n_d \rangle_{E_i, E_f}(t \rightarrow \infty) = \langle n_d \rangle_{E_f, E_i}(t = 0). \quad (3.14)$$

To show that this is indeed the case, Eq. (3.12) is used to reformulate the condition given in Eq. (3.14)

$$\lim_{t \rightarrow \infty} |K_{E_i, E_f}(\epsilon, t)|^2 = |K_{E_f, E_i}(\epsilon, 0)|^2 \quad (3.15)$$

$$\Leftrightarrow \frac{2D}{\pi} \frac{\Gamma}{(\epsilon - E_f)^2 + \Gamma^2} = \frac{2D}{\pi} \frac{\Gamma}{(\epsilon - E_i)^2 + \Gamma^2}. \quad (3.16)$$

Hereby we have shown that after the quench the system approaches a new thermal state, which is the same state as if the system had been prepared in the state with $E_d(t) = E_i$. For $t \rightarrow \infty$ the function $|K_{E_i, E_f}(\epsilon, t \rightarrow \infty)|^2$, Eq. (3.10), is a Lorentzian of width Γ , as one expects from the discussion above. In this case $|K_{E_i, E_f}(\epsilon, t \rightarrow \infty)|^2$

¹ Note that Eqs. (50) and (51) in [76] are slightly different and are more general as they allow a quench of V as well.

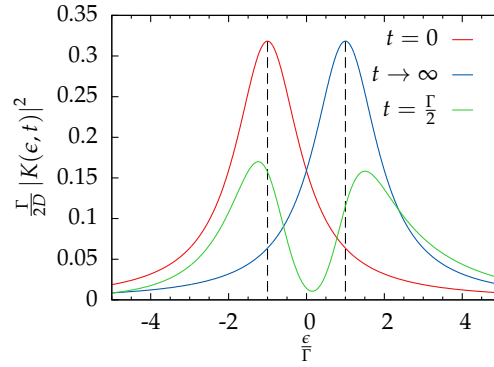


Figure 3.1: The function $|K(\epsilon, t)|^2$, where the integral kernel $K(\epsilon, t)$ is defined in Eq. (3.13), at different times. The system is quenched from $E_i = -\Gamma$ to $E_f = -\Gamma$ at $t = 0$. The dashed lines indicate the position of E_i and E_f .

coincides – up to a normalization factor – with the spectral function $A(\omega)$ of thermal state with $E_d(t) \equiv E_f$.

In Ref. 76 it is noted that the decay of the impurity occupation is governed by the two relaxation rates 2Γ and Γ . This result is deduced from an exact expression for $\langle n_d \rangle(t)$ at $T = 0$.² We want to show that this still holds for finite temperatures.

In this case the impurity occupation number is calculated by Eq. (3.12). As the Fermi function does not depend on time, the decay is due to $|K(\epsilon, t)|^2$. The function $|K(\epsilon, t)|^2$ has a peak at $\epsilon = E_i$ for $t = 0$ and for $t \rightarrow \infty$ there is one peak at $\epsilon = E_f$. At all other times it has two peaks located in the vicinity of $\epsilon = E_i$ and $\epsilon = E_f$, where the first peak shrinks in time while the other one grows (cf. Fig. 3.1). The exact positions of the two peaks for intermediate times depends on overlying oscillations. However, to measure the decay the position of the peak is not important but the value of $|K(\epsilon, t)|^2$ for $\epsilon = E_i$,

$$|K(E_i, t)|^2 = \frac{e^{-2t\Gamma} 2D (\Gamma^2 e^{2t\Gamma} + (E_f - E_i)^2)}{\pi\Gamma (\Gamma^2 + (E_f - E_i)^2)}. \quad (3.17)$$

This shows that the relaxation rate of the first peak is given by 2Γ . In the same way one can show that the built-up rate of the second peak is 2Γ as well.

For $\epsilon \notin \{E_i, E_f\}$ one observes overlying Rabi oscillations with frequency E_f . For example, for $\epsilon = 0$ one obtains

$$\begin{aligned} \frac{1}{C(0)} |K(0, t)|^2 = & e^{-2t\Gamma} (E_f - E_i)^2 + (E_i^2 + \Gamma^2) \\ & + e^{-t\Gamma} (2\Gamma \sin(tE_f) (E_f - E_i) + 2E_i \cos(tE_f) (E_f - E_i)). \end{aligned} \quad (3.18)$$

² In the following, the subscripts E_i and E_f are dropped.

An explicit expression for the factor $C(0)$ is given below in Eq. (3.19).

Eq. (3.18) shows that the Rabi-type oscillations with frequency E_f decay with the relaxation rate Γ . For $\epsilon \notin \{E_i, E_f, 0\}$ one obtains an expression similar to Eq. (3.18) but with additional terms $\propto \cos(\epsilon t)e^{-t\Gamma}$ and $\propto \sin(\epsilon t)e^{-t\Gamma}$ and further ϵ dependencies. These terms decay on the time scale $\frac{1}{\Gamma}$. Furthermore, for an arbitrary ϵ the factor $C(0)$ in Eq. (3.18) is replaced by

$$C(\epsilon) = \frac{2D\Gamma}{\pi \left(\Gamma^2 + (E_i - \epsilon)^2 \right) \left(\Gamma^2 + (E_f - \epsilon)^2 \right)}. \quad (3.19)$$

Hence, we can calculate the limit $|K(|\epsilon| \rightarrow \infty, t)|^2 \rightarrow 0$.

3.2.3 Exact diagonalization of the discretized model

To calculate the nonequilibrium impurity occupation expectation value $\langle n_d \rangle(t)$ for the discretized model one could approximately diagonalize the Hamiltonian Eq. (3.2) with the NRG. This induces truncation errors and when comparing $\langle n_d \rangle(t)$ for the discretized model with the continuous solution it is not clear to what extent the deviations are due to the discretization or due to the truncation.

However, as the Hamiltonian Eq. (3.2) is bilinear one can efficiently diagonalize it exactly. The derivation of an exact expression for the impurity occupation after a sudden local quench, $E_d(t) = E_i\Theta(-t) + E_f\Theta(t)$, is presented in Appendix C. The central result is that the occupation of the m th site of the chain, where $m = 0$ denotes the impurity and $m \geq 1$ denotes the Wilson chain site $m - 1$, is given by

$$\langle n_m \rangle(t) = \sum_{k=1}^{N-1} \sum_{k'=0}^{k-1} 2 \cos \left((\epsilon_k^f - \epsilon_{k'}^f) t \right) \Theta_{kk'}^m + \sum_{k=0}^{N-1} \Theta_{kk}^m. \quad (3.20)$$

The eigenvalues of the final Hamiltonian are ϵ_k^f and the matrix elements of Θ^m depend on the inverse temperature β , the site index m , the eigenvalues of the initial Hamiltonian ϵ_k^i , the eigenstates of the final Hamiltonian, and the overlap between the eigenstates of the initial and the final Hamiltonian. A formula to calculate Θ^m is given in Eq. (C.23).

Unlike the occupation of the continuous model, Eq. (3.20) does in general not approach a steady-state for $t \rightarrow \infty$. For a steady state all oscillating terms have to cancel each other out. This is trivially fulfilled for $\Theta_{kk'}^m \equiv 0$; in this case there is no time dependence, $E_d(t) \equiv E$. In other words, the initial Hamiltonian, $H^i = H(t < 0)$, and the final Hamiltonian, $H^f = H(t > 0)$, are the same, $H^i = H^f$.

If all frequencies $\omega_{kk'} = \epsilon_k^f - \epsilon_{k'}^f$ are mutually commensurable, that means $\frac{\omega_{kk'}}{\omega_{ll'}}$ is a rational number for all k, k', l , and l' , there is a time t^* at which the state returns to the initial state,

$$\langle n_m \rangle(pt^*) \equiv \langle n_m \rangle(qt^*) \quad p, q \in \mathbb{N}_0. \quad (3.21)$$

This is the opposite scenario to a thermalized state as the system does not equilibrate. However, the time scale t^* can be orders of magnitudes longer than all other relevant time scales. The maximum value is $t^* = \prod_{kk'} \frac{2\pi}{\omega_{kk'}}$.

In general, some frequencies might be close to commensurability while most others are not. This leads to small oscillations in the occupation for most times but at some points in time the almost commensurable oscillations add up to larger peaks or dips in the occupation number. Nonetheless, as not all frequencies are involved the peaks or dips do not gain the height of the initial occupation and because the frequencies are usually not strictly commensurable the peaks and dips are broadened in time. The exact behavior depends on the details of the chain and is subject to the discussion below.

3.3 Reflections within the chain

Strictly speaking, when solving the discretized RLM numerically all frequencies are commensurable, as the numerical precision is limited. This means that after the time t^* the system returns to the initial state. However, the time t^* is several orders of magnitudes larger than all relevant time scales of the system. Therefore this effect is neglected.

Relevant recurrences are due to conservation laws, the discretization of the continuous bath, and the finiteness of the system. For a quench of $E_d(t)$ the occupation of the local level changes. The operator of the total occupation $N = d^\dagger d + \sum_n^{N-1} c_n^\dagger c_n$ commutes with the Hamiltonian Eq. (3.2), $[H, N] = 0$. Hence the total charge is a conserved quantity and changing the local occupation inevitably changes the occupation of the Wilson chain sites. By shifting the local level position $E_i \rightarrow E_f$ the local occupation changes and the chain has to compensate the excess charge: a charge wave is injected into the chain and propagates through the chain, governed by the continuity equation.

The details of this propagation depend on the choice of the chain parameters. If one sets all hopping parameters to the same value which is of the order of the bandwidth one ends up with a tight-binding chain. These chains are characterized by a constant velocity of the charge wave and no internal reflections. The chain has to be sufficiently long to reach a good energy resolution of the conduction band at low-energies.

If one wants to reach this resolution with a short chain, one can opt for a Wilson chain. Here, the conduction band is sampled on a logarithmic mesh resulting in expo-

nentially decaying hopping parameters and therefore the velocity of the charge wave is decreased as it moves along the chain. This results in internal reflections, as discussed below.

To avoid internal reflections we propose the concept of hybrid chains: combining one discretization scheme for high-energies with another discretization for the low-energy sector. In practice, this results in a short Wilson chain with a large discretization parameter Λ reducing the effective bandwidth of the system rapidly over a few sites. This chain is, in turn, coupled to a second chain, with arbitrary parameters: these can be constant, exponentially decreasing, or be determined by the continued fraction expansion (CFE) [79] of the effective bath needed to restore the continuum at the last Wilson chain site.

We investigate two different hybrid chains: (i) a Wilson tight-binding hybrid chain (WTBC) and (ii) a double Wilson chain (DWC). Both chains consist of a Wilson chain coupled to a (i) tight-binding chain or (ii) a second Wilson chain with a discretization parameter very close to one. The difference between both approaches is that in a WTBC the charge wave propagates within the second chain with a constant velocity proportional to the effective bandwidth. In the DWC, however, the charge wave is slowed further down resulting in longer simulation times. Another advantage of the DWC over the WTBC is the improved energy resolution at the low-energies. The following sections examine these different kinds of chains in more detail.

3.3.1 Tight-binding chain

In this section we investigate a simple tight-binding chain $t_n \equiv D$, where $2D$ is the bandwidth. Only in this case it is possible to transport the whole excess charge, which is transferred from the impurity to the first Wilson chain site, from the first to the last chain site: if not all hopping parameters t_n are equal only a fraction of the whole charge is transported through the chain. To make this claim plausible we consider a chain consisting of three sites with the Hamiltonian

$$H = \sum_{n=0}^1 t_n (c_n^\dagger c_{n+1} + c_{n+1}^\dagger c_n). \quad (3.22)$$

At $t = 0$ the system is prepared in a state in which the total charge n_0 is located at the site $n = 0$, while the two other sites are unoccupied, $\langle c_0^\dagger c_0 \rangle = n_0$ and $\langle c_1^\dagger c_1 \rangle = \langle c_2^\dagger c_2 \rangle = 0$. For the RLM this corresponds to the state just after the quench, when the charge n_0 was transferred from the impurity to the first Wilson chain site, assuming that this

process is infinitely fast, $\Gamma \rightarrow \infty$. The time-dependent occupation numbers of the first and last site are computed to be

$$\langle c_0^\dagger c_0 \rangle(t) = n_0 \frac{\left(t_1^2 + t_0^2 \cos \left(\sqrt{t_0^2 + t_1^2} t \right) \right)^2}{\left(t_0^2 + t_1^2 \right)^2} \quad (3.23)$$

$$\langle c_2^\dagger c_2 \rangle(t) = n_0 \frac{t_1^2 t_0^2 \left(\cos \left(\sqrt{t_0^2 + t_1^2} t \right) - 1 \right)^2}{\left(t_0^2 + t_1^2 \right)^2} \quad (3.24)$$

The maximum occupation numbers are

$$\max \langle c_0^\dagger c_0 \rangle(t) = n_0 \quad (3.25)$$

$$\text{and } \max \langle c_2^\dagger c_2 \rangle(t) = n_0 \frac{4t_0^2 t_1^2}{\left(t_0^2 + t_1^2 \right)^2}. \quad (3.26)$$

Equation Eq. (3.26) has the same form as the Breit-Wigner formula, which can be used to calculate the transmission of a QD coupled to two leads [153, Sec. 5.4.3]. Here, one has to identify the hopping parameters with the transition rates to the left and right lead: $t_0^2 \propto \Gamma_R$ and $t_1^2 \propto \Gamma_L$. Hence, this toy model – consisting of three sites – yields the same functional form of the transmission coefficient as a QD coupled to two leads. One can therefore consider the central site as the QD and the right and left site as a representation of the left and right lead and calculate the current through the QD [154]. This current is maximal for a symmetric coupling to the left and the right lead, $\Gamma_L = \Gamma_R$.

From Eq. (3.26) follows that the whole charge n_0 does reach the second site if and only if $|t_0| = |t_1|$. Hence, only in a tight-binding chain the charge n_0 is transferred from the first to the last chain site. In all other cases only a fraction of the initial charge reaches the last site. In this calculation and for all following results in this chapter we set the temperature to $T = 0$.

Physically, in the RLM the charge propagates through the chain as a wave package with an initial width $\propto \frac{1}{\Gamma}$ until it reaches the end of the chain. Due to conservation of charge the wave package is reflected and moves back to the impurity (cf. Fig. 3.2a). Since for a tight-binding chain the hopping-parameters are all the same, the velocity of the wave package is constant and its form does not change while propagating through the chain as shown in Fig. 3.2b. At the first and last sites the right and left moving parts of the wave package add up to a larger occupation. Therefore, at both ends of the chain the form of the wave package is different.

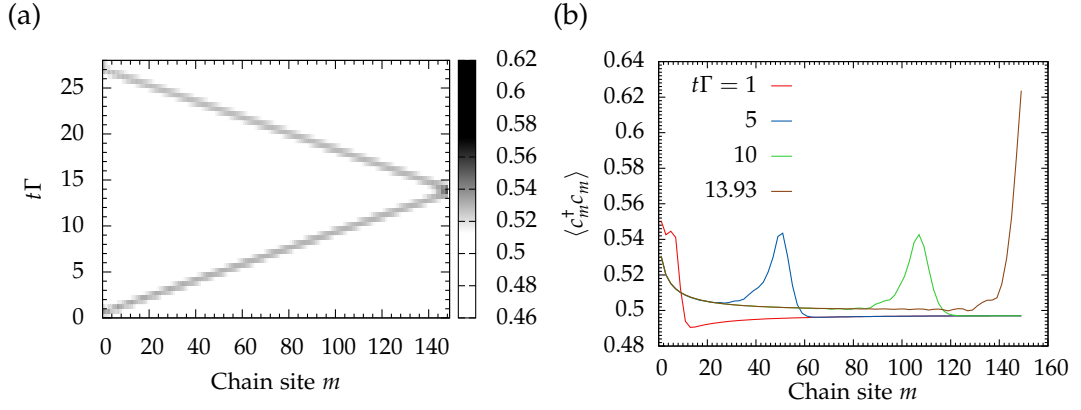


Figure 3.2: Site and time-dependent occupation of chain sites for Hamiltonian Eq. (3.2) with tight binding chain calculated with Eq. (3.20). (a) Color coded is the occupation calculated with Eq. (3.20). (b) Cuts through the left panel at certain times. Only even sites are shown. The parameters are $-E_i = E_f = \Gamma$, $D = 10\Gamma$, $T = 0$, $N = 150$, and the tight-binding hopping parameter $t_n = D$.

The maximum simulation is defined as the time, when the charge wave package reaches the impurity again for the first time. For a tight-binding chain this time scales linearly with the number of chain sites and the inverse bandwidth.

For our considerations the tight-binding chain is analogous to classical wave mechanics: imagine a waveguide with one hard end and a linear dispersion. If one injects a wave package at the other end it travels through the waveguide and is reflected at the hard end. Due to the linear dispersion the group velocity equals the phase velocity, hence all frequencies travel with the same velocity and the wave package remains form-invariant.

3.3.2 Wilson chain

For a tight-binding chain recurrences occur due to reflections at the end of the chain: because it is energetically unfavorable to deposit the charge at the last site, the charge wave reverses direction and moves back to the impurity. In this section we show that for Wilson chains reflections within the chain play the major role.

Internal reflections

Unlike for a tight-binding chain, the chain parameters t_n decrease with the site index n for a Wilson chain and Eq. (3.26) states that in this case only the fraction $\frac{4t_n^2 t_{n+1}^2}{(t_n^2 + t_{n+1}^2)^2}$ of the charge is transferred from site n to site $n + 2$. For a Wilson chain the hopping

parameters are $t_n \propto \Lambda^{-\frac{n}{2}}$ and thus the fraction ν of the charge transferred from site n to site $n + 2$ is given by

$$\nu = \frac{4}{(\Lambda + 1)^2}. \quad (3.27)$$

Of course, this equation is not strictly true for an arbitrary site within the Wilson chain, since the effect of the rest-chain is neglected, but it describes the qualitative behavior well. For $\Lambda \rightarrow 1$ one recovers the continuum limit and the Wilson chain coincides with a tight-binding chain. However, for $\Lambda > 1$ a fraction $(1 - \nu)$ of the charge is reflected within the chain and propagates back to the impurity. A small fraction of this back-moving charge can get reflected once more and thus again reverses its moving direction. In principle one has consider an infinite number of reflection processes. However, for the values of Λ considered here $\frac{4}{(\Lambda+1)^2}$ is close enough to one in order to neglect all but the first reflection in the discussion. Of course, in the numerical solution all reflection processes are present.

As shown in Appendix C, the velocity of the charge wave is proportional to the hopping parameter, Eq. (C.32), and therefore the charge wave slows down while propagating through the Wilson chain. Furthermore, it increases in amplitude and eventually enough charge accumulates at a few sites that the fraction of the charge that gets reflected becomes significant and is visible as a back-moving wave.

The round-trip time $T_m^{\text{round-trip}}$ it takes a fraction of the charge to travel from the first Wilson chain site to site m , get reflected, and travel back to the first Wilson chain site can be estimated very accurately. At the core of this estimate is an expression for the time t_{hop} it takes one fermion to hop from one to the next site. The round-trip time is twice the sum of all hopping times from the impurity to the site m . The hopping time t_{hop} is given in Eq. (C.32).

The time T_m^{trip} it takes the charge wave to arrive at site m is given by

$$\frac{1}{2} T_m^{\text{round-trip}} = T_m^{\text{trip}} = \sum_{i=0}^{m-1} t_{\text{hop}}^i = \sum_{i=0}^{m-1} \frac{\pi}{6t_i}. \quad (3.28)$$

Fig. 3.3a shows the occupation of site m versus time t . Obviously the analytic curve indicates the position of the charge wave front and therefore the analytic estimate for the wave velocity agrees well with the numerical results.

Fig. 3.3b shows that the occupation of the impurity declines on time scales of the relaxation rate Γ . For $\Lambda = 1.05$ the occupation reaches a new equilibrium value and is constant on the shown time scale. However, for larger values of Λ oscillations emerge, and thus the impurity occupation does not equilibrate. These oscillations are due to internal reflections within the Wilson chain. The fraction of the reflected charge ν shrinks for increasing Λ and for $\Lambda \rightarrow 1$ the total charge is transferred as $\nu \rightarrow 1$. This

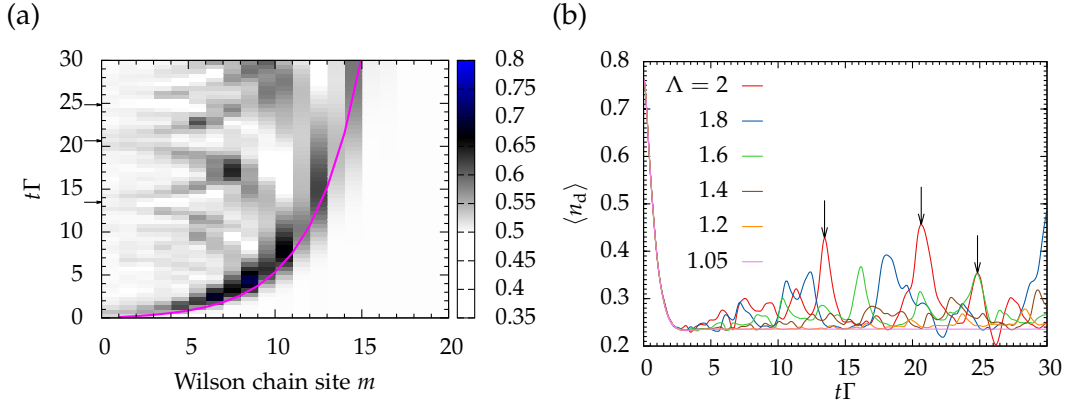


Figure 3.3: Occupation number results for the RLM calculated with Eq. (3.20). (a) The time- and site-dependent occupation $\langle c_m^\dagger c_m \rangle$ of a Wilson chain with $\Lambda = 2$ and $N = 81$ is shown color coded without impurity and only sites $m < 20$. The curve shows the propagation of the charge wave calculated with Eq. (3.28). (b) The occupation of the impurity for different values of Λ . The chain lengths are tuned according to $\Lambda^{-\frac{N}{2}} \approx 5 \cdot 10^{-13}$. The arrows in the left panel indicate, for the $\Lambda = 2$ curve, the same positions as the arrows in the right panel: the positions of the peaks of the impurity occupation number are at the same time, when the back-moving waves reach impurity. The parameters for both plots are $-E_i = E_f = \Gamma$, $D = 10\Gamma$, and $T = 0$.

means for larger values of Λ the internal reflections become more pronounced. In Fig. 3.3a the reflected wave is apparent as back-moving occupation. The points on the time-axis when it hits the impurity are indicated by arrows; the position of these arrows coincide with those points on the time-axis at which the impurity occupation is peaked, Fig. 3.3b. Hence, the dominant source of errors is due to reflections within the Wilson chain: this is a discretization artifact.

Comparing this phenomenon with classical wave mechanics, one could think of a water wave approaching the coast: as the water wave enters shallow water the water depth dependent velocity causes an increase of the amplitude due to particle conservation. This can lead to tsunamis. In analogy the charge wave propagating through the Wilson chain is sometimes referred to as *NRG tsunami* [155].

To illustrate this further Fig. 3.4 shows the occupation number of the Wilson chain sites at different times. At short times, the charge wave moving through the chain is visible as a pronounced peak gaining in amplitude as it propagates through the chain. However, eventually it reaches a site at which a significant fraction of the charge is reflected and moves back headed for the impurity, while the rest occupation of the peak continues the slowed down movement through the chain. In Fig. 3.4 the back-moving peak is indicated with an arrow pointing to the left; this portion of the charge travels back to the impurity and prevents the impurity occupation to reach thermal occupation of the final state permanently.

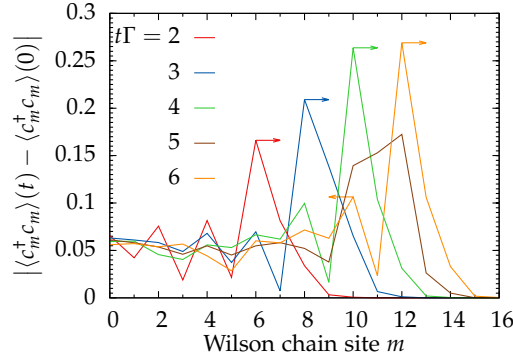


Figure 3.4: Occupation of the Wilson chain at different time steps calculated with Eq. (3.20). The arrows at the peaks indicates the direction in which the corresponding peak is moving. The parameters are $\Lambda = 1.6, N = 120, -E_i = E_f = \Gamma, T = 0$, and $D = 10\Gamma$.

Comparison between discretized and continuous model

The analytic solution for the occupation number of the impurity level $\langle n_d \rangle$, Eq. (3.11), is valid in the wide-band limit. In order to compare the impurity occupation number of the model with a discretized bath, Eq. (3.2), with the solution for the continuous bath we have to determine a value for D for which the wide-band limit is fulfilled. Therefore the equilibrium value of $\langle n_d \rangle_{E_d}$ is calculated for different level positions E_d and values of the bandwidth D (cf. Fig. 3.5). As expected, the curves for the discretized model approach the continuum solution for increasing D . To quantify this, a fit of the function

$$n(E_d) = \frac{1}{2} - \frac{1}{\pi} \arctan \left(\frac{E_d}{\Gamma_r} \right) \quad (3.29)$$

is carried out. The only free fitting parameter is Γ_r . This function has the same form as the analytic occupation in the wide-band limit Eq. (3.11), except that Γ is replaced by the renormalized value Γ_r . Hence we expect $\Gamma_r \rightarrow \Gamma$ for $D \rightarrow \infty$. Fig. 3.5b shows that this is indeed the case. Note, that the curves depend only very weakly on the discretization parameter Λ .

The relaxation rate Γ is defined as the width of the impurity spectral function. This function depends on the bath and is therefore different for a discretized and a continuous bath. To get comparable results one has to make sure that the effective relaxation rates for both models are equal. Hence, for the discretized bath the effective relaxation rate Γ_{eff} is introduced. Usually this means, that one has to tune the bare model parameter Γ in order to make sure that both models operate with the same effective relaxation rate Γ_{eff} . However, in the current setup the difference is small enough to neglect the distinction between Γ_{eff} and Γ ; instead we use $\Gamma_{\text{eff}} \equiv \Gamma$. However, in the next sections, when dealing with hybrid chains, this an issue one has to take care of.

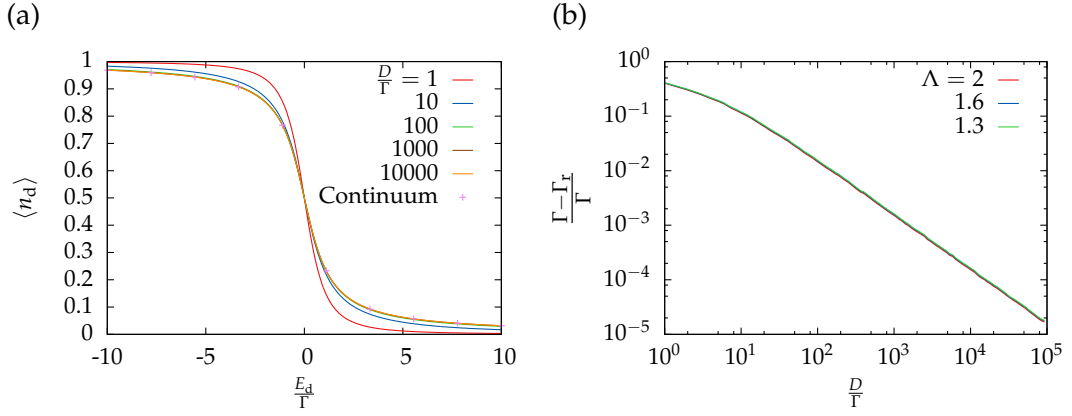


Figure 3.5: (a) Impurity occupation number for a Wilson chain with $\Lambda = 1.8$ and $N = 96$ sites in the ground state. The continuum solution is calculated with Eq. (3.11), all other curves with Eq. (3.20). (b) Γ_r determined by fitting the function Eq. (3.29) to $\langle n_d \rangle_{E_d}$ curves (left panel). The parameter N is chosen such that the energy scale of the last iteration is the same as in the left panel.

Fig. 3.6 shows the time-dependent occupation number of the impurity after a sudden local quench of the impurity level position $E_i \rightarrow E_f$ at $t = 0$. For all choices of the discretization parameter Λ and impurity level energies the discretized model yields on small time scales $\sim \Gamma_{\text{eff}}$ the same behavior as the continuous model. However, eventually charge is reflected within the Wilson chain, propagates back to the impurity (cf. Fig. 3.4), and manifests as peaks in the time-dependent impurity occupation number. These peaks are unphysical and the result of discretization artifacts which vanish for $\Lambda \rightarrow 1$.

For Λ close enough to one, it is possible to faithfully simulate the system up to a certain time. This time does not only depend on Λ but on E_i and E_f as well: the larger the difference between thermal initial and thermal final impurity occupation is the more charge the Wilson chain has to absorb. Hence the amplitude of the charge wave is higher and more charge is reflected at each Wilson chain site; significant back reflections occur earlier in the chain reducing the time scale on which one can faithfully simulate the system.

3.3.3 Hybrid chains

Generally, it is possible to simulate the RLM using a Wilson chain albeit the simulation time is limited for values of Λ which are commonly used for NRG calculations. To reach longer time scales one has to avoid the internal reflections and reflections at the end of the chain. To this end we propose the use of hybrid chains: the first part of the chain of length N_1 is a Wilson chain with discretization parameter Λ_1 ; for the second part, which consists of N_2 chain sites, one employs a different discretization scheme. This is realized by using a second Wilson chain with discretization parameter Λ_2 , a

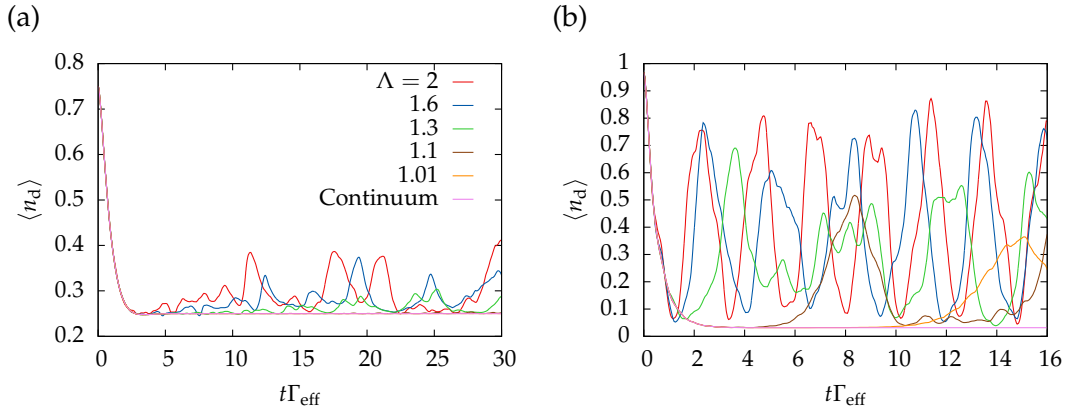


Figure 3.6: Time-dependent impurity occupation number $\langle n_d \rangle$ for different values of Λ calculated with Eq. (3.20) for $T = 0$. (a) $-E_i = E_f = \Gamma_{\text{eff}}$. The continuum curve lies almost on top of the $\Lambda = 1.01$ curve. (b) $-E_i = E_f = 10\Gamma_{\text{eff}}$. For both panels the chain length N is chosen as in Fig. 3.5.

tight-binding chain with constant hopping parameters, or even a chain with arbitrary hopping parameters.

The general goal of all hybrid chain approaches is to find a chain which is a good representation of the continuous bath with a minimum number of chain sites: we want to reproduce the continuum solution with a minimum of numerical effort. Therefore we propose three different kinds of hybrid chains, two of which we investigate further.

Employing a so-called double Wilson chain (DWC) allows one to discretize the conduction band in the low-energy sector, which is defined by the energy scale of the last Wilson chain site of the first Wilson chain, with a higher resolution. Therefore the second discretization parameter Λ_2 is closer to one than Λ_1 . The dynamical properties of the systems we are considering are determined mostly by the low-energy sector and a high energy resolution of this sector improves the results considerably.

We call the second kind of hybrid chains we investigate Wilson tight-binding hybrid chain (WTBC). Here, a tight-binding chain is coupled to the first Wilson chain. The tight-binding chain hopping parameters are given by the effective bandwidth at the last Wilson chain site. The WTBC and the DWC are equal in the limit $\Lambda_2 \rightarrow 1$.

Furthermore, we allow for the second chain to have completely arbitrary chain parameters with the requirement that the total hybrid chain is a good representation of the continuous band. Here, we propose an idea how one could determine the chain parameters of the second chain and fulfill this requirement: the parameters are calculated employing a CFE [79] of an effective bath which restores the continuum on the energy scale of the last Wilson shell.

This bath is constructed in the following manner. At each NRG iteration one selects two representative levels of the continuous bath. Thereby the spectral function of the continuous bath is different from the spectral function of the Wilson chain: in the latter

case, the spectral function consists only of δ -peaks. To recover the continuum one could couple an effective bath to the last Wilson chain site which is constructed in such a way that the spectral function of the Wilson chain including this effective bath and the spectral function of the continuous bath are the same at energy scales of and below the energy scale of the last NRG iteration. Employing a CFE one can then calculate the chain parameters needed to map such a bath to a chain with all hopping parameters being of the same order of magnitude.

The difference between the WTBC and this approach lies in the DOS of the bath the second chain describes for $N_2 \rightarrow \infty$: for a tight-binding chain the DOS is semielliptical with a bandwidth defined by the tight-binding hopping parameters. On the other hand, with the CFE one makes sure that the DOS of the second chain is optimally chosen such that the total chain recovers the DOS of the original band in the energy interval $[-t_{N_1-1}, t_{N_1-1}]$, where t_{N_1-1} is the last hopping parameter of the first Wilson chain. However, this thesis does not pursue this idea further.

Another way of adaptively discretizing the band is investigated in Ref. 62. Here the authors select some representative energy levels of the conduction band on a logarithmic mesh, just like the NRG does [28], up to some energy scale B . Below this energy scale the states are selected on a linear mesh. With this selection of states the usual Householder transformation is carried out to map this system to a chain. This results in a modified Wilson chain which the authors of Ref. 62 solve with variational matrix product states.

Wilson tight-binding hybrid chain

For a WTBC we construct a chain starting with N_1 Wilson chain sites with discretization parameter Λ_1 , which are followed by N_2 sites with constant hopping $t_{\text{TB}} = \Lambda^{-\frac{1}{2}} t_{N_1-1}$ where t_{N_1-1} is the last hopping parameter of the Wilson chain. This corresponds to a logarithmic discretization of the bath up to the energy scale t_{N_1-1} and an approximately linear discretization on lower energy scales.

A priori it is not clear how to choose N_1 and N_2 . However there are some constraints which have to be fulfilled: (i) the chain length N_1 has to be short enough so that there are no internal reflection; and (ii) N_2 has to be sufficiently long in order to reach the needed energy resolution of the bath. The larger N_1 is, the smaller N_2 needs to be to get a sufficient energy resolution. With the tight-binding chain one has to sample the energy interval $[-\Lambda^{-\frac{1}{2}} t_{N_1-1}, \Lambda^{-\frac{1}{2}} t_{N_1-1}]$ of the conduction band. When doing this on a linear mesh one needs more points than on a logarithmic mesh and hence it is advisable to use the logarithmic discretization to get to low energy scales. Therefore, the goal is to maximize N_1 without getting reflections and thereby minimizing the total chain length $N_1 + N_2$.

Finally, (iii) N_2 has to be sufficiently long to avoid reflections at the end of the chain on the time scales one is interested in. For decreasing N_1 the hopping parameter of the

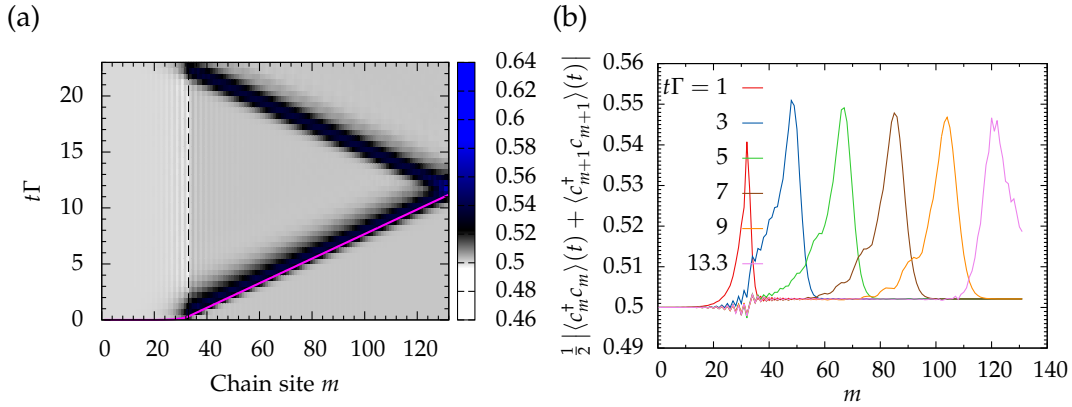


Figure 3.7: Hybrid chain consisting of $N_1 = 34$ Wilson chain sites with $\Lambda = 1.8$ and $N_2 = 100$ tight-binding chain sites. Results are calculated with Eq. (3.20). The parameters are $-E_i = E_f = -\Gamma$, $D = 10^5 \Gamma$, and $T = 0$. (a) Time- and site- dependent occupation number. The full line indicates the position of the wave-front calculated with Eq. (3.28) while the vertical dashed line indicates the position of N_1 . (b) Occupation number of chain sites m (averaged over two sites) at different time steps: without the average this would be horizontal cuts through the left panel.

tight-binding chain t_{TB} increases and hence the velocity of the charge wave increases as well. This results in an increased chain length N_2 for decreasing N_1 if one wants to hold the time at which the charge wave is reflected at the end of the chain constant.

However, so far we have no good estimate how to guess the optimal N_1 . It depends on E_i , E_f , and Γ : the more charge is deposited in the chain the smaller one has to choose N_1 ; and the faster the charge is transferred into the chain, the lower is the index of the site at which reflections occur and hence the smaller one has to choose N_1 .

The length of the first Wilson chain N_1 should be chosen such that the last Wilson chain hopping parameter t_{N_1-1} is comparable to the hybridization, $t_{N_1-1} \approx V$. As long as the transfer velocity $\sim t_n$ fulfills $t_n > V$, the amount of charge x can be transferred from site n to site $n + 1$ in one time unit. However, for $t_n < V$ it is not possible to transfer the charge x in one time unit completely from site n to site $n + 1$. Hence, more charge flows from the site $n - 1$ to n than from site n to $n + 1$. Therefore charge accumulates at site n and is partly reflected.

However, this argument is incomplete as it does not take quantum mechanical effects into account; it treats the hopping from site n to site $n + 1$ as a classical hopping process with rate the t_n . Quantum mechanical one has to consider both, transmission and reflection even if $t_n > V$.³

Fig. 3.7a shows the time- and site-dependent occupation of a WTBC following a quench. After the charge waves reaches the site N_1 it propagates with constant velocity until it reaches the end of the chain as seen in Fig. 3.7a. The form of the wave pack-

³ This is analog to a quantum mechanical particle scattering at a potential barrier: even if the energy of the particle is larger than the potential height a fraction of the wavefunction is reflected.

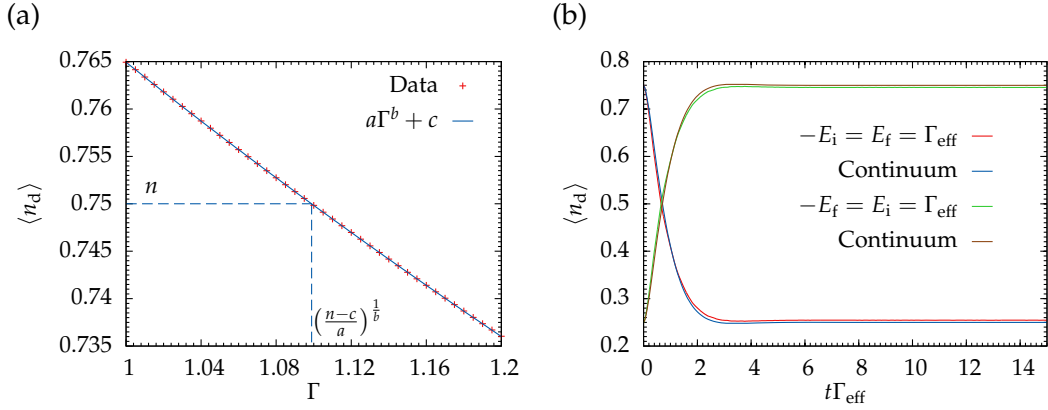


Figure 3.8: (a) Determining the value of Γ in order to keep Γ_{eff} at the same value as the continuous model. (b) Time-dependent impurity occupation number: the $t = 0$ values agree perfectly with the continuum solution, while there is a small deviation for the thermal values. This is even true for exchanging $E_i \leftrightarrow E_f$. Here, the Γ value determined in the left panel is used. In both panels the parameters are $T = 0, \Lambda = 1.8, N_1 = 34, N_2 = 500$, and $D = 10^5 \Gamma_{\text{eff}}$. The impurity occupation number $\langle n_d \rangle$ is calculated with Eq. (3.20).

age does not change during this propagation (cf. Fig. 3.7b). Furthermore, the chain occupation $\langle c_m^\dagger c_m \rangle(t)$ at $t\Gamma = 1$ shows that at this time not the whole charge has been transferred into the chain as, obviously, the area of the peak of the $t\Gamma = 1$ curve is smaller than the area of the other peaks (cf. Fig. 3.7b).

The next step in the analysis of this hybrid chain is to compare the WTBC results to those of the continuous model. As mentioned above, the bath discretization renormalizes the effective value of the level width Γ . We use the effective level width Γ_{eff} as the energy unit and tune the bare model parameter Γ in such a way that Γ_{eff} of the discretized and the continuous model are equal. This is achieved by performing a Γ scan for the discretized model with $E_d = -\Gamma$ and selecting the value of Γ at which the occupation is $\langle n_d \rangle = \frac{3}{4}$, see Fig. 3.8a, which is the corresponding value of the impurity occupation number of the continuous model.

This procedure makes sure that the initial value of $\langle n_d \rangle(t)$ is the same as the one for the continuous model. The time-dependence is qualitatively correct (cf. Fig. 3.8b) and shows no reflections on long time scales.⁴ However, the occupation number does not reach the proper thermal value, but is slightly detuned; on exchange of E_i and E_f and keeping all other parameters constant, the same qualitative behavior is observed: the initial value is correct, but the thermal value is not. In principle, it is therefore possible to determine the correct thermal occupation number for the final Hamiltonian, but the time-evolution does not evolve to the correct state.

The system does not reach the thermal value because the tight-binding chain is too short and therefore the energy resolution at which the conduction band is sampled is

⁴ In Fig. 3.8b the first reflections would be visible at $t\Gamma_{\text{eff}} \approx 105$.

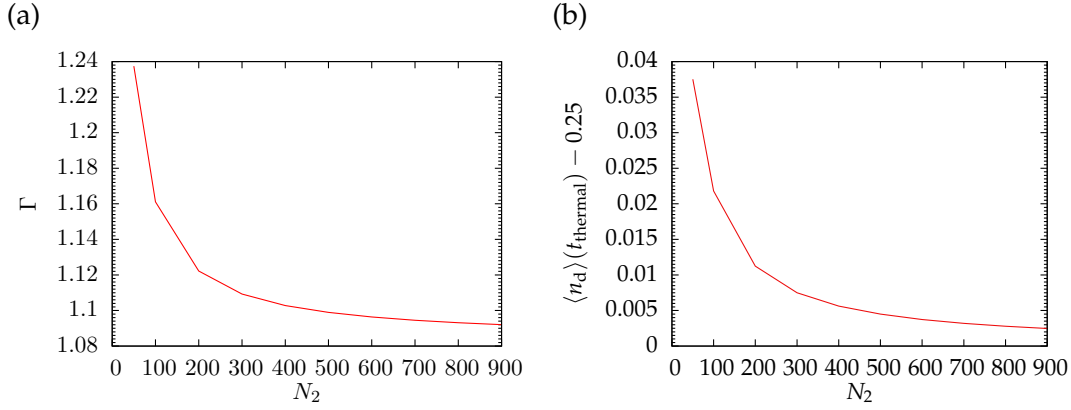


Figure 3.9: (a) Bare value of Γ value determined as shown in left panel of Fig. 3.8 in order to keep effective level-width fixed at $\Gamma_{\text{eff}} = 1$. (b) Thermalized occupation of impurity after quench $-E_i = E_f = \Gamma_{\text{eff}}$. The thermalized expectation value of the continuous model is given by Eq. (3.11), $\langle n_d(E_f) \rangle = 0.25$. The parameters are $\Lambda = 1.8, N_1 = 34, D = 10^5 \Gamma_{\text{eff}}$.

too low. For the time-evolution all energy scales are important. Unlike the logarithmic discretization, the tight-binding chain keeps a lot of states at a certain energy scale but neglects states at other energy scales. If these states are relevant in the time-evolution the reached thermal state has evolved missing some frequencies and hence does not reach thermal state of the final Hamiltonian.

For $N_2 \rightarrow \infty$ one restores the continuum limit in an energy range determined by the tight-binding hopping parameter and the impurity occupation number is able to thermalize, Fig. 3.9b, if the quench strength is not too large.

For a continuous bath $\Gamma = \Gamma_{\text{eff}}$ holds; Fig. 3.9a shows that for increasing N_2 the bare Γ needed for $\Gamma_{\text{eff}} = 1$ approaches $\Gamma \rightarrow 1^+$.⁵ This shows that one recovers the continuum limit with a WTBC, albeit the length of the total chain is large.

Double Wilson chain

The WTBC has the advantage over the pure Wilson chain, that one can push the occurrences of internal reflections to arbitrary time scales by extending the length of the tight-binding chain. Thereby it is possible to actually see a subsystem, which in this case consists only of the impurity, thermalize.

However, for systems deprived of the possibility of an efficient exact diagonalization, the tight-binding chain has to be small enough in order to be solved with other methods. As this limits not only the simulation time but also the accuracy we propose to hybridize the first Wilson chain with a second Wilson chain, using a discretization parameter Λ_2 which is an order of magnitude closer to one than the discretization pa-

⁵ This is only true for N_2 even. Otherwise $\Gamma < 1$ and $\Gamma \rightarrow 1^-$ for $N_2 \rightarrow \infty$.

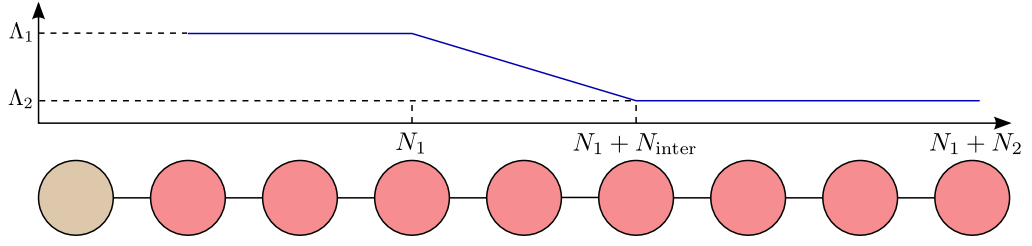


Figure 3.10: Schematic representation of double Wilson chain.

parameter Λ_1 of the first Wilson chain. We call this hybrid approach a double Wilson chain (DWC).

Hopping parameters

The chain parameters of a DWC are determined by patching two separate Wilson chains together. The first N_1 chain sites are connected by the usual Wilson hopping parameters t_n , Eq. (1.39), calculated with the discretization parameter Λ_1 . The second subchain consists of N_2 chain sites and the discretization parameter Λ_2 is used. In order to get a smooth transition, the first N_{inter} sites of the second subchain use a decreasing discretization parameter. The hopping parameters of the second subchain are calculated by (cf. Fig. 3.10)

$$t_{N_1+n-1} = \lambda_n^{-1/2} t_{N_1+n-2} \quad \text{for } n \geq 0 \quad (3.30)$$

$$\text{with } \lambda_n = \begin{cases} \Lambda_1 - \frac{\Lambda_1 - \Lambda_2}{N_{inter}}(n+1) & n < N_{inter} \\ \Lambda_2 & n \geq N_{inter} \end{cases}. \quad (3.31)$$

Chain occupation

The time- and site-dependent occupation for one example DWC calculation is shown in Fig. 3.11a. Unlike the WTBC, the form of the charge wave changes while propagating through the chain after site N_1 because the velocity is not constant (cf. Fig. 3.11b). As a consequence there are some minor reflections within the chain. The charge wave reaches the end of chain on the shown time scales. For an optimal set of parameters the chain site at which the dominant internal reflections occur is the last site of the total chain.

Comparison with continuous model

To compare the results of the DWC to the continuous model one has to determine Γ in order to keep $\Gamma_{eff} = 1$. This is carried out in the same manner as discussed above (cf. Fig. 3.8). Using the so determined value for the bare Γ the time-dependent occupation number of the impurity is calculated and compared with the solution of the continuous model, Eq. (3.12). Fig. 3.12a shows that for large values of Λ_2 one gets results which are

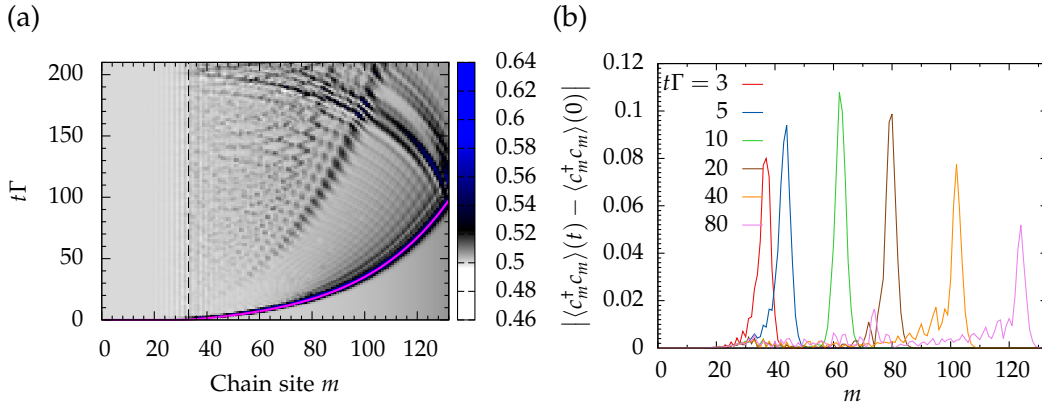


Figure 3.11: DWC consisting of $N_1 = 34$ Wilson chain sites with $\Lambda_1 = 1.8$ and $N_2 = 100$ Wilson chain sites with $\Lambda_2 = 1.06$. The parameters are $-E_i = E_f = -\Gamma, T = 0$, and $D = 10^5\Gamma$. The results are calculated with Eq. (3.20). (a) Time and site dependent occupation number. The full line indicates the position of the wave-front calculated with Eq. (3.28) while the vertical dashed line indicates the position of N_1 . (b) Change of occupation number of the chain sites m at different time steps.

similar to a pure Wilson chain. Here the short time behavior of the impurity occupation agrees with the results of the continuous model, but after the first decay the occupation number is dominated by small wiggles, which are due to reflections within both Wilson chains.

For $\Lambda \rightarrow 1$ the second Wilson chain behaves as a tight-binding chain and hence we see the typical signatures of such a chain: since for these calculations N_2 is low compared to values needed to restore the continuum (cf. Fig. 3.9), one observes a deviation between the final thermal value of the discretized and continuous model; furthermore, after the first decay the curve of time-dependent occupation number is flat except for peaks due to reflections at the end of the chain.

For intermediate values of Λ_2 , e.g. $\Lambda_2 = 1.05$, the curve is almost flat, there are no reflections at the end of the chain, and the thermal value is correct. The small wiggles vanish, because these are due to internal reflections, which do not occur anymore for this choice of parameters. Since the hopping parameters of the second chain are not constant but shrink, the velocity of the charge wave is slowed and hence it does not reach the end of the chain on the shown time scales. From Fig. 3.11a one can estimate that the charge wave reaches the end of the chain for $\Lambda_2 = 1.06$ at $t\Gamma = 100$. By using a second Wilson chain the energy resolution at low energy scales is improved compared to a WTBC and thereby allowing the impurity to thermalize.

In Fig. 3.11b the optimal value of Λ_2 is determined by comparing the results of the discretized model to those of the continuous model. As the curves of the discretized model oscillate the value of $\langle n_d \rangle(t)$ is averaged over times $10 \leq t\Gamma_{\text{eff}} \leq 60$. Furthermore, the plot shows the standard deviation calculated for the same time interval. The mean

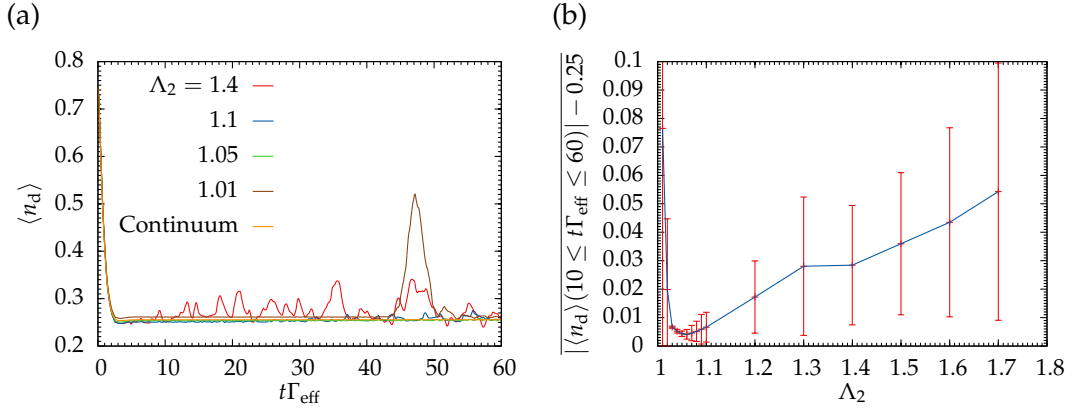


Figure 3.12: Impurity occupation number for the DWC calculated with Eq. (3.20). (a) Time-dependent impurity occupation number for different values of Λ_2 . (b) Mean difference to occupation number of continuous model. The vertical lines indicate the standard deviation and are not related to numerical errors. Same parameters as Fig. 3.11.

value is a measure for the accuracy: the closer this gets to the continuum result, the smaller are the errors due to the discretization. Whereas the standard deviation is a measure how constant this value is in time: the larger the standard deviation is, the more pronounced are the present wiggles. Hence, the goal is to minimize both values. The optimal value is $\Lambda_2 \approx 1.05$. We want to stress, that here the standard deviation is not a measure for numerical errors, but for errors due to the discretization of the bath.

Discretization parameters and chain length

The choice of the chain parameters has a great effect on the results. The smaller Λ_1 and Λ_2 are the better is the energy resolution, but one needs more chain sites to iterate to low energy scales. Furthermore, for Λ_2 close to one the chain length of the second Wilson chain N_2 can be used to control the time scale on which the charge being reflected at the end of the chain, returns to the impurity. Fig. 3.13a shows that for increasing N_2 (i) the thermalized occupation⁶ approaches the continuum value and (ii) the occurrence of the reflection peak is shifted to longer times.

The first effect is further investigated in Fig. 3.13b: here the quadratic deviation between the numerical simulation and the continuum solution is plotted versus N_2 . As the numerical simulation shows small oscillations the plotted values are averaged over the time interval $5 \leq t\Gamma_{\text{eff}} \leq 15$. One can interpret this deviation as the simulation error due to the discretization of the bath. With increasing N_2 one keeps more bath states, hence the representation of the bath is improved, and the errors due to the discretization shrink. For increasing quench strengths $\Delta E = E_f - E_i$ the error increases,

⁶ The thermal occupation is the constant value reached before the reflection peak emerges.

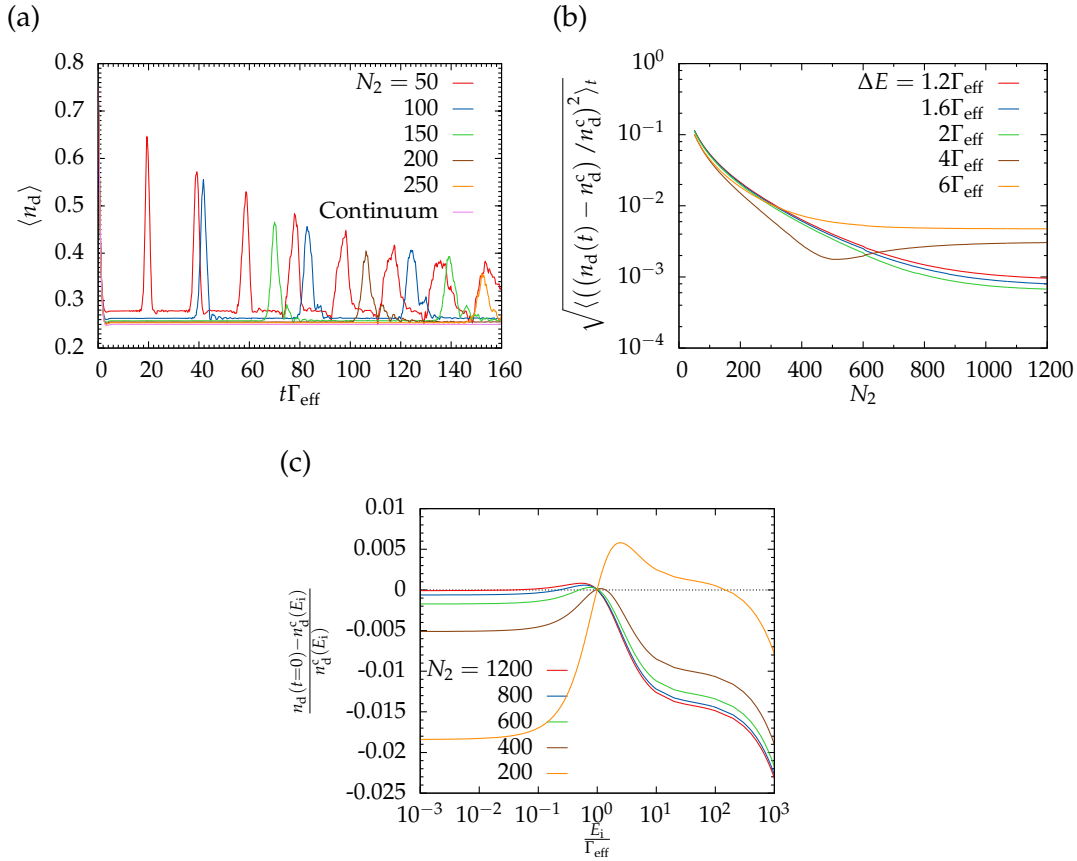


Figure 3.13: Impurity occupation number of the DWC under variation of the second Wilson chain length N_2 calculated with Eq. (3.20). (a) Time-dependent impurity occupation number for different values of N_2 . (b) Relative quadratic deviation between the final impurity occupation number calculated for the discretized model and the continuous solution n_d^c , Eq. (3.11). The value is averaged over the time interval $5 \leq t\Gamma_{\text{eff}} \leq 15$. The energy difference is given by $\Delta E = E_f - E_i$. (c) Difference between continuous and discretized impurity occupation number in equilibrium. If not stated otherwise, the parameters used in all panels are: $T = 0$, $N_1 = 34$, $\Lambda_1 = 1.8$, $\Lambda_2 = 1.01$, $-E_i = E_f = -\Gamma_{\text{eff}}$ and $D = 10^5\Gamma_{\text{eff}}$.

as in this case the overlap of the initial state and thermal state shrinks and one needs more high-energy excitations in order to evolve to thermal state.

Interestingly, the error is the smallest for $\Delta E = 2\Gamma_{\text{eff}}$, that is for a quench from $E_i = -\Gamma_{\text{eff}}$ to $E_f = \Gamma_{\text{eff}}$. To illustrate this further Fig. 3.13c shows the deviation of the equilibrium occupation from the discretized to the continuous model versus the level position E_i . For $E_i = \pm\Gamma_{\text{eff}}$ this deviation vanishes, because the effective level width Γ_{eff} is defined by enforcing that the occupation for $E_i = \pm\Gamma_{\text{eff}}$ is the same for the discretized and the continuous model.

By setting $\Gamma_{\text{eff}} = 1$ it is ensured that the *width* of the spectral function is the same for the discretized and the continuous model, but the *form* is different: for the continuous model the spectral function is a Lorentzian, but this form changes when discretizing

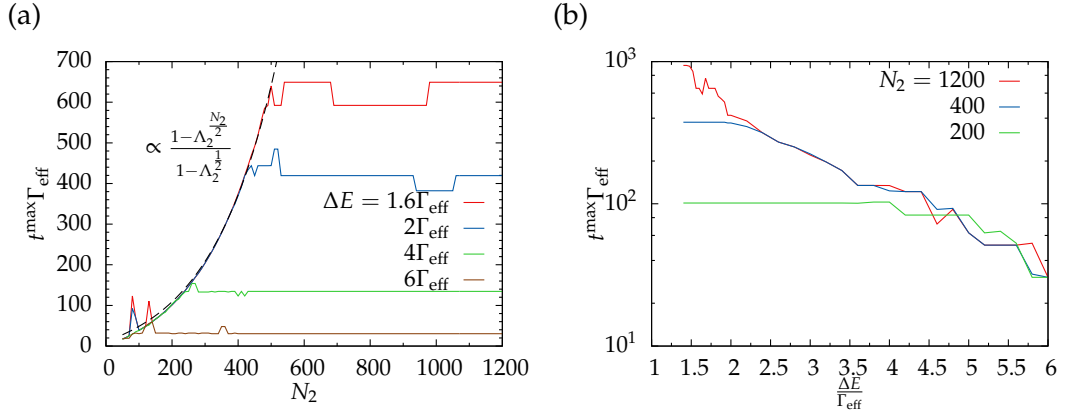


Figure 3.14: (a) Maximum simulation time t^{\max} for different sizes of the second Wilson chain. The dashed line is of the form Eq. (3.33) and indicates the maximum simulation time, if the charge is reflected at the end of the chain. The saturation of the curves shows at which chain length N_2 the dominant reflections occur within and not at the end of the chain. (b) Dependence of t^{\max} on quench strength. Same parameters as Fig. 3.13.

the bath – an effect already visible in Fig. 3.5a. Furthermore, Fig. 3.13c shows that the deviation from a Lorentzian shrinks with decreasing impurity level energy E_i and increasing number of chain sites N_2 : this is another reason for the growth of the discretization error with increasing quench strengths (cf. Fig. 3.13b).

Besides the accuracy of the impurity occupation number the maximum simulation time depends on the length of the second Wilson chain as well. Fig. 3.13a shows that with increasing N_2 the time at which the reflection peak occurs is pushed to longer time scales: for a longer chain, the time needed for the charge wave to propagate through the chain and back to the impurity grows. Fig. 3.14a shows the maximum simulation time t^{\max} , which is defined as the time at which the reflection peaks emerges in the impurity occupation number. The dependence of t^{\max} on the chain length can be estimated with (3.28),

$$t^{\max} \propto \sum_{i=0}^{N_2-1} \frac{1}{t_i}. \quad (3.32)$$

The hopping parameters are $t_i \propto \Lambda_2^{-\frac{i}{2}}$ and thus

$$t^{\max} \propto \sum_{i=0}^{N_2-1} \Lambda_2^{\frac{i}{2}} = \frac{1 - \Lambda_2^{\frac{N_2}{2}}}{1 - \Lambda_2^{\frac{1}{2}}}. \quad (3.33)$$

The curves in Fig. 3.13a follow this form up to a ΔE dependent value of N_2 at which t^{\max} saturates. Because the derivation of (3.33) assumes that the charge is reflected at the end of the chain, this means that beyond the point of saturation the reflections

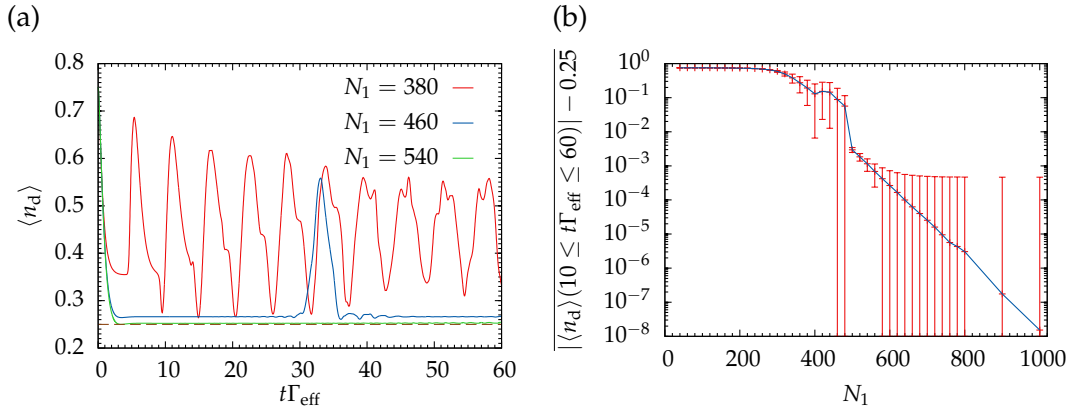


Figure 3.15: Impurity occupation number for the RLM with a Wilson chain calculated with Eq. (3.20). (a) Time-dependent impurity occupation number for different values of N_1 . The dashed horizontal lines marks the final thermal occupation for the continuous model. (b) Mean difference to occupation number of continuous model. The vertical lines indicate the standard deviation. The parameters are $T = 0$, $\Lambda = 1.05$, $-E_i = E_f = \Gamma_{\text{eff}}$, $D = 10^5 \Gamma_{\text{eff}}$.

within the chain become the dominant error. Hence, further increasing the chain length does not increase to simulation time.

The chain length at which the internal reflections are dominant depends on the energy difference ΔE (cf. Fig. 3.14b): if a great amount of charge is injected into the chain, the internal reflections within the chain occur at a site closer to the impurity, because a large charge needs large hopping parameters to be completely transferred from one site to the next in one time unit. The saturation in Fig. 3.14b for small energies is due to reflections at the end of the chain, which occur on time scales independent of ΔE . For large ΔE the maximum time is independent of the chain length N_2 , because here the internal reflections are dominant and corrupt the impurity occupation number before the charge is reflected at the end of the chain.

Because the goal is to reproduce the continuum solution with the discretized model, the chain parameters have to be chosen in such a manner that discretization artifacts do not occur in the time interval one is interested in. To see the difference between the chain parameters of a conventional Wilson chain and a DWC, we determine the chain parameters needed to recapture the continuum dynamics with a pure Wilson chain. Here one needs a chain with $N_1 \sim 500$ sites and the discretization parameter $\Lambda = 1.05$ to get an agreement as good with the continuum solution in the chosen time interval as with the DWC (cf. Fig. 3.15). For the same set of model parameters the total length of the DWC $N = N_1 + N_2 = 34 + 100$ is shorter than the conventional Wilson chain (cf. Fig. 3.12); the discretization parameter Λ_2 of the second subchain was chosen to be equal to the discretization parameter of the conventional Wilson chain Λ .

The reason for the two different approaches to differ so strongly in chain length is due to discretization artifacts. The pure Wilson chain results for large values of Λ are

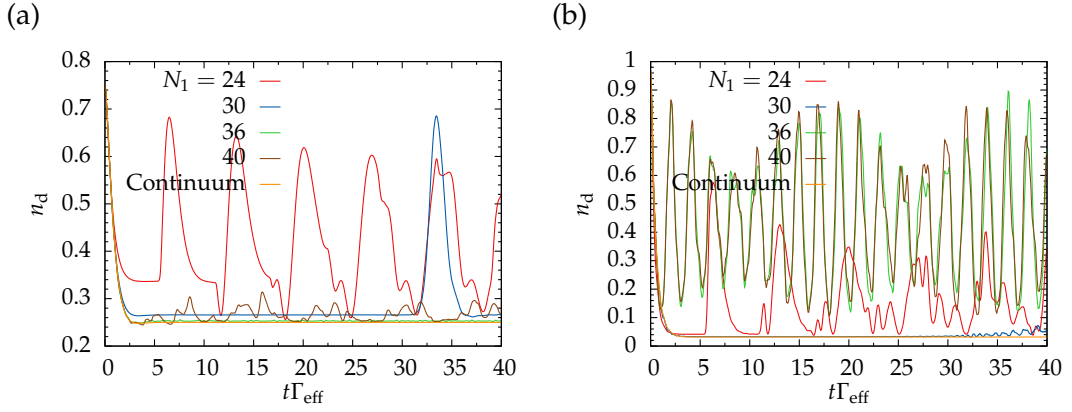


Figure 3.16: Impurity occupation number for the RLM with a DWC and different lengths of the first Wilson chain N_1 calculated with Eq. (3.12) and Eq. (3.20). The parameters are $T = 0, \Lambda_1 = 1.8, \Lambda_2 = 1.01, N_2 = 200, D = 10^5 \Gamma_{\text{eff}}$, (a) $-E_i = E_f = \Gamma_{\text{eff}}$ and (b) $-E_i = E_f = 10 \Gamma_{\text{eff}}$.

corrupted by reflections within the chain. To push the occurrences of these reflections to longer time scales one needs a small value of Λ . In the DWC, however, the cut between the two chains is set to a site N_1 , at which the influence of reflections is negligible. As the discretization parameter of the first part Λ_1 is larger than Λ_2 , the effective bandwidth at site N_1 is strongly reduced. Starting at this reduced bandwidth one does not need as many Wilson chain sites in the second to reach the same final energy scale as one needs with a pure Wilson Chain.

Chain length of first Wilson chain

The accuracy of the simulation and the maximum simulation time depend on the length of the first Wilson chain N_1 . As an example, Fig. 3.16 shows the impurity occupation number for different values of N_1 and quench strengths ΔE . If the first Wilson chain is too short one does not iterate to low energy scales and due to the small value of Λ_2 the second Wilson chain reduces the energy scale only by a factor ~ 0.3 . At large temperatures the occupation probability of the initial state is of the same order of magnitude as the occupation probability of the final state. Hence one observes oscillations between these both states.⁷ If the first Wilson chain is too long internal reflections in the first Wilson chain occur rendering the simulation useless.

In between there is an optimal value of N_1 for which the discretized model shows results close to the continuum model on the time scales one is interested in. The value of the optimal N_1 does not just depend on the discretization parameter Λ_1 but on E_i and E_f as well: the more charge the chain has to adsorb the earlier in the chain internal reflections occur. Generally, the goal is to choose N_1 as large as possible, but the simulation accuracy does not crucially depend on N_1 . As long as no internal

⁷ For presentational reasons such a short chain is not shown in Fig. 3.16.

reflections occur one can slightly vary N_1 by compensating these variations with the choice of Λ_2 and N_2 . For $-E_i = E_f \lesssim 10\Gamma_{\text{eff}}$ a choice in the interval $N_1 \in [28, 34]$ turned out to work well.

The reason why to choose N_1 as large as possible is that increasing N_1 decreases the effective bandwidth at the end of the first Wilson chain. On the one hand this turns out to be advantageous for the hybrid method presented below in Sec. 4; on the other hand this reduces the hopping parameters of the second Wilson chain allowing for longer simulation times, because it takes the charge wave longer to reach the end of the chain. This is why in Fig. 3.16a the reflection peak of the $N_1 = 24$ curve occurs earlier than the reflection peak of the $N_1 = 30$ curve. In Fig. 3.16b the reflection peak of the $N_1 = 30$ curve has vanished; instead the curves shows small wiggles. This indicates that the charge wave is not reflected at the end of the chain but the internal reflections become dominant.

Transition from Wilson chain to double Wilson chain

If one knows for which Wilson chain parameters Λ and N the results are sufficiently accurate, one can estimate⁸ the parameters for a DWC. Of course, one can find many sets of parameters for the DWC, which reproduce the results of a pure Wilson chain. Therefore we make some assumptions: (i) the discretization parameter of the second Wilson chain Λ_2 equals the discretization parameter of the pure Wilson chain, $\Lambda = \Lambda_2$, and (ii) one has already found values for Λ_1 and N_1 so that no reflections occur. Our criterion is then, that the final energy scales, t_N and $t_{N_1+N_2}$, of the pure and the DWC are equal,

$$t_N = D\Lambda_2^{-N/2} = D\Lambda_1^{-N_1/2}\Lambda_2^{-N_2/2}. \quad (3.34)$$

The length of the second Wilson chain is thus given by

$$N_2 = N - N_1 \frac{\log \Lambda_1}{\log \Lambda_2}. \quad (3.35)$$

Given the numbers of Fig. 3.12 and Fig. 3.15, $N = 500$, $N_1 = 34$, $\Lambda_1 = 1.8$, and $\Lambda_2 = 1.05$, one expects, according to this equation, the length of the second chain to be $N_2 \approx 90$. This agrees well to the numerical value $N_2 = 100$. One can use Eq. (3.35) as well to estimate the length of a Wilson chain needed to reproduce the results of a DWC.⁹ However, replacing a DWC by a Wilson chain reduces the simulation time and the accuracy.

⁸ The given equations are just estimates, because the effect of the gradually lowering of Λ over N_{inter} sites is neglected.

⁹ In this case one should use $N'_1 = N_1 + N_{\text{inter}}$ and $N'_2 = N_2 + N_{\text{inter}}$ to compensate the fact that the discretization parameter is decreased over several sites.

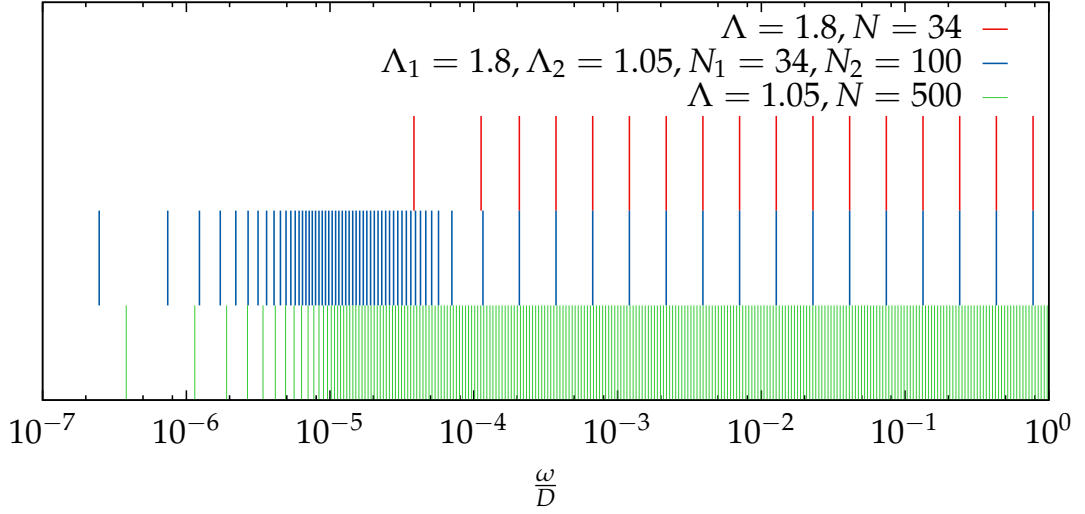


Figure 3.17: Different discretizations of the DOS: two Wilson chains and one DWC. Shown are only the positive frequencies: the DOS is axially symmetric to $\omega = 0$. Each vertical line represents a frequency ω_k of Eq. (3.38). The bare Wilson chains (top and bottom) show the same energy resolution over the whole spectrum, whereas the DWC (middle) shows a good energy resolution only for low-energies, hence the number of states is reduced while keeping the resolution good in the important range.

3.4 Density of states

The purpose of the chain – no matter, if it is a pure Wilson chain, a tight-binding chain, or a hybrid chain – is to be a good representation of the continuous bath. The coupling of the bath to the impurity is described by the propagator

$$\Gamma(\omega) = \text{Im} \sum_k \frac{V^2}{z - \omega_k} = \pi V^2 \rho(\omega) \quad (3.36)$$

as defined in Eq. (3.4). Here we use the DOS $\rho(\omega)$ as defined in Eq. (3.5): for a continuous bath this is a constant function with support in the interval $[-D, D]$ and in the discretized form it is a sum of δ -functions at discrete energies ω_k . One can represent the Green's function at the first Wilson chain site by a continued fraction [156]

$$\ll c_0 | c_0^\dagger \gg (z) = \frac{1}{z - \frac{t_0^2}{z - \frac{t_1^2}{z - \frac{t_2^2}{\ddots}}}} \quad (3.37)$$

This form can easily be derived by an equation of motion ansatz. The function

$$\rho_{\text{dis}}(\omega) = -\lim_{\delta \rightarrow 0} \frac{1}{\pi} \text{Im} \ll c_0 | c_0^\dagger \gg (\omega + i\delta) = \sum_k c_k \delta(\omega - \omega_k) \quad (3.38)$$

is the DOS of the discretized bath and consists of a sum of δ peaks at positions ω_k with the weight c_k . The positions of the peaks are given by the roots of the denominator of Eq. (3.37) or by the eigenvalues of the matrix M , which has the elements t_n on the first diagonal above and below the main diagonal.

For a Wilson chain and in the limit $\Lambda \rightarrow 1, N \rightarrow \infty$ the distribution of the peaks becomes dense and one recaptures the continuous function $\rho(\omega)$. However, for $\Lambda > 1$ one observes discrete peaks: Fig. 3.17 shows the positions of ω_k for three different ways of discretizing the bath. For a pure Wilson chain the positions of the peaks are equidistant on a logarithmic mesh, axially symmetric to $\omega = 0$, the peak for the highest energy is at $\sim D$, and the peak for the lowest energy is at $\sim D\Lambda^{-\frac{N}{2}}$: the energy resolution is determined by Λ and the lowest resolved energy scale is determined by Λ and N . The number of peaks is given by N , whereas one has the same number of peaks at positive and negative frequencies; for odd N one has a peak at $\omega = 0$. The high energy peaks of the hybrid chain are the same as for a pure Wilson chain with the same parameters. However, the merit of the hybrid chain is to improve the energy resolution at low energy scales without inserting more high-energy states.

3.5 Summary

This concludes the examination of discretization artifacts in the numerical renormalization group (NRG). By comparing the results of the exactly solvable resonant-level model (RLM) for a continuous and a discretized bath we have shown that in nonequilibrium calculations these artifacts manifest as reflections within the Wilson chain and thereby corrupting the simulation. As $\Lambda \rightarrow 1$ restores the continuum one strategy to eliminate discretization artifacts is to operate with a discretization parameter Λ very close to one. This strategy is not feasible for practical NRG calculations. Hence we have proposed hybrid chains by which the discretization artifacts are minimized while keeping the chain length on a manageable level.

The central result of this chapter is that by using a double Wilson chain one can minimize the discretization artifacts which are due to internal reflections within the Wilson chain and a limited energy resolution. However, in the present formulation the NRG can only handle pure Wilson chains and to keep the number of kept states on a manageable level the discretization parameter Λ has to be sufficiently large; Wilson chains with $\Lambda = 1.05$, for which the negative effects of the discretization are acceptably small for the investigated parameters, are therefore out of reach for the NRG. In the next chapter we propose a new method which overcomes these obstacles.

Chapter 4

Hybrid Method

Only a few models relevant in condensed matter physics are exactly solvable. For most others one needs methods which rely on different approximations or work only in certain parameter regimes. One numerical method is the numerical renormalization group (NRG) [28, 29] which is designed to investigate the low-temperature properties of quantum impurity systems (QISs): the NRG is well suited for studying the resonant-level model (RLM) coupled to a Wilson chain, as discussed in the previous chapter. However, the discretization artifacts discovered there are present in all time-dependent numerical renormalization group (TD-NRG) calculations. Our proposals which eliminate the discretization artifacts do not work for the NRG as these proposals leave the concept of a pure Wilson chain, and thereby the required separation of energy scales is in general not fulfilled.

In this chapter we extend the NRG to a new hybrid method which picks up the idea of the hybrid chain: a hybrid chain consists of two chains, with the first one being a Wilson chain. Without the second chain it is therefore possible to solve the system with the NRG. Thereby the Hamiltonian of the impurity coupled to the first Wilson chain is diagonalized by an NRG run: since the high-energy states are discarded in the course of the NRG, this yields an effective low-energy Hamiltonian. We understand this diagonal Hamiltonian as a hyper-impurity: it is like a RLM but with more than one non-interacting levels which all couple differently to the second chain. This new effective system – the hyper-impurity coupled to the second chain – is then solved with a different method.

In this chapter we discuss the new hybrid method for the general case in detail; we make no assumptions regarding the impurity or the chain, except that the first M sites of the chain form a Wilson chain. In Ref. 90 we hybridized the NRG with the Chebyshev expansion technique (CET). However, in Ref. 90 no hybrid chains were used and therefore we had the usual setup of an impurity coupling to a Wilson chain.

In this work we explicitly show how to hybridize the NRG with the density-matrix renormalization group (DMRG): we call this scenario the numerical renormalization group density-matrix renormalization group hybrid (NRG+DMRG) method. By com-

paring NRG+DMRG results with the exact results for the RLM we show that this new numerical method indeed yields the correct results.

4.1 Description of new hybrid method

The original TD-NRG approach, summarized above in Sec. 1.3.4, tracks the quench dynamics of a quantum-impurity system in terms of the phase factors $e^{it(E_r^m - E_s^m)}$ and the reduced density-matrices $\rho_{s,r}^{\text{red}}(m)$ assigned to each NRG iteration m . Although quite elegant and useful, it is less transparent how to incorporate ideas from methods such as the time-dependent density-matrix renormalization group (TD-DMRG) or CET, as these deal with wave-functions directly. To develop a convenient and flexible interface between the TD-NRG and these vastly different approaches we reformulate the former approach from a wave-function perspective.¹

4.1.1 Wave-function formulation

Let us commence with accurately stating the problem from a wave-function perspective. We are interested in tracking the time evolution of some initial state $|\psi_0\rangle$ under the dynamics defined by the Hamiltonian H acting on a finite Wilson chain of length N . We shall not concern ourselves at this stage with how the initial state $|\psi_0\rangle$ is generated, but will elaborate on this important point later on.

Formally our task boils down to computing

$$|\psi(t)\rangle = e^{-iHt}|\psi_0\rangle. \quad (4.1)$$

Application of the completeness relation of Eq. (1.71),

$$1 = \sum_{m=m_{\min}}^M \hat{P}_m + \hat{\Gamma}_M^+ \quad (4.2)$$

to the state $|\psi(t)\rangle$ leads to its partitioning according to

$$|\psi(t)\rangle = \sum_{m=m_{\min}}^M |\phi_m(t)\rangle + |\chi_M(t)\rangle \quad (4.3)$$

$$\text{where } |\phi_m(t)\rangle = \hat{P}_m |\psi(t)\rangle \quad (4.4)$$

$$\text{and } |\chi_M(t)\rangle = \hat{\Gamma}_M^+ |\psi(t)\rangle \quad (4.5)$$

are the projections of $|\psi(t)\rangle$ onto the subspaces defined by \hat{P}_m and $\hat{\Gamma}_M^+$, respectively. Eq. (4.3) simply converts the general state $|\psi(t)\rangle$ into a concrete representation in terms of our complete basis set.

¹ The text of this paragraph and of Secs. 4.1.1 - 4.1.3 has been published in [90] and is ©2012 American Physical Society.

4.1.2 Evaluation of expectation values

Given the time-evolved wave function of Eq. (4.3), we proceed to compute time-dependent averages of physical observables A

$$A(t) = \langle \psi(t) | A | \psi(t) \rangle \quad (4.6)$$

To this end, we use the completeness relation of (1.71) to decompose any arbitrary operator A into

$$A = \sum_{m,m'}^M \hat{P}_m A \hat{P}_{m'} + \sum_m^M \left\{ \hat{P}_m A \hat{1}_M^+ + \hat{1}_M^+ A \hat{P}_m \right\} + \hat{1}_M^+ A \hat{1}_M^+, \quad (4.7)$$

where the summations over m and m' start from m_{\min} . Writing the first two terms on the right-hand side of Eq. (4.7) as

$$\sum_{m=m_{\min}} \left[\hat{P}_m A \hat{P}_m + \hat{P}_m A \left(\sum_{m'=m+1}^M \hat{P}_{m'} + \hat{1}_M^+ \right) + \left(\sum_{m'=m+1}^M \hat{P}_{m'} + \hat{1}_M^+ \right) A \hat{P}_m \right] \quad (4.8)$$

and noting that

$$\hat{1}_m^+ = \sum_{m'=m+1}^M \hat{P}_{m'} + \hat{1}_M^+, \quad (4.9)$$

the operator A is recast in the exact form

$$A = \sum_{m=m_{\min}}^M A(m) + A_\chi, \quad (4.10)$$

$$\text{where } A(m) = \hat{P}_m A \hat{P}_m + \hat{1}_m^+ A \hat{P}_m + \hat{P}_m \hat{1}_m^+ \quad (4.11)$$

$$\text{and } A_\chi = \hat{1}_M^+ A \hat{1}_M^+. \quad (4.12)$$

Here the index M can take any value in the range $m_{\min} \leq M \leq N$. Explicitly, the operator $A(m)$ has the formal representation

$$A(m) = \sum_{r,s}^{\text{trun}} \sum_{e,e'} |r, e; m\rangle \langle r, e; m | A | s, e'; m\rangle \langle s, e'; m |, \quad (4.13)$$

where the restricted sum $\sum_{r,s}^{\text{trun}}$ implies, as before, that at least one of the states r and s is discarded at iteration m .

As in the original TD-NRG, we focus hereafter on local operators A that act solely on degrees of freedom that reside either on the impurity itself or on the first m_{\min} sites

along the Wilson chain [77]. For any such local operator, the matrix elements in Eq. (4.13) are diagonal in and independent of the environment variables e and e' :

$$\langle r, e; m | A | s, e'; m \rangle = A_{r,s}^m \delta_{e,e'}. \quad (4.14)$$

Substituting the operator decomposition of Eq. (4.10) into Eq. (4.6) and using the definition $|\chi_M(t)\rangle = \hat{1}_m^+ |\psi(t)\rangle$ of Eq. (4.5), the time-dependent expectation value takes the form

$$A(t) = \sum_{m=m_{\min}}^M \langle \psi(t) | A(m) | \psi(t) \rangle + \langle \chi_M(t) | A | \chi_M(t) \rangle. \quad (4.15)$$

This general expression reduces for a local operator to

$$A(t) = \langle \chi_M(t) | A | \chi_M(t) \rangle + \sum_{m=m_{\min}}^M \sum_{r,s}^{\text{trun}} A_{r,s}^m \rho_{s,r}^m(t), \quad (4.16)$$

$$\text{where } \rho_{s,r}^m(t) = \sum_e \langle s, e; m | \psi(t) \rangle \langle \psi(t) | r, e; m \rangle \quad (4.17)$$

is the reduced density matrix at iteration m .

Three comments should be made about Eqs. (4.16) and (4.17). First, these expressions are both general and exact for the real-time dynamics on the discretized chain. Apart from the restriction to local operators, no further approximations or assumptions are involved. Second, Eqs. (4.16) and (4.17) can be easily extended to a statistical admixture of initial states $\{|\psi_i\rangle\}$ with the statistical weights $\{w_i\}$. This requires the simple substitutions

$$\langle \chi_M(t) | A | \chi_M(t) \rangle \rightarrow \sum_i w_i \langle \chi_{M,i}(t) | A | \chi_{M,i}(t) \rangle \quad (4.18)$$

$$\text{and } \rho(t) = |\psi(t)\rangle \langle \psi(t)| \rightarrow \sum_i w_i |\psi_i(t)\rangle \langle \psi_i(t)| \quad (4.19)$$

in Eqs. (4.16) and (4.17), respectively. Third, the conventional TD-NRG approach is recovered from Eqs. (4.16) and (4.17) by (i) setting $M = N$, (ii) realizing that $A_\chi = 0$ for $N = M$, and (iii) adopting the standard NRG approximation $H|r, e; m\rangle \approx E_r^m |r, e; m\rangle$, which simplifies $\rho_{s,r}^m(t)$ to $e^{i(E_r^m - E_s^m)t} \rho_{s,r}^{\text{red}}(m)$ with

$$\rho_{s,r}^{\text{red}}(m) = \sum_e \langle s, e; m | \psi_0 \rangle \langle \psi_0 | r, e; m \rangle. \quad (4.20)$$

A natural generalization of the TD-NRG is to apply the NRG approximation $H|r, e; m\rangle \approx E_r^m|r, e; m\rangle$ to the early iterations $m \leq M$ only, converting Eq. (4.16) and Eq. (4.17) to

$$A(t) = \sum_{m=m_{\min}}^M \sum_{r,s}^{\text{trun}} e^{i(E_r^m - E_s^m)t} A_{r,s}^m \rho_{s,r}^{\text{red}}(m) + \langle \chi_M(t) | A | \chi_M(t) \rangle. \quad (4.21)$$

This equation, which constitutes one of the central results of this chapter, interpolates between the TD-NRG, corresponding to $M = N$, and the exact time-dependent expectation value, obtained for $M = m_{\min}$. Of course, the latter statement assumes an exact evaluation of $|\chi_M(t)\rangle$, which is an impractical task for $M = m_{\min}$. As discussed below, a proper choice of the parameter M allows for an improved evaluation of $|\chi_M(t)\rangle$ using alternative methods such as the TD-DMRG or CET, with minimal loss of accuracy at the early iterations to which the NRG approximation is applied. Furthermore, by resorting to methods that do not rely on the special structure of the Wilson chain to evaluate $|\chi_M(t)\rangle$, one can abandon the exponential decay of the hopping matrix elements beyond site M , reducing thereby the discretization errors inherent to the Wilson chain. These principles form the core of the hybrid approach. We now turn to elaborate on the technicalities of how M is selected, the interface with the hybridized method, and the way in which the initial state $|\psi_0\rangle$ is constructed.

4.1.3 Interface between the TD-NRG and the hybridized approach

Hierarchy of energy scales and the time evolution of $|\chi_M(t)\rangle$

To turn Eq. (4.21) into an operative platform for hybridizing the TD-NRG with alternative methods of computing the real-time dynamics of $|\chi_M(t)\rangle$, it is useful to go back to the partitioning of $|\psi(t)\rangle$ specified in Eq. (4.3) and gain a deeper insight into the energy scales encoded into the projectors \hat{P}_m . Applying the operator decomposition of Eq. (4.10) to the Hamiltonian H , the latter is written as

$$H = \sum_{m=m_{\min}}^M H(m) + h_\chi, \quad (4.22)$$

$$\text{where } H(m) \equiv \hat{P}_m H \hat{P}_m + \hat{P}_m H \hat{1}_m^+ + \hat{1}_m^+ H \hat{P}_m \quad (4.23)$$

$$\text{and } h_\chi = \hat{1}_M^+ H \hat{1}_M^+. \quad (4.24)$$

It is rather easy to see that the different Hamiltonian terms that appear in Eq. (4.22) generally do not commute with one another, i.e., $[H(m), h_\chi] \neq 0$ and $[H(m), H(m')] \neq 0$ if $m \neq m'$. According to the NRG philosophy, however, the off-diagonal terms $\hat{P}_m H \hat{P}_{m'}$ with $m \neq m'$ are expected to be small, as these couple excitations on different energy

scales. Consequently, one can approximate $H(m)$ with $h_m = \hat{P}_m H \hat{P}_m$ to obtain the approximate Hamiltonian

$$H \approx \sum_{m=m_{\min}}^M h_m + h_\chi. \quad (4.25)$$

Evidently, Eq. (4.25) becomes exceedingly more accurate the smaller is M , acquiring the status of an identity for $M = m_{\min}$, since $H = h_\chi$ in this case. Furthermore, since the Hamiltonian terms h_χ and h_m with $m \leq M$ are confined to the subspaces projected out by $\hat{1}_M^+$ and \hat{P}_m , respectively, the Hamiltonian of Eq. (4.25) is block-diagonal in these subspaces with $[h_m, h_{m'}] = [h_m, h_\chi] = 0$. This allows us to write the time-dependent state $|\psi(t)\rangle$ within this approximation as

$$|\psi(t)\rangle = \sum_{m=m_{\min}}^M e^{-ih_m t} |\phi_m\rangle + e^{-ih_\chi t} |\chi_M\rangle, \quad (4.26)$$

where $|\phi_m\rangle = \hat{P}_m |\psi_0\rangle$ and $|\chi_M\rangle = \hat{1}_M^+ |\psi_0\rangle$ are the projections of the initial state onto the subspaces defined by \hat{P}_m and $\hat{1}_M^+$, respectively. In other terms, it suffices in this approximation to first project out $|\chi_M\rangle$ and $|\phi_m\rangle$ from the initial state, and then propagate them separately in time, each according to its own Hamiltonian.

Physically, Eq. (4.26) prescribes a decomposition of the desired time-dependent state into independent components, each associated with a different time scale $t_m = \frac{1}{D_m} \sim \Lambda^{m/2}$ and evolving according to its own reduced Hamiltonian (either h_m or h_χ). In the case of spinless fermions the reduced Hamiltonian h_m has the explicit form

$$h_m = \sum_{l,e} E_l^m |l, e; m\rangle \langle l, e; m| + \sum_{n=m}^{N-1} t_n \left(\hat{P}_m f_{n+1}^\dagger f_n \hat{P}_m + \text{H.c.} \right), \quad (4.27)$$

where f_n^\dagger creates an electron on the n th site of the Wilson chain, t_n is the dimension-full hopping matrix element between sites n and $n+1$ along the chain, l runs over the NRG eigenstates discarded at iteration m , and E_l^m denotes their corresponding NRG eigenenergies. Note that the projection operators \hat{P}_m in the right-most term are attached in practice only to f_m and f_m^\dagger , as all other operators f_n with $n > m$ do not possess any matrix element that takes us out of the subspace defined by \hat{P}_m . The Hamiltonian h_χ is nearly identical, except that the index m is replaced with M and the discarded states $|l, e; m\rangle$ are replaced with the NRG eigenstates retained at the conclusion of iteration M . In the presence of additional bands the Wilson orbitals f_n^\dagger acquire an additional flavor index ν , which may label the spin σ , an orbital channel α , or the spin-channel tuple $\nu = (\sigma, \alpha)$ as in two-channel Kondo models (see, e.g., Ref. 157). Other than setting $f_n^\dagger \rightarrow f_{n\nu}^\dagger$ and adding a suitable summation over ν , the very same equations carry over to the general multiband case.

Physical role of the parameter M

The Hamiltonian of Eq. (4.27) can be interpreted as modeling a hyper-impurity with the localized configurations $|l\rangle$ and eigenenergies E_l^m , which are tunnel-coupled to a chain of length $N - m$. The size of the impurity is equal to the number of states discarded at iteration m . Thus, the calculation of $|\phi_m(t)\rangle = e^{-iH_m t}|\phi_m\rangle$ becomes exceedingly more affordable with larger m due to the exponential reduction of the Fock space of the chain $R_{m,N}$ attached to the hyper-impurity. We stress, however, that the dimension of the subspace associated with $\hat{P}_{m_{\min}}$ is comparable in size to that of the full Wilson chain, hence an accurate evaluation of $|\phi_{m_{\min}}(t)\rangle$ is similar in complexity to the calculation of the full state $|\psi(t)\rangle$.

There is little computational gain in implementing Eq. (4.26) if all components of the wave function must be accurately computed. Fortunately, this generally is not the case for the class of problems of interest, where $|\psi_0\rangle$ is some low-lying eigenstate (typically the ground state) of an initial Hamiltonian H^i . Under these circumstances $|\psi_0\rangle$ typically has only negligible overlap with the high-energy states of H , i.e., $\langle\phi_m|\psi_0\rangle \ll 1$ for the initial NRG iterations. Overlap becomes significant only upon approaching a characteristic energy scale D_M where the spectra of the full and the unperturbed Hamiltonians begin to notably deviate from one another. Usually this happens at some characteristic low-energy scale of the problem, e.g., the Kondo temperature T_K in case of the Kondo Hamiltonian.

Consequently, the initial NRG iterations with $m \leq M$ can be treated using further approximations such as setting $t_n = 0$ in Eq. (4.27), corresponding to the standard NRG approximation. Since the reduced density matrix $\rho_{s,r}^m(t)$ requires only the matrix element $\langle\psi(t)|r,e;m\rangle$, one can implement $e^{iHt}|r,e;m\rangle$ instead of propagating $|\phi_m(t)\rangle$ in time, which simplifies the exact result of Eq. (4.16) to the approximate expression of Eq. (4.21). The computational effort can therefore be focused on evaluating $|\chi_M(t)\rangle$, which dominates the expectation value $A(t)$. Most importantly, given the initial state $|\chi_M\rangle$ and the effective Hamiltonian h_χ generated by the NRG, the state $|\chi_M(t)\rangle$ can be computed using one's method of choice.

The physical role of the integer M , which so far served as a mere parameter, is now disclosed: it defines the NRG iteration M beyond which the time-dependent state should be accurately computed. Moreover, this partitioning can be used to improve the discrete representation of the continuous bath as noted above. For example, one can use a hybrid chain introduced in Sec. 3.3.3. Such a chain is impractical for pure NRG-based calculations, but is made possible by resorting to alternative methods for tracking the time evolution of $|\chi_M(t)\rangle$. In this manner discretization errors are significantly reduced at the energy scale D_M , corresponding to the time scale $t_M = \frac{1}{D_M}$. The crucial point to notice is that the reduced Hamiltonian h_χ has the effective bandwidth $D_M \propto \Lambda^{-M/2} \ll D$ and acts on a reduced chain of length $N_2 = N - M$. This enables access to long

time scales of order $t_M \gg \frac{1}{D}$ using techniques such as the TD-DMRG or CET, which otherwise are restricted to far shorter times.

The only remaining uncertainty pertains to a suitable choice of the iteration number M . In the absence of a sharp mathematical criterion, the choice of M should be considered on a case-by-case basis. Qualitatively, one expects the scale D_M to correspond to $\max\{\Gamma_0, |\epsilon_d|\}$ for the RLM, and to the Kondo temperature [28, 29] T_K for the Kondo model. The case of an Anderson impurity is clearly more subtle, as spin and charge relax on different time scales [76]. Here a different optimal choice of M may apply to observables acting on the spin and charge sectors.

Construction of the initial state $|\psi_0\rangle$

So far, we have assumed the decomposition of the initial state $|\psi_0\rangle$ according to Eq. (4.3), but did not specify how $|\psi_0\rangle$ is obtained in practice. The construction of $|\psi_0\rangle$ and its projection $|\chi_M\rangle$ onto the low-energy subspace defined by $\hat{1}_M^+$ depends in detail on the method hybridized with the TD-NRG. Our discussion below covers both the TD-DMRG and CET.

We begin with the initial NRG run, which provides us with the low-energy Hamiltonian $h_\chi^i = \hat{1}_{i,M}^+ H^i \hat{1}_{i,M}^+$ corresponding to the initial Hamiltonian H^i . Here $\hat{1}_{i,M}^+$ denotes the projection operator onto the low-energy subspace of H^i retained at the conclusion of iteration M . As detailed in Eq. (4.27), h_χ^i comprises of a hyper-impurity, a residual chain of length $N_2 = N - M$, and a tunnel coupling between both parts of the system. In the next step the ground state $|\psi_0\rangle$ of h_χ^i is computed. In case of the TD-DMRG this is done using the standard DMRG algorithm, Sec. 1.4, while for the CET (for which a shorter chain $R_{M,N}$ is employed) the Davidson method [158] can be used. At the conclusion of this step one has the initial state $|\psi_0\rangle$ at hand, expressed via the kept NRG eigenstates of H_M^i :

$$|\psi_0\rangle = \sum_{k_i, e} c_{k_i, e} |k_i, e; M\rangle. \quad (4.28)$$

Given $|\psi_0\rangle$, the state $|\chi_M\rangle$ is obtained by projecting $|\psi_0\rangle$ onto the low-energy subspace of the full Hamiltonian defined by $\hat{1}_M^+$. This in turn yields

$$|\chi_M\rangle = \sum_{k, e} b_{k, e} |k, e; M\rangle \quad (4.29)$$

$$\text{with } b_{k, e} = \sum_{k_i} S_{k_i, k}^*(M) c_{k_i, e}, \quad (4.30)$$

where $S(M)$ is the overlap matrix defined in Eq. (1.73). This state is then propagated in time according to $|\chi_M(t)\rangle = e^{-ih_\chi t} |\chi_M\rangle$ using either the TD-DMRG or CET and fed into Eq. (4.21). As for the reduced density-matrices $\rho_{s,r}^{\text{red}}(m)$ entering Eq. (4.21), these are computed recursively from $|\psi_0\rangle$ using the standard TD-NRG algorithm [77].

4.1.4 Hybrid NRG+DMRG

To summarize the statements from above and to present a concrete application we now show how to hybridize the TD-NRG with the TD-DMRG. This method, the NRG+DMRG method, is employed in the remaining part of this thesis to solve QISs. Results of the NRG hybridized with the CET are presented in Ref. 90 .

Of course, for a double Wilson chain (DWC) one could consider to hybridize the NRG with itself: using a first NRG run one creates an effective low-energy Hamiltonian of the impurity coupled to the first Wilson chain. This effective low-energy Hamiltonian is, in turn, coupled to the second Wilson chain which defines h_χ . The system consisting of the hyper-impurity coupled to the second Wilson chain is then solved with a second NRG run. However, as the discretization parameter Λ_2 of the second Wilson chain is close to one, one has to retain a lot of states in the second NRG run rendering this approach impractical.

The system considered in the following is an impurity coupled to a DWC consisting of two Wilson chains, where for the first N_1 sites the discretization parameter Λ_1 and for the second chain, consisting of N_2 sites, the discretization parameter Λ_2 is used. Hence, the total chain length is $N = N_1 + N_2$ and the above introduced iteration number M , after which one switches from the NRG to the DMRG, is given by $M = N_1$.²

The procedure can formally be divided into three steps: (i) the TD-NRG forward iterations, (ii) an intermediate TD-DMRG run, and (iii) the TD-NRG backward iterations (cf. Fig. 4.1).

In the forward TD-NRG iterations, Fig. 4.1a, the initial and final Hamiltonian of the impurity coupled to the first Wilson chain are diagonalized,

$$\tilde{H}_{N_1}^i = \sum_{n=0}^{N_s-1} E_n^i |\psi_n^i\rangle \langle \psi_n^i| \quad (4.31)$$

$$\text{and } \tilde{H}_{N_1}^f = \sum_{n=0}^{N_s-1} E_n^f |\psi_n^f\rangle \langle \psi_n^f|, \quad (4.32)$$

where E_n^i (E_n^f) and $|\psi_n^i\rangle$ ($|\psi_n^f\rangle$) are the eigenenergies and eigenstates kept at the last NRG iteration of the initial (final) Hamiltonian. Using this diagonal Hamiltonian as hyper-impurity with N_s degrees of freedom, where N_s is the number of kept states at the last NRG iteration, one constructs an effective low-energy Hamiltonian of the complete chain,

$$H_N^x = \tilde{H}_{N_1}^x + H_{N_2} + H_{\text{mix}}^x, \quad (4.33)$$

$$\text{with } H_{N_2} = \sum_{n=N_1}^{N_1+N_2-1} t_n \left(f_n^\dagger f_{n+1} + f_{n+1}^\dagger f_n \right) \quad (4.34)$$

² In general, for the NRG+DMRG approach M has to fulfill $M \leq N_1$. However, in the all following calculations are with $M = N_1$ and therefore the parameter M is not used anymore.

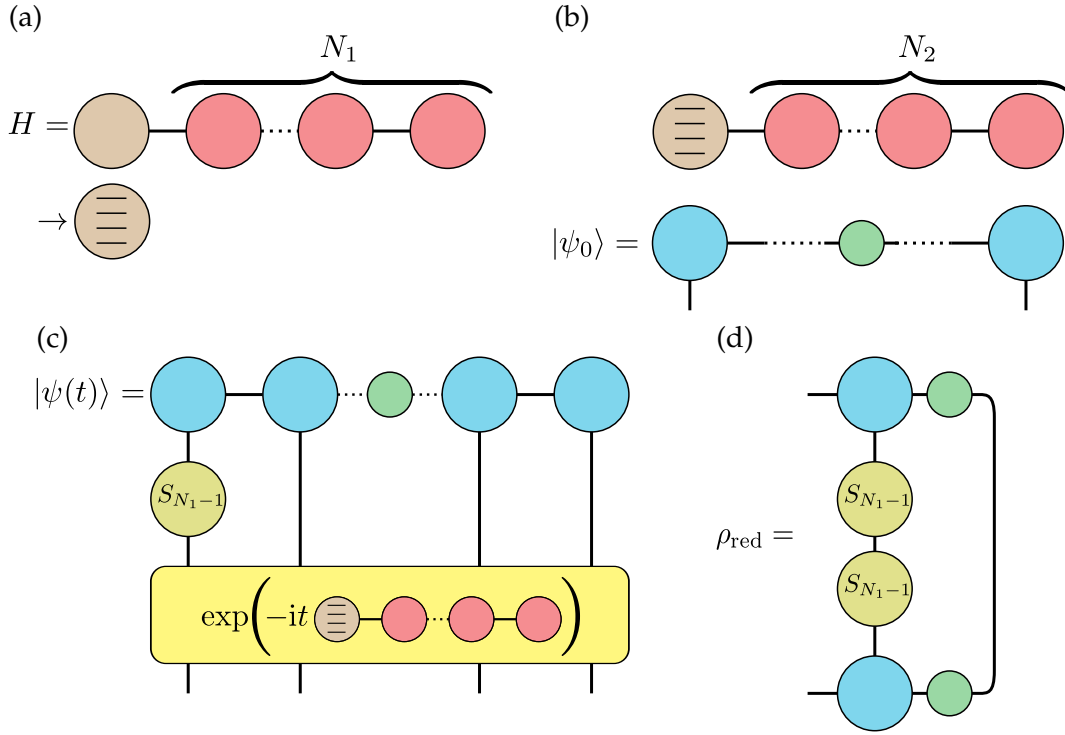


Figure 4.1: Sketch of the NRG+DMRG method. (a) Forward TD-NRG run: the initial, H_i , and final, H_f , Hamiltonian are diagonalized and represented as a hyper-impurity. (b) The hyper-impurity is coupled to the second Wilson chain and the ground state $|\psi_0\rangle$ of H_i is calculated using the DMRG. (c) The time-evolution of $|\psi(t)\rangle$ is calculated by applying the time-evolution operator $U = \exp(-iH_N^f t)$ of the final hyper-impurity attached to the second Wilson chain to $|\psi_0\rangle$. (d) Calculation of the reduced density matrix ρ_{red} which is fed into the backward iterations of the TD-NRG.

$$\text{and } H_{\text{mix}}^x = t_{N_1-1} \left(\left(\tilde{f}_{N_1-1}^x \right)^\dagger f_{N_1} + f_{N_1}^\dagger \tilde{f}_{N_1-1}^x \right), \quad (4.35)$$

where $x = i, f$. The operator f_n^\dagger with $n \geq N_1$ creates a fermion at site n of the original DWC. With $\left(\tilde{f}_{N_1-1}^x \right)^\dagger$ we denote the creation operator of the last chain site of the first Wilson chain, that is at site $n = N_1 - 1$, rotated in the basis in which $H_{N_1}^x$ is diagonal.

The TD-DMRG run, Fig. 4.1b, starts by calculating the ground state of H_N^i ,³

$$|\psi_0\rangle = A^0 A^1 \dots A^{\frac{N_2-1}{2}} \Lambda B^{\frac{N_2-1}{2}} \dots B^0. \quad (4.36)$$

Since the DMRG only targets the ground state all NRG+DMRG results are at temperature $T = 0$. This state describes a system consisting of a hyper-impurity coupled to a Wilson chain. Here A^n is the A-matrix corresponding to the site $N_1 + n$ for $n \geq 1$

³ In this equation we implicitly assume a summation over the physical indices $\{s_0, s_1, \dots, s_{N-1}\}$ and a multiplication with the basis state $|s_1 s_2 \dots s_{N-1}\rangle$. Written out, the ground state has the form Eq. (1.2).

and B^n is the A-matrix corresponding to site $N_1 + N_2 - n - 1$ of the original DWC. The basis of the A-matrices of the sites $n \geq 1$ is formed of the eigenstates of the number operator at this site; the basis at site $n = 0$ is the basis in which H_i is diagonal and hence A^0 is associated with the hyper-impurity.⁴

For the TD-DMRG one has to apply the time-evolution operator $U = e^{-iH_N^f t}$ to this state. As described in Sec. 1.4.3, the Trotter-Suzuki decomposition (TSD) of U is calculated and the two-site operators are consecutively applied to the matrix product state (MPS) $|\psi_0\rangle$. As $|\psi_0\rangle$ and H_N^f are not in the same basis one has to rotate $|\psi_0\rangle$. This concerns only the A-matrix corresponding to the hyper-impurity A^0 as all other A-matrices share the same basis with the corresponding matrix product operators (MPOs) of H_N^f . The rotation is carried out by replacing A^0 by

$$\tilde{A}^0[s'] = \sum_s A^0[s'] S_{s',s}(N_1 - 1). \quad (4.37)$$

Here, $S(N_1 - 1)$ is the overlap matrix of the last iteration of the forward NRG iteration (cf. Fig. 1.9). This matrix connects the Hilbert space of the initial Hamiltonian with the Hilbert space of the final Hamiltonian and is calculated in the course of the TD-NRG. Note, that due to the truncation of the Hilbert space this rotation is in general not complete: the complete Fock-space is only recovered after summing up the terms at all NRG iterations [77]. Formally, the rotation of A^0 and the application of the time-evolution operator U is depicted in Fig. 4.1c. This figure does not show the TSD of U .

With the TD-DMRG one can now calculate the low-energy contribution of a time-dependent expectation value

$$\langle A \rangle_{\text{low}}(t) = \langle \psi(t) | A | \psi(t) \rangle. \quad (4.38)$$

To compute the high-energy contribution one has to calculate the reduced density matrix ρ_{red} of the initial ground state $\{\tilde{A}^0, A^1, \dots, \Lambda, \dots, B^1, B^0\}$ by tracing out all sites $n \geq 1$, Sec. 1.2.5; the result is the reduced density matrix for the hyper-impurity, Fig. 4.1d, which is fed back into the backward iterations of the NRG. This yields the high-energy contribution $\langle A \rangle_{\text{high}}(t)$ and the expectation value of the observable A is given by

$$\langle A \rangle(t) = \langle A \rangle_{\text{low}}(t) + \langle A \rangle_{\text{high}}(t). \quad (4.39)$$

The control parameters of the NRG+DMRG are the number of states kept in the NRG N_s^{NRG} , the number of states kept in the DMRG N_s^{DMRG} , and the Trotter step δt . To

⁴ The superscripts of the A-matrices denote the position in the effective low-energy system – composed of an hyper-impurity with one Wilson chain – whereas the indices of the operators and hopping elements correspond to the original system and denote the position in the DWC.

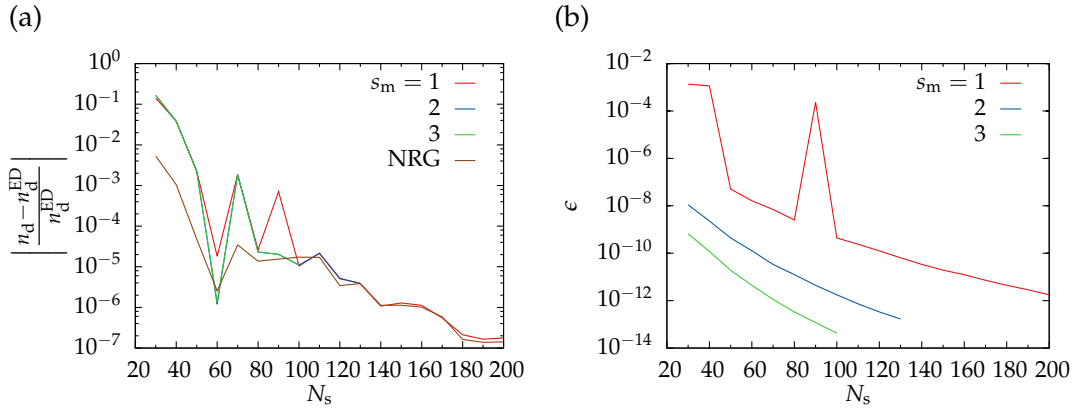


Figure 4.2: Numerical accuracy of the NRG+DMRG method tested on the basis of the RLM. (a) Comparison between the impurity occupation number calculated with the NRG+DMRG, n_d , and exact diagonalization (ED) results, n_d^{ED} (cf. Eq. (3.20)). The number of kept NRG states is $N_s^{\text{NRG}} = s_m N_s$. The NRG results are for a pure Wilson chain with N_1 sites. (b) DMRG Truncation error ϵ , Eq. (1.91), versus the number of kept DMRG states N_s . The parameters for both panels are $\Lambda_1 = 1.8, \Lambda_2 = 1.05, N_1 = 29, N_2 = 101, E = -\Gamma$, and $D = 10^5 \Gamma$.

reduce the available parameter space we set $N_s^{\text{DMRG}} = s_m N_s^{\text{NRG}}$ and the state multiplier s_m is an integer.

In the conventional TD-NRG one considers all states at the last iteration as discarded. In contrast, for the NRG+DMRG method one has to keep some of the states of the last NRG iteration to construct the hyper-impurity. In general the number of kept states at the last iteration is arbitrary. For all results in this thesis all states are kept. If one discards all states the TD-NRG is recovered.

In the next section we use the RLM as a testbed for the NRG+DMRG method. As shown Sec. 3.2, this model is exactly solvable and hence it can be used to examine the capabilities of the NRG+DMRG. After establishing the suitability of the NRG+DMRG for its purposes it in Chapter 5 is applied to the interacting resonant-level model (IRLM). Unlike the RLM the IRLM is not exactly solvable: there are no analytic results for the whole range of the interaction strength U , but we can compare the numeric results with analytic results in the $U \rightarrow \infty$ limit.

4.2 Hybrid method results for the resonant-level model

To benchmark the NRG+DMRG method presented above this section is devoted to the comparison between exact results for the RLM and results obtained with the NRG+DMRG method.

4.2.1 Choice of parameters

In equilibrium the accuracy of the simulation is controlled by the number of kept NRG states N_s^{NRG} and the number of DMRG states N_s^{DMRG} . For simplicity we only consider cases where $N_s^{\text{DMRG}} = s_m N_s^{\text{NRG}}$, and the state multiplier s_m being an integer. Hence, the two free parameters are the number of NRG states N_s and the state multiplier s_m .

In Fig. 4.2a the equilibrium occupation number of the impurity calculated with the NRG+DMRG method are compared to the ED results for the same system. The accuracy tends to increase with the number of states. On the other hand, the effect of the state multiplier on the accuracy is negligible: henceforth this parameter is set to $s_m = 1$. As expected, Fig. 4.2b shows that with an increasing number of states the DMRG truncation error shrinks. As the state multiplier influences the number of DMRG states the truncation error shrinks with increasing s_m . However, the accuracy of the Lanczos algorithm to calculate the ground state is set to 10^{-7} and thus sets a lower bound of the numerical accuracy, which is almost reached by the results in Fig. 4.2a. Because of this and due to the observation that increasing s_m does not improve the results, we presume that the main error is due to the NRG calculations.

To check this presumption Fig. 4.2a shows furthermore the error of a bare NRG calculation for a system consisting of the impurity coupled to the first Wilson chain: this is the hyper-impurity part of the NRG+DMRG calculation. For $N_s \leq 100$ the accuracy of the bare NRG calculation is by one order of magnitude higher than for the hybrid method. When further increasing the number of states, both methods yield the same accuracy. Note that the NRG calculation only solves the impurity with the first Wilson chain, whereas the NRG+DMRG method solves a system consisting of the impurity and a DWC.

In the following we are not interested in highly accurate results, but rather want to show the functionality of the NRG+DMRG method. If not stated differently, all following calculations are carried out with $N_s = 60$ states and the state multiplier $s_m = 1$.

4.2.2 Norm of initial state

The initial state $|\psi_0\rangle$ of the TD-DMRG time evolution is the ground state of a system consisting of the hyper-impurity and the second Wilson chain. This state is calculated with the DMRG in the basis of the initial Hamiltonian. For the time evolution this state has to be rotated in the basis of the final Hamiltonian. This can be done with the overlap matrix S of the last NRG iteration, Eq. (4.37).

The transformation from the initial to the final basis is unitary if and only if no states are discarded in the course of the NRG (forward) iterations. As this is in general not the case the transformation does not conserve the norm of the initial state, i.e. $\langle\psi_0|\psi_0\rangle < 1$.

The norm of $|\psi_0\rangle$ depends on various parameters:

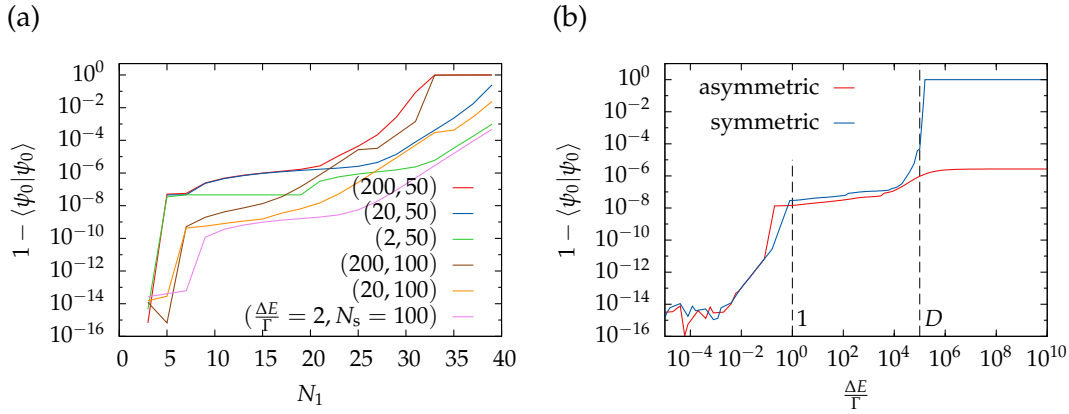


Figure 4.3: Norm of the initial state $|\psi_0\rangle$, i.e. the ground state of H^i , after its rotation in the basis of the final Hamiltonian for different parameters. (a) The length of the system is held constant, $N_1 + N_2 = 42$, and the partition site M is varied. The results are for a RLM coupled to a Wilson chain with $\Lambda_1 = \Lambda_2 = 1.8$, and $D = 10^5\Gamma$. The numbers in the legend give the energy difference $\Delta E = \frac{E_f}{2} = -\frac{E_i}{2}$ and the number of kept states N_s in the form $(\frac{\Delta E}{\Gamma}, N_s)$. The state multiplier between the number of NRG and DMRG states is $s_m = 1$. (b) For the symmetric switch the energies are given by $-E_i = E_f = \frac{\Delta E}{2}$ and in the asymmetric case $E_i = \Delta E, E_f = 0$. The chain parameters are $N_1 = 34, N_2 = 5, \Lambda_1 = \Lambda_2 = 1.8, N_s = 70, s_m = 1$, and $D = 10^5\Gamma$.

- (i) **Chain partition:** Fig. 4.3a shows the norm for different chain partitions. Here the total length of the chain is kept constant, $N_1 + N_2 = 42$, and the partition site is moved through the chain. The first N_1 sites of the chain are solved with the NRG to build the hyper-impurity and the DMRG solves a system consisting of the hyper-impurity and N_2 sites; the underlying physical model is independent of the partitioning.

All curves in Fig. 4.3a show the same principle behavior: the deviation of the norm from 1 rises with for $N_1 \gtrsim 20$ and show a plateau for $7 \lesssim N_1 \lesssim 20$. The norm of the initial state $|\psi_0\rangle$ depends on the overlap matrix S . If one retains all states during the NRG run this matrix is unitary, no norm is lost in the rotation from the initial to the final basis, and hence the $\langle \psi_0 | \psi_0 \rangle = 1$. However, in general one does not retain all states and therefore the loss of spectral weight is due to an incomplete rotation with the S matrix. If one increases the chain length N_1 in total more states are truncated and this implies that the overlap between the subspaces of H_i and H_f shrinks.

- (ii) **Number of states:** The more states are retained in the NRG run, the greater is the overlap between the truncated H_i and H_f subspaces. Therefore the norm gets closer to one if one increases the number of retained states (cf. Fig. 4.3a).

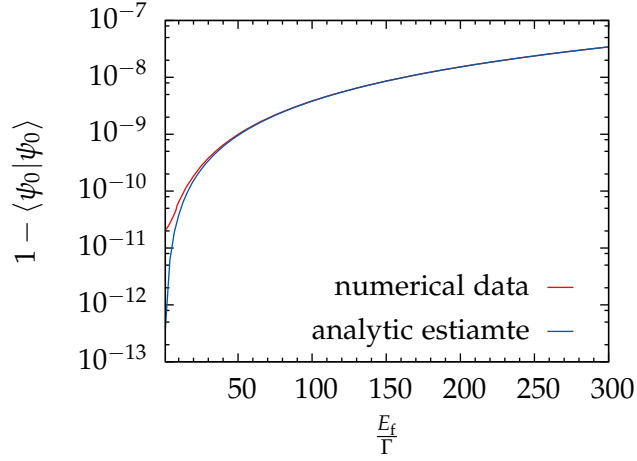


Figure 4.4: Norm of the initial state $|\psi_0\rangle$ after its rotation in the basis of the final Hamiltonian for different E_f . The chain parameters are $D = 10^5\Gamma$, $N_1 = 15$, $N_2 = 27$, and $\Lambda_1 = \Lambda_2 = 1.8$. $N_s = 110$, $s_m = 1$ states are kept. The initial energy is $E_i = -E_f$. The analytic curve is calculated with Eq. (4.41) and $V = 5.7 \cdot 10^5$ is the best-fit parameter.

- (iii) **Energy difference:** It is clear that the completeness of a rotation with the overlap matrix S has to depend somehow on the similarity between the initial Hamiltonian H_i and the final Hamiltonian $H_f = H_i + \delta H$. If the difference δH is small one expects that the truncated subspaces of both Hamiltonians should almost be the same, whereas one expects to find large deviations for strong differences.

To estimate the dependence of the overlap on the energy we consider a system consisting only of the impurity level and the first Wilson chain site,

$$H = E(t)d^\dagger d + V(d^\dagger c_0 + c_0^\dagger d). \quad (4.40)$$

The annihilation operators on the two sites are d and c respectively, V is the hybridization and $E(t) = E_i\Theta(-t) + E_f\Theta(t)$ is the impurity energy. For a symmetric switch, $-E_i = E_f = E$, the overlap $\langle\psi_0^i|\psi_0^f\rangle$ of the ground states of the initial and the final Hamiltonian is given by

$$\langle\psi_0^i|\psi_0^f\rangle = \frac{2}{\sqrt{\frac{E^2+4V^2}{V^2}}}. \quad (4.41)$$

Of course, this estimate is very crude and does not take any truncation effects or influences from the rest-chain into account. However, the qualitative shape of the curve is correct (cf. Fig. 4.4) and proves the claim that the difference between the initial and final Hamiltonian has an effect on the overlap matrix elements. To be

precise, the difference is caused by the overlap of the eigenstates and is therefore a result of the energy difference.

For large energy differences and symmetric switching the limit of Eq. (4.41) is given by

$$\lim_{E \rightarrow \infty} \langle \psi_0^i | \psi_0^f \rangle = 0. \quad (4.42)$$

However, in the case of an asymmetric switch, if one switches from an arbitrary $E_i < 0$ to $E_f = 0$, the overlap of the ground states is given by

$$\langle \psi_0^i | \psi_0^f \rangle = \frac{1}{2} \frac{2V + E_i + \sqrt{E_i^2 + 4V^2}}{\sqrt{E_i^2 + E_i \sqrt{E_i^2 + 4V^2} + 4V^2}} \quad (4.43)$$

and in this case the limit is given by

$$\lim_{E_i \rightarrow \infty} \langle \psi_0^i | \psi_0^f \rangle = \frac{\sqrt{2}}{2}. \quad (4.44)$$

In this case the overlap does not vanish for large E_i .

By the loss of norm of the initial state one can distinguish different regimes. Fig. 4.3b shows that for a symmetric switch the overlap vanishes for large $\Delta E = |E_f - E_i|$ and approaches a constant in the asymmetric case. This is in agreement with the analytic estimates, Eq. (4.43). Furthermore, one can identify three different regimes: (i) disregarding numerical noise, the overlap $\langle \psi_0 | \psi_0 \rangle = 1$ for $\Delta E \lesssim \Gamma$: in this case only the effective low-energy Hamiltonian is relevant and there is no need for the NRG backward iterations. (ii) In the range $\Gamma \lesssim \Delta E \lesssim D$ the overlap is of the order $1 - \langle \psi_0 | \psi_0 \rangle \sim \mathcal{O}(10^{-8})$. Hence, there are small corrections due to the coupling between high-energy and low-energy states. (iii) For $D \lesssim \Delta E$ and a symmetric switch the overlap vanishes, $\langle \psi_0 | \psi_0 \rangle = 0$: the low-energy states are negligible as all the dynamics happens in the high-energy sector and in this case there is no advantage of the NRG+DMRG method over a conventional TD-NRG run. However, in the asymmetric case the final state lies in the low-energy sector and therefore one cannot discard this sector.

This means that if both energies fulfill $E_i, E_f \lesssim \Gamma$ it is save to neglect the backward NRG iterations; for $D \lesssim E_i, E_f$ one can perform a conventional TD-NRG run with only the first Wilson chain; and in all other cases one has to use the hybrid method in order to allow for excitations between the high- and low-energy sectors.

Concluding, the loss of norm is caused by the truncation of states. In general one needs all states of the initial Hamiltonian to represent one state of the final Hamiltonian. Due to the truncation the high energy states are not available anymore and

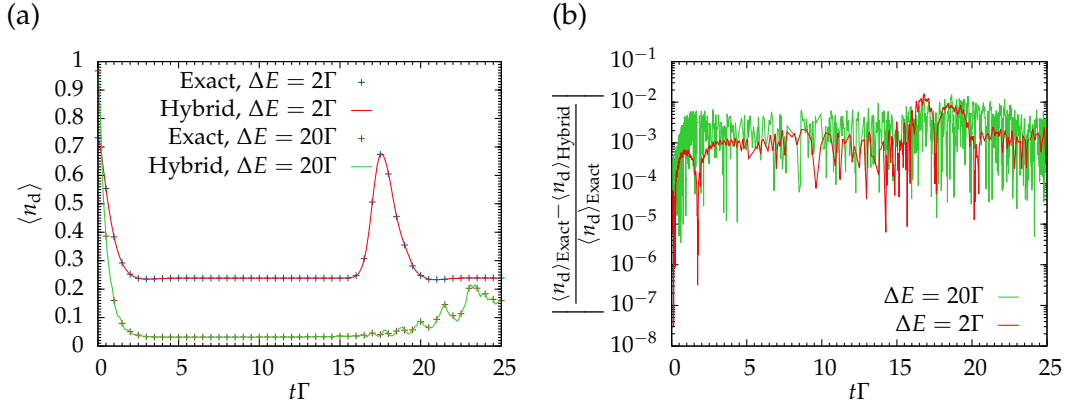


Figure 4.5: Time-dependent impurity occupation number $\langle n_d \rangle$ for $-E_i = E_f = \frac{\Delta E}{2}$ for the RLM. (a) Comparison of NRG+DMRG with ED (cf. Eq. (3.20)) results: the curves lie on top of each other. (b) Relative difference of the curves shown in the left panel. The chain parameters are $N_1 = 30, N_2 = 101, \Lambda_1 = 1.8, \Lambda_2 = 1.02, N_s = 60, s_m = 1$, and $D = 10^5\Gamma$.

therefore the representation in the initial basis is incomplete. In the NRG one recovers the complete basis by taking into account terms on all energy scales [77].

4.2.3 Time-dependence

The results presented in the previous sections are merely for the equilibrium case. The main advantage of the NRG+DMRG method is to track the real-time dynamics of strongly correlated systems with a large bandwidth. Hence in this section we show the accuracy of this method by demonstrating that it reproduces the ED results of the RLM. Once the reliability of the method is proven, the method can be applied to models lacking an exact solution.

In this section we focus on comparing the NRG+DMRG with the ED results obtained for the RLM with Eq. (3.20); we no longer compare the results to the continuum solution as it was already shown in Sec. 3.2 that by using a DWC one can reproduce the continuum results. In the following all calculations are carried out for an impurity coupled to a DWC.

As argued in Sec. 1.4.3 the Trotter time step of the TD-DMRG has to be chosen smaller than the inverse bandwidth D . As a consequence an increasing bandwidth makes it harder to perform the simulation for the TD-DMRG. We want to show that the NRG+DMRG method is able to simulate systems with a large bandwidth (compared to Γ) very accurately and therefore show results for $D = 10^5\Gamma$.

Impurity occupation number

Fig. 4.5a shows the time-dependent impurity occupation after a sudden local quench, at which the position of the impurity level position is shifted $E_i \rightarrow E_f$ at $t = 0$. The chain

is solved with ED, Eq. (3.20), and these results are compared with the NRG+DMRG results: both curves lie on top of each other. To quantify this further, Fig. 4.5b shows the relative difference between the curves. This value is for $t = 0$ of the order $\mathcal{O}(10^{-6}) - \mathcal{O}(10^{-5})$ and for $t\Gamma > 0$ it approaches $\mathcal{O}(10^{-3})$. The $\Delta E = 2\Gamma$ curve in Fig. 4.5a shows at $t\Gamma \approx 17.6$ a peak of almost the height of the initial occupation. This indicates that the charge-wave propagates through the whole chain and is reflected at the end of the chain: almost no charge is reflected internally. This is different for the larger quench, $\Delta E = 20\Gamma$: for $t\Gamma \gtrsim 15$ small wiggles appear. Hence, not the whole charge is reflected and these wiggles are therefore due to reflections within the Wilson chain.

Before the reflections arrive at the impurity the impurity occupation number in Fig. 4.5a reaches a steady-state value. This value depends on the final impurity level E_f . If the system shows true thermalization the steady-state value of the impurity occupation for the time-evolution is equal to the equilibrium impurity occupation number of the final system. As size of the system is finite it cannot thermalize as a whole; however, it is possible that a subsystem thermalizes [159]. For thermalization all expectation values have to be time-independent and must take the equilibrium values of the final system. In general, it is not enough to define thermalization just over one expectation value, e.g. the impurity occupation number. Because it is cumbersome to calculate and compare all independent expectation values we use the fidelity F , Eq. (1.19), to quantify the degree of thermalization.

Fidelity

The fidelity measures the distance between two reduced density matrices. Here, these density matrices correspond to the time-dependent density matrix $\rho(t) = e^{-iH_f t} \rho_0 e^{iH_f t}$, with $\rho_0 = \frac{1}{Z_i} e^{-\beta H_i}$, calculated by the TD-DMRG and the equilibrium density matrix $\sigma = \frac{1}{Z_f} e^{-\beta H_f}$ of the final system. Here Z_x is the partition sum for the initial ($x = i$) and the final ($x = f$) system and, since the DMRG targets the ground state, the inverse temperature is $\beta \rightarrow \infty$.

As only a subsystem is able to thermalize we partition the whole system in two subsystem, where the system part is formed by the hyper-impurity and the environment by the second Wilson chain. Thus, the reduced density-matrices are obtained by tracing over the environment degrees of freedom.

Technically the reduced density matrix $\rho_S(t) = \text{Tr}_E [\rho(t)]$ is obtained from the A-matrix corresponding to the hyper-impurity; this is the A-matrix A^0 of the time-dependent MPS (cf. Fig. 1.3b). To obtain the reduced density matrix $\sigma_S = \text{Tr}_E [\sigma]$ of the final system one has to calculate the ground state of H_f employing an additional equilibrium DMRG run. An additional NRG run is not necessary as for the TD-NRG both the initial and the final Hamiltonian are diagonalized in any case.

The time evolution of the fidelity for two different quenches is shown in Fig. 4.6a. The value at $t = 0$ gives the fidelity for the initial and final system. For an increasing

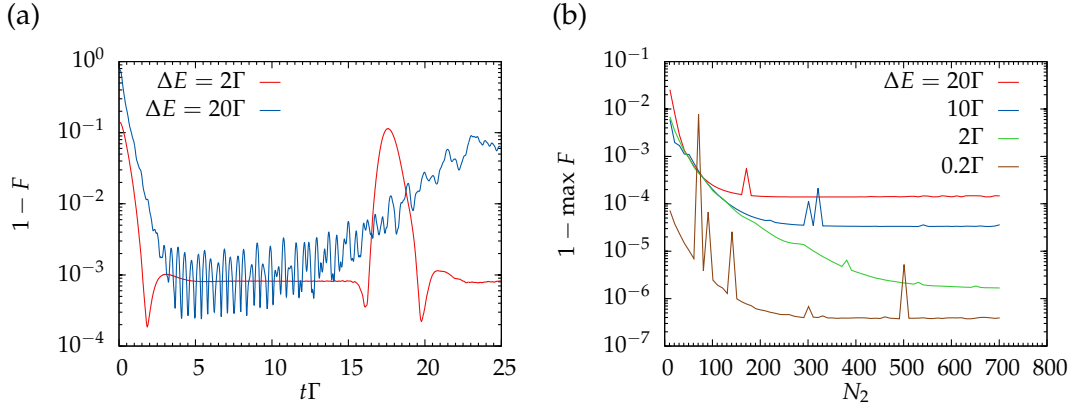


Figure 4.6: Fidelity F , Eq. (1.19), of the subsystem consisting of the impurity with N_1 Wilson chain sites for the time-dependent reduced density matrix and thermal reduced density matrix of the final Hamiltonian. (a) Time-dependent and (b) maximum fidelity with chain and model parameters from Fig. 4.5.

energy difference ΔE the ground states of the final and initial Hamiltonian move away from each other and thereby lowering the fidelity. With the time evolution the fidelity approaches the value $F = 1$ indicating that the system thermalizes. For $\Delta E = 2\Gamma$ one can still observe the reflection at the end of the chain as a dip in the fidelity. The reason for the oscillations of the fidelity in the $\Delta E = 20\Gamma$ curve is that in this case charge is transferred into the first Wilson chain due to internal reflections; with regard to the reduced density matrix $\rho_S(t)$ this part of chain is the considered the system and thus charge moving into and from the system creates oscillations in the fidelity.

The maximum fidelity F for different number of sites in the second Wilson chain N_2 and energy differences is shown in Fig. 4.6b. For smaller energy differences the initial and final state are closer to each other and therefore the maximum fidelity is larger. A long second Wilson chain is better suited to represent the continuous bath; hence, the fidelity grows with increasing N_2 .

However, for large N_2 the curves saturate at a ΔE dependent value. One reason are the numerical errors during the time-evolution which prevent the initial state to evolve into the final state. Another reason is the first Wilson chain: the discretized high-energy modes of the bath are represented by the first Wilson chain. The importance of these states for the time-evolution grows with the energy difference ΔE , as for a large quench more high-energy states are excited than for a small quench. Hence, the fidelity for $N_2 \rightarrow \infty$ cannot reach one, but approaches one for $\Delta E \rightarrow 0$.

These studies of the fidelity show that the system equilibrates into a thermal state, which is equal to the equilibrium ground state of the final Hamiltonian.

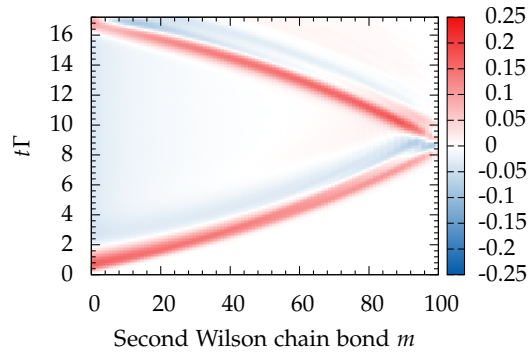


Figure 4.7: Time-dependent difference of von Neumann entropy $S_m = S_m(t) - S_m(t = 0)$, Eq. (1.22), of the m th bond of the second Wilson chain. Same parameters as Fig. 4.5.

Von Neumann entropy

To visualize the propagation of the charge wave through the second chain Fig. 4.7 shows the von Neumann entropy calculated with Eq. (1.22). The plot shows the difference of entropy between $t = 0$ and t for a bipartitioning of the system at bond m . The propagation of the charge wave is clearly visible and follows the expected form (cf. Fig. 3.11a). Note, that Fig. 4.7 shows only the second Wilson chain of the DWC as the first chain is incorporated in the hyper-impurity. Thus bond $m = 0$ in Fig. 4.7 is the bond connecting the hyper-impurity with the second Wilson chain. The plot shows, that the time at which the von Neumann entropy wave reaches bond $m = 0$ is almost the same at which the fidelity drops (cf. Fig. 4.6a) and the impurity occupation shows a peak (cf. Fig. 4.5a).

4.3 Summary

The purpose of this chapter was to introduce the new hybrid method and to show its applicability. After introducing and discussing the new versatile hybrid method for the general case – with unspecified impurity, chain, and second method – we explicitly showed how to hybridize the numerical renormalization group (NRG) with the density-matrix renormalization group (DMRG). Here, the NRG generates an effective low-energy Hamiltonian which is, in turn, solved with the DMRG. This scheme allows to solve models employing the concept of hybrid chains introduced in Chapter 3.

Using the numerical renormalization group density-matrix renormalization group hybrid (NRG+DMRG) method we first discussed the loss of norm of the initial state due to the incomplete basis rotation needed to rotate the state from the eigenbasis of the initial into the eigenbasis of the final Hamiltonian. We ascribed the loss of norm to the overlap between the Hilbert spaces of the initial and final Hamiltonian. This depends on the number of kept NRG states, the initial and final positions of impurity

level, and the length of the Wilson chain. Due to the complete Fock space summation the loss of norm is compensated in the subsequent backward NRG iterations.

We showed data for the time-dependent impurity occupation number calculated with the NRG+DMRG method and compared these with exact diagonalization (ED) data: here we found an excellent agreement. To prove that the time-evolution of the NRG+DMRG evolves the initial state into the ground state of the final Hamiltonian we calculated the fidelity. Lastly, the bond-dependent von Neumann entropy showed that the charge wave propagates through the chain as expected from preliminary studies in which the resonant-level model (RLM) was solved exactly (cf. Chapter 3).

Conclusively, we have provided plenty of evidence that the new hybrid method works excellent. In the next chapter this method and the concept of hybrid chains is applied to the interacting resonant-level model (IRLM), a model which is not exactly solvable.

Nonequilibrium Simulations of the Interacting Resonant-Level Model

In the previous chapter it was shown that the numerical renormalization group density-matrix renormalization group hybrid (NRG+DMRG) method yields excellent results for the resonant-level model (RLM). As the RLM is exactly solvable it is perfectly suited to benchmark our new method. Now we add an interaction term, accounting for the Coulomb repulsion U between the impurity electron and the lead electrons, to the RLM Hamiltonian in order to construct the interacting resonant-level model (IRLM) [23, 147]. This model is no longer exactly solvable and, therefore, one has to rely on approximative methods or limiting cases to make statements about physical properties. Hence, before presenting the results of our studies we shortly give a brief overview of other studies dealing with the IRLM.

The renormalization group (RG) and functional RG [160] approaches have proven fruitful for dealing with the IRLM. Using the real time RG [161] it is possible to calculate transport properties: a quantum dot (QD) is coupled to two leads and is therefore described by an IRLM with two conduction bands. By shifting the chemical potential of both bands in different directions a voltage is applied to the QD. In the regime of strong charge fluctuations [162, 163] or in the scaling limit [164] some nonequilibrium properties for this setup can be determined employing the real time RG or functional RG respectively. Using the time-dependent density-matrix renormalization group (TD-DMRG) the current and conductance are measured for the same setup [165, 166, 167] or for a similar model in which a single Hubbard site is coupled to two leads [94]. Refs. 148, 168 investigate the IRLM with a different number of leads employing bosonization, the Anderson-Yuval approach, and the numerical renormalization group (NRG). Other methods applied to the IRLM include Bethe ansatz [22, 169] or perturbative methods [170].

When considering the two ground states of the IRLM with two different interaction parameters U_i and U_f or the two ground states of the RLM with two different level positions – for example the initial and the final state of the quench dynamics discussed

in Sec. 4.2 – these ground states are orthogonal in the thermodynamic limit. This is the so-called Anderson orthogonality catastrophe [171]. In Refs. 172, 173 the IRLM served as testbed to examine the effects of the Anderson orthogonality catastrophe in the NRG.

With the concept of the Anderson orthogonality catastrophe in mind one might ask the question how a system is able to thermalize; or in other words, how is it possible to start from the ground state $|I\rangle$ of the initial Hamiltonian and to let this state unitarily evolve under H_f until it equilibrates in the ground state $|F\rangle$ of the final Hamiltonian, even though $|I\rangle$ and $|F\rangle$ are orthogonal?¹ Of course, the answer is that this is not possible. Nevertheless one observes thermalization, for example in Fig. 3.12. However, what one observes is not thermalization of the total system but only of a subsystem and this is possible even though the total system does not thermalize [159, 174]. This is why our fidelity graphs – Fig. 4.6 and Fig. 5.6 below – show the distance between two reduced density-matrices and not between the time-dependent density matrix of the total system and the equilibrium density matrix of the final Hamiltonian.

In this chapter we first present the IRLM and then discuss renormalization effects for the level width Γ due to the Coulomb repulsion U . Using the NRG+DMRG method, the renormalized Γ is determined numerically. Accounting for the renormalization of Γ we calculate the time-dependent impurity occupation number for different values of U after a sudden local quench and discover the emergence of oscillations. These are explained in a strong coupling treatment of the model. The results of the strong coupling treatment for the oscillation frequency and damping rate agree for large U excellent with the numerical data. However, the NRG+DMRG method is capable of solving the IRLM in the whole parameter regime.

Furthermore, we calculate the fidelity to show that the initial state evolves into the ground state of the final Hamiltonian. At the end of the chapter we discuss the numerical errors thereby justifying some of our parameter choices and briefly discuss our expectations if one would simulate the same systems with the TD-DMRG.

5.1 Model Hamiltonians

The Hamiltonian of the IRLM is given by

$$H = E_d d^\dagger d + \frac{V}{\sqrt{N_l}} \sum_k (c_k^\dagger d + d^\dagger c_k) + U \left(d^\dagger d - \frac{1}{2} \right) \frac{1}{N_l} \sum_{k,k'} : c_k^\dagger c_{k'} : + \sum_k \epsilon_k c_k^\dagger c_k. \quad (5.1)$$

Here d^\dagger creates an electron on the level and c_k^\dagger creates a band electron with momentum k . N_l is the number of k -values. The energy of the local level, which we later assume to be time-dependent, is E_d and the band dispersion is given by ϵ_k . V is the coupling

¹ Strictly speaking the states are only orthogonal in thermodynamic limit.

strength between the impurity and the band. $: c_k^\dagger c_{k'} : = c_k^\dagger c_{k'} - \delta_{k,k'} \theta(-\epsilon_k)$ stands for normal ordering with respect to the filled Fermi sea. The contact interaction U accounts for the capacitive coupling between the local level and the band.

For the IRLM to be treatable with the NRG the bath has to be mapped to a finite Wilson chain, Sec. 1.3.1. Essentially, this yields the discretized Hamiltonian of the RLM, Eq. (3.2), with an additional interaction term. Thus the Hamiltonian of the discretized IRLM with a constant and symmetric density of states (DOS) reads

$$H_N = E_d d^\dagger d + V \left(d^\dagger c_0 + c_0^\dagger d \right) + U \left(d^\dagger d - \frac{1}{2} \right) \left(c_0^\dagger c_0 - \frac{1}{2} \right) + \sum_{n=0}^{N-1} t_n \left(c_n^\dagger c_{n+1} + c_{n+1}^\dagger c_n \right). \quad (5.2)$$

Now, c_n^\dagger and c_n denote the creation and annihilation operators of the n th Wilson chain site. As we are interested in a bath with a constant DOS the parameters t_n are, for a Wilson chain, given by Eq. (1.39). For other choices of chains one has to take the appropriate chain parameters as discussed in Sec. 3.3. Through our preliminary studies based on the RLM we know that the optimal choice for the bath discretization is a double Wilson chain (DWC); hence, this kind of hybrid chain is employed in this chapter.

In this section this Hamiltonian is solved with the NRG+DMRG method. As for the RLM, we are interested in tracking the time evolution of the impurity occupation number $n_d(t) = \langle d^\dagger d \rangle(t)$ after a quench at $t = 0$ from $E_d = E_i$ to $E_d = E_f$.

5.2 Fixed point properties

At low energies the Coulomb repulsion U causes a renormalization of the level width Γ [23] and the IRLM has the same fixed point as the RLM. The crossover from the free orbital fixed point to the low energy fixed point is governed by an effective Γ . The effective level width Γ_{eff} can be tuned by varying the bare model parameter Γ . These two quantities are connected by [90]

$$\Gamma_{\text{eff}} = D \left(\frac{\Gamma}{D} \right)^{\frac{1}{1+\alpha}}, \quad (5.3)$$

where $\Gamma = \pi\rho V^2$ is the non-interacting hybridization width and

$$\alpha = 2\tilde{\delta} - \tilde{\delta}^2 \quad \text{with} \quad \tilde{\delta} = \frac{2}{\pi} \arctan \left(\frac{\pi\rho U}{2} \right). \quad (5.4)$$

As the IRLM and RLM share the same low energy fixed point the thermodynamic properties are the same and, therefore, one could expect that dynamic properties are the same as well. This is not the case: due to the repulsive Coulomb interaction the

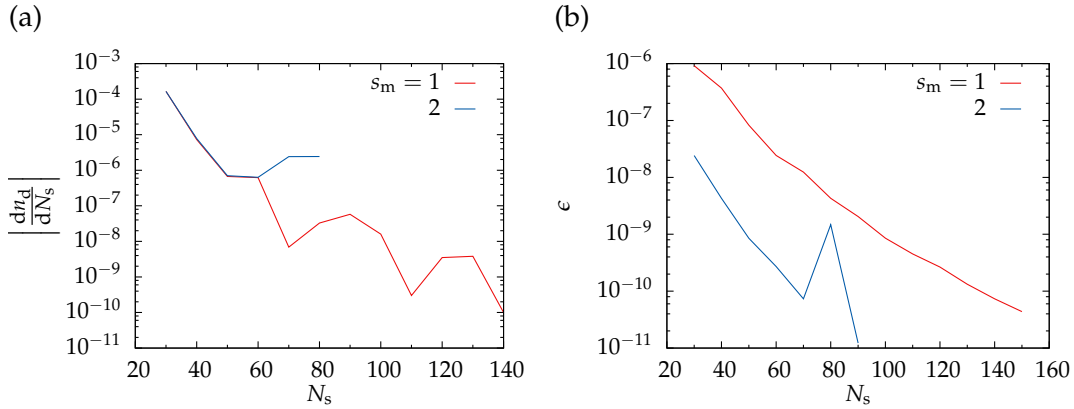


Figure 5.1: Numerical accuracy of the NRG+DMRG method for solving the IRLM. (a) Derivative of the impurity occupation number. (b) Truncation error ϵ , Eq. (1.91). The parameters for both panels are $\Lambda_1 = 1.8, \Lambda_2 = 1.02, N_1 = 29, N_2 = 151, E = -\Gamma$, and $D = 10^5 \Gamma$.

IRLM favors both the impurity and the first Wilson chain site to be half filled, in addition it suppresses charge fluctuations. This leads to Rabi-like oscillations (see Appendix D) and introduces a new U dependent time scale.

To measure transport properties one can extend the IRLM to the case of two leads. In particular, the case in which one applies a voltage and calculates the steady-state current is interesting. As expected, increasing the voltage increases the current. However, one observes a negative differential conductance as well: in some cases the current decreases with increasing voltage [165]. Perturbative treatments suggest that this effect is due to a renormalization of the hopping amplitude [168, 175].²

This work considers only the IRLM with one lead, because we are mainly interested in a proof-of-principle for our new hybrid method. However, we are confident that the hybrid method is also applicable to the case of two leads and could make valuable contributions.

5.3 Choice of parameters

Unlike the RLM the IRLM is not exactly solvable and thus one cannot compare the NRG+DMRG results to exact diagonalization (ED) calculations as in Sec. 4.2.1. Hence, one has to compare results for different number of states N_s and state multipliers s_m to determine the optimal parameters. Optimal in this sense is that the number of kept states is as low as possible to reduce the numerical demands and that increasing the number of states does not improve the results further.

Fig. 5.1a shows that the change of the occupation number with the number of state N_s is the same for $s_m = 1$ and $s_m = 2$ for $N_s \leq 60$. For $N_s > 60$ the derivative is of

² A different explanation is given in Ref. 176.

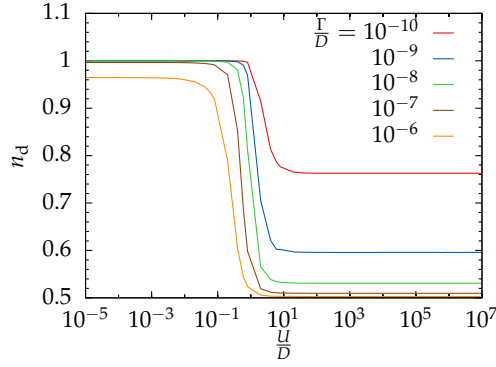


Figure 5.2: Equilibrium impurity occupation n_d versus interaction strength U for different Γ for the ground state of the IRLM calculated with the NRG+DMRG method. The position of the impurity level is $E_d = -10^{-5}D$. The bandwidth D serves as energy unit. The chain parameters are $\Lambda_1 = 1.8$, $\Lambda_2 = 1.02$, $N_1 = 29$, and $N_2 = 151$.

the same order as the Lanczos error and furthermore, occasionally, it changes its sign (not visible in the plot). That the $s_m = 1$ and $s_m = 2$ curve start deviating at $N_s = 60$ indicates that the change of the occupation at the precision $\sim 10^{-7}$ is dominated by numerical errors. Hence, for all following calculations we choose $N_s = 60$ and $s_m = 1$. This choice is justified, as well, by the truncation error, which is below the Lanczos error (cf. Fig. 5.1b).

5.4 Determining effective Γ

As argued in Sec. 5.2 the RLM and IRLM share the same low energy fixed point, with a renormalized level width Γ_{eff} depending on U . To produce comparable results for different values of U all calculations are carried out with an equal effective level width Γ_{eff} for all U values. Hence for each set of parameters the bare Γ has to be tuned in such a way that $\Gamma_{\text{eff}} = 1$. This section shows how this is achieved.

The numerical value of the parameter Γ for which $\Gamma_{\text{eff}} = 1$ holds does not just depend on U , but, in principle, depends on the choice of the chain parameters. However, because Γ is determined in equilibrium this dependence is very weak. Furthermore, when one chooses a value for Γ which is slightly off the value needed for this chain this would cause a small shift in the impurity occupation and a slightly detuned time scale. The qualitative behavior of the system does not change.

As the repulsive Coulomb interaction favors the impurity level to be half-filled we expect for $E_d < 0$ a shrinking impurity occupation $n_d = \langle d^\dagger d \rangle$ for increasing U ; that this is indeed the case is shown in Fig. 5.2. Furthermore, for the bare $\Gamma \rightarrow 0^+$ the hybridization V shrinks resulting in a completely filled impurity for $E_d < 0$ (cf. Fig. 5.2).

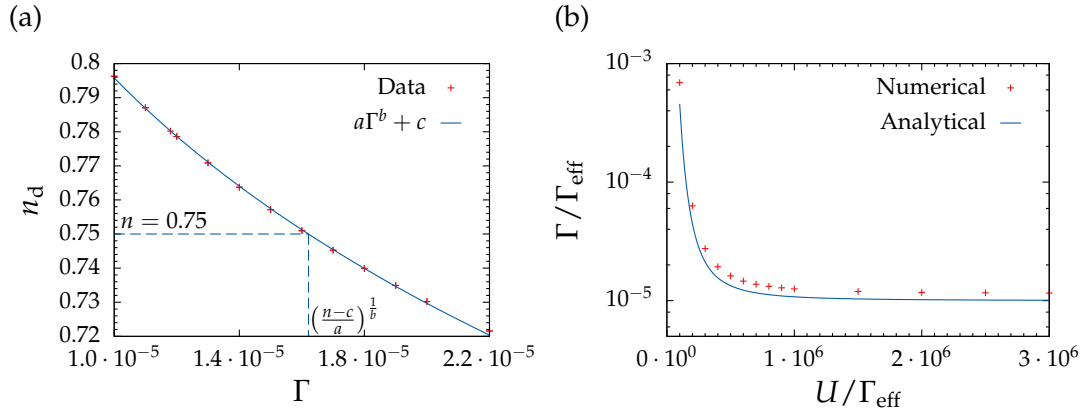


Figure 5.3: Determining effective Γ . (a) Γ scan for IRLM. To keep Γ_{eff} constant, Γ is set to the value at which the impurity occupation of the $U \neq 0$ and $U = 0$ case coincide. This figure shows an example of a Γ scan for $U = 5 \cdot 10^5 \Gamma_{\text{eff}}$, which has to be done for each value of U . The horizontal dashed line indicates the $U = 0$ occupation. (b) Numerical determined Γ which implies $\Gamma_{\text{eff}} = 1$ for different U . The analytical curve was calculated solving Eq. (5.3) for Γ ; this yields $\frac{\Gamma}{\Gamma_{\text{eff}}} = \left(\frac{\Gamma_{\text{eff}}}{D}\right)^\alpha$. The chain parameters of both plots are the same as Fig. 5.2.

When increasing U the parameter Γ is tuned in such a way that Γ_{eff} is the same for all values of U . To achieve this, a Γ scan is performed for each U value (cf. Fig. 5.3a) and the impurity occupation is compared to the non-interacting case. As in Sec. 3.3.3, to find the value at which the occupation of the interacting case coincides with the occupation of the non-interacting case, we interpolate the data points with a power-law function. Comparing the numerical values for Γ with the analytic values calculated with Eq. (5.3) shows a good qualitative agreement (cf. Fig. 5.3b).

In the following calculations, for all different sets of chain parameters the bare value of Γ is set to the value which implies $\Gamma_{\text{eff}} = 1$; hence, Γ_{eff} serves as the energy unit.

5.5 Time dependence

As for the non-interacting case, we investigate the behavior of the IRLM after a sudden quench at $t = 0$, when the local level is shifted from E_i to E_f , by tracking the time-evolution of the impurity occupation number $n_d(t)$ (cf. Fig. 5.4). Since the non-interacting and the interacting model operate with the same effective level width Γ_{eff} the initial value $n_d(t = 0)$ is independent of the Coulomb repulsion U . The final steady-state value reached after a quench at $t = 0$ for $U > 0$ coincides with the thermal expectation value of the final Hamiltonian.

For $U > 0$ damped oscillations emerge due to which the thermal value of the final Hamiltonian is reached at later times as compared to the $U = 0$ case. For increasing U the time needed to reach the steady-state increases. In Fig. 5.4a for $U = 3D$ the charge, which is reflected at the end of the DWC, arrives at the impurity before the system

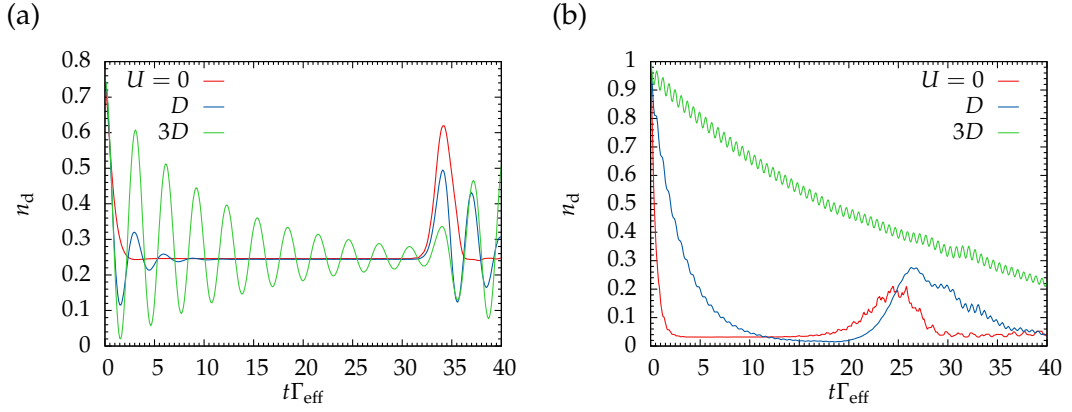


Figure 5.4: Time-dependent impurity occupation number for the IRLM with different interaction strengths U calculated with the NRG+DMRG method with (a) $-E_i = E_f = \Gamma_{\text{eff}}$ and (b) $-E_i = E_f = 10\Gamma_{\text{eff}}$. Same chain parameters as in Fig. 5.2.

reaches the steady-state. Comparing the $\Delta E = 2\Gamma_{\text{eff}}$ data (Fig. 5.4a) to the $\Delta E = 20\Gamma_{\text{eff}}$ data (Fig. 5.4b) shows that the damping and frequency of the oscillations, and the decline of the envelope depend on the quench strength ΔE .

One observation is that in Fig. 5.4a, this means for a small quench, both the $U = 0$ and the $U = D$ curves reach the steady-state. Furthermore the reflection peak due to the charge reflected at the end of the DWC appears in the impurity occupation number in both cases at the same time. In contrast to that, for a large quench, Fig. 5.4b, the reflections within the Wilson chain of the $U = 0$ arrive earlier at the impurity than for $U = D$: due to the interaction, the rate at which the charge is injected into the chain is suppressed. The current injected into the DWC is therefore smaller and thus the reflections occur at later sites of the DWC. This means that, unlike for a small quench, for a large quench, when the reflections occur within rather than at the end of the DWC, the time scale on which the back-moving charge wave reaches the impurity depends on U .

We want to test if for a small quench, that is, the dominant reflections occurs at the end of the DWC, the time scale on which the reflections reach the impurity depend on U . Therefore, Fig. 5.5 shows the time-dependent impurity occupation number for three different values of U and different sizes of the second Wilson chain N_2 . By increasing the length of the second Wilson chain the reflection peak is moved to longer time scales. For all three values of U the curves with different N_2 lie on top of each other up to a certain time t_{max}^{81} at which the $N_2 = 81$ curve starts to deviate from the other two curves: the short-time behavior is recaptured faithfully even with small chains, but if one is interested in the behavior on long times scales one has to choose a chain with enough sites to delay the reflections. By comparing the different U curves one observes that the deviation time t_{max}^{81} is the same for all values of U : this indicates that the time

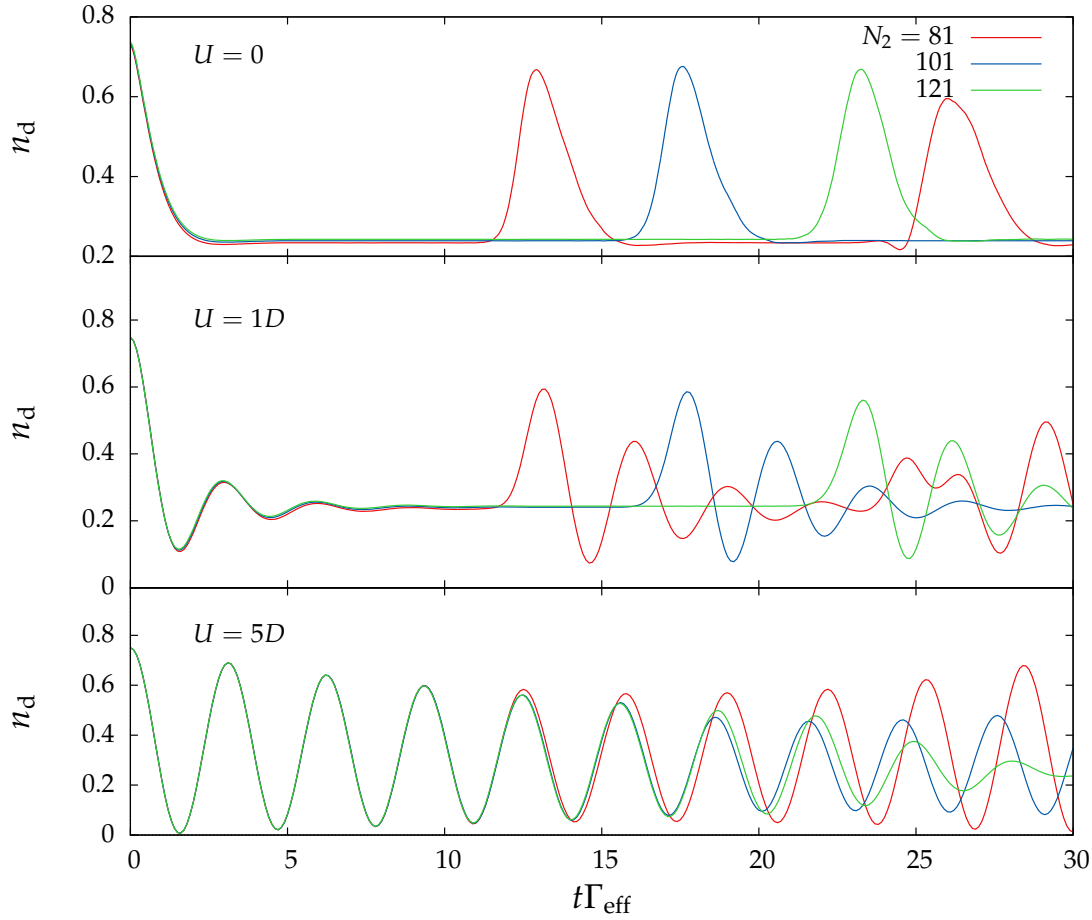


Figure 5.5: Time-dependent impurity occupation number for increasing second Wilson chain length N_2 with different values for the interaction strength U . The quench is $-E_i = E_f = \Gamma_{\text{eff}}$ and the chain parameters are as in Fig. 5.2.

scale at which the reflection occurs is for a small quench U independent. A definite proof of this claim is given in the next section by analyzing the fidelity curves.

5.5.1 Fidelity

To further investigate this point, Fig. 5.6a shows the time-dependent fidelity $F(t)$ of the reduced density matrix of the hyper-impurity during the time evolution with the equilibrium reduced density matrix of the hyper-impurity for the final Hamiltonian. It is important to notice that the fidelity grows during the time evolution and that the maximum fidelity depends on N_2 ; hence we expect that in the limit $N_2 \rightarrow \infty, \Lambda_2 \rightarrow 1$ and $t\Gamma_{\text{eff}} \rightarrow \infty$ the fidelity approaches $F \rightarrow 1$. This shows that one can indeed observe thermalization of a subsystem for the IRLM with the NRG+DMRG.

For finite system sizes reflections at the end of the chain set an upper bound to the maximum fidelity. Fig. 5.6a shows that the fidelity curves for different N_2 lie on top of each other, up to the time $t_{\text{max}}^{N'_2}$ at which the N'_2 curve starts to deviate from the curves

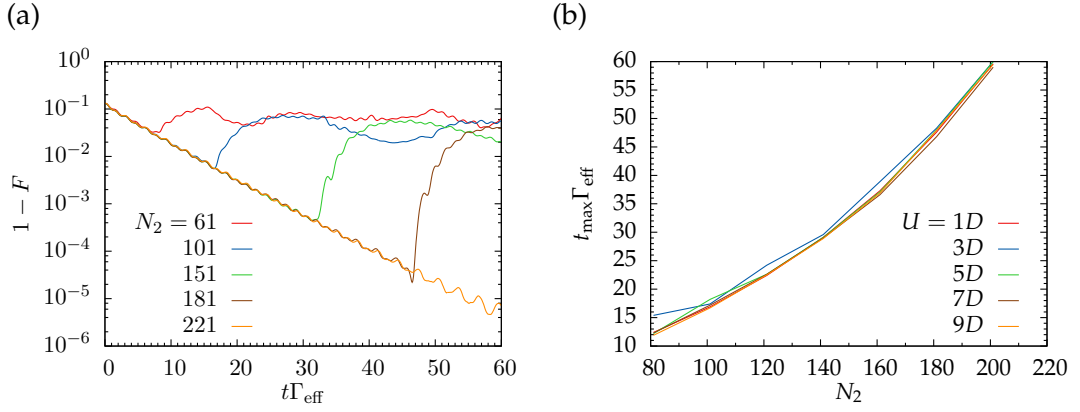


Figure 5.6: Time-dependent fidelity F , Eq. (1.19), for $-E_i = E_f = \Gamma_{\text{eff}}$. For calculating the reduced density-matrices to determine the fidelity the hyper-impurity constitutes the system and the second Wilson chain the environment. The fidelity is calculated with the time-dependent reduced density matrix and the thermal reduced density matrix of the final Hamiltonian. (a) Different values for the chain length N_2 for $U = 3D$. (b) Maximum simulation time determined by the time at which the fidelity curves (left panel) start to deviate from the $N_2 = 301$ fidelity curve. For both panels same chain parameters as in Fig. 5.2 are used.

corresponding to chains with more chain sites. As for the impurity occupation number the reason for this deviation are the reflections at the end of the DWC.

Furthermore the maximum fidelity approaches $F = 1$ with increasing N_2 . To calculate the fidelity the system is partitioned in a system, in this case the hyper-impurity, and a bath, in this case the second Wilson chain. By increasing N_2 the relative size of the bath increases in comparison to the system. When tracing out the bath states one is left with less information and this allows for a better thermalization [159].

Fig. 5.6b shows the maximum time t_{max} for which a fidelity curve of given N_2 and U lies on top of a curve with $N_2 = 301$ sites: the time for which one can faithfully simulate the IRLM with the NRG+DMRG is independent of U . All U dependencies visible in Fig. 5.6b are solely due to the numerical method employed to extract t_{max} from the fidelity $F(t)$ curves.

5.5.2 Von Neumann entropy

In the case of the exactly solvable RLM the occupation of each chain site can easily be calculated. In principle, one could calculate the time-dependent occupation number of each chain site of the second Wilson, because this part is solved with the TD-DMRG. Hence one could track the propagation of the charge wave through the second Wilson chain similar to Fig. 3.11. However, instead of the occupation number we show the von Neumann entropy, as the numerical effort to calculate this quantity is not as high as calculating expectation numbers.

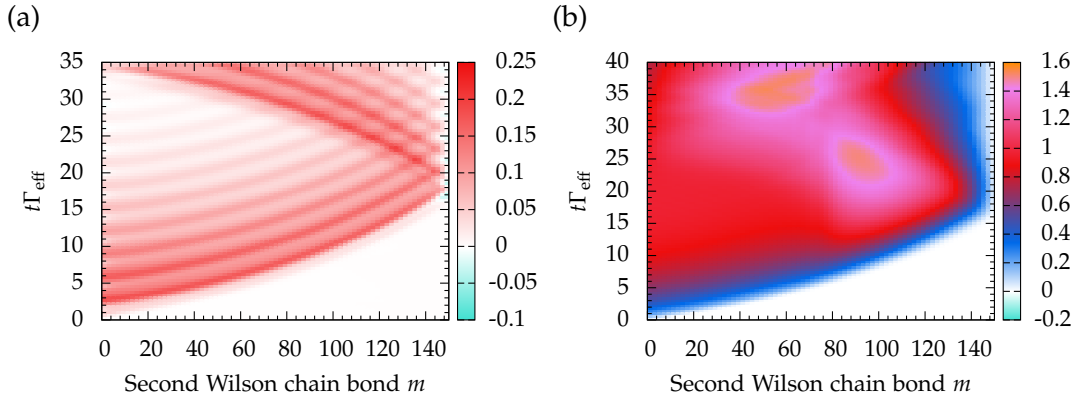


Figure 5.7: Difference of time-dependent von Neumann entropy $S_m = S_m(t) - S_m(t = 0)$ of the m th site of the second Wilson chain for $U = 3D$, (a) $\Delta E = 2\Gamma_{\text{eff}}$ and (b) $\Delta E = 20\Gamma_{\text{eff}}$. The occupation number of the impurity is shown in Fig. 5.4. Same parameters as Fig. 5.2.

In Fig. 5.7a the propagation of the charge wave through the second Wilson chain is clearly visible. The occupation number of the impurity shows a damped oscillation (cf. Fig. 5.4a) and in each oscillation period one further charge wave is injected into the DWC. At $t\Gamma_{\text{eff}} \approx 16$ the first charge wave reaches the end of the chain, is reflected, and at $t\Gamma_{\text{eff}} \approx 32$ it arrives at the hyper-impurity. At this point the decline of the impurity occupation number stops and the occupation number rises (cf. Fig. 5.4a); furthermore, at this time the fidelity drops (cf. Fig. 5.6).

For the larger quench, $-E_i = E_f = 10\Gamma_{\text{eff}}$, the oscillations are smaller and faster, and the decay of the impurity occupation number is slower compared to the smaller quench (cf. Fig. 5.4b). Hence, Fig. 5.7b shows a first wave propagating through the chain with the same velocity as in Fig. 5.7a. However, due to the fast oscillations of the impurity occupation one cannot as clearly distinguish the subsequent charge waves injected into the chain as in Fig. 5.7a.

5.5.3 Analytic frequency and damping

Unlike the RLM the IRLM lacks an exact solution and hence we cannot compare the NRG+DMRG results to ED results. However, for $U \rightarrow \infty$ one can derive an expression for the frequency Ω of the oscillations of the impurity occupation number and for the damping τ of the oscillations,

$$\Omega = \sqrt{E_f^2 + 4V^2} \quad (5.5)$$

$$\tau = \left(\frac{\pi \left(\frac{8DV}{\pi^2 U} \right)^2}{\sqrt{(E_f/2)^2 + V^2}} \right)^{-1}. \quad (5.6)$$

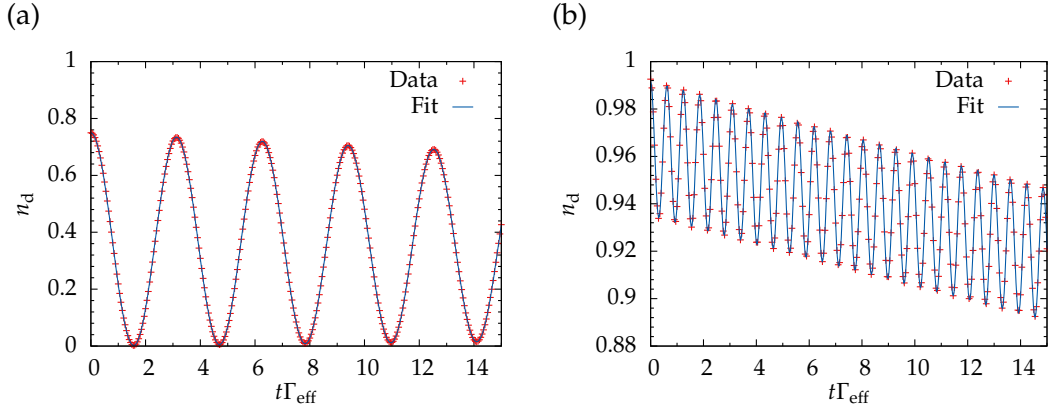


Figure 5.8: Fit of the function Eq. (5.7) to the numerical data of the impurity occupation number for $U = 10D$ to determine the frequency Ω and damping rate τ of the oscillation. The model parameters are (a) $-E_i = E_f = \Gamma_{\text{eff}}$ and (b) $-E_i = E_f = 10\Gamma_{\text{eff}}$. Same parameters as Fig. 5.2.

The time-dependent impurity occupation number is then given by

$$n_d(t) = A \left(e^{-\frac{t}{2\tau}} \cos(\Omega t) \sqrt{1 - e^{-\frac{t}{\tau}} \cos(\theta)^2} - e^{-\frac{t}{\tau}} \sin(\theta) \right) + (1 - n_0) \left(1 - e^{-\frac{t}{\tau}} \right) + n_0 e^{-\frac{t}{\tau}}, \quad (5.7)$$

with the initial occupation $n_0 = n_d(t = 0)$ and the parameter θ . The derivation of these equations is sketched in Appendix D. To compare the analytic expressions for Ω and τ with the NRG+DMRG results Eq. (5.7) is fitted to the NRG+DMRG data for the impurity occupation number, where all parameters are regarded as free fitting parameters (cf. Fig. 5.8).

The fit results are shown in Fig. 5.9. Note, though Eq. (5.5) does not explicitly depend on U the analytic results given in Fig. 5.9a depend on U : to assure $\Gamma_{\text{eff}} = 1$ one has to U dependently tune the hybridization V and thus Ω depends implicitly on U . Fig. 5.9 shows a good agreement between the analytic and the numeric results for $U \rightarrow \infty$. As expected the agreement is poor for small U , because the analytic expressions for Ω and τ are only valid in the large U limit. However, the NRG+DMRG is applicable in the whole parameter regime.

5.6 Numerical errors

In Sec. 5.3 the criteria to determine the optimal numerical parameters are the equilibrium occupation number of the impurity and the density-matrix renormalization group (DMRG) truncation error. With this choice of parameters nonequilibrium results consistent with the ED results for $U = 0$ were obtained, e.g. the obtained reflection times are the same. However, so far there is no rigorous justification that the optimal

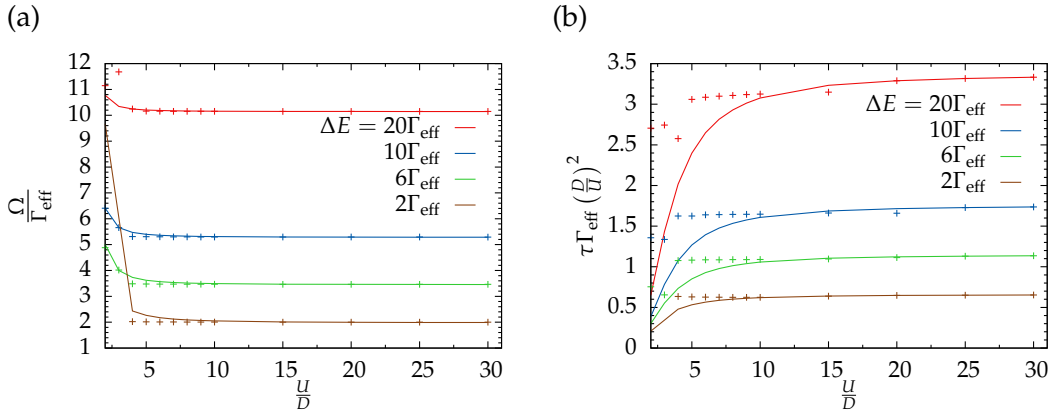


Figure 5.9: Fitted (a) frequency Ω and (b) damping τ . The function Eq. (5.7) is fitted to the impurity occupation number for $0 \leq t\Gamma_{\text{eff}} \leq 15$ (cf. Fig. 5.8). The crosses indicate the numerical data and the lines the analytical strong coupling estimates, Eq. (5.5) and Eq. (5.6). Same parameters as Fig. 5.2.

value for the number of kept states obtained by an equilibrium calculation is suited for a nonequilibrium calculation.

The TD-DMRG suffers from two major error sources: the truncation and the Trotter error [177]. The truncation error is due to the weight of the density matrix discarded at each application of the time-evolution operator. Fig. 5.10a shows the truncation error ϵ measured at the central bond of the second Wilson chain during the time-evolution: for all parameter choices the truncation error is bounded from above by $\mathcal{O}(10^{-6})$ on the time scales one is interested in, that is, before the reflections reach the impurity. This indicates that the truncation error for a single application of U is negligible.

Due to the Trotter-Suzuki decomposition (TSD) one has to apply the time-evolution operator U multiple times to the matrix product state (MPS) and at each step one discards some weight of the density matrix. Hence, the important quantity is not just the truncation error, but the cumulative truncation error. To estimate this error we let the system evolve up to time $t = T/2$ and then reverse the direction of the time by changing the sign of the Trotter time step $\delta t \rightarrow -\delta t$ in Eq. (1.95). Afterwards we let the system evolve up to time T . In total we have applied the time-evolution operator N_T times, thus the total evolution time is $T = N_T |\delta t|$. However, due to the reversion of the time direction at $t = T/2$ the effective system is $t = 0$: the system has evolved back to its initial state. The Trotter errors from the forward and backward iteration cancel each other out [177], thus the deviation of the impurity occupation numbers at $t = 0$ and $t = T$ is only due to the accumulated truncation error.

Fig. 5.10b shows that on the time scales one is interested in, that is $TT_{\text{eff}} \lesssim 30$, the relative error is $\mathcal{O}(10^{-3})$. The relative error is measured by the relative deviation of the initial value and the value after the forward and backward run. If one would

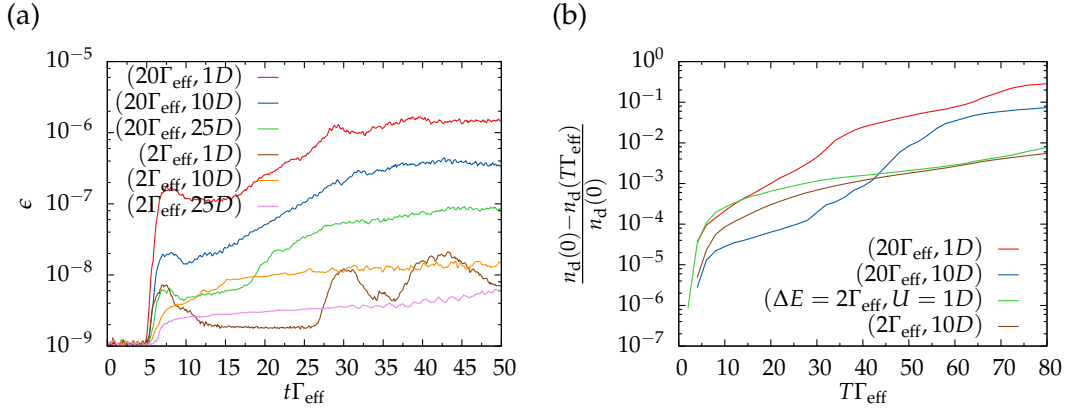


Figure 5.10: (a) Truncation error ϵ measured at the central bond of the second Wilson chain. The numbers in the legend are of the form $(\Delta E, U)$. (b) Forward and backward run. Shown is the relative difference between the impurity occupation at $t = 0$ and $t = T\Gamma_{\text{eff}}$. At $t = \frac{T\Gamma_{\text{eff}}}{2}$ the direction of time is reversed by changing the sign of time-step $\delta t \rightarrow -\delta t$ in Eq. (1.95). This is a measure of the cumulative Trotter error. Same parameters as Fig. 5.2.

like to reduce this error further, one has to increase the number of states during the time-evolution. For the purposes of this thesis this error is sufficiently small.

Besides the truncated weight the other major error source of the TD-DMRG is the Trotter error. This error depends on the Trotter time step δt : for $\delta t \rightarrow 0$ the Trotter error shrinks. However, the smaller δt is the more applications N_t , Eq. (1.97), of the time evolution operator are needed to reach the time t , hence the cumulative truncation error grows.

The dependence of the numerical error on the Trotter time step δt can be quantified by the derivative of the impurity occupation number $n_d(t, \delta t)$ with respect to the Trotter time step,

$$\frac{dn_d(t, \delta t)}{d\delta t} = \frac{n_d(t, \delta t) - n_d(t, \delta t')}{\delta t - \delta t'}. \quad (5.8)$$

This derivative is evaluated at different Trotter time steps and model parameters in Fig. 5.11. For $\delta t \lesssim 0.01\Gamma_{\text{eff}}$ the numerical value of the derivative saturates and therefore decreasing δt does not significantly improve the accuracy of the simulation. That is why all simulations presented in this chapter are carried out with $\delta t = 0.01\Gamma_{\text{eff}}$.

It is important that the Trotter time step is below the inverse of the effective bandwidth. The chain parameters used in all simulations of this section are given in Fig. 5.2. With these parameters the effective bandwidth is given by

$$D_{\text{eff}} \sim D\Lambda_1^{-\frac{N_1}{2}} \approx 20\Gamma_{\text{eff}}. \quad (5.9)$$

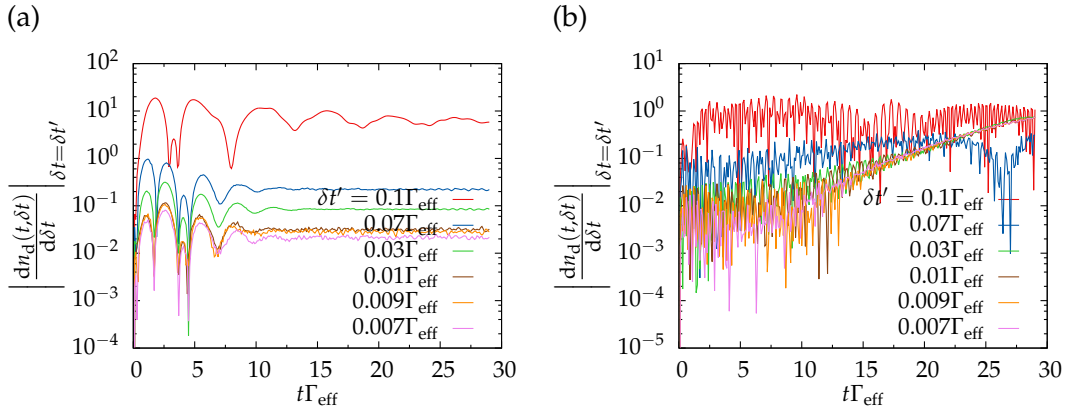


Figure 5.11: Derivative of the impurity occupation number with respect to the Trotter time step δt evaluated for different $\delta t'$. The model parameters are (a) $-E_i = E_f = \Gamma_{\text{eff}}$, $U = D$ and (b) $-E_i = E_f = 10\Gamma_{\text{eff}}$, $U = 10D$. All other parameters are the same as in Fig. 5.2.

Hence the upper bound for the Trotter step is

$$\delta t_{\text{max}} = \frac{1}{D_{\text{eff}}} = \frac{0.05}{\Gamma_{\text{eff}}}. \quad (5.10)$$

Since $\delta t_{\text{max}} > \delta t$ the requirement that the Trotter step is below the inverse effective bandwidth is fulfilled.

Concluding, for our NRG+DMRG calculations errors are present. But on the time scales on which the simulations yields physical meaningful results these errors are reasonable small. The time scale on which the simulation yields physical meaningful results is bounded above from the time the first reflection peaks occur in the impurity occupation number. As argued in Chapter 3 this time scale is set by the chain parameters and the quench strength. Hence, the maximum simulation time is not bounded by numerical but by discretization errors.

5.7 Comparison to TD-DMRG

The discretization errors are eliminated by using hybrid chains; hence, one cannot use the NRG anymore and that is why we proposed the new hybrid method. However, the DMRG is more flexible than the NRG as one can simulate chains with arbitrary chain parameters: it should be possible for the TD-DMRG to simulate the IRLM with hybrid chains.

In principle this is true, but it is very hard to simulate systems with a bandwidth as high as in our studies. We focused on systems with the bandwidth $D = 10^5\Gamma_{\text{eff}}$. For TD-DMRG simulations of such systems the Trotter step has to be at least one order of magnitude below the inverse bandwidth, $\delta t\Gamma_{\text{eff}} = 10^{-6}$. In our NRG+DMRG

simulations the Trotter time step is $\delta t \Gamma_{\text{eff}} = 0.1$: simulating the same system with the TD-DMRG one needs 10^5 more time steps to reach the same time scales. Assuming that the CPU time scales linearly with the number of time steps, this would boost the needed CPU time from a few hours to decades!

In this work we employed the so-called adaptive TD-DMRG [109], which relies on a TSD of the time evolution operator. However, other proposals to implement a time evolution with the DMRG discretize the total simulation time in single time steps, which have to be below the inverse bandwidth, as well [110, 115]. Thus, the CPU time needed by these methods is of the same order of magnitude as for the adaptive TD-DMRG. Hence, all TD-DMRG methods are not suited well for the simulation of systems with a large bandwidth.

Besides the huge computational resources needed, we expect the accumulated truncation error to grow as the number of applications of the time evolution operators is 10^5 times as high as compared to the NRG+DMRG. Hence we expect the time scales on which one can simulate the system reliably to be drastically reduced.

5.8 Summary

In this chapter we have investigated the real-time dynamics of the interacting resonant-level model (IRLM). Therefore we applied the numerical renormalization group density-matrix renormalization group hybrid (NRG+DMRG) method to the IRLM. Before we could calculate the time-dependent impurity occupation number we had to numerically determine the bare model parameter Γ , which is renormalized due to the interaction, in such a way that the effective level width Γ_{eff} is equal for all simulations in order to make the results comparable.

With the NRG+DMRG method we were able to simulate the IRLM in the whole parameter regime: from a small to a large bandwidth, from a vanishing interaction strength, over moderate interactions up to the strong coupling limit, and from small to large quenches. Here we observed that oscillations in the time dependent impurity occupation numbers emerge for a non-vanishing interaction. We could not only explain the origin of these oscillations in a strong coupling treatment, but were also able to derive analytic expressions for the oscillation frequency and the damping rate in the large U limit: a comparison between the numerical frequency and damping rate and the analytic values shows a perfect match. Interestingly, the frequency of these oscillations introduces a new time scale not present in the thermodynamic properties of the IRLM. This explains, why, though the resonant-level model (RLM) and the IRLM share the same fixed point and therefore the thermodynamic properties of both models are equal, the real-time dynamics of RLM and the IRLM are different.

By the use of double Wilson chains (DWCs) we reduced discretization errors considerably. On the one hand, this improves the numerical accuracy. On the other hand,

the NRG+DMRG approach allows us to access exceptionally long times scales out of reach for the time-dependent density-matrix renormalization group (TD-DMRG). In the TD-DMRG simulations the Trotter timestep has to be at least one order of magnitude below the inverse bandwidth. This renders the TD-DMRG unfeasible for large bandwidth calculations. However, the merit of the hybrid method is, that the numerical renormalization group (NRG) produces an effective low-energy Hamiltonian which the TD-DMRG can easily simulate.

In this chapter the NRG+DMRG has proven itself as versatile and reliable method which allows to simulate the IRLM in parameter regimes and on time scales inaccessible by other methods.

Chapter 6

Conclusions

We made a good deal of progress in improving techniques to simulate quantum impurity systems (QISs) in and out-of equilibrium. These improvements are made possible by the deeper understanding we developed of the implications the bath discretization has for numerical renormalization group (NRG) calculations. Our results have undoubtedly shown that discretization artifacts corrupt the nonequilibrium simulation of QISs if the discretization of the bath is carried out in the usual Wilsonian manner. In equilibrium, for bosonic systems the discretization and the iterative diagonalization cause a dynamic renormalization of the critical coupling strength, due to which the NRG yields wrong critical exponents: this is the so-called mass-flow error.

For both issues we presented solutions. We demonstrated that (i) for nonequilibrium calculations one can recover the real-time dynamics of the continuous bath with a modified bath discretization; and (ii) for equilibrium calculations the correct critical exponents of the spin-boson model (SBM) are calculated by the density-matrix renormalization group (DMRG)

The solution of the mass-flow error is to take the rest-chain properly into account: at each NRG iteration a part of the Wilson chain is neglected. However, in the sweeping phase the DMRG is able to respect the effect of the rest-chain – a feat not accomplishable with the NRG, yet. Thereby the DMRG is able to eliminate the mass-flow effect and our DMRG calculations yield the correct critical exponents of the sub-ohmic SBM.

The success of our DMRG calculations for the SBM is made possible by optimizing the truncated bosonic basis by displacing the basis states. One way which we investigated to determine the displacement parameters is a variational optimization in the DMRG sweeping phase. After a few sweeps the so determined displacement parameters converge. Furthermore, we proposed an alternative algorithm based on a mean-field scheme to calculate the optimal displacement parameters. By this semi-analytic approach we gained a deeper insight in the cause of the bosonic state displacements. We believe that this approach is as well applicable to other Hamiltonians containing terms which generate a displacement of the bosons. These results are of relevance

for all bosonic DMRG and NRG calculations, as these suffer from a truncation of the bosonic Hilbert space.

With traditional nonequilibrium simulations of the resonant-level model (RLM) we discovered severe problems due to the mapping of the bath to a Wilson chain. After a sudden local quench a charge wave is injected into the Wilson chain and propagates along the chain. Due to the logarithmic discretization of the bath the Wilson hopping parameters decay exponentially and we showed that this decay leads to internal reflections of the charge wave within the Wilson chain. A fraction of the charge propagates back to the impurity corrupting, for example, the results of the impurity occupation number.

As a solution, we proposed to use hybrid chains consisting of a Wilson chain coupled to a second chain with arbitrary hopping parameters in order to enhance the accuracy and accessible time scales of the simulations. Here, the double Wilson chain (DWC) turned out to yield the best results. The idea of a DWC is to patch two Wilson chains with different discretization parameters together: the discretization parameter of the second Wilson chain is significantly closer to one than the discretization parameter of the first Wilson chain. By exactly solving the RLM we demonstrated that this setup yields results in excellent agreement with a continuum solution.

Since for hybrid chains the separation of energy scales is not ensured anymore, the NRG is not able to handle such chains. Therefore, as a central result of this thesis, we proposed a new hybrid method which enables us to hybridize the NRG with other suitable methods. Explicitly, we showed how to hybridize the time-dependent numerical renormalization group (TD-NRG) with the time-dependent density-matrix renormalization group (TD-DMRG). An NRG run constructs an effective low-energy Hamiltonian which is regarded as a hyper-impurity. The hyper-impurity is then coupled to the second Wilson chain and this system is simulated with the TD-DMRG. This boosts the accessible simulation times of the TD-DMRG to magnitudes out of its usual reach. By comparing results we obtained by exact diagonalization (ED) and the new hybrid method for the RLM we established the reliability of the new method.

In a next step we calculated the real-time dynamics of the interacting resonant-level model (IRLM) with the new hybrid method. We analyzed interaction-enhanced oscillations of the impurity occupation number and compared these to analytic results obtained in the strong-coupling limit. In this limit, both methods yield the same results, whereas the hybrid method is able to simulate the IRLM in the whole parameter regime. We measured the fidelity to show that the time-evolved reduced density matrix of the impurity thermalizes.

With the numerical renormalization group density-matrix renormalization group hybrid (NRG+DMRG) method we have devised a technique to simulate systems on time scales out of reach of pure TD-NRG or TD-DMRG simulations. A pure TD-NRG simulation suffers from discretization artifacts leading to unphysical results. This is not

a problem for TD-DMRG simulations as one could simulate DWCs with this method. However, the TD-DMRG is unfeasible for systems with a large bandwidth, as the Trotter timestep has to be one order of magnitude below the inverse bandwidth. For large bandwidth simulations this leads to excessive demands of CPU time.

This thesis had an explicit technical focus: new numerical techniques were devised and applied to few physical systems as a proof-of-principle. Of course, the story does not end here. Hence, in the following we give a brief outlook of possible future applications.

An optimal bosonic basis is important for all simulations of bosonic systems in which one has to truncate the bosonic Hilbert space. Hence, it is worthwhile to follow our ideas how to construct such a basis up. Furthermore, it would be desirable to conceive a way how to take the rest-chain – or, in general, the rest-bath – into account at a given NRG iteration. This would not only cure the mass-flow error, but we also believe that one could extend such an approach to a technique which allows to determine the NRG broadening parameter for calculating spectral functions.

We are confident that the outstanding capabilities of the new hybrid method open the door to investigate systems in regimes which were inaccessible before. A natural extension of the presented work is to apply the NRG+DMRG method to an IRLM with two leads to measure transport properties and to investigate the negative differential conductance observed in the IRLM [165, 168, 175].

Furthermore, one could investigate the single impurity Anderson model (SIAM): for the IRLM we have seen that there is one relevant time scale Γ for the charge fluctuations. In the SIAM there is an additional time scale due to spin fluctuations. It would be interesting to examine if the concept of hybrid chains still works in the presented manner. Finally, the new hybrid method does not only allow single quenches but one could consider varying model parameters at arbitrary times. This would, for example, render the simulation of pulses applied to quantum dots (QDs) with the NRG or the hybrid method possible.

Though the first experiments pioneering the field of low-temperature physics and impurity systems were performed over a century ago there are still open questions today, e.g. the way how small systems interact with large environments is not fully understood or building large scale quantum computers is still an unresolved challenge. Ahead of us lies a very vivid research field with a lot of exciting discoveries and groundbreaking technical progress to come.

Appendix A

Diagonalization of the Dissipative Harmonic Oscillator

In this appendix we exactly diagonalize the dissipative harmonic oscillator (DHO). This is first done analytically for the continuous bath and afterwards numerically for the discretized bath.

A.1 Continuous bath

The Hamiltonian of the DHO with a continuous bath is given by

$$H = \Omega a^\dagger a + \underbrace{(a^\dagger + a)}_{X_a} \underbrace{\sum_q \lambda_q (b_q^\dagger + b_q)}_X + \sum_q \omega_q b_q^\dagger b_q. \quad (\text{A.1})$$

Our goal is to calculate the critical coupling α_c and the critical exponent p for this model. The following derivation is a summary of [178].

A.1.1 Critical coupling

The bath is described by the propagator

$$\Gamma(z) = \sum_q \frac{\lambda_q^2}{z - \omega_q} \quad (\text{A.2})$$

which is defined

$$\text{Im}\Gamma(\omega - i\delta) = \pi \sum_q \lambda_q^2 \delta(\omega - \omega_q) = J(\omega) \quad (\text{A.3})$$

with the standard parametrization

$$J(\omega) = \begin{cases} 2\pi\alpha\omega_c^{1-s}\omega^s & 0 \leq \omega \leq \omega_c \\ 0 & \text{otherwise} \end{cases}. \quad (\text{A.4})$$

Using an equation of motion ansatz one gets for the impurity Green's function

$$\begin{aligned} \ll a|a^\dagger \gg (\omega - i\delta) &= \frac{(\omega + \Omega + A_r(\omega)) (\omega^2 - \Omega(\Omega + 2A_r(\omega))) - 2\Omega A_i^2(\omega)}{(\omega^2 - \Omega(\Omega + 2A_r(\omega)))^2 + 4\Omega^2 A_i^2(\omega)} \\ &+ iA_i(\omega) \frac{(\Omega + \omega)^2}{(\omega^2 - \Omega(\Omega + 2A_r(\omega)))^2 + 4\Omega^2 A_i^2(\omega)} \end{aligned} \quad (\text{A.5})$$

with the definition

$$A(z) = \Gamma(z) + \Gamma(-z), \quad (\text{A.6})$$

$$A_r(\omega) = \text{Re}A(\omega - i\delta), \quad (\text{A.7})$$

$$\text{and } A_i(\omega) = \text{Im}A(\omega - i\delta) = J(\omega) - J(-\omega). \quad (\text{A.8})$$

Hence the spectral function is given by

$$\pi\rho_a(\omega) = \text{Im} \ll a|a^\dagger \gg (\omega - i\delta) = A_i(\omega) \frac{(\Omega + \omega)^2}{(\omega^2 - \Omega(\Omega + 2A_r(\omega)))^2 + 4\Omega^2 A_i^2(\omega)}. \quad (\text{A.9})$$

$\text{Re}\Gamma(\omega)$ is determined by the Hilbert transformation

$$\text{Re}\Gamma(\omega) = 2\alpha\omega_c^{1-s} \text{P} \int_0^{\omega_c} d\epsilon \frac{\epsilon^s}{\omega - \epsilon}. \quad (\text{A.10})$$

By considering the two cases $|\omega| > \omega_c$ and $|\omega| < \omega_c$ separately one can find an analytic expression for the integral:

$$\text{Re}\Gamma(\omega) = 2\alpha\omega_c C_r \left(\frac{|\omega|}{\omega_c} \right)^s - 2\alpha\omega_c \sum_{n=0}^{\infty} \frac{1}{s-n} \left(\frac{\omega}{\omega_c} \right)^n \quad (\text{A.11})$$

$$\text{with } r := \text{sign}(\omega) \quad (\text{A.12})$$

$$\text{and } C_r := \frac{1}{s} + 2s \sum_{n=0}^{\infty} \frac{r^n}{s^2 - n^2}. \quad (\text{A.13})$$

The DHO shows a phase transition from a phase with a finite occupation number to one in which the occupation number diverges. Since the occupation number is defined by

$$n_a = \int_{-\infty}^{\infty} d\omega \frac{1}{e^{\beta\omega} - 1} \rho_a(\omega) \quad (\text{A.14})$$

the model is unstable if, for an arbitrary finite ω , the denominator of Eq. (A.9) vanishes,

$$\left(\omega^2 - \Omega(\Omega + 2A_r(\omega))\right)^2 + 4\Omega^2 A_i^2(\omega) \stackrel{!}{=} 0. \quad (\text{A.15})$$

To make the second term vanish we choose $\omega = 0$

$$\Rightarrow \Omega^2 (\Omega + 2A_r(0))^2 = 0 \quad (\text{A.16})$$

$$\Rightarrow \Omega = -2A_r(0) = \frac{8\alpha\omega_c}{s} \quad (\text{A.17})$$

Therefore the critical coupling is given by

$$\alpha_c = \frac{s\Omega}{8\omega_c}. \quad (\text{A.18})$$

A.1.2 Critical exponent

To determine the critical exponent p the deviation of the oscillator frequency from its critical value is defined as

$$\omega_d = \Omega - \Omega_c. \quad (\text{A.19})$$

By using that the bare oscillator frequency gets renormalized by the bath the spectral functions for $\omega \rightarrow 0$ and $\omega_d \ll 1$ is given by

$$\rho(\omega) = \text{sign}(\omega) \frac{2\alpha\omega_c^{1-s} |\omega|^s \left(1 + \frac{\omega}{\Omega}\right)^s}{\left(\omega_d + 4\alpha\omega_c^{1-s} B |\omega|^s\right)^2 + 16\pi^2 \alpha^2 \omega_c^{2(1-s)} |\omega|^{2s}}. \quad (\text{A.20})$$

Here $B = C_+ + C_-$ is a constant. We identify the two regimes

$$(i) \quad 4\alpha\omega_c B \left(\frac{|\omega|}{\omega_c}\right)^2 \gg \omega_d \quad (\text{A.21})$$

$$\text{and } (ii) \quad 4\alpha\omega_c B \left(\frac{|\omega|}{\omega_c}\right)^2 \ll \omega_d \quad (\text{A.22})$$

and define the crossover scale ω_m by

$$4\alpha\omega_c B \left(\frac{|\omega_m|}{\omega_c} \right)^2 = \omega_d. \quad (\text{A.23})$$

The spectral function in these regimes is then given by

$$(i) \quad \rho^{(i)}(\omega) = \text{sign}(\omega) \frac{1}{8\alpha\omega_c (B^2 + \pi^2)} \left(\frac{|\omega|}{\omega_c} \right)^{-s} \quad (\text{A.24})$$

$$\text{and } (ii) \quad \rho^{(ii)}(\omega) = \text{sign}(\omega) \frac{2\alpha\omega_c}{\omega_d^2} \left(\frac{|\omega|}{\omega_c} \right)^s. \quad (\text{A.25})$$

The integral to calculate the occupation Eq. (A.14) is split at the crossover scale into two parts and the Bose function is approximated by $\frac{1}{x}$. This leads with the variable substitution $x = \beta\omega$ to

$$n_a = T \int_0^{\beta\omega_m} dx \frac{\rho^{(ii)}(Tx)}{x} + T \int_{\beta\omega_m}^{\infty} dx \frac{\rho^{(i)}(Tx)}{x} \quad (\text{A.26})$$

$$\approx T(C_1\omega_d + C_2\omega_d^{-1}) \rightarrow \omega_d^{-1} \quad (\text{A.27})$$

with two constants C_1 and C_2 . Thus the critical exponent is $p = -1$.

A.2 Discretized bath

The numeric solutions aims at solving the Hamiltonian of the DHO with a discretized bath Eq. (2.12). The central result of this section is an equation to calculate the occupation of the impurity and the bath oscillators by numerically diagonalizing the Hamilton matrix. To calculate $\langle n_d \rangle$ we want to transform the Hamiltonian

$$H = \Omega a^\dagger a + \sqrt{\alpha} V (a^\dagger + a) (a_0^\dagger + a_0) + \sum_{n=0}^{N-1} \epsilon_n a_n^\dagger a_n + \sum_{n=0}^{N-2} t_n (a_n^\dagger b_{n+1} + a_{n+1}^\dagger a_n) \quad (\text{A.28})$$

into a diagonal form

$$H = \sum_n \omega_n b_n^\dagger b_n. \quad (\text{A.29})$$

In a matrix representation the Hamiltonian (A.28) has the general form¹

$$H = \frac{1}{2} \vec{a}^\dagger M \vec{a} - \text{Tr}[A] \quad (\text{A.30})$$

¹ In the calculation we use the method presented in Section 3.2 of [179].

$$\text{where } M = \begin{pmatrix} A & B \\ B^* & A^* \end{pmatrix}, \quad A = A^\dagger, B = B^T, \quad (\text{A.31})$$

$$\vec{\alpha} = \begin{pmatrix} a \\ a_0 \\ a_1 \\ \vdots \\ a^\dagger \\ a_0^\dagger \\ a_1^\dagger \\ \vdots \end{pmatrix} \quad \text{and} \quad \vec{\alpha}^\dagger = \left(a^\dagger \quad a_0^\dagger \quad a_1^\dagger \quad \cdots \quad a \quad a_0 \quad a_1 \quad \cdots \right). \quad (\text{A.32})$$

In the special case of the Hamiltonian (A.28) the matrices A and B are defined as

$$A = \begin{pmatrix} \Omega & \sqrt{\alpha}V & 0 & 0 & 0 \\ \sqrt{\alpha}V & \epsilon_0 & t_0 & 0 & 0 \\ 0 & t_0 & \epsilon_1 & t_1 & 0 \\ 0 & 0 & t_1 & \epsilon_2 & t_2 \\ 0 & 0 & 0 & t_2 & \ddots \end{pmatrix} \quad \text{and} \quad B = \begin{pmatrix} 0 & \sqrt{\alpha}V & 0 & 0 & 0 \\ \sqrt{\alpha}V & 0 & 0 & 0 & 0 \\ 0 & 0 & 0 & 0 & 0 \\ 0 & 0 & 0 & 0 & 0 \\ 0 & 0 & 0 & 0 & \ddots \end{pmatrix}. \quad (\text{A.33})$$

Here a and a^\dagger are the impurity operators and a_i and a_i^\dagger are the chain operators.

To diagonalize the Hamiltonian we have to solve the eigenvalue problem

$$\eta M \vec{V}_n = \omega_n \vec{V}_n, \quad (\text{A.34})$$

with the metric

$$\eta = \begin{pmatrix} \mathbb{1} & \\ & -\mathbb{1} \end{pmatrix} \Rightarrow \eta M = \begin{pmatrix} A & B \\ -B^* & -A^* \end{pmatrix}. \quad (\text{A.35})$$

Here one can see the fundamental difference between a fermionic and a bosonic model. Unlike the fermionic case, the bosonic case requires the above defined metric to fulfill the proper commutation relations. As a consequence the matrix M is of dimension $2N \times 2N$, where N is the number of degrees of freedom in the model, e.g. in our case the number of sites. Because the Hamilton matrix of the original model has N eigenvalues, the $2N$ eigenvalues of M cannot be independent. There are N positive eigenvalues and N negative eigenvalues with the relation $\omega_n = -\omega_{n+N}, n \leq N$.

Using the para-eigenvectors² \vec{V}_n we can define the creation and annihilation operators of the normal modes

$$b_n^\dagger = \vec{\alpha}^\dagger \eta \vec{V}_n \quad \text{for } \omega_n > 0 \quad (\text{A.36})$$

$$\text{and } b_n = \vec{V}_n^\dagger \eta \vec{\alpha} \quad \text{for } \omega_n > 0 \quad (\text{A.37})$$

Now one can write the Hamiltonian in the diagonal form of Eq. (A.29)

$$H = \sum_{n \text{ with } \omega_n > 0} \omega_n b_n^\dagger b_n + E_0, \quad (\text{A.38})$$

$$\text{with } E_0 = \frac{1}{2} \sum_{n, \omega_n > 0} \omega_n - \frac{1}{2} \text{Tr}[A]. \quad (\text{A.39})$$

Special care should be taken about the zero modes $\omega_n = 0$ [181, 182], which indicate the instability of the model. When one eigenvalue vanishes the occupation number diverges. Since we are only interested in finite occupation numbers we neglect the case of vanishing eigenvalues. Indeed the lowest α for which there is a vanishing eigenvalue is our criterion for the critical coupling strength α_c^D .

Calculation of the occupation number

Now we turn back to the calculation of the occupation of the impurity harmonic oscillator,

$$\langle n_d \rangle = \frac{\text{Tr} \left[e^{-\beta H} a^\dagger a \right]}{Z}. \quad (\text{A.40})$$

In order to evaluate this expression, we have to express $a^\dagger a$ through the operators in the new basis:

$$\eta \vec{\beta} = \begin{pmatrix} \vec{b} \\ -\vec{b}^\dagger \end{pmatrix} = V^\dagger \eta \vec{\alpha}, \quad (\text{A.41})$$

where V is the matrix containing the paravectors of M to both positive and negative paravalues as column vectors. V has the form

$$V = \begin{pmatrix} X & Y^* \\ Y & X^* \end{pmatrix}. \quad (\text{A.42})$$

² The para notation is introduced in [180]. In short, we define a *paravalue* of the matrix M as an *eigenvalue* of the matrix ηM . A *paravector* of M is the corresponding *eigenvector* of ηM . For the eigenvalue $\omega_n = 0$ the corresponding *paravalue* is $\omega_n = 0$.

By inverting Eq. (A.41) we obtain

$$a = \vec{X}_0 \vec{b} + \vec{Y}_0^* \vec{b}^\dagger. \quad (\text{A.43})$$

$$\text{and } a^\dagger = \vec{Y}_0 \vec{b} + \vec{X}_0^* \vec{b}^\dagger. \quad (\text{A.44})$$

With X_0 (Y_0) we denote the first vector of the matrix X (Y).

Using Eqs. (A.43), (A.44) and (A.40) we calculate the occupation number of the impurity:

$$\langle n_d \rangle = \sum_{k,k'} \underbrace{\frac{\text{Tr} [e^{-\beta H} b_k^\dagger b_{k'}]}{Z}}_{\delta_{k,k'} g(\omega_k)} X_{0k}^* X_{0k'} + \sum_{k,k'} \frac{\text{Tr} [e^{-\beta H} b_k b_{k'}^\dagger]}{Z} Y_{0k}^* Y_{0k'} \quad (\text{A.45})$$

$$= \left(X \cdot \text{diag} (g(\omega_1), g(\omega_2), \dots) \cdot X^\dagger \right)_{00} + \sum_k \underbrace{\frac{\text{Tr} [e^{-\beta H} b_k^\dagger b_k] + \text{Tr} [e^{-\beta H_D}]}{Z}}_{g(\omega_k)+1=-g(-\omega_k)} Y_{0k}^* Y_{0k} \quad (\text{A.46})$$

$$= \underbrace{\left(X \cdot \text{diag} (g(\omega_1), g(\omega_2), \dots) \cdot X^\dagger \right)_{00}}_{=:f_x} - \underbrace{\left(Y \cdot \text{diag} (g(\omega_1), g(\omega_2), \dots) \cdot Y^\dagger \right)_{00}}_{=:f_y}. \quad (\text{A.47})$$

where $g(\omega)$ is the Bose function at temperature β . The occupation number of any chain site n is calculated analogously and the result is

$$\langle a_n^\dagger a_n \rangle = \left(X \cdot \text{diag} (g(\omega_1), g(\omega_2), \dots) \cdot X^\dagger \right)_{n'n'} - \left(Y \cdot \text{diag} (g(\omega_1), g(\omega_2), \dots) \cdot Y^\dagger \right)_{n'n'} \quad (\text{A.48})$$

with $n' := n + 1$.

Fig. 2.8 shows the matrix elements m_{00} of the impurity occupation. These are calculated by

$$m_{00} = \left(X \cdot \text{diag} (1, 0, \dots) \cdot X^\dagger \right)_{00} - \left(Y \cdot \text{diag} (1, 0, \dots) \cdot Y^\dagger \right)_{00}. \quad (\text{A.49})$$

Notice that in Eq. (A.46) for the second term the negative paravalues ω_k have to be taken. Since we just use the positive paravalues in Eq. (A.47), the minus sign of the paravalue cancels out and we use only the positive paravalues for the Bose function. However, the minus sign of the second term in Eq. (A.47) remains, causing numerical errors if both terms are of the same order of magnitude and the difference is some orders of magnitude lower. In this regime the results are dominated by numerical noise and it is possible that the expectation value drops below zero. The plots displaying

this value use a logarithmic scale, which does not allow values below zero. Thus in the numerical noise regime the plots show the absolute value of $\langle a_n^\dagger a_n \rangle$ instead: the sign of the value is not correct but by plotting the absolute value one is able to make the numerical error visible on the logarithmic scale.

A.2.1 Green's function

Since the Hamiltonian Eq. (A.28) is bilinear one can solve it with Green's function. We are interested in the impurity Green's function $\ll a_0 | a_0^\dagger \gg$, which is given by Eq. (A.5) for the case of a continuous bath. An equation of motion ansatz yields the matrix equation

$$\underbrace{\begin{pmatrix} z - \Omega & 0 & -\sqrt{\alpha}V & -\sqrt{\alpha}V & 0 & 0 & & \\ 0 & z + \Omega & \sqrt{\alpha}V & \sqrt{\alpha}V & 0 & 0 & & \\ -\sqrt{\alpha}V & -\sqrt{\alpha}V & z - \epsilon_0 & 0 & -t_0 & 0 & & \\ \sqrt{\alpha}V & \sqrt{\alpha}V & 0 & z + \epsilon_0 & 0 & t_0 & & \\ 0 & 0 & -t_0 & 0 & z - \epsilon_1 & 0 & \ddots & \\ 0 & 0 & 0 & t_0 & 0 & z + \epsilon_1 & & \ddots \\ & & & & \ddots & & & \ddots \end{pmatrix}}_G \begin{pmatrix} \ll a_0 | a_0^\dagger \gg \\ \ll a_0^\dagger | a_0^\dagger \gg \\ \ll a_1 | a_0^\dagger \gg \\ \ll a_1^\dagger | a_0^\dagger \gg \\ \ll a_2 | a_0^\dagger \gg \\ \ll a_2^\dagger | a_0^\dagger \gg \\ \vdots \end{pmatrix} = \begin{pmatrix} 1 \\ 0 \\ 0 \\ 0 \\ 0 \\ 0 \\ \vdots \end{pmatrix}. \quad (\text{A.50})$$

This can be solved with a matrix inversion,

$$\ll a_0 | a_0^\dagger \gg (z) = G(z)_{00}^{-1} = \frac{1}{z - \Omega - \Sigma(z)} \quad (\text{A.51})$$

and the self-energy Σ is then given by

$$\Sigma(z) = \frac{(z - \Omega) \ll a_0 | a_0^\dagger \gg (z) - 1}{\ll a_0 | a_0^\dagger \gg (z)}. \quad (\text{A.52})$$

For example, the self-energy for a chain with length $N = 1$ is given by

$$\Sigma(z) = -2 \frac{\sqrt{\alpha}V^2 \epsilon_0 (z + \Omega)}{-z^2 \Omega + \Omega \epsilon_0^2 - 2\epsilon_0 \sqrt{\alpha}V^2 - z^3 + z\epsilon_0^2}. \quad (\text{A.53})$$

Appendix B

Fits of Critical Exponents

In this appendix the fits are shown by which the critical exponents β (cf. Fig. B.1) and δ (cf. Fig. B.2) are determined for the SBM. To this end a power-law function is fitted to the data points calculated with the DMRG. The results of these fits are shown in Fig. 2.33.

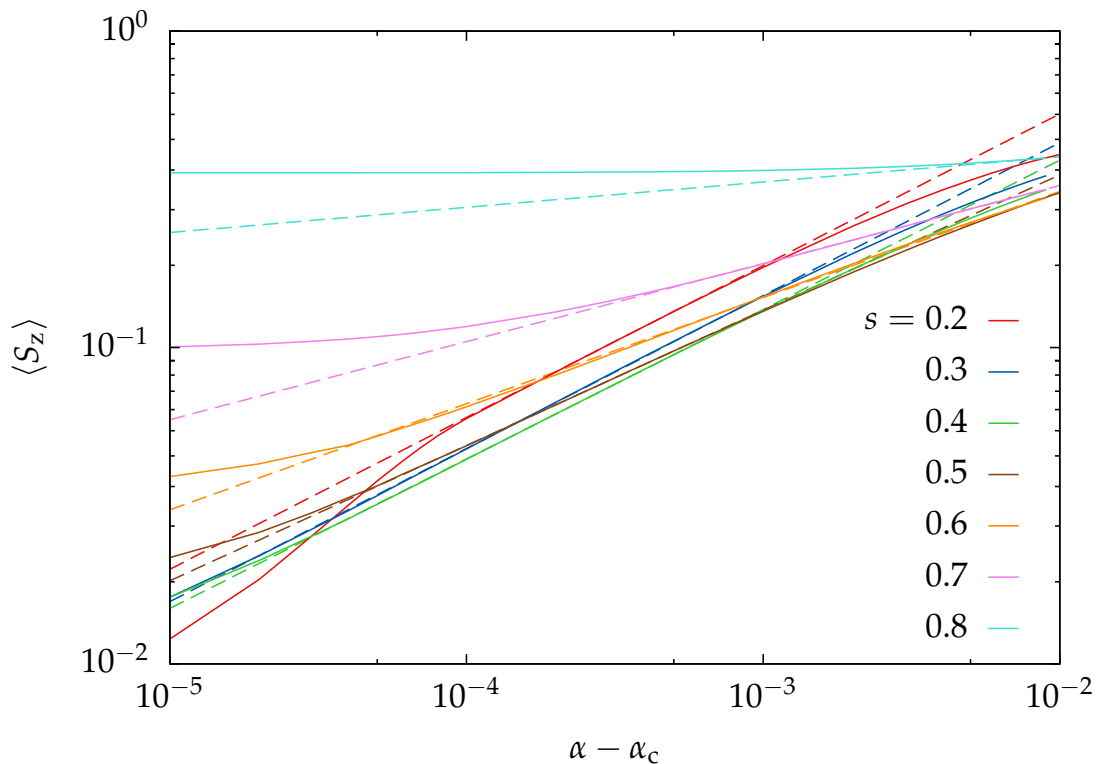


Figure B.1: Determination of the critical exponent β by fitting of the function $f(\epsilon) = a\epsilon^\beta$ to the data points. The chain parameters are $\Lambda = 2$ and $N = 40$. In the DMRG calculation $N_s = 24$ states and $N_b = 8$ bosonic modes are kept. The bosonic basis is optimized until convergence is reached. The model parameters are $\Delta = 0.1\omega_c$ and $\epsilon = 10^{-7}\omega_c$.

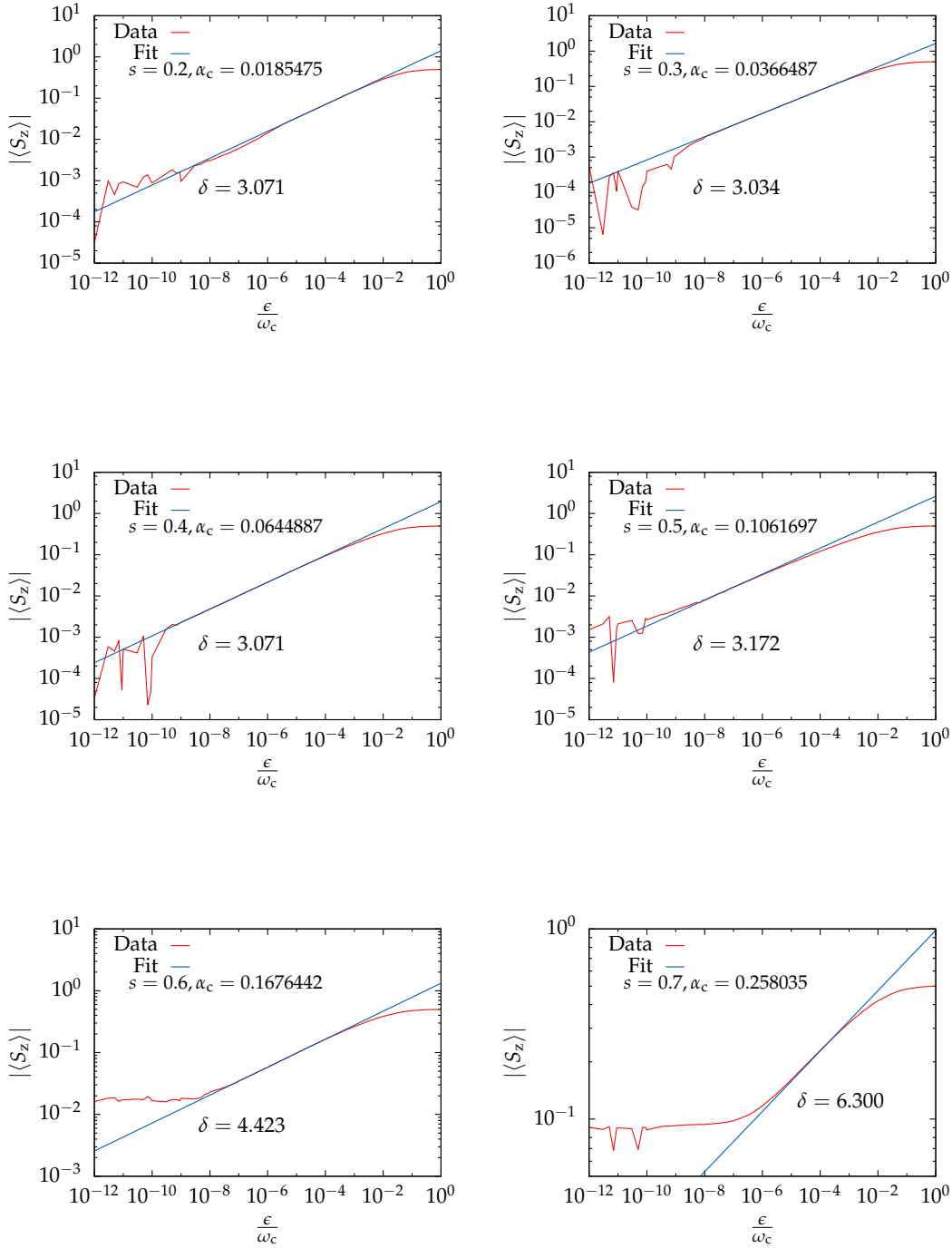


Figure B.2: Determination of the critical exponent δ by fitting of the function $f(\epsilon) = a\epsilon^{\frac{1}{\delta}}$ to the data points. The chain parameters are $\Lambda = 2$ and $N = 40$. In the DMRG calculation $N_s = 24$ states and $N_b = 8$ bosonic modes are kept. The bosonic basis is optimized until convergence is reached. The model parameter is $\Delta = 0.1\omega_c$.

Appendix C

Diagonalization of Resonant-Level Model

In this appendix the RLM Hamiltonian is exactly diagonalized and the occupation of the chain sites are calculated. After that we give an estimate of the time it takes a charge to move through the chain.

C.1 Level occupation

The discretized Hamiltonian of the RLM Eq. (3.2) can be written as

$$H_N = \vec{\alpha}^\dagger M(t) \vec{\alpha}, \quad (\text{C.1})$$

$$\text{with } \vec{\alpha} = \begin{pmatrix} d \\ c_0 \\ c_1 \\ \vdots \end{pmatrix} \quad \text{and} \quad \vec{\alpha}^\dagger = \left(d^\dagger \quad c_0^\dagger \quad c_1^\dagger \quad \dots \right). \quad (\text{C.2})$$

The Hamilton matrix $M(t)$ is defined by

$$M(t) = \begin{pmatrix} E_d(t) & V & 0 & 0 & 0 \\ V & 0 & t_1 & 0 & 0 \\ 0 & t_1 & 0 & t_2 & 0 \\ 0 & 0 & t_2 & 0 & \ddots \\ 0 & 0 & 0 & \ddots & \ddots \end{pmatrix}. \quad (\text{C.3})$$

Unlike H_N the dimension of this matrix grows linearly with the system size N and therefore one can efficiently diagonalize it,

$$M(t) = U(t)^\dagger \text{diag}(\epsilon_1(t), \epsilon_2(t), \dots) U(t). \quad (\text{C.4})$$

For the quench $E_d(t) = E_i\Theta(-t) + E_f\Theta(t)$ the diagonal form of the Hamiltonian reads

$$H(t < 0) \equiv H^i = \sum_n \epsilon_n^i f_n^{i\dagger} f_n^i \quad \text{and} \quad H(t > 0) \equiv H^f = \sum_n \epsilon_n^f f_n^{f\dagger} f_n^f. \quad (\text{C.5})$$

With the new operators

$$f_n^i = \sum_l U_{nl}^i \alpha_l \quad f_n^{i\dagger} = \sum_l \alpha_l^\dagger U_{ln}^{i\dagger} \quad (\text{C.6})$$

$$\text{and } f_n^f = \sum_l U_{nl}^f \alpha_l \quad f_n^{f\dagger} = \sum_l \alpha_l^\dagger U_{ln}^{f\dagger}. \quad (\text{C.7})$$

Here U^i (U^f) and ϵ_n^i (ϵ_n^f) are the eigenvectors and eigenvalues of the initial (final) Hamilton matrix.

We define the occupation operator of the m th site as

$$n_m = \alpha_m^\dagger \alpha_m = \begin{cases} d^\dagger d & m = 0 \\ c_{m-1}^\dagger c_{m-1} & m \geq 1 \end{cases}. \quad (\text{C.8})$$

The expectation value of this operator is given by

$$\langle n_m \rangle(t) = \text{Tr} [\rho(t) n_m], \quad (\text{C.9})$$

and the time-dependent density operator

$$\rho(t) = e^{-iH_f t} \rho_0 e^{iH_f t}. \quad (\text{C.10})$$

The initial condition is

$$\rho_0 = \frac{e^{-\beta H_i}}{Z} = \frac{e^{-\beta \sum_n \epsilon_n^i f_n^{i\dagger} f_n^i}}{\text{Tr} \left[e^{-\beta \sum_n \epsilon_n^i f_n^{i\dagger} f_n^i} \right]}. \quad (\text{C.11})$$

$$\Rightarrow \langle n_m \rangle(t) = \text{Tr} \left[e^{-iH_f t} \rho_0 e^{iH_f t} n_m \right] = \text{Tr} \left[\rho_0 e^{iH_f t} n_m e^{-iH_f t} \right] \quad (\text{C.12})$$

$$n_m(t) = e^{iH_f t} n_m e^{-iH_f t} \quad (\text{C.13})$$

$$= \sum_{nn'} e^{iH_f t} f_n^{f\dagger} f_{n'}^f e^{-iH_f t} U_{nm}^f U_{n'm}^f \quad (\text{C.14})$$

$$= \sum_{nn'} \underbrace{e^{iH_f t} f_n^{f\dagger} e^{-iH_f t}}_{f_n^{f\dagger}(t)} \underbrace{e^{iH_f t} f_{n'}^f e^{-iH_f t}}_{f_{n'}^f(t)} U_{nm}^f U_{n'm}^f \quad (\text{C.15})$$

$$\partial_t f_n^f(t) = i \left[H_f, f_n^f(t) \right] = -i \epsilon_n^f f_n^f(t) \quad (\text{C.16})$$

$$\Rightarrow f_n^f(t) = e^{-i\epsilon_n^f t} f_n^f \quad (\text{C.17})$$

From Eq. (C.12) and Eq. (C.15) follows

$$\langle n_m \rangle(t) = \sum_{mm'} e^{i(\epsilon_n^f - \epsilon_{n'}^f)t} \text{Tr} \left[\rho_0 f_n^{f\dagger} f_{n'}^f \right] U_{nm}^f U_{n'm'}^f. \quad (\text{C.18})$$

Using Eq. (C.6) and Eq. (C.7) to transform $f_n^{f\dagger}$ and $f_{n'}^f$ in the initial basis yields

$$\langle n_m \rangle(t) = \sum_{kk'} \sum_{mm'} e^{i(\epsilon_k^f - \epsilon_{k'}^f)t} \text{Tr} \left[\underbrace{\rho_0 f_n^{i\dagger} f_{n'}^i}_{f(\epsilon_n^i) \delta_{n,n'}} \right] U_{km}^f U_{k'm}^f \left(U^i U^{i\dagger} \right)_{nk} \left(U^f U^{f\dagger} \right)_{k'n'} \quad (\text{C.19})$$

$$= \sum_{kk'} e^{i(\epsilon_k^f - \epsilon_{k'}^f)t} U_{km}^f U_{k'm}^f \sum_n f(\epsilon_n^i) \left(U^i U^{i\dagger} \right)_{nk} \left(U^f U^{f\dagger} \right)_{k'n} \quad (\text{C.20})$$

$$= \sum_{kk'} e^{i(\epsilon_k^f - \epsilon_{k'}^f)t} U_{km}^f U_{k'm}^f \sum_n \left(U^f U^{f\dagger} \right)_{k'n} f(\epsilon_n^i) \left(U^i U^{i\dagger} \right)_{nk} \quad (\text{C.21})$$

$$= \sum_{kk'} e^{i(\epsilon_k^f - \epsilon_{k'}^f)t} \Theta_{kk'}^m = \sum_{k=1}^{N-1} \sum_{k'=0}^{k-1} 2 \cos \left((\epsilon_k^f - \epsilon_{k'}^f)t \right) \Theta_{kk'}^m + \sum_{k=0}^{N-1} \Theta_{kk}^m \quad (\text{C.22})$$

$$\text{with } \Theta_{kk'}^m = U_{km}^f U_{k'm}^f \cdot \left(\left(U^f U^{f\dagger} \right) \text{diag} \left(f(\epsilon_1^i), f(\epsilon_2^i), \dots \right) \left(U^i U^{i\dagger} \right) \right)_{k'k}. \quad (\text{C.23})$$

C.2 Propagation time

To calculate the time it takes a particle to hop from one site a to the next site b we start with a simple model Hamiltonian describing this hopping process

$$H_{\text{hop}} = V \left(a^\dagger b + b^\dagger a \right). \quad (\text{C.24})$$

a^\dagger, a and b^\dagger, b are the fermionic creation and annihilation operators for the both sites and V is the hopping parameter. Hopping can only occur in the subspace with one electron. We denote the base vectors for this subspace with $|1, 0\rangle$ and $|0, 1\rangle$. The Hamilton matrix in this subspace is given by

$$H = \begin{pmatrix} 0 & V \\ V & 0 \end{pmatrix} \quad (\text{C.25})$$

with the eigenvalues $\lambda_\pm = \pm V$ and the eigenvectors

$$\vec{v}_\pm = \frac{1}{\sqrt{2}} \begin{pmatrix} 1 \\ \pm 1 \end{pmatrix}. \quad (\text{C.26})$$

The base vectors are thus given by

$$|1,0\rangle = \sqrt{2}(v_+ + v_-) \quad \text{and} \quad |0,1\rangle = \frac{\sqrt{2}}{2}(v_+ - v_-). \quad (\text{C.27})$$

To determine the time t_{hop} it takes a particle to hop from site a to site b we prepare the system in the state $|1,0\rangle$ and calculate the time when the probability to find the particle in the state $|0,1\rangle$ is one.

Prepared in the initial state $|1,0\rangle$ the time-dependent state of the system is given by

$$|\psi(t)\rangle = e^{iHt}|1,0\rangle. \quad (\text{C.28})$$

Solving the equation

$$\left| \langle 0,1 | \psi(t_{\text{hop}}) \rangle \right|^2 \stackrel{!}{=} 1 \quad (\text{C.29})$$

yields the hopping time. The overlap is given by

$$\langle 0,1 | \psi(t_{\text{hop}}) \rangle = v_+^\dagger e^{iHt} v_+ + v_-^\dagger e^{iHt} v_- = 2i \sin(Vt). \quad (\text{C.30})$$

The time-dependent probability to find the particle on site b is therefore

$$\left| \langle 0,1 | \psi(t_{\text{hop}}) \rangle \right|^2 = 4 \sin^2(Vt). \quad (\text{C.31})$$

With Eq. (C.29) we find for the hopping time

$$\sin(Vt_{\text{hop}}) = \frac{1}{2} \quad \Rightarrow \quad t_{\text{hop}} = \frac{\pi}{6V}. \quad (\text{C.32})$$

Summing up the hopping times for a chain with N sites gives the recurrence time:

$$T_{\text{rec}} = 2 \sum_{i=0}^{N-2} t_{\text{hop}}^i = \sum_{i=0}^{N-2} \frac{\pi}{3t_i} \quad (\text{C.33})$$

For a Wilson chain, $t_i \approx \frac{D}{2} (1 + \Lambda^{-1}) \Lambda^{-\frac{i}{2}}$, this yields

$$\Rightarrow T_{\text{rec}} \approx \frac{\pi}{3} \frac{2}{D(1 + \Lambda^{-1})} \sum_{i=0}^{N-2} \Lambda^{\frac{i}{2}} = \frac{\pi}{3} \frac{2}{D(1 + \Lambda^{-1})} \frac{1 - \Lambda^{\frac{N-1}{2}}}{1 - \Lambda^{\frac{1}{2}}}. \quad (\text{C.34})$$

Appendix D

Strong Coupling Treatment of Interacting Resonant-Level Model

In the $U \rightarrow \infty$ limit one can derive for the IRLM an equation for the damping rate, the oscillation frequency, and the functional form of the time-dependent impurity occupation. The following presentation is a summary of [183].

The Hamiltonian of the IRLM mapped to a Wilson chain is given by (5.2) and reads

$$H = H_{\text{loc}} + H_{\text{mix}} + H_{\text{chain}} \quad (\text{D.1})$$

$$\text{with } H_{\text{loc}} = E_{\text{d}} d^\dagger d + V \left(d^\dagger c_0 + c_0^\dagger d \right) + U \left(d^\dagger d - \frac{1}{2} \right) \left(c_0^\dagger c_0 - \frac{1}{2} \right), \quad (\text{D.2})$$

$$H_{\text{mix}} = t_0 \left(c_0^\dagger c_1 + c_1^\dagger c_0 \right), \quad (\text{D.3})$$

$$\text{and } H_{\text{chain}} = \sum_{n=1}^{\infty} t_n \left(c_n^\dagger c_{n+1} + c_{n+1}^\dagger c_n \right). \quad (\text{D.4})$$

We start by diagonalizing H_{loc} . The total occupation operator of the impurity and the first Wilson chain site is given by $N = d^\dagger d + c_0^\dagger c_0$. Because N commutes with H_{loc} , $[N, H_{\text{loc}}] = 0$, we diagonalize H_{loc} in the three different particle number sectors,

$N = 0$: One state

$$|0\rangle = |n_{\text{d}} = 0, n_0 = 0\rangle, E_0 = \frac{U}{4} \quad (\text{D.5})$$

$N = 2$: One state

$$|2\rangle = |n_{\text{d}} = 1, n_0 = 1\rangle, E_2 = E_{\text{d}} + \frac{U}{4} \quad (\text{D.6})$$

$N = 1$: Two states $|1, 0\rangle$ and $|0, 1\rangle$. The eigenstates and eigenenergies are

$$|a\rangle = \alpha|1, 0\rangle + \beta|0, 1\rangle, \quad E_a = \frac{E_{\text{d}}}{2} - \frac{U}{4} - \sqrt{\left(\frac{E_{\text{d}}}{2}\right)^2 + V^2} \quad (\text{D.7})$$

$$|b\rangle = \beta|1, 0\rangle - \alpha|0, 1\rangle, \quad E_b = \frac{E_{\text{d}}}{2} - \frac{U}{4} + \sqrt{\left(\frac{E_{\text{d}}}{2}\right)^2 + V^2} \quad (\text{D.8})$$

The parameters α and β are defined by

$$\alpha^2 + \beta^2 = 1 \quad (\text{D.9})$$

$$\text{and } 2\alpha\beta = -\frac{V}{\sqrt{\left(\frac{E_d}{2}\right)^2 + V^2}} \quad (\text{D.10})$$

For $U \rightarrow \infty$ the $N = 0$ and $N = 2$ states decouple from the chain. As the first site of the Wilson chain is included in H_{loc} we end up with an effective new chain starting from the second chain site. For this chain the mapping of the bath onto a Wilson chain is reversed resulting in an effective bath with a reduced bandwidth. Hence we end up with a two-state system coupled to an effective bath. For this setup the decay rate τ of the state $|b\rangle$ to the state $|a\rangle$ can be calculated with Fermi's golden rule. To calculate the matrix element $\langle a|H|b\rangle$ needed to evaluate the transition probability with the golden rule the Schrieffer-Wolff transformation [42, Sec 1.4] is employed to eliminate the coupling to the bath in linear order of t_0 and only the quadratic order terms are taken into account. In this transformation the large U limit is exploited. The decay rate of the state $|b\rangle$ is then given by

$$\tau^{-1} = 4\pi \left(\frac{4D}{\pi^2 U}\right)^2 \frac{V^2}{\sqrt{\left(\frac{E_d}{2}\right)^2 + V^2}}. \quad (\text{D.11})$$

For $U \rightarrow \infty$ the decay rate diverges, $\tau^{-1} \rightarrow 0$ indicating that the H_{loc} decouples from the chain: the system shows coherent Rabi-like oscillations without decay.

To determine the functional form of $n_d(t)$ one writes the state of the system as a product of local and bath states,

$$|\psi(t)\rangle = c_a(t)|a\rangle \otimes |\psi_a(t)\rangle_{\text{bath}} + c_b(t)|b\rangle \otimes |\psi_b(t)\rangle_{\text{bath}}. \quad (\text{D.12})$$

The impurity occupation number is then given by

$$n_d(t) = \langle \psi(t) | d^\dagger d | \psi(t) \rangle \quad (\text{D.13})$$

$$= \left(\langle \psi_a(t) | \langle a | c_a^*(t) + \langle \psi_b(t) | \langle b | c_b^*(t) \right) d^\dagger d \left(|\psi_a(t)\rangle |a\rangle c_a(t) + |\psi_b(t)\rangle |b\rangle c_b(t) \right) \quad (\text{D.14})$$

$$= |c_a(t)|^2 \langle a | d^\dagger d | a \rangle + |c_b(t)|^2 \langle b | d^\dagger d | b \rangle + c_a^*(t) c_b(t) \langle a | d^\dagger d | b \rangle \langle \psi_a(t) | \psi_b(t) \rangle + c_b^*(t) c_a(t) \langle b | d^\dagger d | a \rangle \langle \psi_b(t) | \psi_a(t) \rangle. \quad (\text{D.15})$$

From the Fermi's golden rule argument from above we know that the coefficient $c_b(t)$ decays with the rate τ and since the norm of $|\psi(t)\rangle$ is conserved the equations

$$|c_a(t)|^2 = 1 - |c_b(0)|^2 e^{-\frac{t}{\tau}} \quad \text{and} \quad |c_b(t)|^2 = |c_b(0)|^2 e^{-\frac{t}{\tau}} \quad (\text{D.16})$$

hold. Hence the first two terms in Eq. (D.15) generate a decay with rate τ . In the last two terms in Eq. (D.15) we neglect the time dependence of $|\psi_a(t)\rangle$ and $|\psi_b(t)\rangle$ and, furthermore, notice that in general $\langle \psi_a | \psi_b \rangle \neq 0$. From Eq. (D.16) we know $c_b(t) \propto e^{-\frac{t}{2\tau}}$ and therefore the products $c_a^*(t)c_b(t)$ and $c_b^*(t)c_a(t)$ in Eq. (D.15) generate, among others, terms decaying with the rate 2τ thereby introducing a second time scale for the system.

Finally, the time-dependent impurity occupation number contains terms $\propto e^{-\frac{t}{2\tau}}$ and $\propto e^{-\frac{t}{\tau}}$ and from Eq. (D.15) one can deduce the form

$$\begin{aligned} n_d(t) = & A \left(e^{-\frac{t}{2\tau}} \cos(\Omega t) \sqrt{1 - e^{-\frac{t}{\tau}} \cos^2(\theta)} - e^{-\frac{t}{\tau}} \sin(\theta) \right) \\ & + (1 - n_0) \left(1 - e^{-\frac{t}{\tau}} \right) + n_0 e^{-\frac{t}{\tau}}. \end{aligned} \quad (\text{D.17})$$

In the calculation the parameters

$$A \propto |c_b(0)| \langle \psi_a(0) | \psi_a(0) \rangle \quad (\text{D.18})$$

$$\text{and } B = |c_b(0)|^2 =: \cos^2 \theta \quad (\text{D.19})$$

are introduced.

Thus the impurity occupation number decays with rate τ and this decay is overlaid with damped Rabi oscillations with frequency

$$\Omega = E_b - E_a = 2 \sqrt{\left(\frac{E_d}{2}\right)^2 + V^2} \quad (\text{D.20})$$

and decay rate 2τ . In the non-interacting case one can observe damped Rabi oscillations as well (cf. Eq. (3.18)). However, here the frequency only depends on final impurity energy E_f . In the $U \rightarrow \infty$ limit the frequency Ω is renormalized by the hybridization, Eq. (D.20). In both cases, $U = 0$ and $U \rightarrow \infty$, the decay of the occupation number is twice as fast as the damping of the Rabi oscillations. The reason that the model shows the same behavior in these cases is that for low energies the IRLM is equivalent to the RLM with renormalized parameters.

Bibliography

- [1] DE HAAS, W. J.; DE BOER, J.; VAN DEN BERG, G. J.: The electrical resistance of gold, copper and lead at low temperatures. In: *Physica* 1 (1934), No. 7-12, p. 1115 – 1124. doi: [10.1016/S0031-8914\(34\)80310-2](https://doi.org/10.1016/S0031-8914(34)80310-2)
- [2] KONDO, J.: Resistance Minimum in Dilute Magnetic Alloys. In: *Progress of Theoretical Physics* 32 (1964), No. 1, p. 37–49. doi: [10.1143/PTP.32.37](https://doi.org/10.1143/PTP.32.37)
- [3] HEWSON, A. C.: *The Kondo Problem to Heavy Fermions*. Cambridge : Cambridge University Press, May 1997 doi: [10.2277/0521599474](https://doi.org/10.2277/0521599474)
- [4] VAN DELFT, D.; KES, P.: The discovery of superconductivity. In: *Physics Today* 63 (2010), No. 9, p. 38–43. doi: [10.1063/1.3490499](https://doi.org/10.1063/1.3490499)
- [5] BARDEEN, J.; COOPER, L. N.; SCHRIEFFER, J. R.: Theory of Superconductivity. In: *Phys. Rev.* 108 (1957), p. 1175–1204. doi: [10.1103/PhysRev.108.1175](https://doi.org/10.1103/PhysRev.108.1175)
- [6] ANDERSON, M. H.; ENSHER, J. R.; MATTHEWS, M. R.; WIEMAN, C. E.; CORNELL, E. A.: Observation of Bose-Einstein Condensation in a Dilute Atomic Vapor. In: *Science* 269 (1995), No. 5221, p. 198–201. doi: [10.1126/science.269.5221.198](https://doi.org/10.1126/science.269.5221.198)
- [7] DAVIS, K. B.; MEWES, M. O.; ANDREWS, M. R.; VAN DRUTEN, N. J.; DURFEE, D. S.; KURN, D. M.; KETTERLE, W.: Bose-Einstein Condensation in a Gas of Sodium Atoms. In: *Phys. Rev. Lett.* 75 (1995), p. 3969–3973. doi: [10.1103/PhysRevLett.75.3969](https://doi.org/10.1103/PhysRevLett.75.3969)
- [8] BLOCH, I.; DALIBARD, J.; ZWARGER, W.: Many-body physics with ultracold gases. In: *Rev. Mod. Phys.* 80 (2008), p. 885–964. doi: [10.1103/RevModPhys.80.885](https://doi.org/10.1103/RevModPhys.80.885)
- [9] LEWENSTEIN, M.; SANPERA, A.; AHUFINGER, V.; DAMSKI, B.; SEN(De), A.; SEN, U.: Ultracold atomic gases in optical lattices: mimicking condensed matter physics and beyond. In: *Advances in Physics* 56 (2007), No. 2, p. 243–379. doi: [10.1080/00018730701223200](https://doi.org/10.1080/00018730701223200)
- [10] GREINER, M.; MANDEL, O.; ESSLINGER, T.; HÄNSCH, T. W.; BLOCH, I.: Quantum phase transition from a superfluid to a Mott insulator in a gas of ultracold atoms. In: *Nature* 415 (2002), p. 39–44. doi: [10.1038/415039a](https://doi.org/10.1038/415039a)
- [11] JÖRDENS, R.; STROHMAIER, N.; GÜNTER, K.; MORITZ, H.; ESSLINGER, T.: A Mott insulator of fermionic atoms in an optical lattice. In: *Nature* 455 (2008), p. 204–207. doi: [10.1038/nature07244](https://doi.org/10.1038/nature07244)
- [12] ANDERLINI, M.; LEE, P. J.; BROWN, B. L.; SEBKY-STABLEY, J.; PHILLIPS, W. D.; PORTO, J. V.: Controlled exchange interaction between pairs of neutral atoms in an optical lattice. In: *Nature* 448 (2007), No. 7152, p. 452–456. doi: [10.1038/nature06011](https://doi.org/10.1038/nature06011)
- [13] MONROE, C.: Quantum information processing with atoms and photons. In: *Nature* 416 (2002), No. 6877, p. 238–246. doi: [10.1038/416238a](https://doi.org/10.1038/416238a)
- [14] TROTZKY, S.; CHEN, Y.-A.; FLESCHE, A.; MCCULLOCH, I. P.; SCHOLLWOCK, U.; EISERT, J.; BLOCH, I.: Probing the relaxation towards equilibrium in an isolated strongly correlated one-dimensional Bose gas. In: *Nature Physics* 8 (2012), p. 325–330. doi: [10.1038/nphys2232](https://doi.org/10.1038/nphys2232)

- [15] REED, M. A.; RANDALL, J. N.; AGGARWAL, R. J.; MATYI, R. J.; MOORE, T. M.; WETSEL, A. E.: Observation of discrete electronic states in a zero-dimensional semiconductor nanostructure. In: *Phys. Rev. Lett.* 60 (1988), p. 535–537. doi: [10.1103/PhysRevLett.60.535](https://doi.org/10.1103/PhysRevLett.60.535)
- [16] LIU, R.-B.; YAO, W.; SHAM, L.J.: Quantum computing by optical control of electron spins. In: *Advances in Physics* 59 (2010), No. 5, p. 703–802. doi: [10.1080/00018732.2010.505452](https://doi.org/10.1080/00018732.2010.505452)
- [17] HANSON, R.; KOUWENHOVEN, L. P.; PETTA, J. R.; TARUCHA, S.; VANDERSYPEN, L. M. K.: Spins in few-electron quantum dots. In: *Rev. Mod. Phys.* 79 (2007), p. 1217–1265. doi: [10.1103/RevModPhys.79.1217](https://doi.org/10.1103/RevModPhys.79.1217)
- [18] LADD, T. D.; JELEZKO, F.; LAFLAMME, R.; NAKAMURA, Y.; MONROE, C.; O'BRIEN, J. L.: Quantum computers. In: *Nature* 464 (2010), p. 45–53. doi: [10.1038/nature08812](https://doi.org/10.1038/nature08812)
- [19] DIVINCENZO, D. P.: The Physical Implementation of Quantum Computation. In: *Fortschritte der Physik* 48 (2000), No. 9-11, p. 771–783. doi: [10.1002/1521-3978\(200009\)48:9/11<771::AID-PROP771>3.0.CO;2-E](https://doi.org/10.1002/1521-3978(200009)48:9/11<771::AID-PROP771>3.0.CO;2-E)
- [20] ELZERMAN, J. M.; HANSON, R.; WILLEMS VAN BEVEREN, L. H.; WITKAMP, B.; VANDERSYPEN, L. M. K.; KOUWENHOVEN, L. P.: Single-shot read-out of an individual electron spin in a quantum dot. In: *Nature* 430 (2004), p. 431–435. doi: [10.1038/nature02693](https://doi.org/10.1038/nature02693)
- [21] LEGGETT, A. J.; CHAKRAVARTY, S.; DORSEY, A. T.; FISHER, M. P. A.; GARG, A.; ZWERGER, W.: Dynamics of the dissipative two-state system. In: *Rev. Mod. Phys.* 59 (1987), p. 1–85. doi: [10.1103/RevModPhys.59.1](https://doi.org/10.1103/RevModPhys.59.1)
- [22] FILYOV, V. M.; WIEGMANN, P. B.: A method for solving the Kondo problem. In: *Physics Letters A* 76 (1980), No. 3–4, p. 283 – 286. doi: [10.1016/0375-9601\(80\)90494-6](https://doi.org/10.1016/0375-9601(80)90494-6)
- [23] SCHLOTTMANN, P.: Simple spinless mixed-valence model. II. Solution of the isolated f -level problem. In: *Phys. Rev. B* 22 (1980), p. 622–631. doi: [10.1103/PhysRevB.22.622](https://doi.org/10.1103/PhysRevB.22.622)
- [24] ANDERSON, P. W.: Localized Magnetic States in Metals. In: *Phys. Rev.* 124 (1961), p. 41–53. doi: [10.1103/PhysRev.124.41](https://doi.org/10.1103/PhysRev.124.41)
- [25] GOLDBABER-GORDON, D.; SHTRIKMAN, H.; MAHALU, D.; ABUSCH-MAGDER, D.; MEIRAV, U.; KASTNER, M. A.: Kondo effect in a single-electron transistor. In: *Nature* 391 (1998), p. 156 – 159. doi: [10.1038/34373](https://doi.org/10.1038/34373)
- [26] CRONENWETT, S. M.; OOSTERKAMP, T. H.; KOUWENHOVEN, L. P.: A Tunable Kondo Effect in Quantum Dots. In: *Science* 281 (1998), No. 5376, p. 540–544. doi: [10.1126/science.281.5376.540](https://doi.org/10.1126/science.281.5376.540)
- [27] VAN DER WIEL, W. G.; FRANCESCHI, S. D.; FUJISAWA, T.; ELZERMAN, J. M.; TARUCHA, S.; KOUWENHOVEN, L. P.: The Kondo Effect in the Unitary Limit. In: *Science* 289 (2000), No. 5487, p. 2105–2108. doi: [10.1126/science.289.5487.2105](https://doi.org/10.1126/science.289.5487.2105)
- [28] WILSON, K. G.: The renormalization group: Critical phenomena and the Kondo problem. In: *Rev. Mod. Phys.* 47 (1975), p. 773–840. doi: [10.1103/RevModPhys.47.773](https://doi.org/10.1103/RevModPhys.47.773)
- [29] BULLA, R.; COSTI, T. A.; PRUSCHKE, T.: Numerical renormalization group method for quantum impurity systems. In: *Rev. Mod. Phys.* 80 (2008), p. 395–450. doi: [10.1103/RevModPhys.80.395](https://doi.org/10.1103/RevModPhys.80.395)
- [30] ANDREI, N.: Diagonalization of the Kondo Hamiltonian. In: *Phys. Rev. Lett.* 45 (1980), p. 379–382. doi: [10.1103/PhysRevLett.45.379](https://doi.org/10.1103/PhysRevLett.45.379)
- [31] VIGMAN, P. B.: Exact solution of s - d exchange model at $T = 0$. In: *Pis'ma Zh. Eksp. Teor. Fiz.* 31 (1980), p. 392–398. http://www.jetpletters.ac.ru/ps/1353/article_20434.shtml

- [32] WHITE, S. R.: Density matrix formulation for quantum renormalization groups. In: *Phys. Rev. Lett.* 69 (1992), p. 2863–2866. doi: [10.1103/PhysRevLett.69.2863](https://doi.org/10.1103/PhysRevLett.69.2863)
- [33] CAMPO, V. L.; OLIVEIRA, L. N.: Alternative discretization in the numerical renormalization-group method. In: *Phys. Rev. B* 72 (2005), p. 104432. doi: [10.1103/PhysRevB.72.104432](https://doi.org/10.1103/PhysRevB.72.104432)
- [34] ŽITKO, R.; PRUSCHKE, T.: Energy resolution and discretization artifacts in the numerical renormalization group. In: *Phys. Rev. B* 79 (2009), p. 085106. doi: [10.1103/PhysRevB.79.085106](https://doi.org/10.1103/PhysRevB.79.085106)
- [35] ROSCH, A.: Wilson chains are not thermal reservoirs. In: *The European Physical Journal B - Condensed Matter and Complex Systems* 85 (2012), p. 1–2. doi: [10.1140/epjb/e2011-20880-7](https://doi.org/10.1140/epjb/e2011-20880-7)
- [36] VOJTA, M.; BULLA, R.; GÜTTGE, F.; ANDERS, F.: Mass-flow error in the numerical renormalization-group method and the critical behavior of the sub-Ohmic spin-boson model. In: *Phys. Rev. B* 81 (2010), p. 075122. doi: [10.1103/PhysRevB.81.075122](https://doi.org/10.1103/PhysRevB.81.075122)
- [37] VOJTA, M.; TONG, N.-H.; BULLA, R.: Erratum: Quantum Phase Transitions in the Sub-Ohmic Spin-Boson Model: Failure of the Quantum-Classical Mapping [*Phys. Rev. Lett.* 94, 070604 (2005)]. In: *Phys. Rev. Lett.* 102 (2009), p. 249904. doi: [10.1103/PhysRevLett.102.249904](https://doi.org/10.1103/PhysRevLett.102.249904)
- [38] VOJTA, M.: Numerical renormalization group for the sub-Ohmic spin-boson model: A conspiracy of errors. In: *Phys. Rev. B* 85 (2012), p. 115113. doi: [10.1103/PhysRevB.85.115113](https://doi.org/10.1103/PhysRevB.85.115113)
- [39] KIRCHNER, S.: Spin Path Integrals, Berry Phase, and the Quantum Phase Transition in the Sub-Ohmic Spin-Boson Model. In: *Journal of Low Temperature Physics* 161 (2010), p. 282–298. doi: [10.1007/s10909-010-0193-4](https://doi.org/10.1007/s10909-010-0193-4)
- [40] WILSON, K. G.: *Nobel Lectures in Physics 1981-1990*. Chap. The Renormalization Group and Critical Phenomena. Singapore : World Scientific Publishing Co, 1993, http://www.nobelprize.org/nobel_prizes/physics/laureates/1982/wilson-lecture.html
- [41] LLOYD, S.: Universal Quantum Simulators. In: *Science* 273 (1996), p. 1073–1078. doi: [10.1126/science.273.5278.1073](https://doi.org/10.1126/science.273.5278.1073)
- [42] MAHAN, G.D.: *Many-Particle Physics*. Kluwer Academic/Plenum Publishers, 2000 (Physics of Solids and Liquids)
- [43] BRUUS, H.; FLENSBERG, K.: *Many-body Quantum Theory In Condensed Matter Physics: An Introduction*. Oxford University Press, 2004 (Oxford graduate texts in mathematics)
- [44] NOACK, R. M.; MANMANA, S. R.: Diagonalization- and Numerical Renormalization-Group-Based Methods for Interacting Quantum Systems. In: *AIP Conference Proceedings* 789 (2005), No. 1, p. 93–163. doi: [10.1063/1.2080349](https://doi.org/10.1063/1.2080349)
- [45] LANZOS, C.: An Iteration Method for the Solution of the Eigenvalue Problem of Linear Differential and Integral Operators. In: *Journal of Research of the National Bureau of Standards* 45 (1950), No. 4, p. 255–282
- [46] YAMADA, S.; IMAMURA, T.; MACHIDA, M.: 16.447 TFlops and 159-Billion-dimensional Exact-diagonalization for Trapped Fermion-Hubbard Model on the Earth Simulator. In: *Supercomputing, 2005. Proceedings of the ACM/IEEE SC 2005 Conference*, doi: [10.1109/SC.2005.1](https://doi.org/10.1109/SC.2005.1), Nov 2005, p. 44
- [47] WEISSE, A.; WELLEIN, G.; ALVERMANN, A.; FEHSKE, H.: The kernel polynomial method. In: *Rev. Mod. Phys.* 78 (2006), p. 275–306. doi: [10.1103/RevModPhys.78.275](https://doi.org/10.1103/RevModPhys.78.275)
- [48] ALVERMANN, A.; FEHSKE, H.: Sparse Polynomial Space Approach to Dissipative Quantum Systems: Application to the Sub-Ohmic Spin-Boson Model. In: *Phys. Rev. Lett.* 102 (2009), p. 150601. doi: [10.1103/PhysRevLett.102.150601](https://doi.org/10.1103/PhysRevLett.102.150601)

- [49] CARDY, J. L.: *Scaling and Renormalization in Statistical Physics*. Cambridge University Press, 1996 (Cambridge Lecture Notes in Physics)
- [50] VOJTA, M.: Quantum phase transitions. In: *Reports on Progress in Physics* 66 (2003), No. 12, p. 2069. doi: [10.1088/0034-4885/66/12/R01](https://doi.org/10.1088/0034-4885/66/12/R01)
- [51] SCHOELLER, H.: An Introduction to Real-Time Renormalization Group. In: BRANDES, T. (Editor): *Low-Dimensional Systems* Volume 544. Springer Berlin / Heidelberg, 2000, p. 137–166. doi: [10.1007/3-540-46438-7_7](https://doi.org/10.1007/3-540-46438-7_7)
- [52] VON DER LINDEN, W.: A quantum Monte Carlo approach to many-body physics. In: *Physics Reports* 220 (1992), No. 2–3, p. 53 – 162. doi: [10.1016/0370-1573\(92\)90029-Y](https://doi.org/10.1016/0370-1573(92)90029-Y)
- [53] FOULKES, W. M. C.; MITAS, L.; NEEDS, R. J.; RAJAGOPAL, G.: Quantum Monte Carlo simulations of solids. In: *Rev. Mod. Phys.* 73 (2001), p. 33–83. doi: [10.1103/RevModPhys.73.33](https://doi.org/10.1103/RevModPhys.73.33)
- [54] EVERTZ, H. G.: The loop algorithm. In: *Advances in Physics* 52 (2003), No. 1, p. 1–66. doi: [10.1080/0001873021000049195](https://doi.org/10.1080/0001873021000049195)
- [55] HIRSCH, J. E.; FYE, R. M.: Monte Carlo Method for Magnetic Impurities in Metals. In: *Phys. Rev. Lett.* 56 (1986), p. 2521–2524. doi: [10.1103/PhysRevLett.56.2521](https://doi.org/10.1103/PhysRevLett.56.2521)
- [56] GULL, E.; MILLIS, A. J.; LICHTENSTEIN, A. I.; R., Alexey N.; TROYER, M.; WERNER, P.: Continuous-time Monte Carlo methods for quantum impurity models. In: *Rev. Mod. Phys.* 83 (2011), p. 349–404. doi: [10.1103/RevModPhys.83.349](https://doi.org/10.1103/RevModPhys.83.349)
- [57] WERNER, P.; OKA, T.; MILLIS, A. J.: Diagrammatic Monte Carlo simulation of nonequilibrium systems. In: *Phys. Rev. B* 79 (2009), p. 035320. doi: [10.1103/PhysRevB.79.035320](https://doi.org/10.1103/PhysRevB.79.035320)
- [58] SCHIRÓ, M.; FABRIZIO, M.: Real-time diagrammatic Monte Carlo for nonequilibrium quantum transport. In: *Phys. Rev. B* 79 (2009), p. 153302. doi: [10.1103/PhysRevB.79.153302](https://doi.org/10.1103/PhysRevB.79.153302)
- [59] METZNER, W.; VOLLHARDT, D.: Correlated Lattice Fermions in $d = \infty$ Dimensions. In: *Phys. Rev. Lett.* 62 (1989), p. 324–327. doi: [10.1103/PhysRevLett.62.324](https://doi.org/10.1103/PhysRevLett.62.324)
- [60] GEORGES, A.; KOTLIAR, G.; KRAUTH, W.; ROZENBERG, M. J.: Dynamical mean-field theory of strongly correlated fermion systems and the limit of infinite dimensions. In: *Rev. Mod. Phys.* 68 (1996), p. 13–125. doi: [10.1103/RevModPhys.68.13](https://doi.org/10.1103/RevModPhys.68.13)
- [61] SABERI, H.; WEICHELBAUM, A.; VON DELFT, J.: Matrix-product-state comparison of the numerical renormalization group and the variational formulation of the density-matrix renormalization group. In: *Phys. Rev. B* 78 (2008), p. 035124. doi: [10.1103/PhysRevB.78.035124](https://doi.org/10.1103/PhysRevB.78.035124)
- [62] WEICHELBAUM, A.; VERSTRAETE, F.; SCHOLLWÖCK, U.; CIRAC, J. I.; VON DELFT, Jan: Variational matrix-product-state approach to quantum impurity models. In: *Phys. Rev. B* 80 (2009), p. 165117. doi: [10.1103/PhysRevB.80.165117](https://doi.org/10.1103/PhysRevB.80.165117)
- [63] SCHOLLWÖCK, U.: The density-matrix renormalization group in the age of matrix product states. In: *Annals of Physics* 326 (2011), No. 1, p. 96 – 192. doi: [10.1016/j.aop.2010.09.012](https://doi.org/10.1016/j.aop.2010.09.012)
- [64] PIŽORN, I.; VERSTRAETE, F.: Variational Numerical Renormalization Group: Bridging the Gap between NRG and Density Matrix Renormalization Group. In: *Phys. Rev. Lett.* 108 (2012), p. 067202. doi: [10.1103/PhysRevLett.108.067202](https://doi.org/10.1103/PhysRevLett.108.067202)
- [65] GÜTTGE, F.: *Simulationenmethoden quantenmechanischer Systeme im thermodynamischen Limes*, RWTH Aachen, Master thesis, 2008
- [66] SCHMIDT, E.: Zur Theorie der linearen und nichtlinearen Integralgleichungen. In: *Mathematische Annalen* 63 (1907), p. 433–476. doi: [10.1007/BF01449770](https://doi.org/10.1007/BF01449770)

- [67] EKERT, A.; KNIGHT, P. L.: Entangled quantum systems and the Schmidt decomposition. In: *American Journal of Physics* 63 (1995), No. 5, p. 415–423. doi: [10.1119/1.17904](https://doi.org/10.1119/1.17904)
- [68] NIELSEN, M.A.; CHUANG, I.L.: *Quantum Computation and Quantum Information*. 10th Anniversary Edition. Cambridge University Press, 2010
- [69] MCCULLOCH, I. P.: From density-matrix renormalization group to matrix product states. In: *Journal of Statistical Mechanics: Theory and Experiment* 2007 (2007), No. 10, p. P10014. doi: [10.1088/1742-5468/2007/10/P10014](https://doi.org/10.1088/1742-5468/2007/10/P10014)
- [70] AMICO, L.; FAZIO, R.; OSTERLOH, A.; VEDRAL, V.: Entanglement in many-body systems. In: *Rev. Mod. Phys.* 80 (2008), p. 517–576. doi: [10.1103/RevModPhys.80.517](https://doi.org/10.1103/RevModPhys.80.517)
- [71] HORODECKI, R.; HORODECKI, P.; HORODECKI, M.; HORODECKI, K.: Quantum entanglement. In: *Rev. Mod. Phys.* 81 (2009), p. 865–942. doi: [10.1103/RevModPhys.81.865](https://doi.org/10.1103/RevModPhys.81.865)
- [72] EISERT, J.; CRAMER, M.; PLENIO, M. B.: *Colloquium*: Area laws for the entanglement entropy. In: *Rev. Mod. Phys.* 82 (2010), p. 277–306. doi: [10.1103/RevModPhys.82.277](https://doi.org/10.1103/RevModPhys.82.277)
- [73] KRISHNA-MURTHY, H. R.; WILKINS, J. W.; WILSON, K. G.: Renormalization-group approach to the Anderson model of dilute magnetic alloys. I. Static properties for the symmetric case. In: *Phys. Rev. B* 21 (1980), p. 1003–1043. doi: [10.1103/PhysRevB.21.1003](https://doi.org/10.1103/PhysRevB.21.1003)
- [74] BULLA, R.; TONG, N.-H.; VOJTA, M.: Numerical Renormalization Group for Bosonic Systems and Application to the Sub-Ohmic Spin-Boson Model. In: *Phys. Rev. Lett.* 91 (2003), p. 170601. doi: [10.1103/PhysRevLett.91.170601](https://doi.org/10.1103/PhysRevLett.91.170601)
- [75] BULLA, R.; LEE, H.-J.; TONG, N.-H.; VOJTA, M.: Numerical renormalization group for quantum impurities in a bosonic bath. In: *Phys. Rev. B* 71 (2005), p. 045122. doi: [10.1103/PhysRevB.71.045122](https://doi.org/10.1103/PhysRevB.71.045122)
- [76] ANDERS, F. B.; SCHILLER, A.: Real-Time Dynamics in Quantum-Impurity Systems: A Time-Dependent Numerical Renormalization-Group Approach. In: *Phys. Rev. Lett.* 95 (2005), p. 196801. doi: [10.1103/PhysRevLett.95.196801](https://doi.org/10.1103/PhysRevLett.95.196801)
- [77] ANDERS, F. B.; SCHILLER, A.: Spin precession and real-time dynamics in the Kondo model: Time-dependent numerical renormalization-group study. In: *Phys. Rev. B* 74 (2006), p. 245113. doi: [10.1103/PhysRevB.74.245113](https://doi.org/10.1103/PhysRevB.74.245113)
- [78] WEICHSELBAUM, A.: Tensor networks and the numerical renormalization group. In: *Phys. Rev. B* 86 (2012), p. 245124. doi: [10.1103/PhysRevB.86.245124](https://doi.org/10.1103/PhysRevB.86.245124)
- [79] KARSKI, M.; RAAS, C.; UHRIG, G. S.: Single-particle dynamics in the vicinity of the Mott-Hubbard metal-to-insulator transition. In: *Phys. Rev. B* 77 (2008), p. 075116. doi: [10.1103/PhysRevB.77.075116](https://doi.org/10.1103/PhysRevB.77.075116)
- [80] HEWSON, A. C.; MEYER, D.: Numerical renormalization group study of the Anderson-Holstein impurity model. In: *Journal of Physics: Condensed Matter* 14 (2002), No. 3, p. 427. doi: [10.1088/0953-8984/14/3/312](https://doi.org/10.1088/0953-8984/14/3/312)
- [81] BULLA, R.; PRUSCHKE, T.; HEWSON, A. C.: Anderson impurity in pseudo-gap Fermi systems. In: *Journal of Physics: Condensed Matter* 9 (1997), No. 47, p. 10463. doi: [10.1088/0953-8984/9/47/014](https://doi.org/10.1088/0953-8984/9/47/014)
- [82] WEICHSELBAUM, A.: Discarded weight and entanglement spectra in the numerical renormalization group. In: *Phys. Rev. B* 84 (2011), p. 125130. doi: [10.1103/PhysRevB.84.125130](https://doi.org/10.1103/PhysRevB.84.125130)
- [83] OLIVEIRA, W. C.; OLIVEIRA, L. N.: Generalized numerical renormalization-group method to calculate the thermodynamical properties of impurities in metals. In: *Phys. Rev. B* 49 (1994), p. 11986–11994. doi: [10.1103/PhysRevB.49.11986](https://doi.org/10.1103/PhysRevB.49.11986)
- [84] HOFSTETTER, W.: Generalized Numerical Renormalization Group for Dynamical Quantities. In: *Phys. Rev. Lett.* 85 (2000), p. 1508–1511. doi: [10.1103/PhysRevLett.85.1508](https://doi.org/10.1103/PhysRevLett.85.1508)

- [85] PETERS, R.; PRUSCHKE, T.; ANDERS, F. B.: Numerical renormalization group approach to Green's functions for quantum impurity models. In: *Phys. Rev. B* 74 (2006), p. 245114. doi: [10.1103/PhysRevB.74.245114](https://doi.org/10.1103/PhysRevB.74.245114)
- [86] CHENG, M.; GLOSSOP, M. T.; INGERSENT, K.: Quantum phase transitions in a charge-coupled Bose-Fermi Anderson model. In: *Phys. Rev. B* 80 (2009), p. 165113. doi: [10.1103/PhysRevB.80.165113](https://doi.org/10.1103/PhysRevB.80.165113)
- [87] ANDERS, F. B.; BULLA, R.; VOJTA, M.: Equilibrium and Nonequilibrium Dynamics of the Sub-Ohmic Spin-Boson Model. In: *Phys. Rev. Lett.* 98 (2007), p. 210402. doi: [10.1103/PhysRevLett.98.210402](https://doi.org/10.1103/PhysRevLett.98.210402)
- [88] HACKL, A.; ROESEN, D.; KEHREIN, S.; HOFSTETTER, W.: Nonequilibrium Spin Dynamics in the Ferromagnetic Kondo Model. In: *Phys. Rev. Lett.* 102 (2009), p. 196601. doi: [10.1103/PhysRevLett.102.196601](https://doi.org/10.1103/PhysRevLett.102.196601)
- [89] ANDERS, F. B.: Steady-State Currents through Nanodevices: A Scattering-States Numerical Renormalization-Group Approach to Open Quantum Systems. In: *Phys. Rev. Lett.* 101 (2008), p. 066804. doi: [10.1103/PhysRevLett.101.066804](https://doi.org/10.1103/PhysRevLett.101.066804)
- [90] EIDELSTEIN, E.; SCHILLER, A.; GÜTTGE, F.; ANDERS, F. B.: Coherent control of correlated nanodevices: A hybrid time-dependent numerical renormalization-group approach to periodic switching. In: *Phys. Rev. B* 85 (2012), p. 075118. doi: [10.1103/PhysRevB.85.075118](https://doi.org/10.1103/PhysRevB.85.075118)
- [91] SCHOLLWÖCK, U.: The density-matrix renormalization group. In: *Rev. Mod. Phys.* 77 (2005), p. 259–315. doi: [10.1103/RevModPhys.77.259](https://doi.org/10.1103/RevModPhys.77.259)
- [92] HALLBERG, K. A.: New trends in density matrix renormalization. In: *Advances in Physics* 55 (2006), No. 5-6, p. 477–526. doi: [10.1080/00018730600766432](https://doi.org/10.1080/00018730600766432)
- [93] NISHIMOTO, S.; JECKELMANN, E.: Density-matrix renormalization group approach to quantum impurity problems. In: *Journal of Physics: Condensed Matter* 16 (2004), No. 4, p. 613. doi: [10.1088/0953-8984/16/4/010](https://doi.org/10.1088/0953-8984/16/4/010)
- [94] DIAS DA SILVA, L. G. G. V.; HEIDRICH-MEISNER, F.; FEIGUIN, A. E.; BÜSSER, C. A.; MARTINS, G. B.; ANDA, E. V.; DAGOTTO, E.: Transport properties and Kondo correlations in nanostructures: Time-dependent DMRG method applied to quantum dots coupled to Wilson chains. In: *Phys. Rev. B* 78 (2008), p. 195317. doi: [10.1103/PhysRevB.78.195317](https://doi.org/10.1103/PhysRevB.78.195317)
- [95] GUO, C.; WEICHELBAUM, A.; KEHREIN, S.; XIANG, T.; VON DELFT, J.: Density matrix renormalization group study of a quantum impurity model with Landau-Zener time-dependent Hamiltonian. In: *Phys. Rev. B* 79 (2009), p. 115137. doi: [10.1103/PhysRevB.79.115137](https://doi.org/10.1103/PhysRevB.79.115137)
- [96] ÖSTLUND, S.; ROMMER, S.: Thermodynamic Limit of Density Matrix Renormalization. In: *Phys. Rev. Lett.* 75 (1995), p. 3537–3540. doi: [10.1103/PhysRevLett.75.3537](https://doi.org/10.1103/PhysRevLett.75.3537)
- [97] DUKELSKY, J.; MARTÍN-DELGADO, M. A.; NISHINO, T.; SIERRA, G.: Equivalence of the variational matrix product method and the density matrix renormalization group applied to spin chains. In: *EPL (Europhysics Letters)* 43 (1998), No. 4, p. 457. doi: [10.1209/epl/i1998-00381-x](https://doi.org/10.1209/epl/i1998-00381-x)
- [98] SHI, Y.-Y.; DUAN, L.-M.; VIDAL, G.: Classical simulation of quantum many-body systems with a tree tensor network. In: *Phys. Rev. A* 74 (2006), p. 022320. doi: [10.1103/PhysRevA.74.022320](https://doi.org/10.1103/PhysRevA.74.022320)
- [99] VERSTRAETE, F.; MURG, V.; CIRAC, J.I.: Matrix product states, projected entangled pair states, and variational renormalization group methods for quantum spin systems. In: *Advances in Physics* 57 (2008), No. 2, p. 143–224. doi: [10.1080/14789940801912366](https://doi.org/10.1080/14789940801912366)
- [100] SCHOLLWÖCK, U.: Progress in density matrix renormalization: What quantum information is teaching us. In: *Journal of Magnetism and Magnetic Materials* 310 (2007), No. 2, Part 2, p. 1394 – 1400. doi: [10.1016/j.jmmm.2006.10.415](https://doi.org/10.1016/j.jmmm.2006.10.415)

- [101] VERSTRAETE, F.; CIRAC, J. I.: Valence-bond states for quantum computation. In: *Phys. Rev. A* 70 (2004), p. 060302. doi: [10.1103/PhysRevA.70.060302](https://doi.org/10.1103/PhysRevA.70.060302)
- [102] VERSTRAETE, F.; WOLF, M. M.; PEREZ-GARCIA, D.; CIRAC, J. I.: Criticality, the Area Law, and the Computational Power of Projected Entangled Pair States. In: *Phys. Rev. Lett.* 96 (2006), p. 220601. doi: [10.1103/PhysRevLett.96.220601](https://doi.org/10.1103/PhysRevLett.96.220601)
- [103] LIU, L.; YAO, H.; BERG, E.; WHITE, S. R.; KIVELSON, S. A.: Phases of the Infinite U Hubbard Model on Square Lattices. In: *Phys. Rev. Lett.* 108 (2012), p. 126406. doi: [10.1103/PhysRevLett.108.126406](https://doi.org/10.1103/PhysRevLett.108.126406)
- [104] SCHOLLWÖCK, U.; CHAKRAVARTY, Sudip; FJÆRESTAD, J. O.; MARSTON, J. B.; TROYER, M.: Broken Time-Reversal Symmetry in Strongly Correlated Ladder Structures. In: *Phys. Rev. Lett.* 90 (2003), p. 186401. doi: [10.1103/PhysRevLett.90.186401](https://doi.org/10.1103/PhysRevLett.90.186401)
- [105] MCCULLOCH, I. P.: Infinite size density matrix renormalization group, revisited. In: *arxiv:0804.2509* (2008). <http://arxiv.org/abs/0804.2509>
- [106] VIDAL, G.: Classical Simulation of Infinite-Size Quantum Lattice Systems in One Spatial Dimension. In: *Phys. Rev. Lett.* 98 (2007), p. 070201. doi: [10.1103/PhysRevLett.98.070201](https://doi.org/10.1103/PhysRevLett.98.070201)
- [107] VERSTRAETE, F.; GARCÍA-RIPOLL, J. J.; CIRAC, J. I.: Matrix Product Density Operators: Simulation of Finite-Temperature and Dissipative Systems. In: *Phys. Rev. Lett.* 93 (2004), p. 207204. doi: [10.1103/PhysRevLett.93.207204](https://doi.org/10.1103/PhysRevLett.93.207204)
- [108] PRESKILL, J.: Quantum computing and the entanglement frontier. In: *arXiv preprint* (2012), p. 1203.5813. <http://arxiv.org/abs/1203.5813>
- [109] DALEY, A. J.; KOLLATH, C.; SCHOLLWÖCK, U.; VIDAL, G.: Time-dependent density-matrix renormalization-group using adaptive effective Hilbert spaces. In: *Journal of Statistical Mechanics: Theory and Experiment* 2004 (2004), No. 04, p. P04005. doi: [10.1088/1742-5468/2004/04/P04005](https://doi.org/10.1088/1742-5468/2004/04/P04005)
- [110] SCHMITTECKERT, P.: Nonequilibrium electron transport using the density matrix renormalization group method. In: *Phys. Rev. B* 70 (2004), p. 121302. doi: [10.1103/PhysRevB.70.121302](https://doi.org/10.1103/PhysRevB.70.121302)
- [111] VIDAL, G.: Efficient Simulation of One-Dimensional Quantum Many-Body Systems. In: *Phys. Rev. Lett.* 93 (2004), p. 040502. doi: [10.1103/PhysRevLett.93.040502](https://doi.org/10.1103/PhysRevLett.93.040502)
- [112] SUZUKI, M.: Fractal decomposition of exponential operators with applications to many-body theories and Monte Carlo simulations. In: *Physics Letters A* 146 (1990), No. 6, p. 319 – 323. doi: [10.1016/0375-9601\(90\)90962-N](https://doi.org/10.1016/0375-9601(90)90962-N)
- [113] VIDAL, G.: Efficient Classical Simulation of Slightly Entangled Quantum Computations. In: *Phys. Rev. Lett.* 91 (2003), p. 147902. doi: [10.1103/PhysRevLett.91.147902](https://doi.org/10.1103/PhysRevLett.91.147902)
- [114] McLACHLAN, R. I.: On the Numerical Integration of Ordinary Differential Equations by Symmetric Composition Methods. In: *SIAM Journal on Scientific Computing* 16 (1995), No. 1, p. 151–168. doi: [10.1137/0916010](https://doi.org/10.1137/0916010)
- [115] FEIGUIN, A. E.; WHITE, S. R.: Time-step targeting methods for real-time dynamics using the density matrix renormalization group. In: *Phys. Rev. B* 72 (2005), p. 020404. doi: [10.1103/PhysRevB.72.020404](https://doi.org/10.1103/PhysRevB.72.020404)
- [116] WEISS, U.: *Quantum dissipative systems*. World Scientific, 2008 (Series in modern condensed matter physics)
- [117] HAYASHI, T.; FUJISAWA, T.; CHEONG, H. D.; JEONG, Y. H.; HIRAYAMA, Y.: Coherent Manipulation of Electronic States in a Double Quantum Dot. In: *Phys. Rev. Lett.* 91 (2003), p. 226804. doi: [10.1103/PhysRevLett.91.226804](https://doi.org/10.1103/PhysRevLett.91.226804)

- [118] CHIROLLI, L.; BURKARD, G.: Decoherence in solid-state qubits. In: *Advances in Physics* 57 (2008), No. 3, p. 225–285. doi: [10.1080/00018730802218067](https://doi.org/10.1080/00018730802218067)
- [119] ANDERS, F. B.: Dynamics of large anisotropic spin in a sub-ohmic dissipative environment close to a quantum-phase transition. In: *New Journal of Physics* 10 (2008), No. 11, p. 115007. doi: [10.1088/1367-2630/10/11/115007](https://doi.org/10.1088/1367-2630/10/11/115007)
- [120] LEGGETT, A. J.: Quantum tunneling in the presence of an arbitrary linear dissipation mechanism. In: *Phys. Rev. B* 30 (1984), p. 1208–1218. doi: [10.1103/PhysRevB.30.1208](https://doi.org/10.1103/PhysRevB.30.1208)
- [121] KEHREIN, S. K.; MIELKE, A.: On the spin-boson model with a sub-ohmic bath. In: *Physics Letters A* 219 (1996), No. 5–6, p. 313 – 318. doi: [10.1016/0375-9601\(96\)00475-6](https://doi.org/10.1016/0375-9601(96)00475-6)
- [122] LUIJTEN, E.; BLÖTE, Henk W. J.: Classical critical behavior of spin models with long-range interactions. In: *Phys. Rev. B* 56 (1997), p. 8945–8958. doi: [10.1103/PhysRevB.56.8945](https://doi.org/10.1103/PhysRevB.56.8945)
- [123] SPOHN, H.; DÜMCKE, R.: Quantum tunneling with dissipation and the Ising model over \mathbb{R} . In: *Journal of Statistical Physics* 41 (1985), p. 389–423. doi: [10.1007/BF01009015](https://doi.org/10.1007/BF01009015)
- [124] VOJTA, M.; TONG, N.-H.; BULLA, R.: Quantum Phase Transitions in the Sub-Ohmic Spin-Boson Model: Failure of the Quantum-Classical Mapping. In: *Phys. Rev. Lett.* 94 (2005), p. 070604. doi: [10.1103/PhysRevLett.94.070604](https://doi.org/10.1103/PhysRevLett.94.070604)
- [125] VOJTA, M.: Impurity quantum phase transitions. In: *Philosophical Magazine* 86 (2006), No. 13-14, p. 1807–1846. doi: [10.1080/14786430500070396](https://doi.org/10.1080/14786430500070396)
- [126] FISHER, M. E.; MA, S.-k.; NICKEL, B. G.: Critical Exponents for Long-Range Interactions. In: *Phys. Rev. Lett.* 29 (1972), p. 917–920. doi: [10.1103/PhysRevLett.29.917](https://doi.org/10.1103/PhysRevLett.29.917)
- [127] WINTER, A.; RIEGER, H.; VOJTA, M.; BULLA, R.: Quantum Phase Transition in the Sub-Ohmic Spin-Boson Model: Quantum Monte Carlo Study with a Continuous Imaginary Time Cluster Algorithm. In: *Phys. Rev. Lett.* 102 (2009), p. 030601. doi: [10.1103/PhysRevLett.102.030601](https://doi.org/10.1103/PhysRevLett.102.030601)
- [128] GUO, C.; WEICHELBAUM, A.; VON DELFT, J.; VOJTA, M.: Critical and Strong-Coupling Phases in One- and Two-Bath Spin-Boson Models. In: *Phys. Rev. Lett.* 108 (2012), p. 160401. doi: [10.1103/PhysRevLett.108.160401](https://doi.org/10.1103/PhysRevLett.108.160401)
- [129] HOU, Y.-H.; TONG, N.-H.: Criticality of the mean-field spin-boson model: boson state truncation and its scaling analysis. In: *The European Physical Journal B - Condensed Matter and Complex Systems* 78 (2010), p. 127–135. doi: [10.1140/epjb/e2010-10426-0](https://doi.org/10.1140/epjb/e2010-10426-0)
- [130] TONG, N.-H.; HOU, Y.-H.: Scaling analysis in the numerical renormalization group study of the sub-Ohmic spin-boson model. In: *Phys. Rev. B* 85 (2012), p. 144425. doi: [10.1103/PhysRevB.85.144425](https://doi.org/10.1103/PhysRevB.85.144425)
- [131] KIRCHNER, S.; INGERSENT, K.; SI, Q.: Quantum criticality of the sub-Ohmic spin-boson model. In: *Phys. Rev. B* 85 (2012), p. 075113. doi: [10.1103/PhysRevB.85.075113](https://doi.org/10.1103/PhysRevB.85.075113)
- [132] ZHANG, Y.-Y.; CHEN, Q.-H.; WANG, K.-L.: Quantum phase transition in the sub-Ohmic spin-boson model: An extended coherent-state approach. In: *Phys. Rev. B* 81 (2010), p. 121105. doi: [10.1103/PhysRevB.81.121105](https://doi.org/10.1103/PhysRevB.81.121105)
- [133] CHIN, A. W.; PRIOR, J.; HUELGA, S. F.; PLENIO, M. B.: Generalized Polaron Ansatz for the Ground State of the Sub-Ohmic Spin-Boson Model: An Analytic Theory of the Localization Transition. In: *Phys. Rev. Lett.* 107 (2011), p. 160601. doi: [10.1103/PhysRevLett.107.160601](https://doi.org/10.1103/PhysRevLett.107.160601)
- [134] TORNOW, S.; TONG, N.-H.; BULLA, R.: Electron transfer in donor-acceptor systems: Many-particle effects and influence of electronic correlations. In: *Europhysics Letters* 73 (2006), No. 6, p. 913. doi: [10.1209/epl/i2005-10479-1](https://doi.org/10.1209/epl/i2005-10479-1)

- [135] ONDRECHEN, M. J.; RATNER, M. A.: Intramolecular electron transfer in simple model systems: A propagator study. In: *Journal of Chemical Physics* 66 (1977), p. 938. doi: [10.1063/1.434002](https://doi.org/10.1063/1.434002)
- [136] TORNOW, S.; BULLA, R.; ANDERS, F. B.; NITZAN, A.: Dissipative two-electron transfer: A numerical renormalization group study. In: *Phys. Rev. B* 78 (2008), p. 035434. doi: [10.1103/PhysRevB.78.035434](https://doi.org/10.1103/PhysRevB.78.035434)
- [137] KLEINE, C.: *Zwei-Elektronen-Transfer in einem Donator-Akzeptor-System*, TU Dortmund, Master thesis, 2011
- [138] TONG, N.-H.; VOJTA, M.: Signatures of a Noise-Induced Quantum Phase Transition in a Mesoscopic Metal Ring. In: *Phys. Rev. Lett.* 97 (2006), p. 016802. doi: [10.1103/PhysRevLett.97.016802](https://doi.org/10.1103/PhysRevLett.97.016802)
- [139] LOTH, S.; BAUMANN, S.; LUTZ, C. P.; EIGLER, D. M.; HEINRICH, A. J.: Bistability in Atomic-Scale Antiferromagnets. In: *Science* 335 (2012), No. 6065, p. 196–199. doi: [10.1126/science.1214131](https://doi.org/10.1126/science.1214131)
- [140] PLA, J. J.; TAN, K. Y.; DEHOLLAIN, J. P.; LIM, W. H.; MORTON, J. J. L.; JAMIESON, D. N.; DZURAK, A. S.; MORELLO, A.: A single-atom electron spin qubit in silicon. In: *Nature* 489 (2012), No. 7417, p. 541–545. doi: [10.1038/nature11449](https://doi.org/10.1038/nature11449)
- [141] PALMA, G. M.; SUOMINEN, K.-A.; EKERT, A. K.: Quantum Computers and Dissipation. In: *Proceedings of the Royal Society of London. Series A: Mathematical, Physical and Engineering Sciences* 452 (1996), No. 1946, p. 567–584. doi: [10.1098/rspa.1996.0029](https://doi.org/10.1098/rspa.1996.0029)
- [142] THORWART, M.; HÄNGGL, P.: Decoherence and dissipation during a quantum XOR gate operation. In: *Phys. Rev. A* 65 (2001), p. 012309. doi: [10.1103/PhysRevA.65.012309](https://doi.org/10.1103/PhysRevA.65.012309)
- [143] MONROE, C.; MEEKHOF, D. M.; KING, B. E.; ITANO, W. M.; WINELAND, D. J.: Demonstration of a Fundamental Quantum Logic Gate. In: *Phys. Rev. Lett.* 75 (1995), p. 4714–4717. doi: [10.1103/PhysRevLett.75.4714](https://doi.org/10.1103/PhysRevLett.75.4714)
- [144] ALVERMANN, A.; FEHSKE, H.; TRUGMAN, S. A.: Polarons and slow quantum phonons. In: *Phys. Rev. B* 81 (2010), p. 165113. doi: [10.1103/PhysRevB.81.165113](https://doi.org/10.1103/PhysRevB.81.165113)
- [145] PETTA, J. R.; JOHNSON, A. C.; TAYLOR, J. M.; LAIRD, E. A.; YACOBY, A.; LUKIN, M. D.; MARCUS, C. M.; HANSON, M. P.; GOSSARD, A. C.: Coherent Manipulation of Coupled Electron Spins in Semiconductor Quantum Dots. In: *Science* 309 (2005), No. 5744, p. 2180–2184. doi: [10.1126/science.1116955](https://doi.org/10.1126/science.1116955)
- [146] GAUDREAU, L.; GRANGER, G.; KAM, A.; AERS, G. C.; STUDENIKIN, S. A.; ZAWADZKI, P.; PIORO-LADRIERE, M.; WASILEWSKI, Z. R.; SACHRAJDA, A. S.: Sachrajda, A. S. In: *Nature Physics* 8 (2012), p. 54–58. doi: [10.1038/nphys2149](https://doi.org/10.1038/nphys2149)
- [147] VIGMAN, P. B.; FINKEL'SHTEIN, A. M.: Resonant-level model in the Kondo problem. In: *Sov. Phys. JETP* 48 (1978), No. 1, p. 102–107.
<http://www.jetp.ac.ru/cgi-bin/e/index/e/48/1/p102?a=list>
- [148] BORDA, L.; VLADÁR, K.; ZAWADOWSKI, A.: Theory of a resonant level coupled to several conduction-electron channels in equilibrium and out of equilibrium. In: *Phys. Rev. B* 75 (2007), p. 125107. doi: [10.1103/PhysRevB.75.125107](https://doi.org/10.1103/PhysRevB.75.125107)
- [149] YOSHIDA, M.; WHITAKER, M. A.; OLIVEIRA, L. N.: Renormalization-group calculation of excitation properties for impurity models. In: *Phys. Rev. B* 41 (1990), p. 9403–9414. doi: [10.1103/PhysRevB.41.9403](https://doi.org/10.1103/PhysRevB.41.9403)
- [150] ŽITKO, Rok: Quantitative determination of the discretization and truncation errors in numerical renormalization-group calculations of spectral functions. In: *Phys. Rev. B* 84 (2011), p. 085142. doi: [10.1103/PhysRevB.84.085142](https://doi.org/10.1103/PhysRevB.84.085142)
- [151] SCHOTTE, K. D.; SCHOTTE, U.: Interpretation of Kondo experiments in a magnetic field. In: *Physics Letters A* 55 (1975), No. 1, p. 38 – 40. doi: [10.1016/0375-9601\(75\)90386-2](https://doi.org/10.1016/0375-9601(75)90386-2)

- [152] JAUHO, A.-P.; WINGREEN, N. S.; MEIR, Y.: Time-dependent transport in interacting and non-interacting resonant-tunneling systems. In: *Phys. Rev. B* 50 (1994), p. 5528–5544. doi: [10.1103/PhysRevB.50.5528](https://doi.org/10.1103/PhysRevB.50.5528)
- [153] NAZAROV, Y. V.; BLANTER, Y. M.: *Quantum Transport: Introduction to Nanoscience*. Cambridge University Press, 2009
- [154] MEIR, Y.; WINGREEN, N. S.: Landauer formula for the current through an interacting electron region. In: *Phys. Rev. Lett.* 68 (1992), p. 2512–2515. doi: [10.1103/PhysRevLett.68.2512](https://doi.org/10.1103/PhysRevLett.68.2512)
- [155] SCHMITTECKERT, P.: Calculating Green functions from finite systems. In: *Journal of Physics: Conference Series* 220 (2010), No. 1, p. 012022. doi: [10.1088/1742-6596/220/1/012022](https://doi.org/10.1088/1742-6596/220/1/012022)
- [156] GROSSO, G.; PASTORI PARRAVICINI, G.: *Continued Fractions in the Theory of Relaxation*. Volume 62. p. 81–132. In: *Advances in Chemical Physics* Volume 62, John Wiley & Sons, Inc., 1985, doi: [10.1002/9780470142868.ch3](https://doi.org/10.1002/9780470142868.ch3)
- [157] LEBANON, E.; SCHILLER, A.; ANDERS, F. B.: Enhancement of the two-channel Kondo effect in single-electron boxes. In: *Phys. Rev. B* 68 (2003), p. 155301. doi: [10.1103/PhysRevB.68.155301](https://doi.org/10.1103/PhysRevB.68.155301)
- [158] DAVIDSON, E. R.: The iterative calculation of a few of the lowest eigenvalues and corresponding eigenvectors of large real-symmetric matrices. In: *Journal of Computational Physics* 17 (1975), No. 1, p. 87 – 94. doi: [10.1016/0021-9991\(75\)90065-0](https://doi.org/10.1016/0021-9991(75)90065-0)
- [159] LINDEN, N.; POPESCU, S.; SHORT, A. J.; WINTER, A.: Quantum mechanical evolution towards thermal equilibrium. In: *Phys. Rev. E* 79 (2009), p. 061103. doi: [10.1103/PhysRevE.79.061103](https://doi.org/10.1103/PhysRevE.79.061103)
- [160] METZNER, W.; SALMHOFER, M.; HONERKAMP, C.; MEDEN, V.; SCHÖNHAMMER, K.: Functional renormalization group approach to correlated fermion systems. In: *Rev. Mod. Phys.* 84 (2012), p. 299–352. doi: [10.1103/RevModPhys.84.299](https://doi.org/10.1103/RevModPhys.84.299)
- [161] SCHOELLER, H.: A perturbative nonequilibrium renormalization group method for dissipative quantum mechanics. In: *The European Physical Journal - Special Topics* 168 (2009), p. 179–266. doi: [10.1140/epjst/e2009-00962-3](https://doi.org/10.1140/epjst/e2009-00962-3)
- [162] KARRASCH, C.; ANDERGASSEN, S.; PLETYUKHOV, M.; SCHURICHT, D.; BORDA, L.; MEDEN, V.; SCHOELLER, H.: Non-equilibrium current and relaxation dynamics of a charge-fluctuating quantum dot. In: *EPL (Europhysics Letters)* 90 (2010), No. 3, p. 30003. doi: [10.1209/0295-5075/90/30003](https://doi.org/10.1209/0295-5075/90/30003)
- [163] ANDERGASSEN, S.; PLETYUKHOV, M.; SCHURICHT, D.; SCHOELLER, H.; BORDA, L.: Renormalization group analysis of the interacting resonant-level model at finite bias: Generic analytic study of static properties and quench dynamics. In: *Phys. Rev. B* 83 (2011), p. 205103. doi: [10.1103/PhysRevB.83.205103](https://doi.org/10.1103/PhysRevB.83.205103)
- [164] KENNES, D. M.; MEDEN, V.: Quench dynamics of correlated quantum dots. In: *Phys. Rev. B* 85 (2012), p. 245101. doi: [10.1103/PhysRevB.85.245101](https://doi.org/10.1103/PhysRevB.85.245101)
- [165] BOULAT, E.; SALEUR, H.; SCHMITTECKERT, P.: Twofold Advance in the Theoretical Understanding of Far-From-Equilibrium Properties of Interacting Nanostructures. In: *Phys. Rev. Lett.* 101 (2008), p. 140601. doi: [10.1103/PhysRevLett.101.140601](https://doi.org/10.1103/PhysRevLett.101.140601)
- [166] BRANSCHÄDEL, A.; SCHNEIDER, G.; SCHMITTECKERT, P.: Conductance of inhomogeneous systems: Real-time dynamics. In: *Annalen der Physik* 522 (2010), No. 9, p. 657–678. doi: [10.1002/andp.201000017](https://doi.org/10.1002/andp.201000017)
- [167] CARR, S. T.; BAGRETS, D. A.; SCHMITTECKERT, P.: Full Counting Statistics in the Self-Dual Interacting Resonant Level Model. In: *Phys. Rev. Lett.* 107 (2011), p. 206801. doi: [10.1103/PhysRevLett.107.206801](https://doi.org/10.1103/PhysRevLett.107.206801)

- [168] BORDA, L.; SCHILLER, A.; ZAWADOWSKI, A.: Applicability of bosonization and the Anderson-Yuval methods at the strong-coupling limit of quantum impurity problems. In: *Phys. Rev. B* 78 (2008), p. 201301. doi: [10.1103/PhysRevB.78.201301](https://doi.org/10.1103/PhysRevB.78.201301)
- [169] NISHINO, A.; HATANO, N.: Resonance in an Open Quantum Dot System with a Coulomb Interaction: a Bethe-Ansatz Approach. In: *Journal of the Physical Society of Japan* 76 (2007), No. 6, p. 063002. doi: [10.1143/JPSJ.76.063002](https://doi.org/10.1143/JPSJ.76.063002)
- [170] DOYON, B.: New Method for Studying Steady States in Quantum Impurity Problems: The Interacting Resonant Level Model. In: *Phys. Rev. Lett.* 99 (2007), p. 076806. doi: [10.1103/PhysRevLett.99.076806](https://doi.org/10.1103/PhysRevLett.99.076806)
- [171] ANDERSON, P. W.: Infrared Catastrophe in Fermi Gases with Local Scattering Potentials. In: *Phys. Rev. Lett.* 18 (1967), p. 1049–1051. doi: [10.1103/PhysRevLett.18.1049](https://doi.org/10.1103/PhysRevLett.18.1049)
- [172] WEICHELBAUM, A.; MÜNDELER, W.; VON DELFT, J.: Anderson orthogonality and the numerical renormalization group. In: *Phys. Rev. B* 84 (2011), p. 075137. doi: [10.1103/PhysRevB.84.075137](https://doi.org/10.1103/PhysRevB.84.075137)
- [173] MÜNDELER, W.; WEICHELBAUM, A.; GOLDSTEIN, M.; GEFEN, Y.; VON DELFT, J.: Anderson orthogonality in the dynamics after a local quantum quench. In: *Phys. Rev. B* 85 (2012), p. 235104. doi: [10.1103/PhysRevB.85.235104](https://doi.org/10.1103/PhysRevB.85.235104)
- [174] POLKOVNIKOV, A.; SENGUPTA, K.; SILVA, A.; VENGALATTORE, M.: *Colloquium*: Nonequilibrium dynamics of closed interacting quantum systems. In: *Rev. Mod. Phys.* 83 (2011), p. 863–883. doi: [10.1103/RevModPhys.83.863](https://doi.org/10.1103/RevModPhys.83.863)
- [175] BORDA, L.; ZAWADOWSKI, A.: Perturbative treatment of the multichannel interacting resonant-level model in steady-state nonequilibrium. In: *Phys. Rev. B* 81 (2010), p. 153303. doi: [10.1103/PhysRevB.81.153303](https://doi.org/10.1103/PhysRevB.81.153303)
- [176] NISHINO, A.; IMAMURA, T.; HATANO, N.: $I - V$ characteristics of an open quantum dot with a Coulomb interaction: Extension of the Landauer formula with exact scattering eigenstates. In: *Phys. Rev. B* 83 (2011), p. 035306. doi: [10.1103/PhysRevB.83.035306](https://doi.org/10.1103/PhysRevB.83.035306)
- [177] GOBERT, D.; KOLLATH, C.; SCHOLLWÖCK, U.; SCHÜTZ, G.: Real-time dynamics in spin- $\frac{1}{2}$ chains with adaptive time-dependent density matrix renormalization group. In: *Phys. Rev. E* 71 (2005), p. 036102. doi: [10.1103/PhysRevE.71.036102](https://doi.org/10.1103/PhysRevE.71.036102)
- [178] ANDERS, F.B.: *Dissipative bosonic model (DBM)*. 2009. – private communication
- [179] BLAIZOT, J.-P.; RIPKA, G.: *Quantum Theory of Finite Systems*. The MIT Press, 1986
- [180] COLPA, J. H. P.: Diagonalization of the quadratic boson hamiltonian. In: *Physica A: Statistical and Theoretical Physics* 93 (1978), No. 3-4, p. 327 – 353. doi: [DOI: 10.1016/0378-4371\(78\)90160-7](https://doi.org/10.1016/0378-4371(78)90160-7)
- [181] COLPA, J. H. P.: Diagonalization of the quadratic boson Hamiltonian with zero modes: I. Mathematical. In: *Physica A: Statistical and Theoretical Physics* 134 (1986), No. 2, p. 377 – 416. doi: [10.1016/0378-4371\(86\)90056-7](https://doi.org/10.1016/0378-4371(86)90056-7)
- [182] COLPA, J. H. P.: Diagonalization of the quadratic boson Hamiltonian with zero modes: II. Physical. In: *Physica A: Statistical and Theoretical Physics* 134 (1986), No. 2, p. 417 – 442. doi: [10.1016/0378-4371\(86\)90057-9](https://doi.org/10.1016/0378-4371(86)90057-9)
- [183] SCHILLER, A.: *Interaction-induced oscillations: A strong-coupling treatment*. May 2012. – private communication

Acknowledgments

At the end of this thesis I wish to express my gratitude to all those who supported me. Special thanks go to various people:

- First of all, I want to thank Frithjof Anders for giving me the opportunity to work in his group. I am grateful for his interest in my work, his support, that he always has time to answer questions or discuss difficulties (though he has other urgent matters on his schedule), and his "Daumenschrauben".
- Götz Uhrig for co-refereeing this work.
- Avi Schiller's very kind hospitality made my stay in Jerusalem great. Thanks for showing me around the city and spending time with me discussing the real-time dynamics of the interacting resonant-level model.
- Hard to imagine how it would have been without Sebastian Schmitt. I would have missed endless discussions concerning all possible topics (occasionally even about physics) and a lot of fun hours in and out of the office. Luckily, this is not the case ...
- Tim Fischer for his heroic effort to proofread the whole manuscript and Julian Güttge for valuable advice regarding the layout of this thesis.
- Carsten Raas for keeping the computers up and running.
- My colleagues Johannes Hackmann, Jasmin Jäger, Andre Jovchev, Christian Kleine, Benedikt Lechtenberg, and Jan Stubben for the distraction during working hours – how could I have survived without?
- The current and former members of the T1 and T2 chairs for the pleasant working atmosphere, which I very much appreciate.
- Finally, my parents, sister, brothers, and close friends for their support.

Lebenslauf

Name	Fabian Christopher Güttge
Geburtsdatum	29. Juni 1983
Geburtsort	Köln
08/1989 – 07/1993	Donatus Grundschule, Erftstadt
08/1993 – 07/1995	Gottfried-Kinkel-Realschule, Erftstadt
08/1995 – 06/2002	Ville Gymnasium Erftstadt
06/2002	Abitur
07/2002 – 04/2003	Zivildienst ASB Erftstadt
04/2003 – 12/2008	Studium der Physik an der RWTH Aachen
04/2005	Vordiplom
01/2006 – 05/2006	Auslandssemester an der Technischen Hochschule Helsinki, Finnland
06/2007 – 10/2008	Diplomarbeit am Institut für Theoretische Physik C, RWTH Aachen, Prof. Dr. U. Schollwöck: <i>Simulationen quantenmechanischer Systeme im thermodynamischen Limes</i>
12/2008	Diplom
seit 04/2009	Promotionsstudium an der TU Dortmund, Institut für Theoretische Physik II. Betreuer: Prof. Dr. F. Anders
09/2011	Forschungsaufenthalt an der Hebräischen Universität Jerusalem, Israel